# Stochastic Models of Ion Channel Dynamics and Their Role in Short-Term Repolarisation Variability in Cardiac Cells

**Ciara Ellen Dangerfield**
**New College**

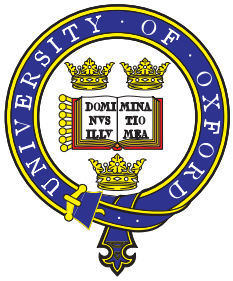


Computational Biology Research Group
Computing Laboratory
University of Oxford

**Michaelmas Term 2012**

This thesis is submitted to the Computing Laboratory, University of Oxford, for the degree of Doctor of Philosophy. This thesis is entirely my own work, and, except where otherwise indicated, describes my own research.

Ciara Ellen Dangerfield
New College

Doctor of Philosophy
Michaelmas Term 2012

# Stochastic Models of Ion Channel Dynamics and Their Role in Short-Term Repolarisation Variability in Cardiac Cells

## Abstract

Sudden cardiac death due to the development of lethal arrhythmias is the dominant cause of mortality in the UK, yet the mechanisms underlying their onset, maintenance and termination are still poorly understood. Therefore biomarkers are used to determine arrhythmic risk within patients and of new drug compounds. In recent years, the magnitude of variations in the length of successive beats, measured over a short period of time, has been shown to be a powerful predictor of arrhythmic risk. This beat-to-beat variability is thought to be the manifestation of the random opening and closing dynamics of individual ion channels that lie within the membrane of cardiac cells. Computational models have become an important tool in understanding the electrophysiology of the heart. However, current state-of-the-art electrophysiology models do not incorporate this intrinsic stochastic behaviour of ion channels. Those that do use computationally costly methods, restricting their use in complex tissue scale simulations, or employ stochastic simulation methods that result in negative numbers of channels and so are inaccurate. Therefore, using current stochastic modelling techniques to investigate the role of stochastic ion channel behaviour in beat-to-beat variability presents difficulties.

In this thesis we take a mathematically rigorous and novel approach to develop accurate and computationally efficient models of stochastic ion channel dynamics that can be incorporated into existing electrophysiology models. Two different models of stochastic ion channel behaviour, both based on a system of stochastic differential equations (SDEs), are developed and compared. The first model is based on an existing SDE model from population dynamics called the Wright-Fisher model. The second approach incorporates boundary conditions into the SDE model of ion channel dynamics that is obtained in the limit from the discrete-state Markov chain model, and is called a reflected SDE. Of these two methods, the reflected SDE is found to more accurately capture the stochastic dynamics of the discrete-state Markov chain, seen as the 'gold-standard' model and also provides substantial computational speed up. Thus the reflected SDE is an accurate and efficient model of stochastic ion channel dynamics and so allows for detailed investigation into beat-to-beat variability using complex computational electrophysiology models. We illustrate the potential power of this method by incorporating it into a state-of-the-art canine cardiac cell electrophsyiology model so as to explore the effects of stochastic ion channel behaviour on beat-to-beat variability. The stochastic models presented in this thesis fulfil an important role in elucidating the effects of stochastic ion channel behaviour on beat-to-beat variability, a potentially important biomarker of arrhythmic risk.

# Publications

Below are a list of publications which directly relate to the work described in this Thesis.

- **C. E. Dangerfield**, D. Kay and K. Burrage, Modeling ion channel dynamics through reflected stochastic differential equations, *Phys Rev E*, vol. 85, no. 5, 2012.
- **C. E. Dangerfield** D. Kay S. Macnamara and K. Burrage, A Boundary Preserving Numerical Algorithm for the WrightFisher Model with Mutation, *BIT Num. Math*, vol. 52, issue 2, 283-304, 2012.
- **C. E. Dangerfield**, D. Kay, and K. Burrage, Comparison of Continuous and Discrete Stochastic Ion Channel Models, *Proceedings of Annual International Conference of the IEEE*, 704-707, 2011.
- **C E Dangerfield**, D Kay, K Burrage, Stochastic models and simulation of ion channel dynamics, *Procedia Computer Science*, vol 1, 1581-1590, 2010.

# Contents

# Acknowledgements

Firstly, I would like to sincerely thank my supervisors, Dr Blanca Rodriguez, Dr David Kay and Prof. Kevin Burrage, for their guidance and assistance throughout the course of my D.Phil. I would particularly like to thank Kevin for helping to shape the overall direction of my thesis and the amount of time and effort he has contributed to my development as a research student. I would like to thank David for his invaluable input in the mathematical aspects of this thesis and his patient guidance in this area. I would like to thank Blanca for helping to shape the final part of this thesis as well as the time, effort and energy she has contributed to my understanding of cardiac electrophysiology and my development as an academic writer.

I must also acknowledge and give thanks for the help and support of my collaborators: Dr Esther Pueyo for her invaluable input into the simulation study in the final part of this thesis, Oliver Britton for performing the parameter sweeps used to construct the population of models in Chapter 8 and Dr. Norbert Szentandrássy and Dr. Laszlo Virag for providing the single cell experimental data. I must thank the members of the Computational Biology research group. Much of my work would not have been possible without the knowledge and support of members of the group, but, more importantly, the many students, researchers and academics have all contributed to creating a stimulating and enjoyable place to work.

I would like to acknowledge the support of the Engineering and Physical Sciences Research Council, who provided funding for my D.Phil through the Life Sciences Interface Doctoral Training Centre.

Finally, I must thank my family and friends for their unwavering support throughout my D.Phil. In particular, I must thank Justin Pinkney who always made me smile through the good and bad times and put on the right meatloaf song when I needed it. I also want to thank my parents for all their encouragement and support throughout my educational studies, without which I would never have made it this far.

# Notation

| | |
|---|---|
| $V$ | Transmembrane Potential |
| BVR | Beat-to-beat variability in repolarisation duration |
| AP | Action potential |
| APD | Action potential duration |
| $APD_{90}$ | Action potential duration at 90% repolarisation |
| $STV_{APD90}$ | Short-term variability in $APD_{90}$ |
| SDE | Stochastic differential equation |
| ODE | Ordinary differential equation |
| PDE | Partial differential equation |
| $N$ | Number of channels |
| Std | Standard deviation |
| Var | Variance |

# 1

# Introduction

## 1.1 Motivation

Sudden cardiac death (SCD) is one of the major causes of death in Western society. It is a condition where the heart suddenly stops beating, preventing the flow of blood to the brain and other vital organs, and unless treated immediately death rapidly ensues. Cardiovascular disease is the main cause of SCD and in 2008 it accounted for 15% of all deaths in the UK (88,236 people) [1]. Adverse effects of drugs on the heart can also lead to SCD and are one of the main reasons for new drug compounds not reaching the market, at great cost to the pharmaceutical companies and society. Genetic mutations that alter the normal functioning of the heart are another common cause of SCD. The great social and economic costs associated with SCD have prompted huge investment into understanding its causes and underlying mechanisms.

SCD usually occurs due to the development of lethal cardiac arrhythmias such as ventricular fibrillation (VF). Cardiac arrhythmias occur when the electrical wave of excitation, which controls the beating of the heart, becomes disrupted, leading to uncoordinated patterns of electrical excitation. This in turn results in irregular cardiac contractions, severely compromising the efficiency of the pumping action of the heart and reducing the flow of blood around the body. A large area of research into understanding the mechanisms underlying life-threatening arrhyth-

[1] Source: British Heart Foundation (www.bhf.org.uk, www.heartstats.org/eucosts)

mias has developed over the last few decades, which in turn could lead to improved treatment. Furthermore, due to the unpredictable nature of exactly when and how arrhythmias are initiated within an individual, research in this area has identified a number of characteristics of the electrical behaviour of the heart that correlate with the incidence of arrhythmia. Such characteristics are termed *biomarkers* and are used at the single cell, tissue and whole organ level in order to determine the likelihood of arrhythmias occurring both clinically and preclinically. For example, measurements from electrocardiogram (ECG) recordings on patients, such as the QT interval, are used to predict an individual's arrhythmic risk.

Starting with the seminal paper by Noble in 1962 (Noble, 1962), computational models of cardiac electrophysiology have played a pivotal role in furthering understanding of the electrical dynamics of the heart. This is in part due to the fact that they allow for investigation over a much larger range of spatial and temporal scales than experiments alone provide. This is of great importance when studying the dynamics of a multiscale system such as the heart, where alterations at the ionic level can result in significant changes to the dynamics at the whole organ level. With increased computing power, and the development of sophisticated simulation algorithms, cardiac models are now able to capture many of the highly complex features of cardiac electrophysiology in a detailed and efficient manner. This has led to greater mechanistic understanding than experiments alone can provide, as well as helping to identify potential new biomarkers of arrhythmic risk.

One of the main challenges in the investigation of cardiac arrhythmias is the heterogeneity and variability of the electrical dynamics of the heart. Different individuals react differently to the same conditions, and even cells from the same individual can exhibit dramatically different responses under identical circumstances. Furthermore, many cardiac electrophysiology processes, such as the random opening and closing of ion channels within the membrane of cardiac cells, are intrinsically stochastic. This randomness that arises due to factors both extrinsic and intrinsic to the system, introduces both spatial and temporal variability into the electrical

dynamics of the heart.

In experiments and clinical studies, variations in the duration of consecutive cardiac beats within an individual are observed over short periods of time. This phenomenon is termed beat-to-beat variability, and in recent years has become a topic of intensive research as the magnitude of these variations are conjectured to be related to the onset of drug or disease induced arrhythmias, (Hinterseer et al., 2010; Abi-Gerges et al., 2010; Thomsen et al., 2004, 2006). Furthermore, this temporal variability has been found to correlate well with the development of arrhythmias, where greater variations signify higher risk of arrhythmia within an individual, (Oosterhoff et al., 2007; Hinterseer et al., 2009). Therefore, beat-to-beat variability has been proposed as a potentially highly effective biomarker for determining an individual's risk of developing life-threatening arrhythmias. This biomarker has also been shown to be predictive of proarrhythmic potential of new drug compounds, both at the single cell, (Abi-Gerges et al., 2010) and tissue level (Thomsen et al., 2004). This temporal variability could therefore lead to better diagnosis of patients at high arrhythmic risk, as well as identifying drugs with unwanted effects on the dynamics of the heart early in the drug development process.

It has been hypothesised that beat-to-beat variability is the manifestation of the stochastic opening and closing behaviour of ion channels that lie within the membrane of cardiac cells, (Zaniboni et al., 2000; Pueyo et al., 2011; Lemay et al., 2011). Due to the multiscale nature of cardiac electrophsyiology, investigating such a hypothesis using experiments alone is challenging, therefore computational models provide a powerful tool to elucidate the role of stochastic ion channel behaviour in beat-to-beat variability. However, most cardiac electrophsyiology models are deterministic and so unable to capture beat-to-beat variability. Therefore, incorporating stochastic ion channel dynamics into cardiac cell models is crucial to allow for investigation of potential mechanisms underlying beat-to-beat variability as well as to further understanding into their link to arrhythmias.

The recent studies by Lemay et al. (2011) and Pueyo et al. (2011) have investigated the hypoth-

esis that stochastic ion channel dynamics cause beat-to-beat variability. However, in (Pueyo et al., 2011) the stochastic behaviour of only one type of ion channel is considered, while Lemay et al. (2011) take a purely computational approach. Furthermore, both these studies use a fixed conductance for each current, and only vary the number of channels in each simulation according to some predefined statistical distribution. In this thesis we build on these investigations to explore the effects of stochastic ion channel dynamics on beat-to-beat variability in a canine cardiac myocyte. As in (Pueyo et al., 2011), we use a combined experimental and computational approach to construct models that capture the stochastic behaviour of a number of different ionic currents, rather than just one as in (Pueyo et al., 2011). Furthermore, we take a novel approach to represent the differences in the conductance of ionic currents between cells by constructing a population of models, each with a unique parameter set, rather than just varying the number of channels as in (Pueyo et al., 2011) and (Lemay et al., 2011). This approach means that the results obtained are not linked to a particular parameter set, as in (Pueyo et al., 2011) and (Lemay et al., 2011).

There are three main modelling regimes that have previously been employed to describe the dynamics of ion channels. The first two capture the intrinsic stochastic behaviour of ion channel dynamics while the final regime ignores this stochastic behaviour, modelling the time evolution in the number of channels by an ordinary differential equation (ODE). The first stochastic modelling regime takes into account that ion channels are discrete entities and describes how the discrete number of channels that are open or closed varies over time, as a result of the random movement between these states. This approach is termed the *discrete-state Markov chain model* and is often seen as the 'gold-standard'. The second stochastic approach is obtained as an approximation from the discrete-state Markov chain model in the limit of large channel numbers (usually on the order of a few hundred) and uses a stochastic differential equation (SDE) to describe the time evolution in the *proportion* of open channels. The variance of the SDE model scales with $1/N$, where $N$ is the number of channels, and so converges to the ODE model in the

limit as $N$ tends to infinity; therefore the ODE model captures the mean ion channel dynamics. Unlike the discrete-state Markov chain model, the SDE model assumes that the random changes in the number of open channels over time is continuous, and so it does not account for the discrete nature of the ion channels, but is a good approximation to the discrete-state Markov chain model.

When the number of ion channels exceeds a few hundred, it becomes computationally intensive to simulate individual paths of the discrete-state Markov chain model. Furthermore, since each simulation results in a different outcome, multiple simulations are needed in order to calculate distributional properties in the number of open channels, such as the mean and the variance, further increasing the computational cost of employing such a model. Thus trying to incorporate such an approach into large-scale tissue simulations, or complex cardiac cell models typically involving as many as $48$ variables and, where a small time step must be taken in the simulation to resolve the highly nonlinear dynamics, quickly becomes computationally intractable. The SDE model can be simulated using one of the many existing numerical methods for approximating solutions to SDEs. Many of these are based on ODE numerical methods, and require little more computational cost than their ODE counterparts. Therefore, the SDE method is far more computationally efficient to simulate than the discrete-state Markov chain model, allowing multiple simulations to be performed for complex electrophysiology models both at the cell and tissue level. For this reason it has been employed in recent years to study stochastic ion channel behaviour within neurons (Fox, 1997; Sun et al., 2011), cardiac myocytes (Pueyo et al., 2011) and pancreatic beta cells (De Vries and Sherman, 2000).

However, solutions to the standard SDE model of ion channel dynamics can become negative and even imaginary when simulated using existing numerical methods, thus raising questions about the biological applicability of such an approach. Indeed this is a problem in the stochastic simulation of many biological systems (Higham, 2011). While this issue is frequently sidestepped by adjusting the numerical simulation method to force simulations to remain within a

biologically realistic region, (Pueyo et al., 2011), such methods may introduce bias, and indeed are not even guaranteed to converge to the SDE model. In recent years this issue with the SDE model has been highlighted, with a break down in the assumptions of the approximation and inadequacies of the numerical methods being put forward as potential causes for this problem, (Higham, 2011), (Gillespie, 2002). However, no thorough investigation into the root of this issue has been undertaken, nor has there been an accurate approach developed to overcome this issue. The development of modelling and numerical techniques that allow for computationally efficient and accurate simulation of ion channel dynamics are therefore needed to allow for investigation into the effects of stochastic ion channel behaviour on the electrical dynamics of complex cardiac cell and tissue models. Indeed such techniques are essential to allow for in-depth investigation into the role of stochastic ion channel behaviour in beat-to-beat variability, which is thought to be a potential biomarker of arrhythmic risk.

## 1.2 Thesis Goal

The goal of this thesis is two fold. Firstly it is the aim to develop a stochastic model of ion channel dynamics that is computationally efficient, and so allows for incorporation into complex cardiac cell electrophysiology models, as well as ensuring analytic and numerical solutions to this model remain in a biologically realistic region. The second objective is to use such methods to investigate the role of stochastic ion channel dynamics in beat-to-beat variability in electrophysiological function at single cell level.

As discussed in the previous section, incorporating a stochastic model of ion channel dynamics into existing cardiac cell models poses a computational challenge due to the complexity of state-of-the-art cardiac electrophysiology models. While the discrete-state Markov chain model represents the ‘gold standard’ method for simulating stochastic ion channel behaviour, it becomes computationally intractable when employed within cardiac electrophsyiology models. On the other hand the ODE model of ion channel dynamics is very computationally efficient,

but does not allow for investigation into beat-to-beat variability using computational electrophysiology models. Thus, a model that is computationally efficient to simulate but still captures the stochastic behaviour of ion channels is key to incorporating stochastic ion channel dynamics into existing electrophysiology models. The SDE model poses as the ideal candidate, since it provides a bridge between the discrete-state Markov chain and ODE modelling regimes. Due to the issues that arise in simulations of the SDE model, our first goal is to explore the SDE models of ion channel dynamics that ensure solutions remain within a biologically realistic region. Here we take two different approaches, firstly approximating the SDE model of ion channel dynamics by a different SDE whose analytic solutions, which are the proportion of open channels, are guaranteed to remain within the interval $[0, 1]$. Our second approach is to incorporate boundary conditions into the SDE model of ion channel dynamics directly, to ensure solutions remain positive.

The next goal is to construct the numerical methods to ensure that simulations of the two models preserve the boundaries of these equations. For the first approach, where the SDE model is approximated by another SDE, no numerical methods exist in the literature that ensure simulations preserve the boundaries inherent in the model. Therefore we construct such a method and show the strong convergence of this method. For the second approach, where boundary conditions are incorporated directly into the SDE model, we employ previously developed numerical methods. The two different approaches are then compared to determine which is the most accurate and computationally efficient for modelling ion channel dynamics within cell electrophsyiology models.

Few computational studies have investigated the role of stochastic ion channel behaviour in the beat-to-beat variability observed experimentally due to the difficulties of capturing this intrinsic stochastic behaviour within existing cardiac electrophysiology models. Therefore the final goal of this thesis is to use the methods developed here to investigate the role of stochastic ion channel dynamics on beat-to-beat variability in canine cardiac myocytes, using a combined

experimental and computational approach. Unlike previous studies, (Pueyo et al., 2011; Lemay et al., 2011), we account for cell-to-cell variations by constructing a population of stochastic models, each with a unique parameter set. Thus the stochastic model is not tied to a single parameter set, allowing for investigation into the effects of stochastic ion channel dynamics on beat-to-beat variability within different cells. Such a study is crucial to provide a better understanding into the role of stochastic ion channel behaviour on beat-to-beat variability, a potentially powerful biomarker of arrhythmic risk.

## 1.3 Outline of Thesis

We now describe the framework of this thesis and in particular highlight how the aims of this thesis will be addressed.

Chapter 2 provides the biological background on cardiac cell models underpinning the research undertaken in this thesis. The basic structure and function of the heart is described. In particular, we discuss the electrical dynamics of the heart, the role of ion channels in the normal electrical functioning of cardiac cells and the beat-to-beat variability observed experimentally. We also provide a review of the evidence suggesting that beat-to-beat variability is correlated to proarrhythmic behaviour, and so could be used to predict arrhythmic risk. The second part of this chapter is devoted to computational modelling of cardiac cell electrophysiology. We give a review of the history of this field, the current state and the basic structure of existing models of the electrical dynamics of cardiac cells. In particular, we discuss the recent studies that have investigated the effects of variability both within the cell and between cells on the electrical dynamics at the cell and tissue level. We end this chapter with a brief discussion of the experimental techniques employed to obtain the data that is used to construct the models in the final part of this thesis.

In Chapter 3 we describe in detail the different stochastic models of ion channel dynamics.

This chapter provides the mathematical foundation for the modelling and simulation techniques developed in this thesis. We begin by describing the discrete-state Markov chain model of ion channel dynamics for a simple two state model and extend this to a more general description of ion channel behaviour. We then provide mathematical background on SDEs and derive the SDE for the simple two state model and more general model of ion channel dynamics. The ODE model is also given and the link between these three modelling regimes discussed. Finally, we briefly review split-step numerical methods for ODEs and discuss how such techniques can be used to deal with the coupling of ion channel dynamics to the cell membrane potential.

The challenges in modelling ion channel dynamics using an SDE formulation, namely computational efficiency and biological accuracy, are described in Chapter 4. We show that by correct formulation of the model, in terms of the underlying discrete-state Markov chain model, the SDE model is computationally efficient whilst preserving relevant statistical properties of the discrete-state Markov chain model. The remainder of this chapter is devoted to an examination of why solutions to the SDE model can result in the proportion of open channels becoming negative. This analysis provides the rational behind the two different approaches taken in Chapters 5 and 6 in order to resolve the first goal of this thesis.

In Chapter 5 we address the first goal of this thesis by approximating the SDE model of ion channel dynamics by another system of SDEs, called the Wright-Fisher model. We briefly review numerical methods that try to preserve the boundaries inherent in the analytic solutions of SDEs and discuss why such methods are insufficient for our problem. We therefore derive a numerical method that ensures numerical solutions preserve the boundaries inherent in the Wright-Fisher SDE model. The strong convergence of this method is mathematically proved for the simple two state model of ion channel dynamics, and numerically shown for a more general model of ion channel dynamics.

In Chapter 6 an alternative approach is taken to address the first goal of this thesis. We show how boundary conditions can be imposed on the SDE model to ensure solutions remain within

a biologically realistic domain. The resulting system of equations are commonly referred to as reflected SDEs. We review numerical methods for approximating solutions to reflected SDEs and, in particular, describe the algorithm employed in this thesis.

In Chapter 7 we compare the SDE model from Chapter 5, and the reflected SDE model from Chapter 6, with the discrete-state Markov chain model, which is taken as the 'gold-standard'. The simplest cell electrophysiology model, namely the Hodgkin-Huxley model, is used to compare the first two moments in the proportion of open channels, statistics of the action potential and computational speed between the three methods. These results are used to determine the most efficient and accurate model of ion channel dynamics, achieving the first goal of this thesis.

Chapter 8 uses the most suitable model of ion channel dynamics, determined in Chapter 7, to investigate the effect of stochastic ion channel dynamics on beat-to-beat variability in experiments on canine ventricular myocytes. Such effects are investigated both under control conditions and under complete pharmacological block of individual ionic currents. Furthermore, to capture the variability between the different cells we construct a population of stochastic models, each with a unique parameter set. In this chapter we describe the construction of such a population of models and the simulations undertaken to investigate beat-to-beat variability.

We end this thesis with a discussion of the main contributions of this work to the fields of cardiac electrophysiology and stochastic modelling and simulation in Chapter 9. The possible avenues in which the work from this thesis could be extended are also reviewed.

# 2

# Biological Background

*In the first part of this chapter the structural and functional properties of the heart are presented. In particular, the electrical dynamics of cardiac cells and the role of ion channels are described. We also review the experimental work which indicates the potential importance of variability in cardiac electrical dynamics in predicting arrhythmic risk. The second part of the chapter is devoted to the computational models that have been developed to simulate the electrical dynamics of single cardiac myocytes. In particular, we discuss the recent computational studies investigating the causes of variability in the electrical dynamics of cardiac cells. Finally, we briefly describe the estimation of single ion channel properties within cardiac cell models from experimental data.*

## 2.1 Cardiac Physiology

The heart is a muscle that pumps blood around the body by repeated rhythmic contractions, transporting vital material to cells and removing waste via the blood. The rhythmic beating of the heart is called the cardiac cycle and occurs about 72 times per minute in a human, but can range from 30 to 150 beats per minute depending on the activity undertaken and the condition of the heart. Each contraction is controlled by electrical impulses that propagate through the

muscle tissue. In this section the basic anatomical structure of the heart is described and the mechanisms of electrical stimulation, which lead to the contraction of the heart, are explained.

### 2.1.1 Structure and Function of the Heart

**Figure 2.1** Diagram of cardiac structural anatomy for a longitudinal cross-section through the heart. The main features are labelled and the solid arrows indicate the direction of blood flow.

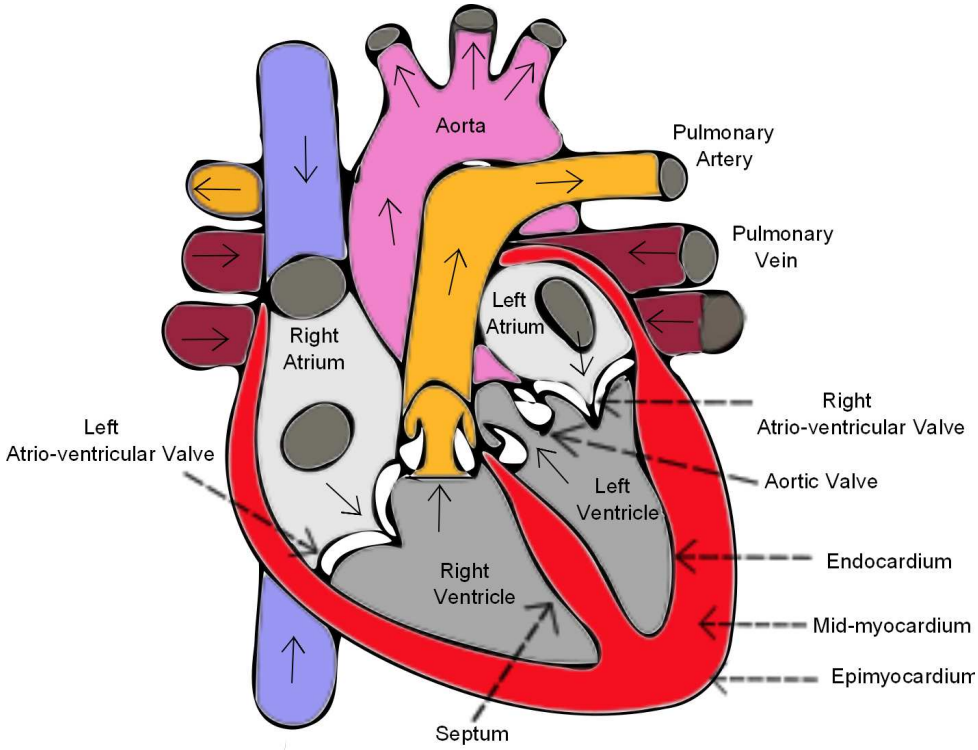


The anatomical structure of the mammalian heart is shown in Figure 2.1. The heart is primarily divided into a left and right side, separated by a muscular partition called the *septum*, and the two sides do not interact with one another. Each side is further divided into an upper chamber, called the *atrium* and a lower chamber, called the *ventricle*. De-oxygenated blood enters the heart through the *superior vena cava* in the right atrium. From here it passes into the right ventricle before being pumped into the lungs via the *pulmonary artery* where it is oxygenated. It then returns from the lungs to the left atrium via the *pulmonary vein* and passes into the left ventricle. Finally, oxygenated blood is pumped to the rest of the body via the *aortic valve*.

The upper and lower chambers exchange blood through an opening which is controlled by the *atrio-ventricular valve*, which ensures that blood flows in the right direction.

The heart is surrounded by a double-walled sac called the *pericardium*. It protects the heart, anchoring it to the surrounding structures as well as preventing the heart from overfilling with blood. The muscular walls of the heart are termed the *myocardium* and it varies in thickness, being thickest in the left ventricle, since the left ventricle pumps blood to the entire body, and is thinnest in the right ventricle, which only pumps blood to the nearby lungs. The myocardium is composed of three layers: the outer layer called the *epicardium*, the middle layer called the *mid-myocardium* and finally the *endocardium* is the name given to the inner layer. This inner layer is in contact with the blood and covers the heart valves. The electrophysiological properties of the cardiac cells in the different layers vary, leading to transmural heterogeneities in the electrical dynamics through the myocardium.

**Figure 2.2** Schematic of myocardial sheets and fibres.

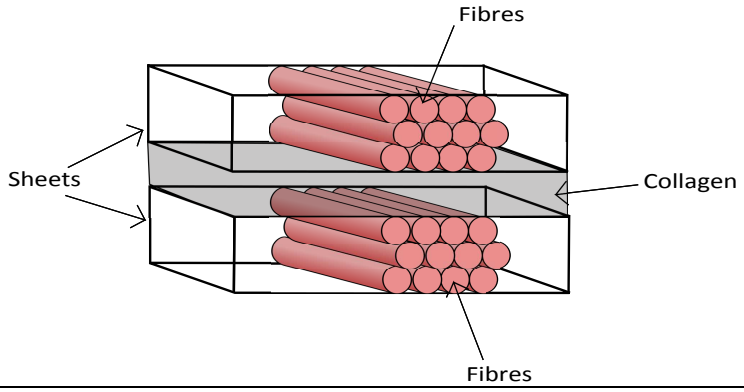


The architecture of the myocardium is very heterogeneous and is constructed from inter-connected sheets of tissue, shown in Figure 2.2 . Within these sheets, cardiac cells, typically $10 - 20\mu m$ in diameter and $50 - 100\mu m$ in length and termed *myocytes*, lie longitudinally to form fibres, shown in Figure 2.2. These fibres rotate to allow the heart to twist as it contracts, resulting in a more efficient pumping action. Alternating segments of thick and thin protein filaments give cardiac muscle its distinctive cross-striated pattern. *Intercalated discs* are cross-bands that

separate opposing ends of myocytes. They help hold myocytes together and, most importantly, transmit the force of contraction from cell to cell, (Katz, 2005).

The propagation of an electrical impulse across the heart provides the stimulus for cells to contract, which in turn causes the heart to beat. This electrical activation is initiated by a small group of self-excitatory pacemaker cells located at the top of the right atrium called the *sinoatrial node*, Figure 2.3. From here, activation propagates through the atria to the *atrioventricular node* that provides the only conducting pathway from the atria to the ventricles. The electrical activity progresses from one cardiac myocyte to the next via specialised intracellular connections, called *gap junctions*, that allow ions to pass freely between cells, thus electrically coupling a myocyte to its neighbours. The bundle of His conducts the electrical stimulus from the atrioventricular node to the ventricles via the left and right bundle branches. Each branch splits into a complex network of fibres, called the *Purkinje system*, near the bottom of the heart, where the stimulus is transferred to the endocardial surface of each ventricle. The many activation sites on the inner side of the ventricular wall cause the formation of an electrical waveform that propagates through the myocardial. As this electrical wave of activation enters the myocardial wall, it spreads upwards and across the tissue causing the cells and fibres to contract. The electrical activation wave spreads across the myocardium in a very uniform and synchronised manner under normal cardiac function, leading to a highly efficient pumping action due to the coordinated contraction of the myocardial walls.

**Figure 2.3** Schematic illustration showing the activation sequence of the heart, green arrows indicate the direction of electrical propagation during normal sinus rhythm.

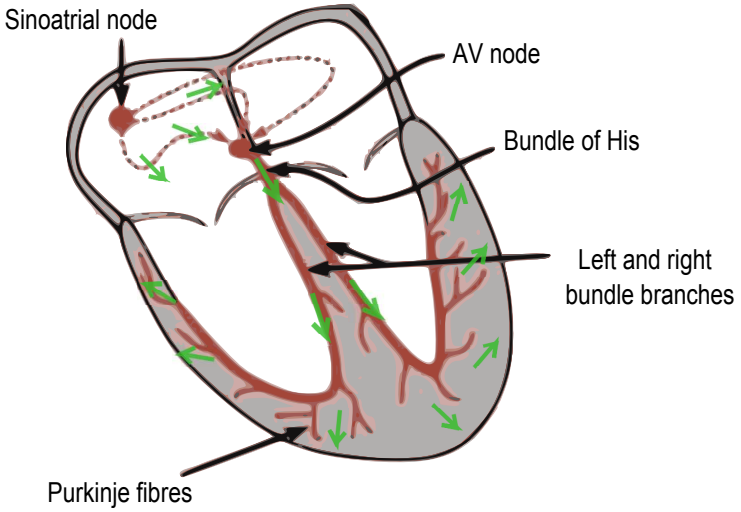


### 2.1.2 The Electrophysiology of a Single Cardiac Cell

The electrical activity of cardiac cells is caused by the presence of proteins inserted in the cell membrane. There are three main types, namely: ion channels, exchangers and pumps. Cardiac cells contain a high concentration of potassium ions ($[K^+]$) and a low concentration of sodium ions ($[Na^+]$), while the reverse is true of the extracellular environment that surrounds the cell. The gradients of $Na^+$ and $K^+$ are maintained by an active ATPase-driven $Na^+/K^+$ pump. This concentration disparity results in a potential difference across the cell membrane called the *transmembrane* or *membrane potential*. For a cell at rest this potential is negative, although the magnitude varies between different cell types, for example myocardial cells have a resting potential of about $-80mV$ while the sinoatrial node resting potential is between $-50mV$ and $-60mV$.

**Figure 2.4** Typical action potential trace of a cardiac cell along with the key inward and outward currents involved at each stage. Downward arrows indicate an inward current, upward arrows indicate an outward current, and a double arrow indicates that the current moves in both an inward and outward direction.

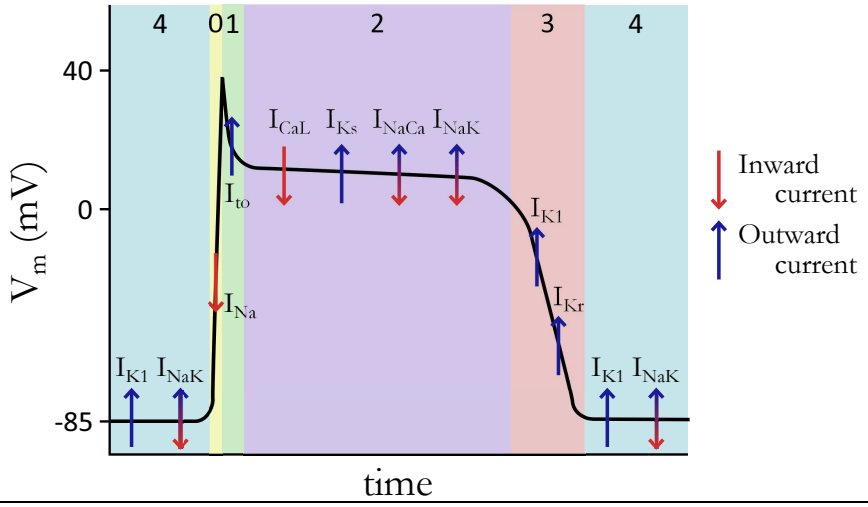


The *action potential* (AP) is the response of an excitable cell to an electrical stimulus and it consists of changes to the membrane potential over time. The shape of the AP varies widely between different cell types, as well as between different species. However, the AP of a cardiac cell can broadly be split into five distinct phases each characterised as follows:

- (*Initial Upstroke*) **Phase 0** is the period of rapid depolarisation of the membrane potential. During this phase $Na^+$ channels open, producing the fast sodium current ($I_{Na}$). This results in a rapid influx of $Na^+$ ions, causing the membrane potential to increase sharply and so the cell undergoes a short period of depolarisation.

- (*Transient Repolarisation*) Once the cell has reached maximum depolarisation, the $Na^+$ channels become deactivated and **phase 1**, a short period of repolarisation, begins. The sharp downward deflection of the AP that characterises this phase, commonly referred to as the *'notch'*, is due to the movement of potassium and chloride ions carried by the transient outward currents, $I_{To1}$ and $I_{To2}$, respectively.

- (*The Plateau*) During **phase 2**, the plateau phase, the membrane potential is sustained

by a balance between the inward movement of calcium ($Ca^{2+}$) ions, due to the opening of the L-type calcium ion channels ($I_{CaL}$), and the movement of potassium ions ($K^+$) through the slow delayed rectifier potassium channels, producing the $I_{Ks}$ current.

- (*Repolarisation*) During **phase 3** the membrane potential undergoes rapid repolarisation as the L-type calcium channels close, while the slow delayed $K^+$ channels remain open. The result is a new outward current leading to a negative change in the membrane potential, which in turn opens more types of $K^+$ ion channels. The other two types of potassium currents that are primarily involved in this stage are the rapid delayed rectifier potassium current ($I_{Kr}$) and the inwardly rectifying potassium current ($I_{K1}$).

- (*Resting Phase*) At the end of phase 3, when the membrane potential is restored to its resting value, the channels that produce $I_{Kr}$ and $I_{Ks}$ currents close. $I_{K1}$ channels remain open throughout **phase 4**, since this current contributes to maintaining the resting membrane potential.

Thus the generation of an AP within cardiac cells is achieved by a dynamic interplay between membrane ionic currents and the transmembrane potential.

The electrical stimulus of each cell is converted into a mechanical contraction by a process called *excitation-contraction coupling*, in which intracellular calcium plays a leading role. During phase 2 of the AP, calcium ions enter the cell through the L-type calcium channel triggering the subsequent release of calcium stored in the sarcoplasmic reticulum in a process called *calcium induced calcium release*. The free calcium binds to a regulatory protein on actin filaments, stimulating contraction of the muscle cell. For further reading on excitation contraction coupling see for example (Katz, 2005).

The AP depends on a delicate balance of ionic currents flowing into and out of the cell. These currents in turn are regulated by a specialised family of proteins called *voltage-gated ion channels* that form a pore in the membrane, allowing the movement of ions across an otherwise

impermeable membrane. Ion channels undergo conformational changes in response to changes in the membrane potential causing it to ‘open’ and conduct ions into and out of the cell, as well as ‘close’, restricting the movement of ions across the membrane, (Bezanilla, 2000), (Bezanilla, 2007). Figure 2.5 is a representation of this opening mechanism.

**Figure 2.5** Cartoon of the gating (open/close) dynamics of voltage-gated ion channels in response to changes in membrane potential.

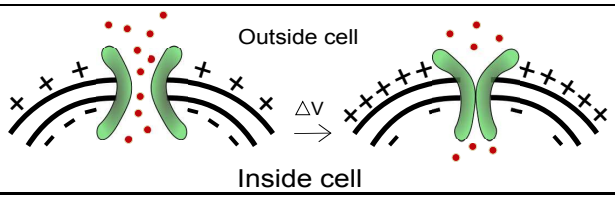


Since ion channels are discrete molecules, the conformational changes of such proteins, and thus their gating mechanisms, are stochastic. Indeed experiments on individual channels using the patch clamp technique showed that each trial with the same depolarising current produces a new pattern of channel openings, illustrating that, at the single channel level, opening and closing occurs at random. Therefore single channel dynamics can be predicted only using probabilities. We note that there are many other types of ion channels with different open/close mechanisms, see (Hille, 1991), for example, for a comprehensive description of ion channels, their dynamics, structure and function.

Each ion channel is highly permeable to one type of ion. The preferred ion interacts with specific sites within the channel which allow only the “correct” ion to pass through. This selective property ensures the flow of ionic currents is controlled in a very specific manner, which is vital in providing the electrical force needed to generate and maintain the AP.

### 2.1.3 Repolarisation Reserve and Arrhythmia

One of the defining characteristics of the cardiac AP is its repolarisation phase. This period begins with the characteristic notch (phase 1), where the membrane potential drops sharply, fol-

lowed by the plateau phase (phase 2), during which the membrane potential gradually decreases in the direction of more negative potentials, and finally there is a period of fast repolarisation (phase 3) when the potential falls sharply to its resting state. This property clearly distinguishes it from the AP of other excitable cells, such as neurons and skeletal muscle, where repolarisation follows rapidly after the depolarisation phase.

Unlike the depolarisation phase of the AP, which is largely controlled by the rapid influx of sodium ions through $I_{Na}$ channels, the plateau and repolarisation phases involve a more complex interplay between a number of different ionic currents, as can be seen in Figure 2.4. Blocking one of these currents does not necessarily cause repolarisation to fail, and so, as with many biological systems, there is redundancy in the repolarisation phase of the AP under normal conditions. This redundancy is referred to as *repolarisation reserve*, a term first coined by Roden in 1998 (Roden, 1998). Since the concept of repolarisation reserve was first described it has been experimentally demonstrated (Varro et al., 2000) and is now an important principle in understanding repolarisation mechanisms.

While the repolarisation phase involves a number of different ionic currents, pumps and exchanges, the outward currents $I_{To}$, $I_{Kr}$, $I_{Ks}$ and the inward current $I_{CaL}$ have been identified as four of the most crucial in ensuring normal repolarisation function. These currents are also considered to play a key role in maintaining repolarisation reserve.

$I_{Kr}$ is thought to be one of the most important outward currents involved in repolarisation, due to the significant lengthening of the AP observed upon complete inhibition of this current (Varro et al., 2000), (Lengyel et al., 2001), (Jost et al., 2005). The $I_{Kr}$ channel is very promiscuous as it interacts with many different drug compounds, and so is a major concern within safety pharmacology, (Vandenberg et al., 2001).

$I_{Ks}$, the other delayed rectifier potassium current, produces small changes to the AP when blocked under normal conditions (Varro et al., 2000), (Jost et al., 2005) and so this current is

thought to be small during a typical AP. The magnitude of this current varies greatly between cells and has been shown to be upregulated upon inhibition of $I_{Kr}$, (Xiao et al., 2008).

The initial fast repolarisation during phase 1 of the AP is largely driven by $I_{To}$. Therefore, changes in this current can alter the amplitude of the plateau phase, which can subsequently modify the dynamics of other transmembrane currents, such as $I_{CaL}$. Thus, while changes to $I_{To}$ alone are suspected to lead to unnoticeable affects on the AP, it is thought to be involved in repolarisation reserve and so together with the dynamics of other currents may influence repolarisation, (Varró and Baczkó, 2011).

Since $I_{CaL}$ is the key inward current that maintains more positive membrane potentials during the plateau phase, changes in this current can also affect the amplitude and duration of the AP and so it is also known to be a component of repolarisation reserve, (Varró and Baczkó, 2011). However, the role of $I_{CaL}$ during repolarisation is complex and still not fully understood due to the dependence of this current on intracellular calcium concentration, as well as voltage, both of which vary dynamically during the AP.

It is clear that cardiac myocytes have developed a complex combination of different ionic currents to preserve the long repolarisation phase of the AP. This property is key to maintaining normal cardiac function since it allows for control of the mechanical contraction of the cell, helping to prevent premature excitation which can disrupt the normal rhythm of the heart. When this happens, chaotic and turbulent electrical activation patterns develop that alter the rhythm of the heart, and this is known as *cardiac arrhythmia*. Such behaviour can arise due to mutations or modifications to the kinetic properties of the ion channels that control the ionic currents, thus leading to abnormalities in the AP. These changes at the ionic level are caused by genetic diseases such as Brugada syndrome (Antzelevitch, 2001) or long QT syndrome (Sanguinetti, 2000), or as a result of the interaction of drugs with the ion channels.

Changes to heart rhythm as a result of cardiac arrhythmia are potentially life-threatening, since

if the heartbeat is too slow (termed *bradycardia*) or too fast (termed *tachycardia*) blood pressure can not be maintained, leading to loss of consciousness and sudden death. Therefore repolarisation reserve is thought to be an inbuilt mechanism within cardiac cells to ensure repolarisation stability and protect against potentially life-threatening arrhythmias.

## 2.2 Biomarkers of Arrhythmic Risk

As was described in Section 2.1.3, repolarisation reserve is an important protective mechanism against abnormal electrical activity that can potentially lead to life-threatening arrhythmias. Therefore, conditions under which repolarisation reserve is reduced, for example due to drugs or disease, increase the risk of arrhythmic behaviour developing. The difficulty is trying to identify reduced repolarisation reserve using measurable quantities of electrical behaviour.

For example, an individual may have reduced repolarisation reserve due to a genetic mutation in one of the potassium current channels, reducing its function. Such a reduction in this current may not lead to abnormalities in the AP, due to the compensatory mechanisms of other ionic currents involved in repolarisation reserve. However, if repolarisation reserve is further compromised, for example due to pharmacological drug block, the individual may subsequently develop life-threatening arrhythmias. The difficulty for clinicians and pharmaceutical companies is firstly trying to distinguish an individual with reduced repolarisation reserve from a normal healthy individual and secondly to identify drug compounds that are proarrhythmic. Therefore, much research in recent years has focused on trying to identify measures that indicate the potential arrhythmic risk of an individual or new drug compound, and these are referred to as *biomarkers*. Biomarkers can broadly be split into two categories, those that use electrocardiogram (ECG) recordings (ECG based biomarkers), and those that use recordings of the AP (AP based biomarkers).

**Figure 2.6** Schematic of a typical recording of an ECG, with the main features and relation of each phase to the electrical dynamics of the heart annotated.

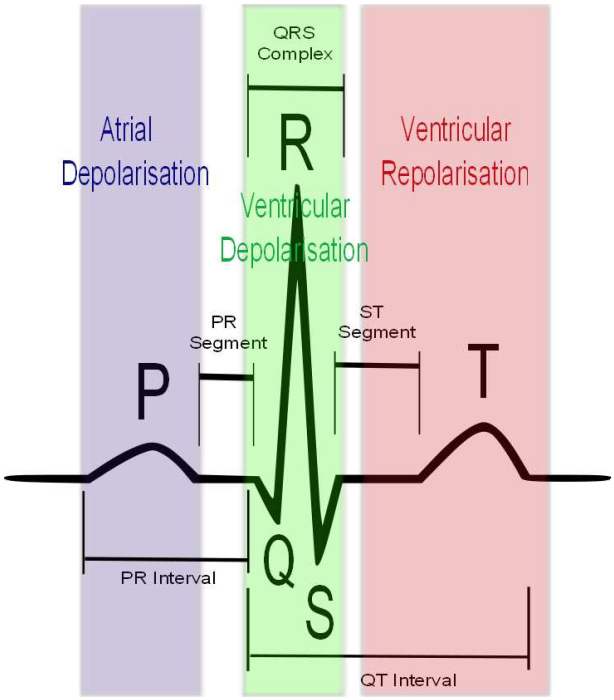


The ECG measures the potential difference between different points on the body surface and is a common method for monitoring and detecting abnormalities in heart rhythm, as it is non-invasive and relatively cheap to perform. A typical ECG recording is composed of a P wave, a QRS complex and a T wave, shown in Figure 2.6. The P wave corresponds to the wave of depolarisation that spreads through the atria from the sinoatrial node. The QRS complex represents ventricular depolarisation and the period following this, the ST segment, roughly corresponds to the plateau phase of the ventricular AP. Finally, ventricular repolarisation results in the T wave. The QT interval is the main ECG based biomarker and is used in clinical studies to determine arrhythmic risk. It is measured from the start of the QRS complex to the end of the T wave and represents the time for both ventricular depolarisation and repolarisation to occur, Figure 2.6. Prolongation of the QT interval is thought to indicate increased arrhythmic risk and is the principal reason many drug compounds fail to reach the market during the final stages of testing. However, studies have shown that the QT interval alone is insufficient to accurately

determine arrhythmic risk (Hondeghem, 2006), (Hondeghem, 2008). In particular, prolongation of the QT interval has been found to correspond poorly with the incidence of a specific type of arrhythmia called Torsade de Pointes (TdP), (Shah and Hondeghem, 2005). Therefore, a number of other ECG based measurements, such as T wave changes, QT/RR slope, T peak to T end interval, have been proposed as potential biomarkers of arrhythmic risk, see the review (Corrias et al., 2010).

AP based biomarkers are used in preclinical studies to determine arrhythmic risk in single cell and tissue experiments. In particular, AP based biomarkers play a crucial role in safety pharmacology early on in the drug development process. Currently the action potential duration (APD), which is the time from maximal depolarisation until the end of repolarisation is used as the primary AP based biomarker, in a similar way that QT interval is the main biomarker at the ECG level. Indeed prolongation of the APD by a potential new drug compound will lead to abandonment of the compound for further development. However, as with ECG based biomarkers, APD alone is thought to poorly predict proarrhythmic behaviour, and so other biomarkers such as AP triangulation, which measures the shape of the AP, have also been suggested, Corrias et al. (2010).

In recent years the magnitude of beat-to-beat variability has been suggested as a potentially powerful predictor of arrhythmic risk. This temporal short term variability manifests as variations in the QT interval of successive beats in ECG recordings, and as differences in the APD between successive beats in AP recordings. Therefore measurements of this variability could provide a potential new biomarker of arrhythmic risk. Due to the importance of beat-to-beat variability within this thesis we discuss the clinical and experimental evidence for this potential new biomarker in a separate section.

## 2.3 Short-Term Variability in Repolarisation

Single cell experiments have shown sizeable variation in the repolarisation phase of the AP between successive beats, leading to fluctuations in the duration of consecutive APs. For example, Figure 2.7 shows $50$ successive AP traces, plotted on top of one another, for a canine cardiac cell paced at $1000ms$ basic cycle length under control conditions. While qualitatively the depolarisation phase is similar for each beat, there is evidently significant variation in the repolarisation phase and ultimately the duration of each AP trace of up to $100ms$.

**Figure 2.7** 50 consecutive AP traces from a single canine ventricular cell experiment under control conditions. AP traces are plotted on top of each other. This was obtained from our experimental collaborators, Professor András Varró's group at the University of Szeged, Hungary.

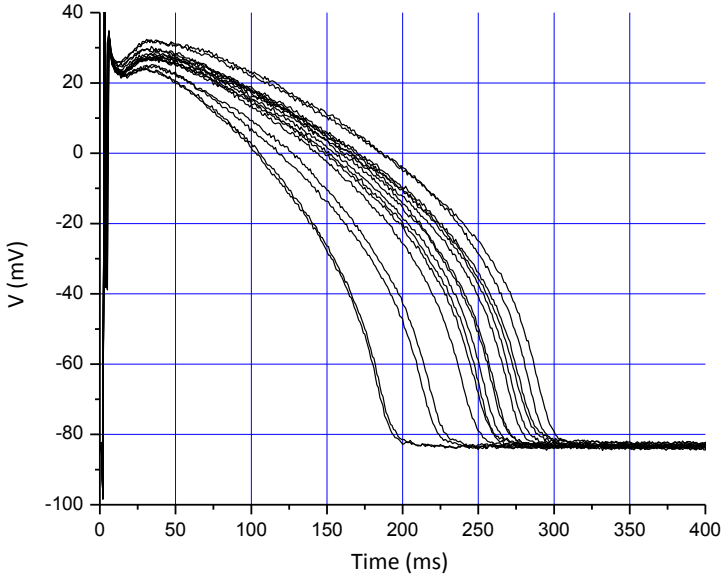


This phenomenon is commonly termed beat-to-beat variability in repolarisation (BVR) and in recent years has been shown to be associated with increased arrhythmic risk. It has therefore become an active area of research, as BVR could provide the key to assessing the arrhythmic risk both within individuals and of potential new drug compounds.

An early study by Berger et al., (Berger et al., 1997), found greater BVR in patients with dilated cardiomyopothy (a condition associated with a high incidence of arrhythmias) compared with control subjects. The authors quantified BVR using QT measurements from ECG recordings of $30$ consecutive heart beats. They introduced a novel measure, the QT variability index (QTVI), which they proposed as an ECG based biomarker of arrhythmic risk. The QTVI assesses BVR from ECG recordings as the logarithm of the ratio of normalised QT variance to heart rate variance. It is calculated as follows

$$QTVI = log_{10}\left(\frac{QT_v/(QT_m)^2}{HR_v/(HR_m)^2}\right),$$

where $QT_m$, $QT_v$ are the temporal mean and variance in the QT interval, respectively, and $HR_m$, $HR_v$ are the temporal mean and variance in the heart rate, respectively. The relation between the QTVI and arrhythmogenesis was further investigated by Atiga et al. (Atiga et al., 1998). In patients presenting with malignant ventricular arrhythmias, they found that the QTVI successfully identified patients with sudden cardiac death, as well as those that survived free of arrhythmia. This study implicated the potential predictive power of this measure to classify the arrhythmic risk of patients.

BVR has also been implicated as a potential parameter for assessing the proarrhythmic properties of drugs. Early investigations into the predictive power of BVR used a measure called short-term variability in repolarisation duration (STV) to quantify BVR. STV was first introduced in (Thomsen et al., 2004), where it was determined in terms of monophasic AP duration (MAPD) measurements. We note that STV can equally well be calculated using AP duration from AP recordings in isolated cells. The repolarisation duration (quantified in terms of MAPD, or APD) of each beat is plotted against the repolarisation duration of the previous beat on a Poincaré plot, an example of which is given in Figure 2.8. A Poincaré plot is simply the repolarisation duration at beat $n-1$ plotted against the repolarisation at beat $n$. STV is then defined as the average distance to the line of identity in the Poincaré plot and is calculated as

follows

$$STV = \sum_{n=2}^{k} |D_n - D_{n-1}|/(\sqrt{2}(k-1)), \tag{2.1}$$

where $D_n$ is the repolarisation duration of beat $n$ (i.e. the APD or MAPD), and $k$ is the total number of beats considered. Typically $30$ or $50$ consecutive beats are used to calculate STV. The advantage of STV over previous measures of BVR is that it directly quantifies the variations between consecutive beats, rather than aggregating these variations over a short period of time, as is the case for example with the QTVI measure. In particular, it is thought that the difference in repolarisation between consecutive beats is an important factor in the generation of arrhythmias (Hinterseer et al., 2008).

**Figure 2.8** Example of a Poincaré plot for $APD_{90}$ values obtained using experimental data for the same cell as in Figure 2.7.

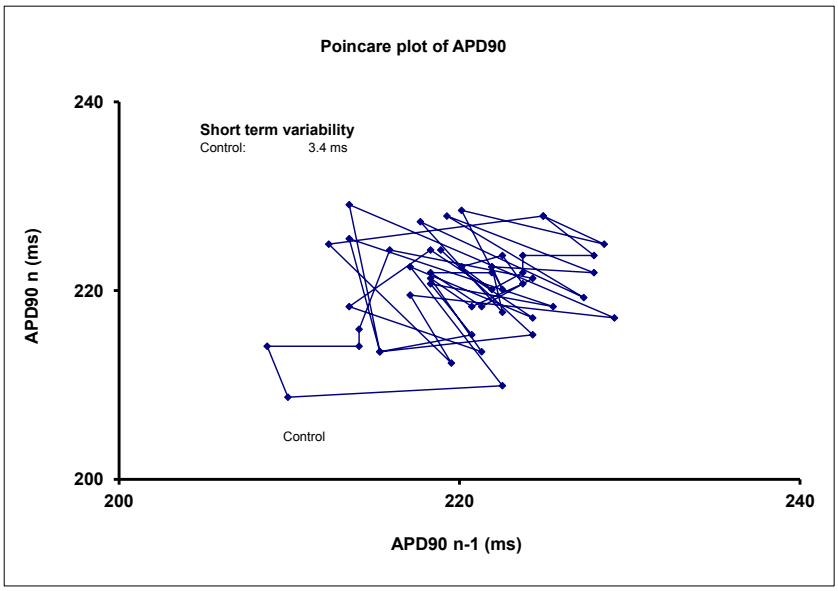


The ability of STV to determine proarrhythmic effects of drugs was first shown using MAPD measurements in dogs with remodelled hearts due to chronic atrioventricular block (CAVB dog model), which leads to reduced repolarisation reserve. Thomsen et al. (2004) showed that

an increase in $STV_{MAPD}$ preceded drug-induced arrhythmia, and this was further confirmed by Detre et al. (2005) for another cardiovascular drug. In (Thomsen et al., 2006) the authors extend this to non-cardiovascular drugs and also show that manipulation of BVR directly alters proarrhythmic outcome. In particular they found that in the CAVB dog model, an increase in STV led to the onset of Torsade de Pointes arrhythmias, while a decrease led to successful antiarrhythmic treatment. Further studies, both in anaesthetised dogs (Thomsen et al., 2007) and conscious dogs (Schneider et al., 2005), have confirmed the ability of STV to correctly predict the pro-arrhythmic effects of drugs. STV has also been found to be a good marker for assessing the arrhythmic potential of multichannel blockers in both dogs (Takahara et al., 2008) (Lengyel et al., 2007) and rabbits (Lengyel et al., 2007). The potential predictive power of STV to predict drug-induced arrhythmias has further been shown in isolated dog cells (Abi-Gerges et al., 2010).

So far we have discussed the potential of STV as an AP based biomarker in preclinical animal studies. However, STV in the QT interval from ECG recordings can be calculated by replacing the APD in (2.1) by the length of the QT interval. Therefore, STV in the QT interval ($STV_{QT}$) has also been identified as a potential ECG based biomarker in clinical studies. The first clinical study into the link between $STV_{QT}$ and arrhythmic risk was in patients with a history of drug-induced long QT syndrome and Torsade de Pointes, (Hinterseer et al., 2008). They showed that $STV_{QT}$ is increased in patients with documented drug-induced proarrhythmia. Furthermore, in the absence of prolongation of the QT interval, it was possible to distinguish such patients from a control group using $STV_{QT}$. Increased $STV_{QT}$ was also shown in patients with congenital long QT syndrome, (Hinterseer et al., 2009). Moreover, this measure was able to ascertain high-risk patients, who were characterised by an even greater increased $STV_{QT}$ than the low risk patients. Finally, a study by Hintseer et al. (Hinterseer et al., 2010) found $STV_{QT}$ was increased in patients with non-ischemic heart failure. The evidence from these studies suggests that STV could provide a powerful tool in differentiating individuals with increased vulnera-

bility to arrhythmias. Furthermore the combination of STV and the QTVI, both measures of BVR, has been shown to increase the predictive value in patients with structural heart disease (Oosterhoff et al., 2011).

While there has been a considerable number of studies over recent years that have demonstrated the potential predictive value of BVR, both in clinical diagnosis and drug development, few investigations into the possible mechanisms of BVR have been undertaken. It has been hypothesised that the stochastic behaviour of ion channels is the most likely cause of BVR (Johnson et al., 2010). Due to the complexity of the AP, investigating the causes of BVR using experiments alone poses significant challenges. Computational models, which allow for investigation over a wide range of temporal and spatial scales, provide a powerful tool to shed light on the potential origins of BVR.

## 2.4 Computational Models

As discussed in Section 2.1.3, the repolarisation phase of the AP is complex, involving a number of different ionic currents which in turn depend on the dynamics of membrane proteins called ion channels. Therefore, investigation of such an intricate multicomponent system using experiments alone is difficult. In recent years, computational models of cardiac electrophysiology have played an increasingly important role in elucidating the complex ionic mechanisms that can disrupt the electrical dynamics of cardiac cells. For example, they have shed light on the changes to ion channel kinetics as a result of genetic diseases, (Clancy and Rudy, 1999), as well as drug interaction, (Clancy et al., 2007), that can lead to abnormalities in the AP associated with arrhythmias.

Since the first cardiac cell model was developed by Noble, cardiac electrophsyiology modelling has developed into an active field of research, with a wealth of biophysically detailed models, able to reproduce cardiac cell electrical dynamics in different species and under different condi-

tions. In the next section we review the advancement in models of single cell electrophysiology; from the ground breaking model of Hodgkin and Huxley over $60$ years ago, to the multitude of biophysically detailed models that are currently in use. We then discuss in greater detail the manner in which ion channel dynamics are modelled within cardiac electrophysiology models.

### 2.4.1 Models in Cardiac Single Cell Electrophysiology

The first mathematical model of the propagation of an AP was described by Hodgkin and Huxley, (Hodgkin and Huxley, 1952), for the squid giant axon. The cell membrane is modelled as a capacitor in parallel with a series of ionic currents and a stimulus current. The change in the membrane potential, $V$, over time can therefore be described by a simple ordinary differential equation (ODE)

$$\frac{dV}{dt} = -\frac{1}{C_m}(I_{ion} + I_{st}), \tag{2.2}$$

where $C_m$ is the membrane capacitance, $I_{ion}$ is the total transmembrane ionic current and $I_{st}$ is the stimulus current. In the original Hodgkin-Huxley model (Hodgkin and Huxley, 1952), $I_{ion}$ is assumed to consist of three ionic currents: a potassium current, $I_K$, a sodium current, $I_{Na}$ and a constant leakage current, $I_L$.

The Hodgkin-Huxley model remains the basis for modern neuronal and cardiac AP models. While these models use the same basic structure to describe the voltage dynamics, the term $I_{ion}$ typically varies between models to include descriptions of different ionic currents, pumps and exchangers.

The seminal paper by Noble in 1962, (Noble, 1962), built upon the work of Hodgkin and Huxley to develop the first mathematical description of the electrical dynamics of cardiac cells. The model was of the AP in a generic Purkinje cell and, similarly to the Hodgkin-Huxley model consisted of three primary currents, a sodium, potassium and background current. Since this first cardiac cell model, the field has developed into a large area of active research, with a wealth of literature detailing models of different cell types in different states, including diseased states.

The improvements in experimental techniques and increased computing power has meant that such models are becoming increasingly complex, as researchers strive for ever more accurate mathematical descriptions of the membrane kinetics of cardiac myocytes, (Noble et al., 2012; Smaill and Hunter, 2010).

Initially work in this field began with refinements to the Noble model, (McAllister et al., 1975). This model extended the number of ionic currents, with the inclusion of a calcium current, two additional potassium currents, a chloride current and two more background currents and more than doubled the complexity of the original Nobel model, involving 10 variables instead of only 4. The final iteration of this model, DiFrancesco and Noble (1985) was the first model to include a description of the sodium-potassium exchanger.

Following these early models, which focused on capturing the dynamics of Purkinje cells, the focus shifted to ventricular cell models. The first such model was described by Beeler and Reuter, (Beeler and Reuter, 1977), and since then a number of groups have developed complex ventricular cell models for a number of different species, including human, (Tusscher et al., 2004). One well known sets of models are those developed by Rudy and co-workers for a number of different animal species including guinea pig (Luo and Rudy, 1991, 1994a,b; Faber and Rudy, 2000), dog (Hund and Rudy, 2004; Decker et al., 2009) and most recently human (O'Hara et al., 2011). All these models were originally developed to study arrhythmias.

A greater abundance of models have been developed for animal cardiac cells than human, mainly due to the difficulties in obtaining experimental data from human hearts. One of the first human ventricular myocyte models was developed in (Priebe and Beuckelmann, 1998), although due to lack of human data, this model was largely based on data from guinea pigs. As more experimental data from humans has become available, models of human myocytes have become more thorough in their formulations of the dynamics of such cells, (Tusscher et al., 2004; Tusscher and Panfilov, 2006b; Fink et al., 2006; Grandi et al., 2010; O'Hara et al., 2011).

As the field of cardiac electrophysiology grew into an active area of research, with many different groups across the world involved in the development of ever more complex cell models, the sharing of models between groups became more difficult as different researchers used various computational platforms to simulate the dynamics of such models. Therefore, the need for tools that allowed models to be read into different simulation software in a consistent format, as well as determining standards for defining such models so that they were easily reproducible became apparent. CellML [1] was initially designed to try to address such issues and provide a platform for straightforward distribution of information and models among scientists. It is an XML-based markup language to describe models of cellular function, such as cardiac electrophysiology models. A model in CellML is composed of several individual components that can be connected to create larger complex models of biological cell dynamics, and it allows an existing model to act as a foundation onto which new components can be included. For further information on the CellML language, its current features and future directions, see the reviews (Lloyd et al., 2004; Garny et al., 2009).

Cardiac cell electrophsyiology models have also been extended to study the propagation of an AP through cardiac tissue. Models of the AP within a single cell can be incorporated into tissue level models using the monodomain or bidomain equations, (Pullan et al., 2005) Chapter 4. These equations essentially describe the AP propagation as a reaction-diffusion model, where the membrane potential is the diffusing quantity and the cellular dynamics the reaction.

### 2.4.2 Mathematical Formulations of Ion Channel Dynamics

As discussed in the previous section, the formulation of the ionic current term, $I_{ion}$, in the equation that describes the dynamics of the membrane potential, (2.2), varies between different models. Typically $I_{ion}$ is assumed to be the sum of a number of different ionic currents. Each current for ions of type $i$ ($I_i$), is calculated using Ohm's law, which determines $I_i$ as the product

[1] www.cellml.org

of the conductance $g_i$ and the driving force $V - E_i$,

$$I_i = g_i(V - E_i), \tag{2.3}$$

where $V$ is the transmembrane potential, and $E_i$ is the equilibrium potential, that is the potential at which $I_i$ changes direction and it is obtained using the Nernst equation, (Rudy and Silva, 2006). Assuming that ions only pass through the channel when it is open, the conductance is calculated as the maximum current when all channels are open, $G_{max}$, multiplied by the proportion of open channels, $P_{open}$.

When Hodgkin and Huxley first developed their model, they had no knowledge of the kinetic behaviour of ion channels, described in Section 2.1.2. They therefore postulated that each ionic channel consisted of a series of hypothetical gates. Each gate can be either open or closed, transitioning between these states at rates that depend on the transmembrane potential. The channel is assumed to be open only when all gating particles are open.

In the Hodgkin-Huxley model the sodium channel is assumed to consist of three identical $m$ gates and one other termed the $h$ gate, while the potassium channel is considered to be composed of four identical $n$ gates. Each gate of type $i$ transitions from the closed to the open state at rate $a_i(V)$, and from the open to the closed state at rate $b_i(V)$. The proportion of open gates of a particular type, $y_i$ for $i = m, h, n$, can be described by the following ordinary differential equation (ODE)

$$\frac{dy_i}{dt} = a_i(V)(1 - y_i) - b_i(V)y_i. \tag{2.4}$$

The channel is assumed to be open only when all gating particles are open. Assuming that the gates open and close independently of one another, the proportion of open channels is therefore equal to the product in the proportion of open gates. That is $P^{Na}_{open} = y^3_m y_h$ and $P^{K}_{open} = y^4_n$, for the sodium and potassium channels in the Hodgkin-Huxley model, respectively. This approach of modelling the dynamics of the ion channels in terms of gating variables is usually referred to as *Hodgkin-Huxley formulation*, and is still used in modern cell electrophysiology models (Decker et al., 2009; Faber and Rudy, 2000; Tusscher and Panfilov, 2006a).

A limitation of the Hodgkin-Huxley formulation is that the gating parameters do not represent specific kinetic states of the channel, which precludes the study of simulating state specific processes such as mutations or state-specific drug binding. Therefore a model of ion channel dynamics termed *Markov formulation* was introduced in (Clancy and Rudy, 1999). We note that such a formalism is not stochastic, although this terminology is usually reserved only for stochastic models within the mathematical modelling community. This method drops the assumption that the channel can be described by independent gates that open and close, and instead models the ion channel itself as being in one of $m$ discrete states. Each state can be thought of as representing a different conformation of the ion channel protein. Such a model is typically represented using a state diagram, such as the one given below for the simplest model where the channel is assumed to be either open or closed.

$$C \underset{b}{\overset{a}{\rightleftarrows}} O$$

The state variables, $x_i(t)$, denote the proportion of ion channels in state $i$ at time $t$. It is assumed that the chance of the channel transitioning from state $i$ to state $j$ depends only on the current state of the channel, that is, it possesses the *Markov property*. For an ion channel with $m$ states, the proportion of channels in state $i$, $x_i$, can be described by the following deterministic equation

$$\frac{dx_i}{dt} = \Sigma_{j=1}^{m}(k_{ji}(V)x_j - k_{ij}(V)x_i), \tag{2.5}$$

for $i = 1, \ldots, m$, where $k_{ij}(V)$ is the voltage dependent transition rate of moving from state $i$ to state $j$. Typically such models assume a single or sometimes two or more open states, and so $P_{open}$ is simply calculated using (2.5) or as the sum of the proportion of channels in each open state, which are again obtained using (2.5). Thus the conductance $g_i$ in equation (2.3) is calculated as for the Hodgkin-Huxley formulation except the proportion of open channels ($P_{open}$) is obtained directly from (2.5), rather than as the product of open gating variables. Markov formulation of ion channel dynamics has been used to study the effects of drug block, (Snyders and Chaudhary, 1996; Clancy et al., 2007), and the mechanisms of genetic defects (Clancy and Rudy, 1999), for a review see (Rudy and Silva, 2006).

## 2.5 Simulation Studies on Causes of Variability on the Action Potential

### 2.5.1 Intrinsic Variability

As discussed in Section 2.1.2, single channel recordings demonstrated that the conformational changes an ion channel undergoes as it opens and closes occur at random. This intrinsic stochastic behaviour causes fluctuations in individual ionic currents that can manifest themselves as variability in the cell membrane potential. The effects of stochastic ion channel behaviour on the electrical dynamics of the whole cell, including the AP, is usually studied by incorporating a stochastic description of ion channel behaviour into existing electrophysiology cell models. We will review the methods for modelling the stochastic behaviour of ion channels in the next chapter. Here we give an account of the few computational studies that have investigated the effects of stochastic ion channel behaviour on the cardiac AP.

The study of stochastic ion channel behaviour on neuronal cells has developed into a considerable field of research, for a review see, for example, (White et al., 2000), where a number of studies have shown that such behaviour can modify the AP within single cells (Strassberg and DeFelice, 1993), (DeFelice and Isaac, 1993), (Chow and White, 1996), (DeFelice and Isaac, 1993) and (Schneidman et al., 1998). However, few computational studies have investigated the effects of such behaviour on cardiac cell electrophysiology dynamics, and in particular the AP. The most likely reasons for this are firstly that cardiac cell models are in general more complex than neuronal cell models, therefore incorporating a stochastic description of ion channel dynamics into such frameworks poses a considerable computational challenge. Secondly, cardiac cells are thought to have a greater number of ion channels, and so the stochastic behaviour is likely to have less of an effect on the cellular dynamics than in neuronal cells. Finally, the coupling together of cardiac cells at the tissue level has been shown to smooth out the effects of variability seen at the single cell level (Pueyo et al., 2011; Lemay et al., 2011), and so it

is thought that the stochastic behaviour of ion channels will have little effect on the dynamics at the tissue level under normal conditions, but this may not be the case under pathological conditions.

However, as was discussed in Section 2.3, variability in the repolarisation duration of the AP is observed in single cell experiments, as well as at the ECG level, and this variability, typically quantified using the short term variability (STV) measure, is thought to be an indicator of arrhythmic risk. The intrinsic stochastic behaviour of ion channels has been speculated to be a possible mechanism underlying this phenomenon of beat-to-beat variability in repolarisation (BVR) and thus STV.

Using isolated ventricular myocytes from guinea pigs, Zaniboni et al. (Zaniboni et al., 2000) demonstrated that stochastic ion channel dynamics can cause variability in the repolarisation phase of the AP, and this was also shown in isolated spontaneously beating cardiac cells in (Krogh-Madsen, 2004). In (Pueyo et al., 2011), the authors show that the stochastic gating of the slow delayed rectifier potassium current ($I_{Ks}$) plays an important role in the variability of the AP duration within isolated human and guinea pig ventricular myocytes. They also show that the coupling of cells at the tissue level does indeed mask such stochastic effects, but that pathological conditions, such as reduced repolarisation reserve and uncoupling of cells, can reveal this stochastic behaviour at the tissue level and can lead to proarrhythmic behaviour. Similar results are presented in (Lemay et al., 2011), who find that in strands of poorly coupled cells stochastic effects gain significance and can determine the occurrence of conduction block. The stochastic behaviour in the L-type calcium current has also been found to influence the generation of early after depolarisations (EADs) (Tanskanen et al., 2005), which can subsequently lead to arrhythmic behaviour.

While the work of Lemay et al. (Lemay et al., 2011) provided a comprehensive investigation into the effects of stochastic ion channel behaviour in a number of the repolarisation currents, this study was entirely computational. In (Pueyo et al., 2011), a combined experimental and

computational approach was taken, with simulation results related back to experimental observations. However, only stochasticity in one of the repolarisation currents was considered. Also, neither study investigated the effects of stochastic ion channel behaviour on the STV measure of BVR, which has been extensively studied experimentally and so both studies ignore the consecutiveness of beats in measuring variability in the AP. Therefore, more comprehensive simulation studies are needed to provide greater insight into the causes of beat-to-beat variability in the AP.

### 2.5.2 Extrinsic Variability

As well as temporal variability in the electrical dynamics of a single cell, there is also variability between individual cells from a given heart and also between different hearts. This variability arises due to fluctuations external to the cellular dynamics and results in different cells behaving differently to certain conditions such as drug block. As with the intrinsic stochastic behaviour of ion channels, such *extrinsic* variability is typically ignored in computational studies, which are usually fit to the mean of experimental data in order to provide a 'representative' of the entire population. However, understanding the different behaviour and response of individual cells to certain conditions could be another element to help aid in determining potential arrhythmic risk.

In (Pueyo et al., 2011), variability in the cell population is incorporated by varying the number of $I_{Ks}$ channels in each simulation of the stochastic model. More specifically, the number of channels is assumed to follow a truncated normal distribution, with the mean of the distribution estimated from experimental data. In each simulation of the stochastic model, the number of channels is then generated randomly from this distribution. A similar approach is taken in (Lemay et al., 2011), except the number of channels is assumed to follow a Poisson distribution, where the mean is estimated from single channel properties reported in the literature. One issue with such an approach is that there is no experimental evidence to suggest that the number of channels in a population of cells follows either of these distributions.

Sensitivity analysis has also been used in deterministic studies to investigate which parameters in the model lead to the greatest changes in the AP dynamics, (Romero et al., 2009). Another approach in deterministic studies of inter-individual variability, introduced recently, is to construct a *population* of deterministic cell models. Each model within the population has the same model structure but a unique set of parameters, obtained by varying multiple parameters simultaneously within the model. Multivariate regression analysis is then used to identify trends between different parameter sets and observed behaviour. Such techniques have been used in the neuroscience community to understand the variability in conductance in the human brain (Marder, 2011) and also in cardiac modelling to examine interpatient variability in response to proarrhythmic drugs (Sarkar and Sobie, 2011). The interested reader is referred to (Marder and Taylor, 2011) and (Sarkar et al., 2012) for further details.

## 2.6 Estimating Single Channel Properties from Experimental Data

In the cardiac cell electrophsyiology models discussed in the previous sections, parameters that determine the single cell electrical properties are estimated from experiments. In particular, the number of ion channels needs to be determined to model the stochastic behaviour of ion channels, as will be discussed in the next chapter.

One of the most commonly used techniques for determining single channel properties, such as single channel current and the number of ion channels, is called fluctuation analysis (Hille, 1991). This method uses the variability in the current traces from patch clamp experiments, (Neher and Sakmann, 1976), that is caused by the stochastic dynamics of individual channels, to estimate electrical properties of single cells. There are two main methods for measuring the variance in the macroscopic current. Firstly, a voltage step can be applied and once steady state has been reached, the variance and the mean macroscopic current are calculated over the last few time points of the trace. Such measurements can be taken for different voltage steps,

giving a set of variance and mean current values for each voltage step. This approach is called *stationary analysis*.

Alternatively, the variance and mean in the current can be measured during the transient changes that occur after the voltage step, using $M$ time courses in response to the same depolarising voltage step. This approach is termed non-stationary analysis. Both approaches result in a set of points for the variance ($\sigma_I^2$) and mean ($I$) in the macroscopic current, which can then be fitted to the following quadratic formula

$$\sigma_I^2 = iI - I^2/N,$$

to obtain estimates for the number of channels $N$ and the single channel current $i$, (Hille, 1991).

Patch clamp experiments are performed on individual cells which can be isolated from adult mammalian hearts using a technique called *enzymatic isolation*. Such a method involves perfusing the heart with buffers and enzymes that degrade and loosen the intracellular and collagen matrices that hold the myocytes in the heart. More specifically, the animal is first killed by an approved procedure and the heart is quickly removed. In mammals, such as dogs, a small tube is then typically inserted into the aorta and an isolation solution is pumped through the heart. The exact composition of the isolation solution varies between species. After perfusion is complete, a section of the tissue is removed from the desired region, for example the atrium or ventricle, and is placed in a beaker containing an altered form of the isolation solution. This beaker is then shaken to release dispersed cells, which are allowed to settle before cells showing clear regular striations are harvested for use. Yields of up to $80\%$ have been reported using such techniques (Mitra and Morad, 1985). For further details on the cell isolation procedure, see for example (Mitra and Morad, 1985; Tytgat, 1994).

## 2.7 Chapter Summary

In this chapter we provided an introduction to the structure and functional properties of the heart. We described in depth the electrophysiology dynamics of single cells, the role of ion channels in ensuring normal electrical function, and the importance of a concept called repolarisation reserve in protecting against potentially life-threatening arrhythmias. The phenomenon of beat-to-beat variability in repolarisation (BVR) was then discussed and the experimental and clinical evidence which indicates BVR as a potential indicator of arrhythmic risk was reviewed.

For the rest of the chapter, computational models used to simulate the electrical dynamics of single cardiac cells were reviewed and described. In particular we discussed the studies that have investigated the causes of variability in the electrical dynamics of single cells. Finally we briefly explained how single cell properties within the computational models can be estimated from experimental data.

# 3

# Stochastic Modelling and Simulation of Ion Channel Dynamics

*In the previous chapter, we described the generation of an electrical action potential (AP) at the single cell level and how the dynamics of each cell are coupled together to allow this electrical activity to propagate throughout the heart. We also reviewed an experimentally observed phenomena called beat-to-beat variability in repolarisation which has been shown to be a potential biomarker of arrhythmia and is thought to arise due to the stochastic behaviour of ion channels. Therefore we want to incorporate the intrinsic stochastic behaviour of ion channel dynamics into electrophysiology models of cardiac cells. Due to the complexity of existing computational models of cardiac electrophsyiology, it is vital that any stochastic model of ion channel dynamics is as computationally efficient as possible to ensure such an investigation remains computationally tractable. However, it is important to ensure that such a gain in efficiency is not at the cost of loss of accuracy.*

*In this chapter we discuss the way in which the intrinsic stochastic behaviour of ion channels can be modelled mathematically. Since the opening and closing behaviour of an ion channel occurs due to conformational changes of the protein, we begin with a brief overview of stochastic modelling in biochemical reaction kinet-*

*ics. We then describe the different modelling regimes for ion channel dynamics: the discrete-state stochastic model, the continuous-state stochastic model and the deterministic model. Each regime will be introduced using the simplest model of ion channel dynamics, where each channel can reside in one of two states (either open or closed). The extension to more complex models will then be discussed. Since the continuous-state stochastic model is described using stochastic differential equations (SDEs) we provide the mathematical background of such systems. Finally we discuss operator splitting methods and describe how such techniques can be used to deal with the dependence of the transition rates in the models of ion channel dynamics on the voltage, which varies over time in electrophysiology models. Throughout this chapter, random variables are denoted by capital letters and individual realisations of these variables by lower case letters. Bold type is used to denote vectors, while scalar values are given in standard type.*

## 3.1 Overview of Stochastic Modelling in Cell Biology

Within each cell of living organisms, there are many complex chemical processes taking place in order to ensure the functioning of the cell. These involve the interaction between many different biomolecules, such as proteins and enzymes, in complex networks of biochemical reactions. Each interaction will generally be of two elementary types: unimolecular, these occur as a result of processes internal to the molecule, or bimolecular which occur as a result of collision between two molecules (higher order reactions, such as trimolecular reactions, are simply approximations of two or more elementary reactions).

These molecular interactions and internal molecular processes are random. Such randomness or stochasticity arises due to heterogeneities within and external to the cellular environment, as well as the chance processes that occur within and between molecules due to the discrete nature of such entities. Environmental fluctuations, i.e. variability arising due to conditions external to

the biochemical processes, are generally referred to as *extrinsic stochasticity (noise)*, and have been shown to play an important role in cellular biology, for example in genetic expression dynamics (Swain et al., 2002). The inherent variability arising from the molecular interactions and internal molecular processes is termed *intrinsic stochasticity (noise)*.

This intrinsic stochastic behaviour is traditionally ignored and the dynamics of the chemical or biochemical reactions are modelled using deterministic ordinary differential equations (ODEs) that describe the mean-field behaviour. Such an approach neglects the discrete nature of the system and instead considers the change in the concentration of a chemical species due to a reaction as a continuous process. When the number of channels is very large (*macroscopic scale*) such a model provides a good approximation to the dynamics of the system, since the random addition or subtraction of an individual molecule will have a small effect on the dynamics of the system.

However, when the number of molecules is small (*microscopic scale*), the discrete stochastic nature of the system has a significant effect on the dynamics, and the deterministic model no longer accurately captures the behaviour. In many biochemical processes, such as gene expression or immunology, there is often very low concentrations of some or all of the reactant molecules and in such situations traditional deterministic models have been shown to inadequately capture the dynamics of the biochemical reaction networks (Elowitz et al., 2002; Kaern et al., 2005; Raj and van Oudenaarden, 2008; Stirk et al., 2010). Chemical or biochemical reactions are assumed to possess the Markov property, namely that the probability of a reaction occurring at some point in the future only depends on the current number of reactant molecules. Therefore the number of each reactant species at time $t$ can be modelled as a discrete-state continuous-time Markov chain. The time evolution of the probability distribution of this random variable is given by a partial differential equation (PDE) called the *Master* or *forward Kolmogorov equation*. This model directly captures the intrinsic stochastic dynamics of the system.

At the *mesoscopic* scale it is meaningful to describe the state of the system by a continuous

variable that is the concentration of each species rather than the discrete number of molecules. However, the stochasticity arising as a result of the random nature of molecular interactions can still have a significant effect on the dynamics of the system. In such situations the stochastic behaviour of the system can be described by a stochastic differential equation (SDE) obtained from the first two moments of the discrete-state Markov chain model and so takes the special form of a *Langevin equation*, (Gillespie, 2000). This description lies between the fully discrete-state stochastic model and the continuous-state deterministic equations.

As described in the previous chapter, an ion channel transitions from a non-conducting (closed) to a conducting (open) state via a series of discrete conformational changes of the protein. That is, each change the ion channel protein goes through is essentially a unimolecular reaction, and the different conformational states of the protein can be considered different chemical species. Therefore, the dynamics of a collection of ion channels can be described by a network of reversible unimolecular reactions and so the modelling regimes discussed above can be applied to this system (see for example the state diagram in Chapter 2 Section 2.4.2, where each arrow represents a different unimolecular reaction).

Traditionally the different modelling regimes are discussed in terms of the algorithms used to simulate the dynamics of the system under each different regime. For example, the discrete-state Markov chain modelling regime is frequently introduced in terms of the stochastic simulation algorithm (SSA) which is used to simulate individual paths of the model. This has led to the separation between the mathematical formulation and assumptions used to *model* the dynamics of the system, and the numerical algorithms employed to *simulate* the behaviour of such mathematical models becoming blurred. Throughout this chapter we therefore try to clearly distinguish between the mathematical models of ion channel dynamics and the simulation methods associated with each model. Thus, for each regime we first discuss the mathematical model and then describe the numerical techniques used to simulate the dynamics of the model.

## 3.2 Discrete-State Markov Chain Model

### 3.2.1 A Simple Model

The simplest model of an ion channel is to assume that it can be in one of two states, open, $O$, or closed, $C$, at time $t$.

$$C \underset{b}{\overset{a}{\rightleftarrows}} O$$

For a collection of $N$ ion channels let the entries of the vector $\boldsymbol{X}(t) = (X_1(t), X_2(t))^T$ denote the number of channels in the open and closed states, respectively. If the system is currently in state $\boldsymbol{x}(t)$, then the probabilities of a single channel transitioning from closed to open, or open to closed in a small time interval $[t, t+\Delta_t)$ are respectively $ax_2\Delta_t$ and $bx_1\Delta_t$. The transition rates, $a$ and $b$, are usually thought to depend on the membrane potential $V$, which for small $\Delta_t$ can be assumed to remain constant over the time step. We shall discuss this approach of freezing the voltage over the time step in greater detail in Section 3.6. Therefore, in the following sections we shall consider the transition rates $a$ and $b$ to be constant.

The process $\boldsymbol{X}(t)$ is conventionally modelled as a **discrete-state continuous-time Markov chain** and the total number of channels $N$ is assumed to remain constant, (Groff et al., 2010). Therefore $\boldsymbol{X}(t)$ will take values on the two dimensional integer lattice $[0,\, N] \times [0,\, N]$. Since $N$ is constant, $X_2 = N - X_1$ and so only the number of channels in the open state, which we denote by $X(t)$, need be considered.

Let $P\,(x,\, t)$ be the probability that the system is in state $x$ (which is integer-valued) at time $t$, given some initial state $x_0$. The evolution of the system can be described by a PDE called the *Master equation*, (Gillespie, 1992), (Van Kampen, 2007) or the *forward Kolmogorov equation*, (Bhattacharya and Waymire, 2007). For the two state system the Master equation is given by

$$\begin{aligned}\frac{\partial P(x,t)}{\partial t} = a(N-(x-1))P(x-1,t) + b(x+1)P(x+1,t) \\ - (bx + a(N-x))P(x,t),\end{aligned} \tag{3.1}$$

for $0 < x < N$, $x \in \mathbb{N}$.

Since the total number of channels remains constant, the following condition must be satisfied

$$\sum_{x=0}^{N} \frac{\partial P(x,t)}{\partial t} = 0.$$

Using this, along with the fact that $X(t)$ cannot be negative or greater than $N$, $P(x,t)$ must satisfy the following equations at the boundary of the interval $[0, N]$.

$$\frac{\partial P(0,t)}{\partial t} = bP(1,t) - aNP(0,t),$$
$$\frac{\partial P(N,t)}{\partial t} = aP(N-1,t) - bNP(N,t).$$

This model of ion channel dynamics is somewhat an over-simplification of true ion channel behaviour within electrically excitable cells. More commonly a channel will reside in a number of different conformational states as it transitions to the open position and so more realistic models are far more complex than the two state model considered thus far (see (Rudy and Silva, 2006), for example). Therefore the discrete-state Markov chain model for more general ion channel dynamics, where the channel can reside in one of $m$ different states at time $t$, is described in the next section.

### 3.2.2 Generalisation to More Complex Ion Channel Models

As before, the total number of channels, $N$, is assumed to remain constant and the state of the system is now given by the vector $\boldsymbol{X}(t) = (X_1(t), \ldots, X_m(t))^T$, whose entries $X_i(t)$ are the number of channels in state $i$ at time $t$. A channel can transition from one state to another via $k$ different reversible transitions, so the total number of transitions possible in the system is $2k$. If transition $l$ results in a channel in state $i$ moving to state $j$ then the probability of transition $l$ occurring is $f_l(\boldsymbol{x}(t)) = r_{ij}x_i(t)$, where $r_{ij}$ is the transition rate of the channel shifting from state $i$ to $j$, for $i \neq j$. Note that if a channel cannot shift from state $i$ to state $j$ in a single

transition, then the transition rate $r_{ij}$ is set to zero. Analogously to the simple model described above, the transition probability that $\boldsymbol{X}(t) = \boldsymbol{x}$ given that $\boldsymbol{X}(t_0) = \boldsymbol{x}_0$ can be described by the following Master Equation (Van Kampen, 2007), (Gillespie, 1992),

$$\frac{\partial P(\boldsymbol{x}, t)}{\partial t} = \sum_{j=1}^{2k} \left( f_j(\boldsymbol{x} - \boldsymbol{v}_j) P(\boldsymbol{x} - \boldsymbol{v}_j, t) - f_j(\boldsymbol{x}) P(\boldsymbol{x}, t) \right), \tag{3.2}$$

where the entries of the vector $\boldsymbol{v}_j$ are the change in the number of channels in each state brought about by one transition of type $j$, $j = 1, \ldots, 2k$. The first term in the equation above is the gain due to transition into state $\boldsymbol{x}$ while the second term is the loss due to transition out of state $\boldsymbol{x}$. At the boundaries, care must be taken to ensure solutions remain in the correct region (namely the m dimensional integer lattice). An example of the form of the Master equation at the boundary is given later in this section.

Throughout this chapter we shall illustrate the generalisation of each modelling regime to complex ion channel models using the following hypothetical system as an example, and it shall be referred to as the three state model. We assume that each channel is either open ($O$), closed ($C$) or inactive ($I$) and that the dynamics satisfy the following state diagram.

**Figure 3.1** State diagram for hypothetical model of channel that can be in three different states.

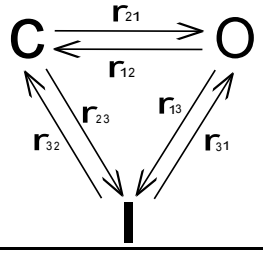


Let $X_1$ denote the number of channels in state $O$, $X_2$ the number of channels in state $C$ and $X_3$ the number of channels in state $I$. The dynamics of this system can be described by the

following Master equation,

$$\begin{aligned}\frac{\partial P(\boldsymbol{x},t)}{\partial t} &= r_{12}(x_1+1)P(\boldsymbol{x}-v_1,t) + r_{21}(x_2+1)P(\boldsymbol{x}-v_2,t) + r_{13}(x_1+1)P(\boldsymbol{x}-v_3,t) \\ &+ r_{31}(x_3+1)P(\boldsymbol{x}-v_4,t) + r_{23}(x_2+1)P(\boldsymbol{x}-v_5,t) + r_{32}(x_3+1)P(\boldsymbol{x}-v_6,t) \\ &- \left[r_{12}x_1 + r_{21}x_2 + r_{13}x_1 + r_{31}x_3 + r_{23}x_2 + r_{32}x_3\right] P(\boldsymbol{x},t). \end{aligned} \tag{3.3}$$

Where $v_1 = (-1,1,0)^T$, $v_2 = (1,-1,0)^T$, $v_3 = (-1,0,1)^T$, $v_4 = (1,0,-1)^T$, $v_5 = (0,-1,1)^T$ and $v_6 = (0,1,-1)^T$, and $0 < x_i < N$ for $i = 1,2,3$. At the boundary $\boldsymbol{x} = (N,0,0)^T$ (where $N$ is the number of channels), the Master equation becomes

$$\begin{aligned}\frac{\partial P(\boldsymbol{x},t)}{\partial t} &= \left[r_{21}P((N-1,1,0)^T,t) + r_{31}P((N-1,0,1)^T,t)\right] \\ &- \left[r_{12}N + r_{13}N\right] P((N,0,0)^T,t). \end{aligned} \tag{3.4}$$

The form of the Master equation at the other two boundaries $\boldsymbol{x} = (0,N,0)^T$ and $\boldsymbol{x} = (0,0,N)^T$ is similar.

### 3.2.3 Simulation Methods

#### Stochastic Simulation Algorithm

Individual trajectories of the process described by the Master equation can be simulated exactly using the stochastic simulation algorithm (SSA), also known as the Gillespie algorithm (Gillespie, 1976). The time until the next transition, $\tau$, is sampled from an exponential distribution whose parameter depends on the transition rates and the current number of channels in each state. The most likely transition to occur in this interval is determined by sampling a uniform random number on $[0,1]$ from $2k$ subintervals where the length of interval $i$ is equal to the probability of transition $i$ occurring, given the current state of the system. The number of channels in each state is then updated by the appropriate transition vector ($\boldsymbol{v}_j$) depending on which transition occurs. The computational efficiency of the SSA is largely governed by the time until the next transition, $\tau$, which varies throughout the simulation. As the number

of channels, $N$, increases the time until a transition occurs becomes very small, and so each simulation will involve a large number of small time-steps, greatly reducing the computational speed of the algorithm.

### Exact Solution

An alternative approach is to sample directly from the distribution at each time-step, where the distribution is obtained by solving the Master equation (MacNamara and Burrage, 2009). While for many systems the exact solution is not known, Jahnke and Huisinga (Jahnke and Huisinga, 2007) recently derived the solution to the Master equation that describes ion channel dynamics, equation (3.2), under the assumption of constant transition rates. If the initial probability distribution is a deterministic condition

$$P(\cdot,0)=\delta_{\xi}(\cdot)=\begin{cases}1 & \text{if } \boldsymbol{x}=\boldsymbol{\xi}\\ 0 & \text{otherwise,}\end{cases} \tag{3.5}$$

where $\boldsymbol{\xi}=(\xi_1,\xi_2,\ldots,\xi_m)\in\mathbb{N}^m$, then the probability distribution at time $t$ is given by,

$$P(\cdot,t)=M(\cdot,\xi_1,p^{(1)}(t))*\cdots*M(\cdot,\xi_m,p^{(m)}(t)) \tag{3.6}$$

$$\frac{dp^j}{dt}=Hp^j \quad p^j(0)=\epsilon_j, \quad j=1,\ldots,m \tag{3.7}$$

where $\epsilon_j$ is column $j$ of the $m$ by $m$ identity matrix and $M(\cdot,n,p)$ denotes the multinomial distribution with parameters $n$ and $p$. The matrix $H$ in (3.7) is the transition rate matrix for the deterministic limit of the discrete-state Markov model (note this is also equal to the transition rate matrix in the diffusion term of the SDE that describes this system and its form is discussed in greater detail in Section 3.4.2). For example, for the three state system the matrix $H$ will be,

$$H=\begin{pmatrix}-(r_{12}+r_{13}) & r_{21} & r_{31}\\ r_{12} & -(r_{21}+r_{23}) & r_{32}\\ r_{13} & r_{23} & -(r_{31}+r_{32})\end{pmatrix}.$$

Individual trajectories of the process can thus be simulated by first solving the differential equations (3.7), for $j=1,\cdots,m$, at each time step to obtain the parameters for the multinomial distributions in (3.6). Next $m$ different multinomial distributed random vectors, each of length

$m$, are generated and summed to give the state of the system at the next time step. This method was recently used by (Lemay et al., 2011) to model ion channel dynamics in a guinea-pig cardiac myocyte model. The advantage of this method is that it uses a fixed time-step. Therefore the computational efficiency largely depends on the generation of the multinomial random vectors, which in turn is dependent on the number of different states of the channel, $m$. So as the number of states becomes large, which is the case in many cardiac models (Rudy and Silva, 2006), this method becomes very computationally costly. In particular, for many cardiac models the time-step must be very small in order to resolve the steep upstroke of the AP (note this was not the case for the model used in (Lemay et al., 2011)) and thus embedding such an approach into many existing cardiac models becomes computationally intractable. Also, the generation of multinomial distributed random numbers is much more computationally intensive than generating uniform random numbers, as in the SSA, and so the gain in computational speed of using a fixed time step can be outweighed by the extra cost of having to generate a number of multinomial distributed random vectors at each time step.

The computational cost of simulating the discrete-state Markov chain model of ion channel dynamics restricts incorporation into tissue level models. Therefore the discrete-state Markov chain model is usually approximated by a continuous-state stochastic process called a *diffusion process*. Individual trajectories of such a process can be described by a stochastic differential equation (SDE) and so in the next section we give a brief introduction to SDEs before describing the diffusion approximation to the discrete-state Markov model in Section 3.4.

## 3.3 Background on Stochastic Differential Equations

### 3.3.1 What is a Stochastic Differential Equation?

Let $\boldsymbol{Z}(t) \in \mathbb{R}^n$ and $q : \mathbb{R}^n \to \mathbb{R}^n$, $g : \mathbb{R}^n \to \mathbb{R}^n \times \mathbb{R}^d$ be some continuous functions. A stochastic differential equation (SDE) is simply an ordinary differential equation (ODE) with

the addition of a randomly fluctuating term,

$$d\boldsymbol{Z} = q(\boldsymbol{Z})dt + g(\boldsymbol{Z})d\boldsymbol{W}, \tag{3.8}$$

where $d\boldsymbol{W}$ is the stochastic differential of the random process $\boldsymbol{W}(t)$ (which is $d$-dimensional), (Øksendal, 2010). Providing $q$ and $g$ satisfy certain regulatory conditions (Kloeden and Platen, 2011), (3.8) has a unique solution that is a stochastic process which consists of two parts: a deterministic part governed by the first term in (3.8) called the *drift coefficient*, and a varying term controlled by the last term in (3.8) called the *diffusion coefficient*.

The simplest random process to use as the randomly fluctuating term in (3.8), $\boldsymbol{W}(t)$, is a vector of Wiener processes, $\boldsymbol{W}(t) = (W_1(t), W_2(t), \ldots, W_d(t))^T$ where $W_i(t)$ is a stochastic process satisfying the following four properties:

1. $W_i(0) = 0$ with probability $1$,
2. $W_i(t + \Delta_t) - W_i(t)$ is independent of $W_i(t)$ for all $\Delta_t > 0$,
3. $W_i(t + \Delta_t) - W_i(t)$ is normally distributed with mean $0$ and variance $\Delta_t$,
4. $W_i(t)$ is continuous with probability $1$,

for $i = 1 \ldots d$. The stochastic differential with respect to the Wiener process ($d\boldsymbol{W}$) is often referred to as a Wiener increment. By the properties of the Wiener process, a sample of a Wiener increment is simply a normal random variable with mean $0$ and variance $\Delta_t$.

The stochastic differential is typically defined in terms of the corresponding stochastic integral. Writing (3.8) in integral form over the time interval $[t, t + \Delta_t]$, we obtain the following solution to (3.8) with initial condition $\boldsymbol{Z}(t)$,

$$\boldsymbol{Z}(t + \Delta_t) = \boldsymbol{Z}(t) + \int_t^{t+\Delta_t} q(\boldsymbol{Z}(s))ds + \int_t^{t+\Delta_t} g(\boldsymbol{Z}(s))d\boldsymbol{W}(s). \tag{3.9}$$

There are two common ways in which the stochastic integral in (3.9) can be defined. The first gives rise to an *Itô type* stochastic integral. This is defined as the mean square limit of Riemann

sums, with values of the integrand taken on the left-hand side of the discretisation intervals,

$$\sum_{i=0}^{l-1} g(\boldsymbol{Z}(t_i)) \left(\boldsymbol{W}(t_{i+1}) - \boldsymbol{W}(t_i)\right),$$

where $\{t_0, t_1, \ldots, t_l\}$ is a partition of the time interval $[t, t + \Delta_t]$, ($t_0 = t$).

The other type of stochastic integral is termed *Stratonovich* and we denote such integrals by $\int_t^{t+\Delta_t} g(\boldsymbol{Z}(s)) \circ d\boldsymbol{W}(s)$ to distinguish them from Itô type stochastic integrals. They are defined similarly as the mean square limit of Riemann sums, but the integrand is taken at the center of the discretisation interval,

$$\sum_{i=0}^{l-1} g\left(\boldsymbol{Z}\left(\tfrac{t_{i+1}+t_i}{2}\right)\right) \left(\boldsymbol{W}(t_{i+1}) - \boldsymbol{W}(t_i)\right).$$

The two types of integral are related by the following formula

$$\int_t^{t+\Delta_t} g(\boldsymbol{Z}(s)) \circ d\boldsymbol{W}(s) = \frac{1}{2}\int_t^{t+\Delta_t} g'(\boldsymbol{Z}(s))ds + \int_t^{t+\Delta_t} g(\boldsymbol{Z}(s))d\boldsymbol{W}(s), \tag{3.10}$$

providing $g$ is a twice continuously differentiable function (Klebaner, 2012). Therefore, SDEs of Itô type can be converted to Stratonovich type and vice-versa using the relation (3.10).

Stratonovich calculus is designed so that the basic rules, such as integration by parts and the chain rule, are the same as standard calculus. However, this is not the case for Itô type stochastic calculus which differs from that of traditional calculus, with the chain rule being one of the key differences. Since in this thesis we focus on SDEs of Itô type, we give a brief overview of the chain rule in the context of Itô stochastic calculus.

### 3.3.2 Itô's Lemma

The chain rule is a formula for the derivative of a composition of functions and for Itô type stochastic calculus it is given by Itô's Lemma.

**Itô's Lemma 3.3.1.** *For a twice continuously differentiable function $f : \mathbb{R}^n \to \mathbb{R}$ and a stochastic process $\boldsymbol{Z}(t)$ whose evolution over time is described by the SDE* (3.8)*, the following formula*

*holds*

$$d(f(\boldsymbol{Z})) = \left( \sum_{i=1}^{n} \frac{\partial f(\boldsymbol{Z})}{\partial Z_i} q_i(\boldsymbol{Z}) + \tfrac{1}{2} \sum_{i=1}^{n} \sum_{j=1}^{n} \frac{\partial^2 f(\boldsymbol{Z})}{\partial Z_i \partial Z_j} e_{ij}(\boldsymbol{Z}) \right) dt + \sum_{i=1}^{n} \frac{\partial f(\boldsymbol{Z})}{\partial Z_i} g_i(\boldsymbol{Z}) d\boldsymbol{W}, \tag{3.11}$$

*where* $e_{ij}(\boldsymbol{Z})$ *are the entries of the matrix* $e(\boldsymbol{Z}) = g(\boldsymbol{Z})g(\boldsymbol{Z})^T$ *and* $g_i(\boldsymbol{Z})$ *denotes row* $i$ *in the matrix-valued function* $g(\cdot)$*, so* $g_i(\boldsymbol{Z}) = (g_{i1}(\boldsymbol{Z}) \dots g_{id}(\boldsymbol{Z}))$ *is a vector-valued function, (Bhattacharya and Waymire, 2007).*

Itô's Lemma is particularly useful as it can be used to obtain the time evolution of the first two moments of the solution to an SDE, (Khanin and Higham, 2008). To calculate the first moment of each element of $\boldsymbol{Z}(t)$ we consider the function $f(\boldsymbol{Z}(t)) = Z_i(t)$. Then, from Itô's formula it follows that (3.11) becomes

$$d(Z_i) = q_i(\boldsymbol{Z})dt + g_i(\boldsymbol{Z})d\boldsymbol{W}, \tag{3.12}$$

for $i = 1, \dots, n$. Taking expectations in (3.12) and using the properties of the Wiener process and Itô integral, we obtain an ODE whose solution gives the time evolution of the mean of each component of $\boldsymbol{Z}$,

$$\frac{d\left(E(Z_i)\right)}{dt} = E\left(q_i(\boldsymbol{Z})\right). \tag{3.13}$$

Similarly by application of Itô's formula to the functions $f(\boldsymbol{Z}) = Z_i^2$ and $f(\boldsymbol{Z}) = Z_i Z_j$, for $i \neq j$, we obtain the following equations which can be used to calculate the variance and covariances,

$$d(Z_i^2) = \left(Z_i q_i(\boldsymbol{Z}) + e_{ii}(\boldsymbol{Z})\right) dt + Z_i g_i(\boldsymbol{Z}) d\boldsymbol{W} \tag{3.14}$$

$$d(Z_i Z_j) = \left(Z_i q_j(\boldsymbol{Z}) + Z_j q_i(\boldsymbol{Z}) + \tfrac{1}{2} e_{ij}(\boldsymbol{Z}) + \tfrac{1}{2} e_{ji}(\boldsymbol{Z})\right) dt + \left(Z_i g_j(\boldsymbol{Z}) + Z_j g_i(\boldsymbol{Z})\right) d\boldsymbol{W}. \tag{3.15}$$

Again, taking expectations of both sides in (3.14) and (3.15) and using the properties of the Wiener process, the following equations are obtained describing the time evolution of the second moments of each component of $\boldsymbol{Z}$,

$$\frac{d\left(E(Z_i^2)\right)}{dt} = E\left(Z_i q_i(\boldsymbol{Z})\right) + E\left(e_{ii}(\boldsymbol{Z})\right), \tag{3.16}$$

$$\frac{d(Z_i Z_j)}{dt} = E\left(Z_i q_j(\boldsymbol{Z})\right) + E\left(Z_j q_i(\boldsymbol{Z})\right) + E\left(\tfrac{1}{2} e_{ij}(\boldsymbol{Z})\right) + E\left(\tfrac{1}{2} e_{ji}(\boldsymbol{Z})\right). \tag{3.17}$$

The above formulae are useful since they allow a straightforward way to exactly obtain the first two moments of the stochastic process $\boldsymbol{Z}(t)$, rather than approximating such values from a large number of simulated paths. Furthermore, in simple cases, the ODEs above can be solved directly to provide analytic formula for the first two moments of $\boldsymbol{Z}(t)$. We shall use this method in Chapters 4 and 5 to directly obtain the first two moments of different formulations of the SDE model of ion channel dynamics for comparison.

### 3.3.3 Numerical Solution of SDEs

The simplest approximation to the integrals in (3.9) would be to apply the rectangle rule. This gives the following discretisation scheme to approximate the solution to (3.9) over the interval $[t, t + \Delta_t]$

$$\boldsymbol{Z}(t + \Delta_t) = \boldsymbol{Z}(t) + q(\boldsymbol{Z}(t))\Delta_t + g(\boldsymbol{Z}(t))\Delta \boldsymbol{W}_t, \tag{3.18}$$

where $\Delta \boldsymbol{W}_t$ is a vector of Wiener increments.

The simple numerical scheme given by (3.18) is called the Euler-Maruyama method and converges to the Itô solution of the SDE (3.8), (Maruyama, 1955). Many, more complex numerical methods have been developed since the Euler-Maruyama method was first introduced that improve the stability and rate of convergence of the numerical approximation to SDEs, such as (3.8). For example, many techniques commonly used to approximate solutions to ODEs, such as multistep methods, Runge-Kutta methods, and split-step methods, have been extended to SDEs. For more details on different numerical SDE methods, see for example (Kloeden and Platen, 2011; Gard, 1987) or the review by (Burrage et al., 2004).

### Convergence of a Numerical Method

To study the ability with which a numerical scheme, such as the Euler-Maruyama method, approximates the true solution, the notion of convergence must be made precise with respect to SDEs. There are two types of convergence in stochastic numerical analysis. Firstly, there are schemes that approximate the sample paths of an SDE, this is termed *strong* convergence. Such convergence is of interest when the behaviour of individual trajectories, rather than the distributional behaviour of the SDE is important. Strong convergence is defined as follows.

**Definition 3.3.1** (Strong Convergence)**.** *The discrete approximation $\boldsymbol{Z}_n$ converges in the strong sense with order $\gamma \in (0, \infty]$ to the exact solution $\boldsymbol{Z}_t$ if there exists a constant $K < \infty$ such that*

$$E\left(|\boldsymbol{Z}_t - \boldsymbol{Z}_n|\right) \leq K\Delta^{\gamma}. \tag{3.19}$$

The Euler-Maruyama method converges to the true solution with strong order $1/2$ when the functions $q(\boldsymbol{Z})$ and $g(\boldsymbol{Z})$ are Lipschitz, (Maruyama, 1955). In fact strong convergence still holds for weaker conditions on $q(\boldsymbol{Z})$ and $g(\boldsymbol{Z})$, (Higham et al., 2003; Berkaoui et al., 2008).

The other type of convergence is termed *weak* order convergence. Such schemes approximate the corresponding distribution of the solution to the SDE. Weak order schemes are used when only the statistical properties of the SDE, rather than individual realisations are of interest. Weak convergence is defined as follows.

**Definition 3.3.2** (Weak Convergence)**.** *The discrete approximation $\boldsymbol{Z}_n$ converges in the weak sense with order $\gamma \in (0, \infty]$ to the exact solution $\boldsymbol{Z}_t$ if for any polynomial $p$ there exists a constant $K_p < \infty$ such that*

$$|E(p(\boldsymbol{Z}_t)) - E(p(\boldsymbol{Z}_n))| \leq K_p\Delta^{\gamma}. \tag{3.20}$$

The Euler-Maruyama method converges with weak order $1$, (Milstein, 1979), and so has a higher weak order than under strong convergence. Methods often converge with higher order

under weak, rather than strong convergence, as the conditions for weak convergence are less strict.

## 3.4 Diffusion Approximation

In this section we discuss the approximation of the discrete-state Markov chain by a continuous-state model using the system size expansion approach of Van Kampen (Van Kampen, 2007). For the Hodgkin-Huxley model (Hodgkin and Huxley, 1952) much of the mathematical theory underlying this limit was presented by Pakdaman et al. (Pakdaman et al., 2010) and Fox and Lu (Fox and Lu, 1994). In these works, the authors explicitly take into account the voltage dependence of the transition rates. Since we assume that the transition rates are constant on a given time step, we give a simpler presentation of the mathematical theory, largely based on (Van Kampen, 2007). First the approximation for the simple model is described in detail and then the extension to the general model of ion channel dynamics is given.

### 3.4.1 Simple Model

As the number of channels becomes large, it makes sense to think of the state of the system in terms of proportions of channels in a certain state rather than discrete numbers. Therefore for the simple two state model we consider the behaviour of the scaled process $Y(t) = X(t)/N$, and so $Y(t)$ is the proportion of channels in the open state. For ease of notation we let $\tilde{y} = y - \frac{1}{N}$ and $\hat{y} = y + \frac{1}{N}$. The Master equation, (3.1), thus becomes

$$\begin{aligned}\frac{\partial P(y,t)}{\partial t} &= N\left[a(1-\tilde{y})P(\tilde{y},t) + b\hat{y}P(\hat{y},t)\right] \\ &\quad - N\left[by + a(1-y)\right]P(y,t),\end{aligned} \tag{3.21}$$

for $0 < y < 1$, $y \in \mathbb{R}$. Note we have not considered the behaviour of the system at the boundary. We shall deal with the boundary conditions for this system in Chapter 6.

Consider taking the Taylor expansion of the first two terms in (3.21) about the point $y$. We assume that $N$ is large enough so that terms of order greater than two can be considered negligible (Van Kampen, 2007; Fox and Lu, 1994). The first two terms can thus be approximated by the following expressions,

$$a(1-\tilde{y})P(\tilde{y},t) \approx a(1-y)P(y,t) - \tfrac{1}{N}\tfrac{\partial}{\partial y}\left(a(1-y)P(y,t)\right) + \tfrac{1}{2N^2}\tfrac{\partial^2}{\partial y^2}\left(a(1-y)P(y,t)\right),$$

$$b(\hat{y})P(\hat{y},t) \approx byP(y,t) + \tfrac{1}{N}\tfrac{\partial}{\partial y}\left(byP(y,t)\right) + \tfrac{1}{2N^2}\tfrac{\partial^2}{\partial y^2}\left(byP(y,t)\right).$$

Replacing these terms in (3.21) by the appropriate expansion we obtain a PDE called the *Fokker-Planck equation*, (Van Kampen, 2007; Fox and Lu, 1994),

$$\begin{aligned}\frac{\partial P(y,t)}{\partial t} &= -\tfrac{\partial}{\partial y}\left[\left(a-(a+b)y\right)P(y,t)\right] \\ &\quad + \tfrac{1}{2N}\tfrac{\partial^2}{\partial y^2}\left[\left(a+(b-a)y\right)P(y,t)\right].\end{aligned} \tag{3.22}$$

This equation describes the evolution in the probability distribution of a continuous-state continuous-time Markov chain model, which is frequently referred to as a *diffusion process*, (Bhattacharya and Waymire, 2007). Therefore, in moving from (3.1) to (3.22) we effectively assume that for large enough $N$, the dynamics of the discrete-state Markov chain can be well approximated by those of a diffusion process.

It is well known that the sample paths of a diffusion process can be described by an SDE, (Gihman and Skorokhod, 1972), and in the case of (3.22) this takes the form of the following *Langevin equation*, (Gillespie, 2000, 2002)

$$dY = \left(a-(a+b)Y\right)dt + \tfrac{1}{\sqrt{N}}\sqrt{a+(b-a)Y}\,dW, \tag{3.23}$$

where, $dW(t)$ is a Wiener increment.

### 3.4.2 Generalisation to Complex Model

The discrete-state Markov chain for the general model of ion channel dynamics in Section 3.2.2 can also be approximated by a diffusion process as $N$ becomes large, by taking the Taylor

expansion of the first term in (3.2).

Let $H$ be an $m \times m$ matrix of the transition rates between states where the diagonal entries, $(i,i)$, are equal to $-\sum_{j=1}^{m} r_{ij}$ and the off diagonal entries, $(i,j)$ $i \neq j$, are equal to $r_{ji}$. Let $\upsilon$ be the matrix whose columns are the state change vectors $\upsilon = (\boldsymbol{v}_1, \ldots, \boldsymbol{v}_m)^T$ and $D(\boldsymbol{y})$ be a diagonal matrix with corresponding transition functions along the diagonal. Then the Fokker-Planck equation for the general model of ion channel dynamics is,

$$\frac{\partial P(y,t)}{\partial t} = -\sum_{i=1}^{m} \frac{\partial}{\partial y_i} \left[A_i(y)P(y,t)\right] + \tfrac{1}{2N} \sum_{i,l=1}^{m} \frac{\partial^2}{\partial y_i y_l} \left[B_{il}(y)P(y,t)\right]. \tag{3.24}$$

where $A(\boldsymbol{y}) = H\boldsymbol{y}$ and the matrix $B(\boldsymbol{y})$ is given by $B(\boldsymbol{y}) = \upsilon D(\boldsymbol{y})\upsilon^T$.

As before, the individual trajectories of the approximate diffusion process can be described by the following Langevin type SDE, (Goldwyn et al., 2011; Fox and Lu, 1994),

$$d\boldsymbol{Y} = H\boldsymbol{Y}dt + \tfrac{1}{\sqrt{N}}\sqrt{B(\boldsymbol{Y})}d\boldsymbol{W}, \tag{3.25}$$

where $d\boldsymbol{W}$ is a vector of independent Wiener increments. Note the diffusion term can be written in a simple way, as the product of a matrix and a vector, due to the linearity of the transition rate functions, $f_l(\boldsymbol{Y})$.

This equation was first described by Fox and Lu, (Fox and Lu, 1994), for the sodium and potassium channels in the Hodgkin-Huxley model and was later implemented by Goldwyn et al. (Goldwyn et al., 2011). The issue with (3.25) is that it involves the square root of a matrix, limiting the computational speed up over the discrete-state Markov chain model (Goldwyn et al., 2011). In Chapter 4 we show how the square root of the matrix $B(\boldsymbol{Y})$ can be written in a simple way as the product of two matrices, due to the special structure of the system. Therefore the computational speed can be increased, since forming the diffusion term in this way does not involve taking the square root of a matrix at each time-step.

For the three state model, the SDE describing the dynamics of this system will take the following

form. Let $Y_1$ denote the proportion of channels in state $O$, $Y_2$ the proportion in state $C$ and $Y_3$ the proportion in state $I$. Then

$$d\boldsymbol{Y} = \begin{pmatrix} -(r_{12}+r_{13}) & r_{21} & r_{31} \\ r_{12} & -(r_{21}+r_{23}) & r_{32} \\ r_{13} & r_{23} & -(r_{31}+r_{32}) \end{pmatrix} \boldsymbol{Y} dt \tag{3.26}$$
$$+ \frac{1}{\sqrt{N}} \sqrt{\begin{pmatrix} f_1(\boldsymbol{Y})+f_3(\boldsymbol{Y}) & -f_1(\boldsymbol{Y}) & -f_3(\boldsymbol{Y}) \\ -f_1(\boldsymbol{Y}) & f_2(\boldsymbol{Y})+f_3(\boldsymbol{Y}) & -f_2(\boldsymbol{Y}) \\ f_3(\boldsymbol{Y}) & f_2(\boldsymbol{Y}) & f_2(\boldsymbol{Y})+f_3(\boldsymbol{Y}) \end{pmatrix}} \begin{pmatrix} dW_1 \\ dW_2 \\ dW_3 \end{pmatrix},$$

where $f_1(\boldsymbol{Y}) = r_{12}Y_1 + r_{21}Y_2$, $f_2(\boldsymbol{Y}) = r_{32}Y_3 + r_{23}Y_2$, $f_3(\boldsymbol{Y}) = r_{13}Y_1 + r_{31}Y_3$.

### 3.4.3 Simulation Methods

There are two different ways in which individual sample paths of the ion channel diffusion model, described above, can be simulated. Firstly the Fokker-Planck equation, (3.22) and (3.24), can be numerically solved at each time-step using a standard PDE solver. This will provide the probability distribution for the process, and so a sample from this distribution can be generated to obtain the state of the system at that time-step. The problem with this method is that it can be quite computationally intensive, since the Fokker-Planck equation, particularly for the complex ion channel model, is not straightforward to solve numerically. Therefore, using this approach there is little, if any, computational gain over simulation methods for the discrete-state Markov chain model.

Alternatively, the SDE associated with the Fokker-Planck equation can be numerically approximated, providing an individual realisation of the ion channel diffusion process. As discussed in Section 3.3.3, there are a wealth of different numerical methods that have been developed to approximate solutions to SDEs, many of which are based on ODE methods and have comparable computational efficiency with such algorithms. For example, the extra cost of employing the Euler-Maruyama method, given by (3.18), over the standard Euler method is that at each time step a normal random variable must be generated. However, this can be initialised at the start of the simulation for all time steps and so the extra computational cost is very minimal. Thus using numerical solutions to the SDE that describes the diffusion process, the stochastic

ion channel dynamics can be simulated with much greater computational efficiency compared with the discrete-state Markov chain model. Furthermore, the computational cost of simulating individual trajectories of the process using an SDE does not greatly increase with the number of channels ($N$) or the number of different states of the channel ($m$), as is the case with the discrete-state Markov model simulation methods. Instead the computational efficiency largely depends on the size of the time-step used in simulation. Unlike the ODE, the computational cost of the SDE also depends on the number of simulations, since multiple simulations need to be performed to infer information about the distributional properties of the dynamics.

## 3.5 Deterministic Model

The diffusion terms in the SDEs that describe the simple and general ion channel models, (3.23) and (3.25) scale with the inverse of the square root of the size of the system, $(\sqrt{N})^{-1}$. Thus taking the limit as $N \to \infty$, the diffusion term disappears and we obtain the following two systems of ODEs that describe the dynamics of the simple and complex ion channel model respectively (Gillespie, 2007),

$$\frac{dY}{dt} = a - (a+b)Y \tag{3.27}$$

$$\frac{d\boldsymbol{Y}}{dt} = H\boldsymbol{Y}. \tag{3.28}$$

In chemical kinetic theory, these equations are termed *reaction rate equations* (RREs) and describe the behaviour of the system if the fluctuations could be ignored, (Gillespie, 2007). That is, they specify the mean-field behaviour of each system.

The deterministic model describes the state of the system by a continuous variable and ignores the randomness within the system. So for a given initial condition the system will always be in the same state at some specified later time point. The deterministic model therefore lies at the opposite end of the spectrum to the discrete-state Markov chain model. The SDE model is continuous, as with deterministic model, but still captures the random fluctuations within the

system, as with discrete-state Markov model. Therefore it can be seen as providing a bridge between these two approaches.

The three different modelling regimes outlined represent different levels of coarseness of the stochastic dynamics, and provide an accurate description of the dynamics depending on the size of the system being modelled. The two coarser modelling regimes can be derived directly from the stochastic dynamics of the discrete-state system, and describe the limiting behaviour as the number of channels becomes large. Figure 3.2 is a schematic of the way in which these three modelling regimes are related.

**Figure 3.2** Schematic of the different modelling regimes and the numerical methods used to simulate the dynamics of each modelling regime.

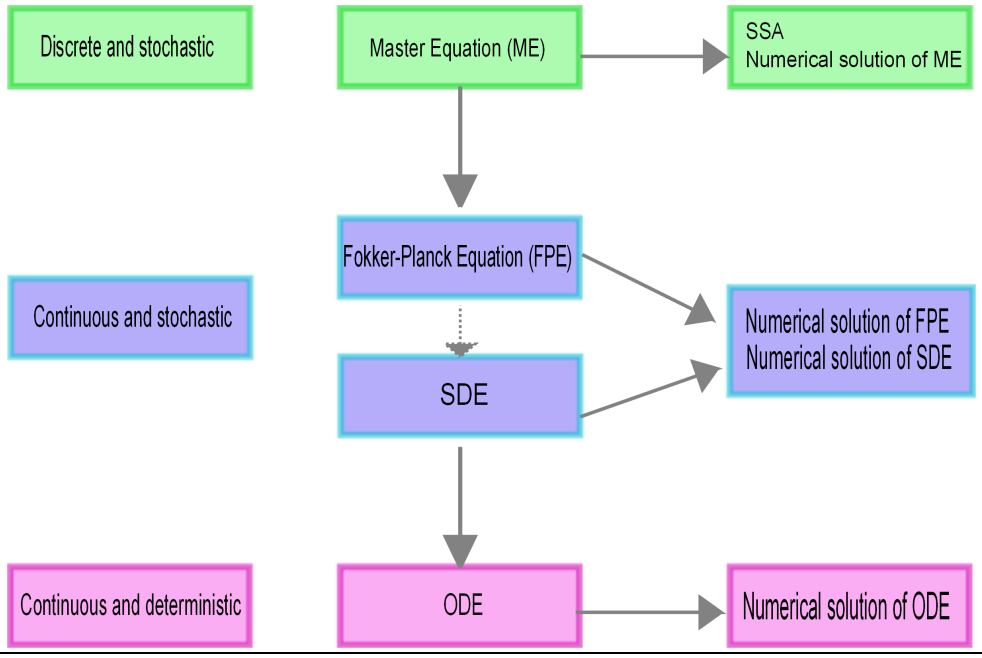


## 3.6 Splitting-Step Methods

So far we have ignored the fact that the transition rates are voltage dependent and just considered simulating stochastic ion channel dynamics when the transition rates are constant. However, in electrophysiology models these transition rates are nonlinear functions of the membrane

potential ($V$) and so the stochastic ion channel dynamics are coupled to the ODE that describes the evolution of the membrane potential, equation (2.2) in the previous chapter.

Consider the simple ODE problem,

$$\frac{du}{dt} = Au, \tag{3.29}$$

where $u \in \mathbb{R}^d$ and $A$ is a square $d \times d$ matrix. The solution of this system over the interval $[t, t + \Delta_t]$ is simply,

$$u(t + \Delta_t) = exp(A\Delta_t)u(t). \tag{3.30}$$

Therefore to obtain the solution at time $t + \Delta_t$ the exponential of a matrix times a vector must be calculated, which can be computationally intensive depending on $A$. Consider decomposing $A$ into two matrices whose exponentials are easier to compute, $A = E + F$. Instead of solving the one ODE, (3.29), we can solve the two following equations over one time-step $[t, t + \Delta_t]$,

$$\frac{du_1}{dt} = Eu_1, \quad u_1(t) = u(t), \tag{3.31}$$

$$\frac{du_2}{dt} = Fu_2, \quad u_2(t) = u_1(t + \Delta_t). \tag{3.32}$$

Using the solution to (3.31) as the initial condition in (3.32), we obtain the following solution over the time interval of length $\Delta_t$,

$$u(t + \Delta_t) \approx exp(F\Delta_t)exp(E\Delta_t)u(t).$$

The original problem can be solved directly to give the following exact solution over a time interval of length $\Delta_t$,

$$u_{exact}(t + \Delta_t) = exp((F + E)\Delta_t)u(t).$$

Usually $u_{exact}(t + \Delta_t) \neq u(t + \Delta_t)$, and so there is some error associated with splitting the original problem, called the *local splitting error*, and it is defined to be

$$\begin{aligned} E_{sp}(t + \Delta_t) &= u_{exact}(t + \Delta_t) - u(t + \Delta_t) \\ &= [exp((F + E)\Delta_t) - exp(F\Delta_t)exp(E\Delta_t)]u(t). \end{aligned}$$

Therefore the local error vanishes providing

$$exp((E+F)\Delta_t) = exp(F\Delta_t)exp(E\Delta_t),$$

which is the case providing $E$ and $F$ commute, that is $EF = FE$.

This simple scheme is often called *sequential splitting* and is an order one method by the Baker-Campbell-Hausdorff Theorem (Hall, 2003). The order of the scheme can be improved by splitting the system of ODEs in different ways. For example, the Strang splitting scheme (Strang, 1968), an order two method, splits (3.29) into a system of three palindromic equations. Once again this method introduces a local splitting error which vanishes if the matrices commute, (Strang, 1968). For more details on different types of splitting-step methods see for example (Burrage, 1995).

Splitting-step methods have also been applied in stochastic numerical analysis, where they have often been employed to ensure the numerical approximation preserves boundaries inherent in the analytic SDE solution. For example, (Moro and Schurz, 2007) developed a method that decomposes the SDE into two equations; an SDE that can be solved analytically and an ODE that is solved numerically. (Ninomiya and Victoir, 2008), introduced a scheme for Stratonovich type SDEs that is based on the Strang splitting method and is shown to ensure numerical solutions are positive for particular financial models under certain parameter regimes. Halley et al. introduced two splitting schemes that aim to preserve positivity in the numerical approximation, one for Stratonovich type SDEs, (Halley et al., 2008), and the other for Itô type SDEs, (Halley et al., 2009). The first scheme uses a Strang splitting approach to decompose the system into the drift and diffusion vector fields. The second method uses a Jacobi split to incorporate implicitness into the diffusion vector field for the Euler-Maruyama and Milstein methods. In Chapter 5 we shall describe a new splitting-step method that aims to preserve the boundaries of a particular SDE called the Wright-Fisher model.

In the same manner as the simple example discussed above, we can deal with the issue of the

voltage dependence of the transition rates by splitting the system into different parts. Consider splitting the full system into the stochastic model that describes the ion channel dynamics (for example the SDE model) and the ODE that describes the voltage. Freezing the membrane voltage over a time step, the stochastic model of ion channel dynamics can then be simulated and finally the voltage for that time step can be updated. In this manner the stochastic model of ion channel dynamics can be simulated within electrophysiology models using the methods described in the previous sections, where the transition rates are assumed to remain constant.

## 3.7 Chapter Summary

In this chapter we provided an overview of the different stochastic modelling regimes used to capture the intrinsic variability within biochemical reaction networks, and discussed how the random state transitions of ion channels can effectively be considered as a system of unimolecular reversible reactions. We discussed in detail the formulation of the discrete-state Markov chain model for the simplest of ion channel dynamics, where the channel can be either open or closed. The extension of this model to more complex and realistic ion channel dynamics was also given. We then described techniques for simulating the behaviour of the discrete-state Markov chain model and discussed the computational limitations of such algorithms.

Since the approximate stochastic model for the discrete-state Markov chain takes the form of a system of stochastic differential equations (SDEs), we gave a brief review of SDEs including the numerical methods used to approximate solutions to such equations. We also defined notions of convergence of stochastic numerical methods and the definition of Itô's Lemma was given. Next the approximation of the discrete-state Markov chain model by an SDE model, in terms of a system size expansion, was discussed for the simple ion channel model and the generalisation of the approximation to more complex models was given. We considered the convergence of the SDE model to the standard deterministic model, in the limit as the number of channels becomes large, and illustrated the relation between the different modelling regimes. Finally, we

briefly discussed split-step numerical methods and described how this approach can be used to deal with the voltage dependent transition rates in the models of ion channels within numerical simulations of electrophysiology models.

# 4

# Challenges with the SDE Model of Ion Channel Dynamics

*In the previous chapter we described the approximation of the discrete-state Markov chain model by a system of SDEs. The SDE model poses as an attractive alternative to the discrete-state Markov chain approach for studying the effects of stochastic ion channel behaviour on the dynamics of electrically excitable cells and tissue, due to the appreciable computational speed up achieved. For this reason it has been frequently utilised to simulate ion channel dynamics within a range of different electrically excitable cells including neuronal cells (Fox, 1997; Sun et al., 2011), cardiac myocytes (Pueyo et al., 2011), and pancreatic beta cells (De Vries and Sherman, 2000). However, the accuracy of the SDE approach has come into question in recent years for two main reasons. Firstly a number of studies have demonstrated that the SDE approach does not faithfully capture the stochastic behaviour of the discrete-state Markov chain model (Mino et al., 2002; Bruce, 2009; Sengupta et al., 2010). Secondly solutions to the SDE model can become negative and even imaginary, and so in such situations have no physical meaning (Dangerfield et al., 2010).*

*In this chapter we investigate the reason such challenges arise with the SDE model.*

*It turns out that the first challenge is due to the way in which the SDE model is formulated within the neuroscience community, which is a slightly different approach to that usually employed in other fields of stochastic modelling. Therefore we show that this challenge can be dealt with in a straightforward manner by correct formulation of the SDE model in terms of the whole channel dynamics. Furthermore we show that the correct SDE can be formulated in a computationally efficient way which, while frequently employed within the stochastic biochemical modelling community, has not previously been used in the neuroscience literature.*

*The second challenge is not so easily dealt with, and indeed the underlying reason why the SDE model does not guarantee biologically realistic simulations is unclear. Therefore the rest of the chapter is devoted to an examination of the difficulties with the numerical methods used to simulate the SDE model, as well as the analytic solutions to the underlying model itself.*

## 4.1 Correct Formulation of the Ion Channel SDE Model

In Chapter 3 Section 3.4.2 we gave the SDE formulation of the general ion channel model that was derived by Fox and Lu for the Hodgkin-Huxley model (Hodgkin and Huxley, 1952). For a general ion channel model, where the channel can be in one of $m$ different states and can undergo $k$ different reversible transitions this SDE is

$$d\boldsymbol{Y} = H\boldsymbol{Y}dt + \tfrac{1}{\sqrt{N}}\sqrt{B(\boldsymbol{Y})}d\boldsymbol{W}, \tag{4.1}$$

where the entries of the vector $\boldsymbol{Y}$ are the proportion of channels in each state. This equation involves the square root of a matrix, limiting the computational speed up over the discrete-state Markov chain simulation approach. Therefore, in Fox and Lu (1994), the authors describe an approximate SDE model of ion channel dynamics to improve the efficiency of the SDE model. However, the increase in computational speed, comes at the cost of accuracy in capturing the

stochastic behaviour of the discrete-state Markov chain model (Bruce, 2009; Mino et al., 2002).

In the next section we describe in greater detail the Fox and Lu SDE model of ion channel dynamics. We then show how the SDE model can be formulated so that it does not involve the square root of a matrix. Finally we compare the first two moments in the number of open channels for the two different SDE models with the discrete-state Markov chain model.

### 4.1.1 Fox and Lu Algorithm

In (Fox and Lu, 1994) Fox and Lu describe the dynamics of each gating variable in the Hodgkin-Huxley model by an SDE. These stochastic gating variables are then used to determine the proportion of open channels, as in the Hodgkin-Huxley formulation of ion channel dynamics.

The dynamics of the whole channel are approximated by the collective behaviour of a series of hypothetical gating variables, where each gate can be either open or closed at any time. Since each gate has two different states, (i.e. the gating behaviour is modelled using the simple model discussed in Chapter 3 Section 3.4.1), it follows that the fraction of open gating particles of type $X$ can be described by the following SDE

$$\frac{dX(t)}{dt} = (a_X - (a_X + b_X)X(t))dt + \frac{1}{\sqrt{N_{tot}}}\sqrt{a_X + (b_X - a_X)X(t)}dW, \tag{4.2}$$

where $N_{tot}$ is the total number of channels and $a_X$, $b_X$ are the rates at which a gate of type $X$ opens and closes, respectively. The channel is assumed to be open only when all gates are open. Therefore the proportion of open channels is estimated to be the product of the proportion of open gating variables. The Hodgkin-Huxley model assumes that the sodium channel is comprised of three identical $m$ gates and another gate termed the $h$ gate, while the potassium channel is assumed to consist of four identical $n$ gates. Thus the proportion of open sodium and potassium channels at time $t$ are given by $m(t)^3h(t)$ and $n(t)^4$, respectively, where the variables $m(t)$, $h(t)$ and $n(t)$ are random and are calculated using (4.2).

This method gives substantial computational speed up over numerically solving the SDE model

given by (4.1). Indeed Goldwyn et al. (2011) the authors report that this approximate SDE method takes $25$ times less computational time than solving (4.1), with the increased computational cost in (4.1) largely a result of the square root term.

### 4.1.2 Fast Simulation of the Full Channel SDE Model

Since the model of ion channel dynamics is essentially a system of reversible unimolecular reactions, it is possible to decompose the matrix $B(\boldsymbol{Y})$ so that the square root can be described exactly by the product of two matrices, (Melykuti et al., 2010). The decomposition of the matrix $B(\boldsymbol{Y})$ is non-unique, that is there are different matrices $\tilde{B}(\boldsymbol{Y})$ such that $\tilde{B}(\boldsymbol{Y})\tilde{B}(\boldsymbol{Y})^T = B(\boldsymbol{Y})$. In (Melykuti et al., 2010) the authors show the smallest dimension of the matrix $\tilde{B}(\boldsymbol{Y})$ that satisfies $\tilde{B}(\boldsymbol{Y})\tilde{B}(\boldsymbol{Y})^T = B(\boldsymbol{Y})$ is $m \times k$, and this matrix takes the form $\tilde{B}(\boldsymbol{Y}) = EF(\boldsymbol{Y})$. Here $E$ is a matrix of $0's$, $-1's$, and $1's$ and $F(\boldsymbol{Y})$ is a diagonal matrix whose entries are of the form $\sqrt{r_{ij}y_i + r_{ji}y_j}$. Therefore (4.1) becomes (Melykuti et al., 2010)

$$d\boldsymbol{Y} = H\boldsymbol{Y}dt + \tfrac{1}{\sqrt{N}}EF(\boldsymbol{Y})d\boldsymbol{W}. \tag{4.3}$$

This form of the the ion channel SDE model was also recently given in (Orio and Soudry, 2012). We use this formulation of the decomposition of the matrix $B(\boldsymbol{Y})$ since it employs fewer Wiener increments than other formulations, such as that given in (Gillespie, 2000) and so is more computationally efficient. While such forms of the diffusion term have been known and utilised in the stochastic biochemical reaction modelling community (Melykuti et al., 2010), this has not been the case in the electrophysiology, and in particular the neuroscience community.

We use the sodium and potassium channels from Hodgkin-Huxley model as examples to describe the form of the matrices $E$ and $F(\boldsymbol{Y})$. In the model the sodium channel is described by three $m$ gates and one $h$ gate while the potassium channel is described by four $n$ gates. Assuming each possible configuration of open and closed gates represent a different state of the channel, the dynamics of the sodium and potassium channels are given by the following state

diagrams respectively:

$$\begin{array}{ccccccc} m_0h_0 & \underset{b_m}{\overset{3a_m}{\rightleftarrows}} & m_1h_0 & \underset{2b_m}{\overset{2a_m}{\rightleftarrows}} & m_2h_0 & \underset{3b_m}{\overset{a_m}{\rightleftarrows}} & m_3h_0 \\ b_h\uparrow\downarrow a_h & & b_h\uparrow\downarrow a_h & & b_h\uparrow\downarrow a_h & & b_h\uparrow\downarrow a_h \\ m_0h_1 & \underset{b_m}{\overset{3a_m}{\rightleftarrows}} & m_1h_1 & \underset{2b_m}{\overset{2a_m}{\rightleftarrows}} & m_2h_1 & \underset{3b_m}{\overset{a_m}{\rightleftarrows}} & m_3h_1 \end{array},$$

$$n_0 \underset{b_n}{\overset{4a_n}{\rightleftarrows}} n_1 \underset{2b_n}{\overset{3a_n}{\rightleftarrows}} n_2 \underset{3b_n}{\overset{2a_n}{\rightleftarrows}} n_3 \underset{4b_n}{\overset{a_n}{\rightleftarrows}} n_4 ,$$

where $a_i$, $b_i$ are the closed to open and open to closed transition rates of gate $i$, respectively, $m_ih_j$ denotes the state where $i$ $m$ gates and $j$ $h$ gates are open and similarly $n_i$ denotes the state where $i$ $n$ gates are open.

Let $y_{ij}(t)$ denote the proportion of sodium channels with $i$ open $m$ gates and $j$ open $h$ gates at time $t$. Similarly let $x_i(t)$ denote the proportion of open potassium channels with $i$ open $n$ gates at time $t$. The state of the potassium channel at time $t$ is given by the vector $\boldsymbol{x}(t) = (x_4, x_3, x_2, x_1, x_0)^T$ and the state of the sodium channel is denoted by,

$$\boldsymbol{y}(t) = (y_{31}, y_{21}, y_{11}, y_{01}, y_{30}, y_{20}, y_{10}, y_{00})^T. \tag{4.4}$$

Formulating the noise term in the same manner as in (4.3), the dynamics of the sodium and potassium channels can be described by the following SDEs, respectively,

$$d\boldsymbol{y} = H_{Na}\boldsymbol{y}dt + \tfrac{1}{\sqrt{N_{Na}}}E_{Na}F_{Na}(\boldsymbol{y})d\boldsymbol{W}^{Na}, \tag{4.5}$$

$$d\boldsymbol{x} = H_K\boldsymbol{x}dt + \tfrac{1}{\sqrt{N_K}}E_KF_K(\boldsymbol{x})d\boldsymbol{W}^K. \tag{4.6}$$

In the above formula

$$F_{Na} = diag\begin{pmatrix} \sqrt{a_my_{21}+3b_my_{31}} \\ \sqrt{2a_my_{11}+2b_my_{22}} \\ \sqrt{3a_my_{01}+b_my_{11}} \\ \sqrt{a_my_{20}+3b_my_{30}} \\ \sqrt{2a_my_{10}+2b_my_{20}} \\ \sqrt{3a_my_{00}+b_my_{10}} \\ \sqrt{a_hy_{00}+b_hy_{01}} \\ \sqrt{a_hy_{10}+b_hy_{11}} \\ \sqrt{a_hy_{20}+b_hy_{21}} \\ \sqrt{a_hy_{30}+b_hy_{31}} \end{pmatrix}, \qquad F_K = diag\begin{pmatrix} \sqrt{a_nx_3+4b_nx_4} \\ \sqrt{2a_nx_2+3b_nx_3} \\ \sqrt{3a_nx_1+2b_nx_2} \\ \sqrt{4a_nx_0+b_nx_1} \end{pmatrix},$$

respectively, and

$$H_{Na} = \begin{pmatrix} -d_1 & a_m & 0 & 0 & a_h & 0 & 0 & 0 \\ 3b_m & -d_2 & 2a_m & 0 & 0 & a_h & 0 & 0 \\ 0 & 2b_m & -d_3 & 3a_m & 0 & 0 & a_h & 0 \\ 0 & 0 & b_m & -d_4 & 0 & 0 & 0 & a_h \\ b_h & 0 & 0 & 0 & -d_5 & a_m & 0 & 0 \\ 0 & b_h & 0 & 0 & 3b_m & -d_6 & 2a_m & 0 \\ 0 & 0 & b_h & 0 & 0 & 2b_m & -d_7 & 3a_m \\ 0 & 0 & 0 & b_h & 0 & 0 & b_m & -d_8, \end{pmatrix}$$

where the diagonal entries $(d_1, \ldots, d_8)$ are equal to

$$(d_1, \ldots, d_4) = (b_h + 3b_m, a_m + 2b_m + b_h, 2a_m + b_m + b_h, 3a_m + b_h)\,,$$

$$(d_5, \ldots, d_8) = (a_h + 3b_m, a_h + a_m + 2b_m, 2a_m + b_m + a_h, a_h + 3a_m)\,.$$

The final matrices in (4.5) and (4.6) are as follows,

$$E_{Na} = \begin{pmatrix} -1 & 0 & 0 & 0 & 0 & 0 & 0 & 0 & 0 & -1 \\ 1 & -1 & 0 & 0 & 0 & 0 & 0 & 0 & -1 & 0 \\ 0 & 1 & -1 & 0 & 0 & 0 & 0 & -1 & 0 & 0 \\ 0 & 0 & 1 & 0 & 0 & 0 & -1 & 0 & 0 & 0 \\ 0 & 0 & 0 & -1 & 0 & 0 & 0 & 0 & 0 & 1 \\ 0 & 0 & 0 & 1 & -1 & 0 & 0 & 0 & 1 & 0 \\ 0 & 0 & 0 & 0 & 1 & -1 & 0 & 1 & 0 & 0 \\ 0 & 0 & 0 & 0 & 0 & 1 & 1 & 0 & 0 & 0 \end{pmatrix},$$

$$H_K = \begin{pmatrix} -4b_n & a_n & 0 & 0 & 0 \\ 4b_n & -(a_n+3b_n) & 2a_n & 0 & 0 \\ 0 & 3b_n & -2(a_n+b_n) & 3a_n & 0 \\ 0 & 0 & 2b_n & -(3a_n+b_n) & 4a_n \\ 0 & 0 & 0 & b_n & -4a_n \end{pmatrix},$$

and

$$E_K = \begin{pmatrix} 1 & 0 & 0 & 0 \\ -1 & 1 & 0 & 0 \\ 0 & -1 & 1 & 0 \\ 0 & 0 & -1 & 1 \\ 0 & 0 & 0 & -1 \end{pmatrix}.$$

The form of the noise term given in (4.3) will require a larger number of Wiener increments than the original formulation given by (4.1), when the number of reversible transitions is greater than the number of different states of the channel. For example, in the Hodgkin-Huxley model, the sodium channel is assumed to consist of $8$ different states which can undergo $10$ different pairs of reversible reactions. The formulation of the SDE (4.1) will require $8$ Wiener increments at each time step, while (4.3) will require $10$ in this case. However, since all Wiener increments for the simulation can be initialised at the start of simulation, the extra computational cost in generating more Wiener increments per simulation is very minimal. Indeed, it is certainly much less computationally intensive than taking the square root of a matrix at each time step, and thus provides substantial improvement in speed over (4.1).

Note that the computational cost of simulating (4.3) can be marginally reduced by lowering the dimension of the system using the assumption that the number of channels, $N$, is conserved and so consequently $\sum_{i=1}^{m} Y_i = 1$. Therefore the dynamics can be described by the following $m-1$ (rather than $m$) SDEs,

$$d\boldsymbol{Y} = \left(\tilde{H}\boldsymbol{Y} + \gamma\right) dt + \tfrac{1}{\sqrt{N}}\tilde{E}F(\boldsymbol{Y})d\boldsymbol{W}, \tag{4.7}$$

where $\tilde{E}$ is equal to the matrix $E$ with the last row removed and $\gamma$ is a vector of length $m-1$ which is equal to the first $m-1$ rows of the last column of $H$. $\tilde{H}$ is a $(m-1)\times(m-1)$ matrix with entries $\tilde{h}_{i,j} = h_{i,j} - h_{i,m}$, for $i, j = 1, \cdots, m-1$, where $h_{i,j}$ is the $i,j$th entry of the matrix $H$. For example, the matrices for the reduced SDE describing the potassium channel dynamics in the Hodgkin-Huxley model will be

$$\tilde{H}_K = \begin{pmatrix} -4b_n & a_n & 0 & 0 \\ 4b_n & -(a_n+3b_n) & 2a_n & 0 \\ 0 & 3b_n & -2(a_n+b_n) & 3a_n \\ 0 & 0 & 2b_n & -(3a_n+b_n+4a_n) \end{pmatrix},$$

$$\gamma = \begin{pmatrix} 0 \\ 0 \\ 0 \\ 4a_n \end{pmatrix},$$

$$\tilde{E}_K = \begin{pmatrix} 1 & 0 & 0 & 0 \\ -1 & 1 & 0 & 0 \\ 0 & -1 & 1 & 0 \\ 0 & 0 & -1 & 1 \end{pmatrix}.$$

### 4.1.3 Inaccuracies in the Fox and Lu Approach

The Fox and Lu approach became the standard method for modelling ion channel dynamics using SDEs and has been applied to the study of stochastic ion channel dynamics in cardiac cells (Pueyo et al., 2011), neuronal cells, (Fox, 1997; Schmid et al., 2004) and pancreatic beta cells, (De Vries and Sherman, 2000). However, in recent years, the SDE approach to modelling ion channel dynamics has come under criticism, with a number of studies showing discrepancies between the behaviour of the discrete-state Markov chain model and the SDE approach of Fox and Lu (Mino et al., 2002; Bruce, 2009; Goldwyn et al., 2011; Sengupta et al., 2010). Namely,

the SDE approach of Fox and Lu was shown to preserve the mean in the number of open channels of the discrete-state Markov chain model, but not the second moment in the number of open channels. These studies suggested that this discrepancy is due to the approximation of the discrete-state Markov model by a continuous-state process, questioning whether the SDE model could accurately capture the dynamics of the discrete-state Markov chain for ion channel dynamics. However, as we shall demonstrate, this discrepancy arises due to the formulation of the SDEs in terms of the individual gating variables, rather than the state dynamics of the whole channel. This work was published in (Ellen et al., 2011) and was also independently shown in (Goldwyn et al., 2011).

To distinguish between the Fox and Lu approach and the formulation of the SDE model described in the previous section, for the rest of this section we refer to the Fox and Lu approach as the subunit based SDE and the SDE model given by (4.3) as the channel based SDE, in keeping with the terminology introduced by Goldwyn et al. (2011).

The work presented here is an extension of the simulations performed in (Bruce, 2009). Therefore the same protocol is used to compare the subunit based SDE and the channel based SDE models with the discrete-state Markov chain model. The first two moments in the number of open sodium and potassium channels in a variant of the Hodgkin-Huxley model, given in Appendix A, for the subunit based SDE, (4.2), and the channel based SDE, (4.3), are compared with the discrete-state Markov chain model. The voltage is kept constant at an initial value, called the holding potential, for the first $0.1ms$ of simulation. The voltage is then stepped to a value $V_c$ and is kept constant at this value for the remainder of the simulation. Two different voltage step sizes were simulated, $V_c = 24mV$ and $V_c = 16mV$. This protocol is commonly referred to as *voltage clamp* protocol.

The transition rates for each gating variable ($a_X$, $b_X$ for $X = m, h, n$) vary with respect to the transmembrane potential, $V$, according to the functions of membrane potential for the variant of the Hodgkin-Huxley model given in Appendix A. For each voltage step the total number of

sodium channels is set to $1000$ or $2000$ and the total number of potassium channels is $333$ or $666$. These values are chosen to be consistent with the simulations in (Bruce, 2009).

The first two moments in the number of open channels for the discrete-state Markov chain is estimated using $1000$ simulations of the SSA. The first moment in the number of open channels for the subunit based SDE, and the channel based SDE can be obtained directly by taking the expectation in (4.5), (4.6) and (4.2). Noting that the expectation of $dW$ is $0$, we obtain the following ODEs

$$\frac{dE(\boldsymbol{y})}{dt} = H_{Na}E(\boldsymbol{y}(t)), \tag{4.8}$$

$$\frac{dE(\boldsymbol{x})}{dt} = H_{K}E(\boldsymbol{x}(t)), \tag{4.9}$$

$$\frac{dE(X)}{dt} = a_X - (a_X + b_X)E(X(t)). \tag{4.10}$$

The first two equations, (4.8), (4.9) describe the time evolution in the mean proportion of channels in each state for the sodium and potassium channels, respectively, while (4.10) gives the mean proportion of open gates of type $X$. Therefore, for the channel based SDE approach, the first moment in the proportion of open channels is simply $E(y_{31})$ for the sodium channel in the solution to (4.8) and for the potassium channel it is $E(x_4)$ in the solution to (4.9) (using the notation of the previous section). For the subunit based SDE approach, since the channel is assumed to be open when all gates are open, the first moment in the proportion of open channels for the sodium and potassium channels are $(E[m])^3E[h]$ and $(E[n])^4$, respectively, where $E[X]$, $X = m, h, n$, is the solution to (4.10) and where we have assumed independence between the subunits.

ODEs describing the time evolution in the second moment in the proportion of open channels for the sodium and potassium channels described by the channel based SDE can be obtained by applying Itô's Lemma, as described in Chapter 3 Section 3.3.2, to the functions $f(\boldsymbol{y}) = y_{31}^2$ and $f(\boldsymbol{x}) = x_4^2$ in (4.5) and (4.6), respectively, and taking expectations. Therefore the second moment in the proportion of open sodium and potassium channels can be described by the

following ODEs respectively,

$$\frac{dE(y_{31}^2)}{dt} = 2(a_h E(y_{31}y_{30}) + a_m E(y_{31}y_{21}) - E(y_{31}^2)(b_h + 3b_m)) + \frac{1}{N_{Na}}(a_h E(y_{31}) + a_m E(y_{21}) + b_h E(y_{30}) + 3b_m E(y_{31})),$$

$$\frac{dE(x_4^2)}{dt} = 2a_n E(x_4 x_3) + \frac{1}{N_K}(4b_n E(x_4) + a_n E(x_3)) - 8b_n E(x_4^2). \tag{4.11}$$

Note that the above equations involve covariance terms. Therefore in order to solve the above ODEs the covariance between states $y_i$ and $y_j$ ($E(y_i y_j)$) and similarly between $x_l$ and $x_k$ for some $i, j, l$ and $k$ must be known. ODEs describing the covariance between states can be obtained by applying Itô's formula to the function $g(\boldsymbol{y}) = y_i y_j$ and taking expectations, however, we do not explicitly derive these formula for the channel based SDEs of the sodium and potassium channels here.

Similarly, applying Itô's Lemma to the function $g(X) = X^2$, the second moment of the stochastic gating variables given by (4.2), is

$$\frac{dE(X^2)}{dt} = \frac{a_X}{N_x} + E(X)\left(2a_X + \frac{(b_X - a_X)}{N_X}\right) - 2(a_X + b_X)E(X^2), \tag{4.12}$$

where $N_X$ is the number of channels for which $X$ is a gating variable. The second moment in the proportion of open sodium and potassium channels for the Fox and Lu algorithm is thus estimated to be $(E[m^2])^3 E[h^2]$, and $(E[n^2])^4$, respectively.

Above we described how to obtain the first two moments in the *proportion*, rather than the *number* of open channels, for the subunit based SDEs and channel based SDEs. Therefore, we scale the first two moments in the proportion of open channels by the number of sodium ($N_{Na}$) or potassium channels ($N_K$).

**Figure 4.1** Time evolution in the first moment of the number of open potassium channels for the three stochastic simulation methods. The number of channels is $333$ (left) or $666$ (right). The voltage step is $16mV$ (top) or $24mV$ (bottom).

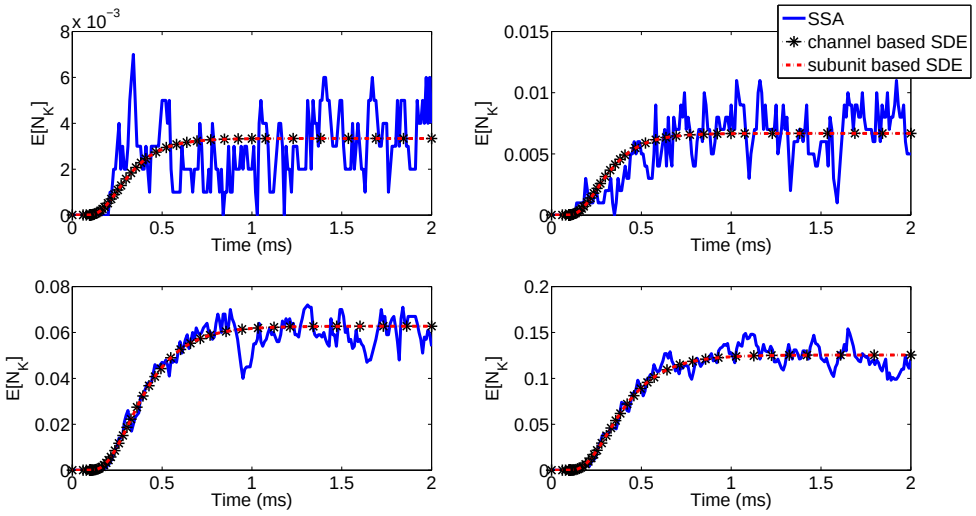


**Figure 4.2** Time evolution in the first moment of the number of open sodium channels for the three stochastic simulation methods. The number of channels set to $1000$ (left) or $2000$ (right). In the bottom two plots the results for the three methods lie virtually on top of one another.

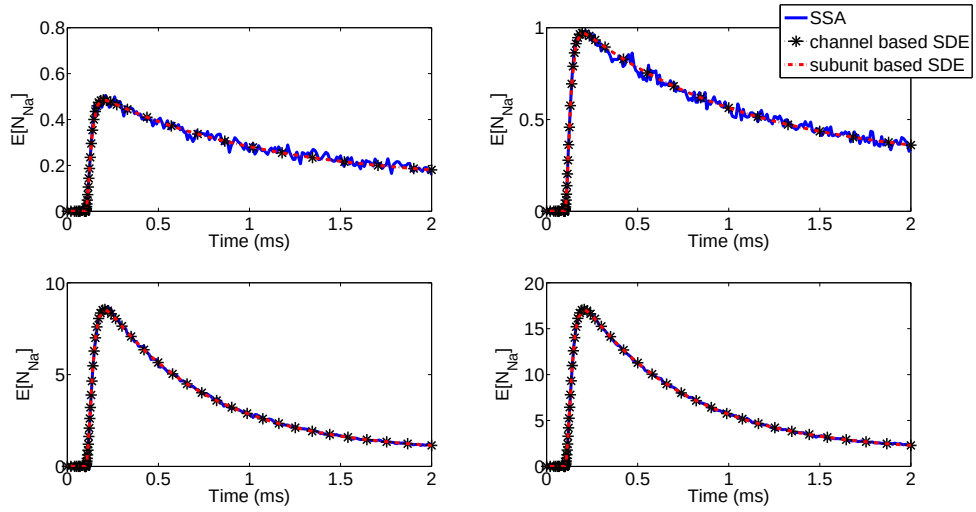

**Figure 4.3** Time evolution in the second moment of the number of potassium open channels for the three stochastic simulation methods. The number of channels is $333$ (left) or $666$ (right). The voltage step is $16mV$ (top) or $24mV$ (bottom).

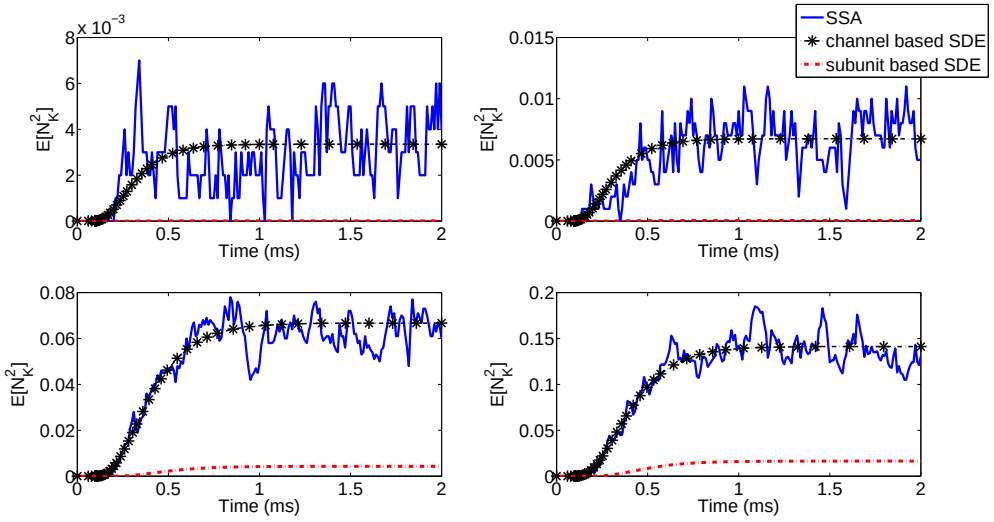


**Figure 4.4** Time evolution in the second moment of the number of sodium open channels for the three stochastic simulation methods. The number of channels set to $1000$ (left) or $2000$ (right).

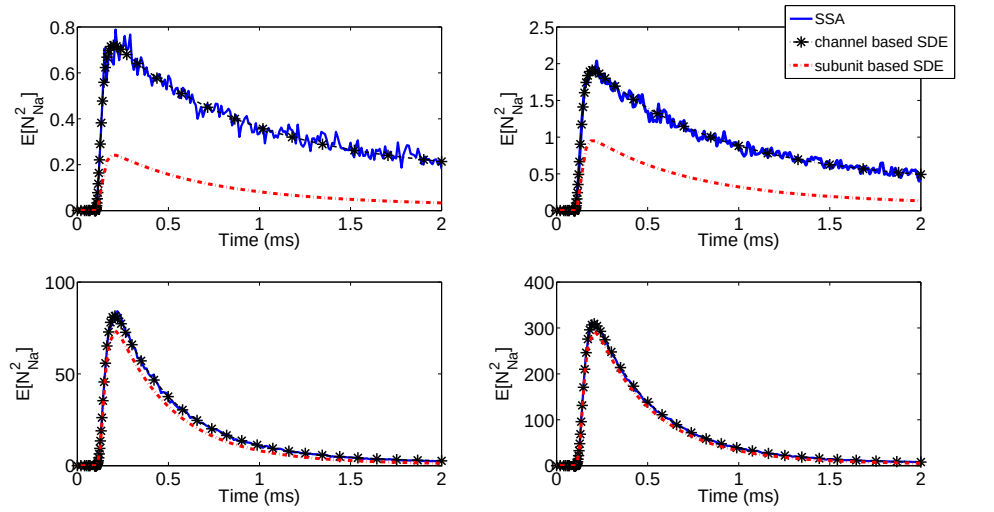


The mean number of open sodium and potassium channels for the subunit based SDE and channel based SDE are both in good agreement with that obtained using multiple simulations of the SSA, as can be seen in Figures 4.1 and 4.2.

From Figures 4.3 and 4.4 it is clear that the second moment in the number of open channels

for the channel based SDE is in good agreement with the discrete-state Markov model, while the subunit based SDE differs significantly from both. In particular we note that this issue with the subunit based SDE does not noticeably improve as the total number of channels increases. Therefore, the SDE model of ion channel dynamics preserves the first two moments of the discrete-state Markov chain model, providing the SDEs are formulated in terms of the kinetic behaviour of the whole channel (channel based SDE) rather than in terms of the individual gating variables (subunit based SDE). For the rest of this thesis the channel based SDE approach will always be adopted, unless explicitly stated, and so from here on we shall refer to this simply as the SDE model.

## 4.2 Negative Channel Numbers in the SDE Model

Complications with the ion channel SDE, (4.3), arise when it comes to simulating the behaviour of such systems using existing SDE numerical techniques, such as the Euler-Maruyama and Milstein methods. Namely, solutions can become negative or greater than $1$, and since the solution describes the proportion of channels in each state, such simulations have no physical meaning. Furthermore, since the entries of the matrix $F(\boldsymbol{Y})$ in the diffusion term involve the square root of some function of the state of the system ($\boldsymbol{Y}$), solutions can indeed become imaginary. This is illustrated in Figure 4.5 for the simple ion channel model (equation (3.23) in Chapter3) which is numerically solved using the Euler-Maruyama method.

Since the issue of biologically unrealistic solutions to the SDE model manifests itself in the numerical simulation, this has led to the assumption within the literature that the issue arises due to the numerical method inadequately preserving the boundaries of the analytic solution to the SDE. Indeed the fact that many numerical methods do not preserve the boundaries inherent in the SDE model is a widely recognised difficulty and has been studied by a number of authors within the stochastic numerical analysis community, as we shall discuss in the next chapter. Therefore, to ensure numerical solutions to the SDE model of ion channel dynamics remain in

a biologically realistic domain, or at least stay real, modifications to the numerical method are frequently employed.

**Figure 4.5** Simulation of the Euler Maruyama discretisation scheme for the simple model, (3.23) in Chapter 3. The real and imaginary parts of the solution are shown on the left and right, respectively. Simulations were performed with initial condition $Y_0 = 0.5$ and parameters $a = 0.001$, $b = 3$, $N = 100$ and using a time step size $\Delta_t = 0.01$.

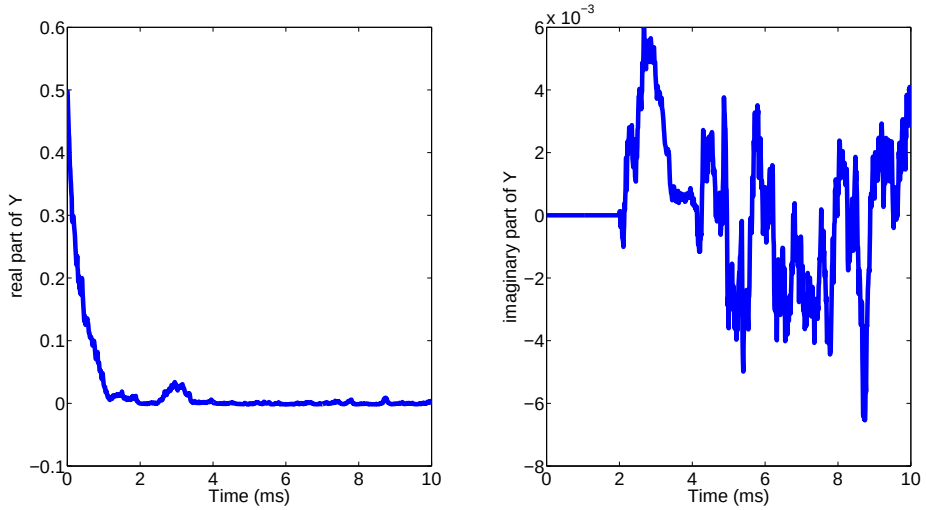


In order to ensure solutions remain real, Goldwyn et al. (2011) replace the values of $\boldsymbol{Y}$ in the noise term in (4.3) by their equilibrium values. Thus this term is independent of the state of the system. However, such an approximation is not valid for all electrophysiology models and so can lead to discrepancies between the behaviour of the discrete-state Markov chain model and the SDE model (Dangerfield et al., 2012), as we shall see in Chapter 7. Another alteration employed to ensure solutions remain real is to take the absolute value under the square root in (4.3), (Orio and Soudry, 2012). While these methods ensure solutions remain real, they can still become negative or greater than $1$.

Other authors make adjustments in the numerical scheme to force the approximation to remain in a biologically realistic region. Firstly, if one of the elements of $\boldsymbol{Y}$ in the approximation becomes negative or greater than one, then the value at that time step is set to zero or one respectively. However, such an alteration could result in the sum over all possible states being

greater or less than one, and so there will not be conservation in the number of channels. Alternatively, if one of the elements of the approximation of $\boldsymbol{Y}$ leaves the interval $[0,\ 1]$ the Wiener increment is resampled until every element of $\boldsymbol{Y}$ at that time point remains within $[0,\ 1]$, as in (Fox and Lu, 1994) and (Pueyo et al., 2011). However, this may lead to the Wiener increment being resampled a large number of times, which is often the case for complex models of ion channel dynamics, and so the SDE simulations can become more computationally intensive than the discrete-state approach. Furthermore, the problem with any such adjustment is that it can introduce bias into the solution, (Lord et al., 2010). To the best of our knowledge, there are no results in the literature confirming that these altered numerical methods converge to the desired SDE solution.

While the issue of biologically unrealistic solutions has been assumed to be related to the numerical method, there has been no formal investigation into whether the analytic solutions to the SDE model for ion channel dynamics do indeed remain within a biologically realistic region. The root of this issue may lie with the form of the SDE model itself, rather than with the numerical methods used to approximate solutions to such systems. In the next section we argue that this is indeed the case by considering the analytic solutions of the SDE that describes the simple two state model of ion channel dynamics.

## 4.3 Analytic Solution to the SDE for the Simple Model

In the previous chapter we showed that the stochastic behaviour of the simplest model of ion channel dynamics (where the channel can be either open or closed) can be approximated by the following SDE, which is in the form of a Langevin equation

$$dY = (a - (a+b)Y)\,dt + \tfrac{1}{\sqrt{N}}\sqrt{a + (b-a)Y}\,dW. \tag{4.13}$$

Here $Y$ is the proportion of open channels, $a$ and $b$ are the transition rates from closed to open and open to closed respectively and $N$ is the total number of channels. Since the number of

channels is assumed to remain constant, it follows that the proportion of open channels, i.e. the solution to (4.13), must lie within the interval $[0, 1]$, otherwise such values of $Y$ have no physical meaning.

Consider the transformation

$$U = a + (b - a)Y. \tag{4.14}$$

By Itô's Lemma, given in Chapter 3 Section 3.3.2, equation (4.13) becomes

$$dU = (\mu + \lambda U)dt + \sigma\sqrt{U}dW, \tag{4.15}$$

where $\mu = 2ab$, $\lambda = -(a + b)$ and $\sigma = \frac{(b-a)}{\sqrt{N}}$. Equation (4.15), more commonly known as the Cox Ingersoll and Ross (CIR) model (Cox et al., 1985), was first proposed in (Feller, 1951), where it was proved that there exists a non-negative solution to (4.15). Consequently $Y(t)$ satisfies the following boundaries: if $a < b$ then $Y(t) \geq \frac{-a}{b-a}$, while if $a > b$ then $Y(t) \leq \frac{-a}{b-a}$. Therefore, $Y(t)$ can leave $[0,\ 1]$ with positive probability, and such solutions have no physical meaning. Furthermore, since the transition rates, $a$ and $b$, depend on the membrane potential, which varies over time in electrophysiology models, there is the added complication that these boundaries on $Y(t)$ will not remain fixed throughout the simulation.

The issue of physically unrealistic solutions to (4.13) has been touched upon by other authors. For example, in the review (Higham, 2011), the author shows that when the solution to (4.13) is close to the boundaries of the interval $[0, 1]$, the noise term in (4.13) can push $Y(t)$ outside this region. However, to the best of our knowledge, there has been no formal demonstration that analytic solutions to (4.13) can leave $[0, 1]$.

Since the above analysis suggests the issue is with the form of the SDE model itself, rather than with the numerical methods, then in the next two chapters we describe two different approaches to constructing an SDE model of ion channel dynamics that ensures analytic and numerical solutions remain within a biologically realistic region.

## 4.4 Chapter Summary

In this chapter we discussed the two challenges that arise in the implementation of the ion channel SDE model. Firstly the SDE model previously employed in the literature, which is an approximation of the ion channel SDE model, does not preserve the moments of the discrete-state Markov chain model. Secondly the ion channel SDE model itself can result in biologically unrealistic simulations of stochastic ion channel dynamics.

We showed that the first issue can be dealt with by formulating the SDE in terms of the full ion channel dynamics, rather than approximating the dynamics in terms of SDEs that describe hypothetical gating variables, as was described by Fox and Lu (1994). This approximation was originally employed to improve the computational speed of numerically solving the ion channel SDE model. However, we demonstrated that a similar improvement in computational efficiency can be obtained by formulating the diffusion term in the SDE model so that it does not involve the square root of a matrix. This can be done due to the special structure of ion channel dynamics. We displayed that this formulation of the SDE model preserves the first two moments of the discrete-state Markov chain model, while the gating variable approximation of Fox and Lu (Fox and Lu, 1994) underestimates the second moment.

In Sections 4.2 and 4.3 we discussed the issue that numerical simulations of the SDE model can leave a biologically realistic region, and we showed that this is not just due to the numerical methods but is a problem with the analytic solution of the ion channel model itself. We therefore argued that the root of the second challenge lies directly with the SDE model of ion channel dynamics. This analysis of the SDE model in Section 4.3 provides the rationale behind the two different approaches taken in the following two chapters.

# 5

# The Wright-Fisher Model and the BISS Method

*In the previous chapter we discussed the challenges that arise when using the SDE model to simulate the stochastic behaviour of ion channel dynamics within electrophsyiology models. In particular, we demonstrated that analytic solutions to the SDE model can go outside a biologically realistic range. We argued that this issue arises from the form of the model itself, rather than from the numerical method used to approximate solutions to the SDE model as is the common assumption in the literature.*

*In this chapter we deal with this issue by describing an alternative SDE model for ion channel dynamics that guarantees analytic solutions are biologically realistic. This model is based on an existing system of SDEs used in population dynamics called the Wright-Fisher model and the parameters are chosen such that the first two moments of the new SDE model are close to those of the discrete-state Markov chain. While analytic solutions to this new system of SDEs remain within the desired region, current numerical methods are unable to preserve such properties of this system of SDEs. Thus in this chapter we also describe a new numerical method that preserves the boundaries of this SDE model and prove this method converges in the strong sense.*

In the first part of this chapter we consider an approximation to the simplest model of ion channel dynamics by an SDE whose solutions are guaranteed to remain in the correct region, namely the interval $[0, 1]$. Recall from Chapter 3 Section 3.4.1 that the simple model assumes the ion channel is either open or closed, and the proportion of open channels can be described by the following SDE,

$$dY = (a - (a + b)Y)\, dt + \tfrac{1}{\sqrt{N}}\sqrt{a + (b - a)Y}\, dW, \tag{5.1}$$

where $a$ and $b$ are the rates at which the channel opens and closes respectively. We now describe the Wright-Fisher model which will be used to approximate the SDE for the simple model of ion channel dynamics.

## 5.1 The Wright-Fisher Model

The Wright-Fisher model describes the stochastic evolution in the genetic structure of a population and was introduced in the 1930s independently in (Fisher, 1930) and (Wright, 1931). The most basic version of the model assumes there are two types of alleles, $r_1$ and $r_2$ for a gene in a population whose total size, $N$, remains constant from one generation to the next. Since the total number of alleles in the population remains constant, i.e. $r_1 + r_2 = N$, it is sufficient to consider the number, $\tilde{X}(\tau)$ of a single allele $r_1$ at generation $\tau$. The gene pool of the $k$th generation is sampled to give the genetic structure of the $(k + 1)$th generation.

This model can be extended to include the possibility of alleles mutating from one generation to the next. Let us assume that a $r_2$ allele mutates to a $r_1$ allele over one generation with probability $\tilde{A}$ and a $r_1$ mutates to a $r_2$ with probability $\tilde{B}$. The transition probabilities that the system moves from state $i$ to state $j$ over one generation, $P_{ij}$, follow a binomial distribution with the probability of success $p_i = \frac{i(1-\tilde{A})+\tilde{B}(N-i)}{N}$ and the number of trials equal to the population size $N$,

$$P_{ij} = \binom{N}{j} p_i^j (1 - p_i)^{N-j}.$$

When the population size is large, the Wright-Fisher model with mutation can be approximated by a continuous state continuous time process, $X(t)$, that represents the proportion of alleles of type $r_1$ in the population at time $t$. Note that $X(t)$ is the process $\tilde{X}$ scaled by the population size and is described by the following SDE, (Karlin and Taylor, 1981)

$$dX = (\tilde{A} - (\tilde{A} + \tilde{B})X)dt + \sqrt{X(1-X)}dW. \tag{5.2}$$

From here on we refer to the Wright-Fisher SDE or model as that which includes mutation between alleles, (5.2). The analytic solution to (5.2) can be shown to remain within $[0, 1]$ for all time, (Karlin and Taylor, 1981).

## 5.2 An Alternative to the SDE Model of Ion Channel Dynamics

Since solutions to the Wright-Fisher model remain within $[0, 1]$, the characteristic we desire from the SDE model, consider approximating (5.1) by the following equation,

$$dX = (A - (A + B)X)dt + C\sqrt{X(1-X)}dW. \tag{5.3}$$

The ion channel SDE model, (5.1), preserves the first two moments of the discrete-state Markov model exactly, due to the linearity of the system. Therefore, in order to ensure that the stochastic behaviour of (5.3) is close to that of the discrete-state Markov chain model, the first two moments of this SDE must be close to that of (5.1). Therefore the constants $A$, $B$ and $C$ are chosen to ensure this is the case, thus (5.3) closely captures the stochastic dynamics of the discrete-state Markov model.

**Theorem 5.2.1.** *Taking $A = a$, $B = b$ and $C^2 = \frac{2(a+b)}{N-1}$ in* (5.3) *ensures that the mean of* (5.3) *is identical to that of* (5.1) *and the difference in the second moment scales as $1/N$.*

*Proof.* Applying Itô's Lemma to $f(x) = x$, in the manner described in Chapter 3 Section 3.3.2, we obtain the following two ODEs describing the time evolution in the mean of the processes

$Y(t)$ and $X(t)$ respectively,

$$\frac{dE(Y)}{dt} = a - (a+b)E(Y), \tag{5.4}$$

$$\frac{dE(X)}{dt} = A - (A+B)E(X). \tag{5.5}$$

Assuming the initial conditions are equal, $E(Y_0) = E(X_0)$, taking $A = a$ and $B = b$ ensures the solutions to (5.1) and (5.3) are identical. Therefore the mean of (5.3) will exactly match that of (5.1).

The ODEs describing the second moment of $Y(t)$ and $X(t)$ can also be derived by application of Itô's Lemma to the function $f(x) = x^2$. Thus,

$$\frac{dE(Y^2)}{dt} = \tfrac{a}{N} + E(Y)\left(2a + \tfrac{b-a}{N}\right) - 2(a+b)E(Y^2), \tag{5.6}$$

$$\frac{dE(X^2)}{dt} = (C^2 + 2A)E(X) - (C^2 + 2(A+B))E(X^2). \tag{5.7}$$

Solving these equations analytically we obtain,

$$\begin{aligned} E(Y^2(t)) = {} & \frac{a(a+b/N)}{(a+b)^2} \\ & + e^{-2(a+b)t}\left(E(Y_0^2) - \frac{a(a+b/N)}{(a+b)^2} - \frac{(2a+(b-a)/N)}{a+b}(E(Y_0) - \tfrac{a}{a+b})\right) \\ & + e^{-(a+b)t}\left(\frac{(2a+(b-a)/N)}{a+b}(E(Y_0) - \tfrac{a}{a+b})\right), \end{aligned} \tag{5.8}$$

$$\begin{aligned} E(X^2(t)) = {} & \frac{(C^2+2A)A}{(C^2+2(A+B))(A+B)} \\ & + e^{-(C^2+2(A+B))t}\left(E(X_0^2) - \frac{(C^2+2A)A}{(C^2+2(A+B))(A+B)} - \frac{C^2+2A}{C^2+A+B}\left(E(X_0) - \tfrac{A}{A+B}\right)\right) \\ & + e^{-(A+B)t}\left(\frac{C^2+2A}{C^2+A+B}\left(E(X_0) - \tfrac{A}{A+B}\right)\right). \end{aligned} \tag{5.9}$$

As before we assume that $E(Y_0) = E(X_0)$ and $E(Y_0^2) = E(X_0^2)$.

For (5.8) and (5.9) to be close, $C$ must be chosen so that the constant term in these two equations are the same. Therefore we take $C^2$ such that $C^2 = \frac{2}{N-1}(a+b)$. The choice of $A$ and $B$ ensures that the last terms in (5.9) and (5.8) decay at the same rate, although it means that the middle terms do not, and the difference between the two rates of decay is $C^2$. By this selection of $C^2$, the difference in the rates of decay will be of the order $\frac{1}{N}$ for $N >> 1$. □

For this choice of constants the difference between the second moment of (5.1) and (5.3) is shown in Figure 5.1. It can clearly be seen that this difference is small and scales with $1/N$, and so we conclude that such a choice of constants in (5.3) preserves the mean in (5.1) and provides a good approximation to the second moment of this equation.

**Figure 5.1** The difference in the second moment of the SDE model of ion channel dynamics, (5.1), and the Wright-Fisher type model, (5.3). The parameter values used for all simulations are $a = 0.001$, $b = 5$, the initial condition was $E(Y_0^2) = E(X_0^2) = 0.5$ and the number of channels are $N = 100$ (top left), $N = 1000$ (top right) and $N = 10000$ (bottom left). The bottom right plot shows the maximum difference in the second moment for each value of $N$.

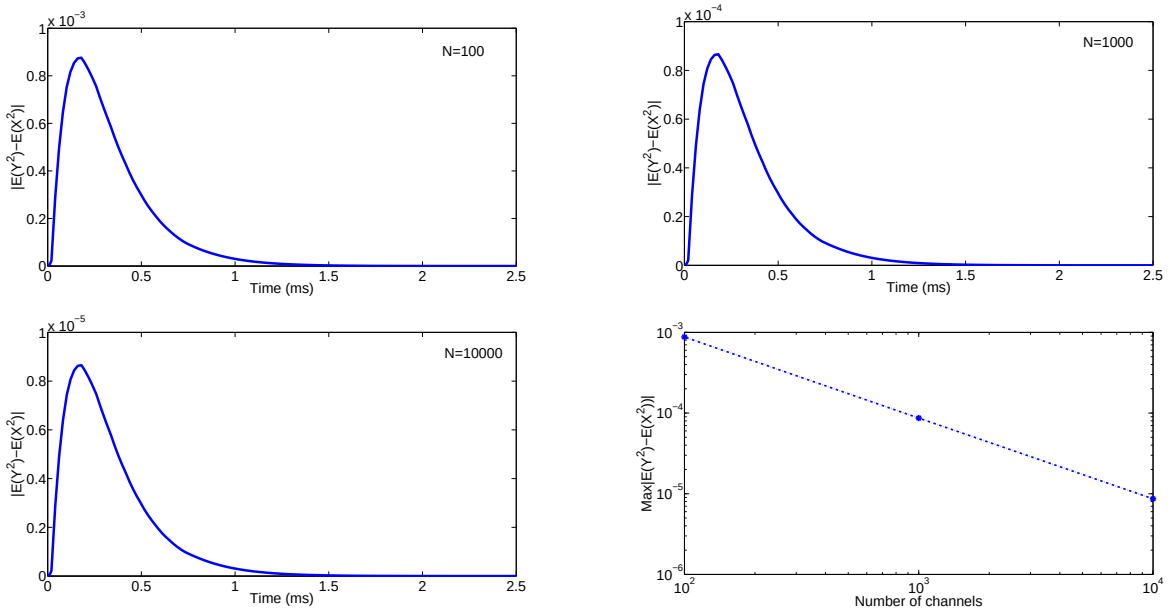


The Wright-Fisher SDE therefore provides an alternative model for ion channel dynamics with intrinsic noise, as it closely approximates the first two moments of the discrete-state Markov

chain model whilst also ensuring that solutions remain in a biologically realistic region.

### 5.2.1 Boundary Preserving Numerical Schemes

Whilst analytic solutions to the alternative model of ion channel dynamics, (5.3), guarantees solutions remain within $[0, 1]$, many commonly used numerical methods, such as the Euler-Maryuama and Milstein methods do not preserve such boundaries in the numerical solution. This is an issue not just with the Wright-Fisher model, but is also the case for other models of real world systems, such as financial models including the Cox Ingersoll and Ross (CIR) model, (Schurz, 1996).

In recent years a number of numerical schemes that aim to preserve the boundaries of solutions to SDEs have been developed. Most techniques have focused on algorithms that ensure positive numerical solutions to mean-reverting square root processes in financial models. The Balanced Implicit Method (BIM) incorporates implicitness into the Euler-Maruyama scheme, (Milstein et al., 1998), and was shown in (Schurz, 1996) to preserve the boundaries of a mean reverting process with cubic diffusion and a model of diffusion of innovation in marketing sciences. In (Kahl and Schurz, 2005) the Balanced Milstein Method (BMM), an extension to the BIM, was developed and shown to preserve positivity for a class of SDEs whose diffusion coefficients satisfied a number of conditions. In recent years a number of splitting-step methods have been constructed to preserve the positivity of solutions to models in finance. A scheme that splits one dimensional SDEs into an SDE whose analytic solution is known and an ODE was developed in (Moro and Schurz, 2007) and shown to preserve positivity for the Cox Ingersoll Ross (CIR) model and constant elasticity volatility models. However this algorithm is difficult to implement for multidimensional systems since few analytical solutions of higher dimensional SDEs are known. Other splitting methods have utilised techniques to solve ODEs such as the Strang splitting method, (Ninomiya and Victoir, 2008; Halley et al., 2008), and Jacobi splitting, (Halley et al., 2009), in order to preserve the positivity of solutions to mean reverting square

root processes under certain parameter regimes. The main issue with current boundary preserving algorithms is that many methods are model dependent (Moro and Schurz, 2007), or only work under certain parameter regimes (Halley et al., 2008, 2009; Ninomiya and Victoir, 2008; Kahl and Jäckel, 2006) and so they do not necessarily generalise to the Wright-Fisher model. Therefore in Section 5.4.3 we introduce a novel numerical method, called the BISS method, that ensures numerical solutions to the Wright-Fisher model remain within $[0, 1]$, and the strong convergence of such a scheme is proved in Section 5.4.5. We begin by formalising what it means for a numerical method to ensure solutions to an SDE remain within a certain bounded domain, with respect to the Wright-Fisher model, (5.3).

## 5.3 The Lifetime of a Numerical Method

The concept of a boundary preserving numerical scheme was formalised by Schurz in (Schurz, 1996). He introduced the notion of an algorithm having *eternal lifetime* that is defined as follows.

**Definition 5.3.1.** *(Schurz, 1996) Let $X_n$ be computed from a stochastic numerical scheme that approximates the solution to the Wright-Fisher model,* (5.3)*, where $X_n$ is the approximation at time $t_n$. The numerical scheme $X_n$ is said to possess eternal lifetime if*

$$P\left(X_n \in [0,\, 1] | X_0 \in [0,\, 1]\right) = 1, \quad \textit{for all } n > 0. \tag{5.10}$$

If (5.10) does not hold then the numerical scheme is said to have *finite lifetime* and so the approximation can leave the interval $[0,\, 1]$ with positive probability. A weaker notion of a boundary preserving numerical scheme is that of *$\epsilon$-lifetime*.

**Definition 5.3.2.** *(Schurz, 1996) Let $X_n$ be computed from a stochastic numerical scheme that approximates the solution to the Wright-Fisher model,* (5.3)*, where $X_n$ is the approximation at time $t_n$. The numerical scheme $X_n$ is said to possess $\epsilon$-lifetime if*

$$P\left(X_n \in [0,\, 1] | X_{n-1} \in [\epsilon,\, 1-\epsilon]\right) = 1, \quad \textit{for some } \epsilon > 0. \tag{5.11}$$

This property provides a one step assurance that the approximation to (5.3) will lie within the correct region if the previous value did. However, since $X_n$ can lie in the region $[0, \epsilon) \cup (1-\epsilon, 1]$ with positive probability, at time $t_{n+1}$ the numerical solution is not guaranteed to remain within $[0, 1]$ and so this property does not ensure the discretisation scheme is boundary preserving for all time.

## 5.4 A Boundary Preserving Numerical Scheme for the Wright-Fisher Model

The Balanced Implicit Split Step (BISS) method is a combination of the Balanced Implicit Method (BIM), first introduced in (Milstein et al., 1998), and the split step method developed in (Moro and Schurz, 2007), both of which have been shown to possess certain boundary preserving properties. The BIM can be constructed in such a way so as to possess $\epsilon$-lifetime for the Wright-Fisher model when $A = B = 0$, as we shall describe below, but eternal lifetime cannot be obtained, (Schurz, 1996). On the other hand, the split-step method from (Moro and Schurz, 2007) possesses eternal lifetime for the Wright-Fisher model, but this is only for a restricted set of parameters and also does not generalise to higher dimensions. Since we require a numerical method for the Wright-Fisher model that possesses eternal lifetime for all parameter regimes and generalises to higher dimensional systems, we combine elements of the BIM with those of the split-step method in order to develop such a scheme.

In what follows we shall consider the numerical approximation to the Wright-Fisher model, (5.3), on a fixed time interval $[0, T]$ with discretisation $t_0 = 0, \cdots, t_M = T$ where $t_{n+1} - t_n = \Delta_{t_n}$ for $0 \leq n \leq M-1$. For simplicity we assume a fixed time step $\Delta_{t_n} = \Delta_t$ throughout. We begin with a brief description of the two methods on which the BISS scheme is based and discuss the boundary preserving properties of these respective schemes.

### 5.4.1 BIM Method

The Balanced Implicit Method (BIM) was introduced in (Milstein et al., 1998) as a method for solving stiff stochastic systems. Unlike drift implicit methods, the scheme introduced implicitness into the diffusion term as well as the drift term through a system of freely chosen control functions, $d^j(X)$. In (Alcock and Burrage, 2006) the optimal choice for the control functions, with respect to the local truncation error in strong convergence, are given and shown to improve the accuracy of the scheme.

The BIM for the Wright-Fisher model, (5.3), can be described by the one-step discretisation scheme

$$X^B_{n+1} = X^B_n + \big(A - (A+B)X^B_n\big)\,\Delta_t + C\sqrt{X^B_n(1-X^B_n)}\Delta W_n + D(X^B_n)(X^B_n - X^B_{n+1}), \quad (5.12)$$

where $\Delta_t$ is the length of the time discretisation interval and $\Delta W_n$ is a Wiener increment. In the update formula above, $D(X^B_n)$ is the system of control functions and takes the form,

$$D(X^B_n) = d^0(X^B_n)\Delta_t + d^1(X^B_n)|\Delta W_n|. \quad (5.13)$$

Although the BIM scheme was originally introduced as a method for solving stiff stochastic systems, in (Schurz, 1996) Schurz showed that by careful choice of the control functions, the BIM scheme possesses $\epsilon$-lifetime for the Wright-Fisher model with no drift, i.e. the case $A = B = 0$. The control functions that ensure such a property are

$$d^1(X) = \begin{cases} C\sqrt{\frac{1-\epsilon}{\epsilon}} \text{ if } X < \epsilon \\ C\sqrt{\frac{1-X}{X}} \text{ if } \epsilon \le X < 1/2 \\ C\sqrt{\frac{X}{1-X}} \text{ if } 1/2 \le X \le 1-\epsilon \\ C\sqrt{\frac{1-\epsilon}{\epsilon}} \text{ if } X > 1-\epsilon, \end{cases} \quad (5.14)$$

for some $0 < \epsilon < 1$. This function is plotted in the left hand side of Figure 5.2 for $C = 1$ and $\epsilon = 0.01$. Since there is no drift term, $d^0(X) = 0$. This choice for the control function satisfies the following property.

**Lemma 5.4.1.** *Assuming* $X \in [0,1]$, *then by the choice of control function,* (5.14), *we have*

$$d^1(X)\sqrt{X(1-X)} \leq C.$$

*Proof.* The proof follows directly from the choice of the control function, providing $0 < \epsilon < 1$ (see Figure 5.2, right hand side). □

This scheme possesses $\epsilon$-lifetime (Schurz, 1996) as will be shown in Section 5.4.4.

**Figure 5.2** Left hand side: The function $d^1(X)$, (5.14), for $C = 1$, $\epsilon = 0.01$. Right hand side: The function $d^1(X)\sqrt{X(1-X)}$ for $C = 1$, $\epsilon = 0.01$.

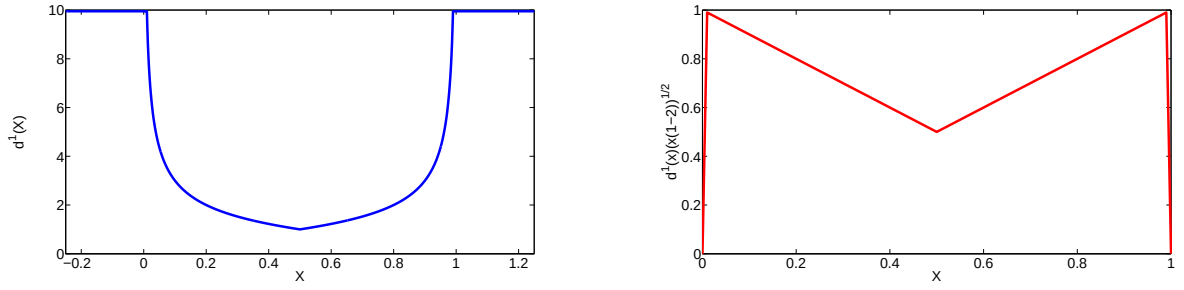


## 5.4.2 Moro and Schurz Method

In (Moro and Schurz, 2007), Moro and Schurz developed a split step scheme that exploits the structure of an SDE so as to guarantee the numerical solution remains within the natural boundaries of the system. The scheme decomposes the SDE into two equations, an SDE and an ODE. The split is taken in such a way so that the exact solution or the conditional probability to the first equation (the SDE) is known. The exact solution to the first equation is then used as the initial condition for the ODE in that time step, which is integrated using any converging deterministic algorithm.

We propose that by splitting the Wright-Fisher model into the SDE and ODE given below, the Moro and Schurz method can be used to obtain numerical solutions that remain within $[0,1]$ for

a wide range of parameter regimes. Equation (5.3) is split into an SDE and an ODE as follows

$$dX_1 = \frac{C^2(1-2X_1)}{4}dt + C\sqrt{X_1(1-X_1)}dW, \tag{5.15}$$

$$dX_2 = \left(A - \frac{C^2}{4} - \left(A + B - \frac{C^2}{2}\right)X_2\right)dt. \tag{5.16}$$

Let $X_n$, $X_{n,1}$ and $X_{n,2}$ denote the approximation to (5.3), (5.15) and (5.16) at the $n$th time step, respectively. According to the Moro and Schurz splitting scheme we take $X_n = X_{n,1}$ at the $(n+1)$th time step (i.e. the value of $X$ at the previous time step is taken as the initial condition in (5.15)). Under the splitting scheme given above, equation (5.15) is equivalent to the Stratonovich SDE $dX_1 = C\sqrt{X_1(1-X_1)} \circ dW$ and the analytic solution to this equation is known (Kloeden and Platen, 2011). Therefore

$$X_{n,1} = \left(sin\left(\frac{C}{2}\Delta W + sin^{-1}\sqrt{X_n}\right)\right)^2, \tag{5.17}$$

where $\Delta_t$ is the step size and $\Delta W$ is the Wiener increment, which is sampled from a normal distribution with variance equal to the step size $\Delta_t$. This solution clearly remains between $0$ and $1$. Using (5.17) as the initial condition in equation (5.16), $X_{n,2} = X_{n+1,1}$, the analytical solution to (5.16) is,

$$\begin{aligned} X_{n,2} =& \frac{A - C^2/4}{C^2/2 - A - B}\left(e^{-(A+B-C^2/2)\Delta_t} - 1\right) \\ &+ e^{-(A+B-C^2/2)\Delta_t}\left(sin\left(\frac{C}{2}\Delta W + sin^{-1}\sqrt{X_n}\right)\right)^2. \end{aligned} \tag{5.18}$$

Finally, since we take $X_{n+1} = X_{n+1,2}$, the formula above gives the approximation of $X$ at the $(n+1)'th$ time step for this numerical scheme. The update formula given by (5.18) remains within the interval $[0,\ 1]$ providing $\frac{a}{a+b} \in \left[\frac{1}{2(N-1)},\ 1 - \frac{1}{2(N-1)}\right]$ and so preserves the boundaries of $0$ and $1$ for a wide range of parameter values. However, converting the SDE into the Stratonovich form introduces an extra term into the ODE part of the split, altering the dynamics of the ODE system and so preventing the scheme from preserving the boundaries for all parameter regimes. This limits the ability for incorporation into an electrophysiological model

where the membrane potential varies over time and hence the parameters, which depend on the membrane potential, can take a wide range of values. Furthermore, few analytic solutions to SDEs in more than one variable (i.e. multidimensional SDEs) are known and so this method does not generalise to more complex models of ion channel dynamics.

In the scheme we present below, the Wright-Fisher SDE is split in a slightly different way to that given by (5.15) and (5.16), so that the first equation contains only the diffusion term and the second equation only the drift term. The BIM is then used to solve the SDE. The idea is to select the control functions so the BIM possesses $\epsilon$-lifetime. $\epsilon$ is then taken as a function of the time step in such a way so as to ensure the approximation to the ODE remains within $[0, 1]$. Thus the scheme can be shown to possess eternal lifetime.

### 5.4.3 BISS Method

The BISS method decomposes equation (5.3) into two equations, as in the Moro and Schurz method. The first is an SDE that consists of the diffusion term of (5.3) only. The second is an ODE that consists of the drift part and so equation (5.3) is separated into the following two equations

$$dX_1 = C\sqrt{X_1(1 - X_1)}dW \tag{5.19}$$

$$dX_2 = (A - (A + B)X_2)\, dt. \tag{5.20}$$

As in the Moro and Schurz method, the numerical solution to (5.19) at the $n$th time step is used as the initial condition in (5.20) (i.e. $X_{n-1,2} = X_{n,1}$) with the solution to this second equation providing the approximation to the true solution at each time step ($X_n = X_{n,2}$). The main difference between the BISS method and the split step method of Moro and Schurz is the way in which the first equation is solved. The BISS method approximates the solution to (5.19) at each time step using the BIM, where the control functions are taken to be (5.14), so that the scheme possesses $\epsilon$-lifetime. The second equation can then be solved using any converging

deterministic algorithm of at least order 1, and so the simplest to use is the Euler method. Therefore the BISS method for (5.3) can be described by the following one step discretisation formula,

$$X_{n+1} = X_n + (A - (A+B)X_n)\Delta_t + \frac{C\sqrt{X_n(1-X_n)}\Delta W_n}{1 + d^1(X_n)|\Delta W_n|}(1 - (A+B)\Delta_t), \qquad (5.21)$$

where $d^1(X_n)$ is given by (5.14). We note that in most electrophysiology models, (Hodgkin and Huxley, 1952; Noble, 1962), the transition rates in the ion channel model, $a$ and $b$ are always strictly postive and since we take $A = a$ and $B = b$ it follows that $A, B > 0$. Also we shall always assume that $N > 1$. Therefore $C > 0$, and so by definition $d^1(X_n) \geq 0$, providing $X_n \in [0, 1]$. In the next section we shall prove that $X_n \in [0, 1]$ for all $n$, and so the denominator of the last term in (5.21) is always greater than or equal to one. Thus the numerical scheme for the BISS method, given by (5.21), will not become unstable, even for very small values of Wiener increments $\Delta W_n$.

While in the standard sense of $\epsilon$-lifetime the $\epsilon$ is constant, as discussed in (Schurz, 1996), in the BISS method the $\epsilon$ is determined in terms of the discretisation time step $\Delta_t$. In particular the $\epsilon$ is chosen to ensure that for a particular time step, $\Delta_t$, the numerical approximation to (5.20) is driven to a distance of $\epsilon$ away from the boundary, i.e. the numerical solution lies in the region $[\epsilon, 1-\epsilon]$. This is always possible since $A$ and $B$ are strictly positive, so the drift of (5.3) pushes the solution away from the boundary. We take $\epsilon$ as

$$\epsilon = min(A\Delta_t, B\Delta_t, 1 - A\Delta_t, 1 - B\Delta_t) > 0 \qquad (5.22)$$

when $\Delta_t$ is sufficiently small. Such a choice will be shown to ensure that the discretisation scheme given by (5.21) possesses $\epsilon$-lifetime.

### 5.4.4 Properties of the BISS Method

We begin by proving a Lemma and a Theorem, which together show that the BISS method possesses eternal lifetime as defined in Section 5.3. The Lemma is stated in (Schurz, 1996),

although no formal proof is given. From these two results it follows immediately that the first two moments of the discretisation scheme (5.21) are bounded, which we state as a Corollary.

**Lemma 5.4.2.** *(Schurz, 1996) The BIM scheme for the Wright-Fisher model with no drift, where the control functions are taken to be* (5.14)*, possesses $\epsilon$-lifetime.*

*Proof.* First let us assume that at time $t_n$, $X_{n,1} \in [\epsilon, 1/2)$. The value at the next time step, according to the BIM scheme, is given by

$$X_{n+1,1} = \frac{X_{n,1} + C\sqrt{X_{n,1}(1-X_{n,1})}\,(\Delta W_n + |\Delta W_n|)}{1 + C\sqrt{(1-X_{n,1})/X_{n,1}}|\Delta W_n|}. \tag{5.23}$$

If $\Delta W_n \leq 0$ then

$$X_{n+1,1} = X_{n,1}\left(\frac{1}{1 + C\sqrt{(1-X_{n,1})/X_{n,1}}|\Delta W_n|}\right),$$

which is clearly non-negative. Since $1 + C\sqrt{(1-X_{n,1})/X_{n,1}}|\Delta W_n| \geq 1$ (as $C > 0$) then because we take $X_{n,1} \in [\epsilon, 1/2)$ it follows that $X_{n+1,1}$ lies in the interval $[0, 1/2)$. Otherwise if $\Delta W_n > 0$ (5.23) becomes

$$X_{n+1,1} = \frac{X_{n,1} + 2C\sqrt{X_{n,1}(1-X_{n,1})}|\Delta W_n|}{1 + C\sqrt{(1-X_{n,1})/X_{n,1}}|\Delta W_n|},$$

which again is clearly non-negative. In order for $X_{n+1,1} \leq 1$ then the following inequality must hold

$$\left(\frac{1}{X_{n,1}} - 1\right) + \left(\frac{1}{X_{n,1}} - 2\right) C\sqrt{\frac{X_{n,1}}{(1-X_{n,1})}}|\Delta W_n| \geq 0.$$

Since $X_{n,1} < 1/2$ and $C > 0$ it follows that the inequality above is satisfied. Hence, given $X_{n,1}$ in $[\epsilon, 1/2)$ then $X_{n+1,1} \in [0, 1]$.

Now let us assume that $X_{n,1} \in [1/2, 1-\epsilon]$, then the value at the next time step is given by

$$X_{n+1,1} = \frac{X_{n,1} + C\sqrt{X_{n,1}/(1-X_{n,1})}\,((1-X_{n,1})\Delta W_n + X_{n,1}|\Delta W_n|)}{1 + C\sqrt{X_{n,1}/(1-X_{n,1})}|\Delta W_n|}. \tag{5.24}$$

If $\Delta W_n \geq 0$, (5.24) becomes,

$$X_{n+1,1} = \frac{X_{n,1} + C\sqrt{X_{n,1}/(1-X_{n,1})}|\Delta W_n|}{1 + C\sqrt{X_{n,1}/(1-X_{n,1})}|\Delta W_n|}. \tag{5.25}$$

This is clearly non-negative and it also follows that $X_{n+1,1} < 1$ since $X_{n,1} < 1$. Otherwise if $\Delta W_n < 0$ then (5.24) can be written as

$$X_{n+1,1} = \frac{X_{n,1} + C\sqrt{X_{n,1}/(1-X_{n,1})}(2X_{n,1}-1)|\Delta W_n|}{1 + C\sqrt{X_{n,1}/(1-X_{n,1})}|\Delta W_n|}. \tag{5.26}$$

It follows directly that this is non-negative and for $X_{n+1,1} \leq 1$ the inequality

$$\left(\frac{1}{X_{n,1}} - 1\right) + 2\left(\frac{1}{X_{n,1}} - 1\right) C\sqrt{\frac{X_{n,1}}{1-X_{n,1}}}|\Delta W_n| \geq 0,$$

must hold. It is clear that this is true since $X_{n,1} < 1$ and $C > 0$. Therefore if $X_{n,1} \in [1/2, 1-\epsilon]$ then $X_{n+1,1} \in [0,1]$.

Thus if $X_{n,1} \in [\epsilon, 1-\epsilon]$, then $X_{n+1,1} \in [0,1]$ with probability $1$ and so the BIM scheme for the Wright-Fisher model with no drift possesses $\epsilon$-lifetime. □

**Theorem 5.4.1.** *The BISS scheme for the Wright-Fisher model possesses eternal lifetime.*

*Proof.* In order to prove the BISS scheme possesses eternal lifetime we must show that $X_{n,2} = X_n \in [0,1]$ for all $n > 0$. By the previous Lemma we have that the solution to the first part of the split in the BISS method remains in $[0,1]$ over a single time step, providing the initial condition is a distance $\epsilon$ away from the boundary. Therefore we must show that given the initial condition to the second equation in the split lies in $[0,1]$, then the choice of $\epsilon$, given by (5.22), guarantees the solution to this equation at each time step lies in the interval $[\epsilon, 1-\epsilon]$.

Let us assume that the initial condition to (5.3), $X_0$, lies in the interval $[\epsilon, 1-\epsilon]$, where $\epsilon$ is given by (5.22). Since $X_0 = X_{0,1}$ then by the previous Lemma it follows that $X_{1,1} \in [0,1]$, due to the $\epsilon$-lifetime property of the BIM scheme for (5.19). Taking $X_{1,1}$ as the initial condition for the second equation in the split, (5.20), and using the Euler method to solve this equation, $X_{1,2}$ is given by

$$X_{1,2} = X_{1,1} + (A - (A+B)X_{1,1})\,\Delta_t. \tag{5.27}$$

The minimum and maximum values attained by $X_{1,1}$ are $0$ and $1$, respectively, and so rearranging (5.27) it follows that for $X_{1,2} \in [\epsilon, 1-\epsilon]$ we must take $\epsilon \leq min(A\Delta_t, 1 - A\Delta_t, B\Delta_t, 1 -$

$B\Delta_t)$. By the definition of $\epsilon$, (5.22), this inequality clearly holds. Therefore it follows that $X_{1,2} \in [\epsilon, 1-\epsilon]$. Since $X_1 = X_{1,2}$, we have that $X_1 \in [\epsilon, 1-\epsilon] \subset [0,1]$.

Now let us assume that $X_n \in [\epsilon, 1-\epsilon]$. Again it follows from the previous Lemma that $X_{n+1,1} \in [0,1]$ and so it remains to show that $X_{n+1,2} \in [\epsilon, 1-\epsilon]$ given that the initial condition to (5.20) is taken to be $X_{n+1,1}$. This follows immediately from the definition of $\epsilon$, (5.22), and by rearrangement of the one step discretisation formula for $X_{n+1,1}$ taken at the maximum and minimum values of $X_{n+1,1}$, namely $1$ and $0$, respectively. Since $X_{n+1} = X_{n+1,2}$ we have that $X_{n+1} \in [\epsilon, 1-\epsilon]$.

Thus by induction it follows that given $X_0 \in [\epsilon, 1-\epsilon]$ we have with probability $1$ $X_n \in [\epsilon, 1-\epsilon] \subset [0,1]$ for all $n > 0$ and so the BISS method possesses eternal lifetime.

□

Note that in the above theorem we prove a slightly stronger condition than the definition of eternal lifetime given by Definition 5.3.1, namely that the BISS method ensures numerical solutions remain a distance $\epsilon$ away from the boundaries for all time and so lie within a subset of $[0,1]$.

**Corollary 5.4.1.** *The first two moments of the method* (5.21) *are bounded. That is there exist positive constants* $0 < G_2 \leq G_1 \leq 1$ *such that*

$$E(X_n) \leq G_1, \tag{5.28}$$

$$E(X_n^2) \leq G_2. \tag{5.29}$$

*Proof.* The proof follows directly from the fact that (5.21) possesses eternal lifetime by the above Theorem, and so $X_n \in [0,\ 1]$ for all $n > 0$. □

### 5.4.5 Strong Convergence of the BISS Method

The BIM method converges with strong order $1/2$ providing the drift and diffusion coefficients are Lipschitz continuous, (Milstein et al., 1998). The Moro and Schurz method converges with strong order $1$ for weaker conditions on the drift and diffusion functions, namely that the drift coefficient is $3$ times differentiable, the diffusion coefficient $4$ times differentiable and the solution to the equation satisfies a certain moment bound. Extending these two results it is relatively straight forward to show that the BISS method converges with strong order $1/2$, under the assumption of Lipschitz continuous drift and diffusion coefficients. However, the diffusion coefficient in the Wright-Fisher model does not satisfy a Lipschitz condition on $[0,\ 1]$ and indeed it is not even differentiable at the end points of this interval. Therefore this proof of strong convergence breaks down.

In recent years a number of authors have tried to tackle the issue of convergence of certain numerical schemes when the diffusion coefficient fails to satisfy the Lipschitz condition (Berkaoui et al., 2008; Higham et al., 2003; Higham and Mao, 2005), but this is still a little explored area. In (Higham and Mao, 2005) the authors use the Yamanda method (Karatzas and Shreve, 1991) to prove strong convergence of the Euler method for the CIR model, whose diffusion coefficient is only Hölder continuous, a weaker condition than Lipschitz continuity. Since the diffusion coefficient for the Wright-Fisher model satisfies the Hölder condition we shall use a similar approach to that presented in (Higham and Mao, 2005) to prove strong convergence of the BISS method.

For ease of notation we let $f(X) = A - (A + B)X$ and $g(X) = \sqrt{X(1 - X)}$. In the convergence analysis we work with the integral form of (5.3),

$$X_T(t) = X_{T,0} + \int_0^t f(X_T(r))dr + \int_0^t Cg(X_T(r))dW(r), \tag{5.30}$$

where $X_T(t)$ denotes the **true** solution to (5.3). We also use the continuous approximation to

(5.21), $X(t)$, defined for $t \in [t_n, t_{n+1})$

$$X(t) := X_n + f(X_n)(t - t_n) + \frac{Cg(X_n)(W(t) - W(t_n))}{1 + d^1(X_n)|\Delta W_n|}(1 - (A + B)\Delta_t), \tag{5.31}$$

where $\Delta W_n = W(t_{n+1}) - W(t_n)$, $\Delta_t = \Delta_{t_n} = t_{n+1} - t_n$ and $W(t)$ is a continuous Wiener process taking values $W(t_n), W(t_{n+1}), \ldots$ at the grid points. Defining $\overline{X}(t)$ and $\overline{W}(t)$ to be the following step functions

$$\overline{X}(t) := X_k \quad \text{for } t \in [t_k, t_{k+1}),$$

$$\overline{W}(t) := W(t_{k+1}) - W(t_k) \quad \text{for } t \in [t_k, t_{k+1}),$$

(5.31) can be re-written in the integral form

$$X(t) = X_0 + \int_0^t f\left(\overline{X}(r)\right) dr + \int_0^t \frac{Cg\left(\overline{X}(r)\right)(1 - (A + B)\Delta_t)}{1 + d^1(\overline{X}(r))|\overline{W}(r)|} dW(r). \tag{5.32}$$

Note that $X(t)$ is equal to $\overline{X}(t)$ at the discretisation points, $t = t_n$.

**Lemma 5.4.3.** *For all $\Delta_t$ sufficiently small (in particular $\Delta t \leq 1/(A + B)$),*

$$sup_{t\in[0,T]} E\left((X(t) - \overline{X}(t))^2\right) \leq H\Delta_t, \tag{5.33}$$

$H = \frac{A^2}{A+B} + (2 + 4C^2K^2)G_1 + (A + B + 4C^2K^2)G_2$*, for some positive constant $K > 0$ independent of $\Delta_t$.*

*Proof.* Letting $t \in [t_k, t_{k+1})$ and using the results of Corollary 5.4.1 along with the fact that

$$1/\left(1 + d^1(\overline{X}(r))|\overline{W}(r)|\right)^2 \leq 1, \tag{5.34}$$

we have

$$\begin{aligned}
&E\left((X(t) - \overline{X}(t))^2\right) \\
&= E\left[\left(f(X_k)(t - t_k) + \frac{Cg(X_k)(1 - (A + B)\Delta_t)(W(t) - W(t_k))}{1 + d^1(X_k)|\Delta W_k|}\right)^2\right] \\
&\leq 2\left(E\left[(f(X_k))^2(t - t_k)^2 + \frac{C^2(g(X_k))^2(1 - (A + B)\Delta_t)^2(W(t) - W(t_k))^2}{(1 + d^1(X_k)|\Delta W_k|)^2}\right]\right) \\
&\leq 2\left(E\left[(f(X_k))^2\right]\Delta_t^2 + E\left[\frac{C^2(g(X_k))^2(1 - (A + B)\Delta_t)^2}{(1 + d^1(X_k)|\Delta W_k|)^2}\right] E(W(t) - W(t_k))^2\right) \\
&\leq 2\left(E\left[(f(X_k))^2\right]\Delta_t^2 + E\left[\frac{C^2(g(X_k))^2(1 - (A + B)\Delta_t)^2}{(1 + d^1(X_k)|\Delta W_k|)^2}\right]\Delta_t\right)
\end{aligned}$$

Since $X_k \in [0,1]$ we have that $\frac{1}{1+d^1(X_k)|\Delta W_k|} \leq K$ for some constant $K > 0$. Recalling that $f(X) = A - (A+B)X$ and $g(X) = \sqrt{X(1-X)}$ it follows that

$$\begin{aligned}
&E\left((X(t) - \overline{X}(t))^2\right) \leq E\left[\left(A^2 - 2(A+B)X_k + (A+B)^2X_k^2\right)\right]\Delta_t^2 \\
&+ C^2K^2E\left[X_k(1-X_k)\left(1 + (A+B)^2\Delta t^2 - 2(A+B)\Delta t\right)\right]\Delta_t \\
&\leq \Delta t^2\left(A^2 + 2(A+B)E(X_k) + (A+B)^2E(X_k^2)\right) + C^2K^2\Delta t(E(X_k) - E(X_k^2)) \\
&+ (A+B)^2C^2K^2\Delta t^3(E(X_k) - E(X_k^2)) + 2(A+B)C^2K^2\Delta t^2(E(X_k) - E(X_k^2)).
\end{aligned}$$

For small enough $\Delta_t$ ($\Delta_t \leq 1/(A+B)$),

$$E\left((X(t) - \overline{X}(t))^2\right) \leq \Delta t\left(\tfrac{A^2}{A+B} + (2 + 4C^2K^2)E(X_k) + (A + B + 4C^2K^2)E(X_k^2)\right).$$

Finally using the boundedness property of the moments of $X_k$, as stated in Corollary 5.4.1, it follows that for $t \in [t_k, t_{k+1})$

$$E\left((X(t) - \overline{X}(t))^2\right) \leq H\Delta t,$$

where $H = \frac{A^2}{A+B} + (2 + 4C^2K^2)G_1 + (A + B + 4C^2K^2)G_2$, and so is independent of $\Delta_t$. Finally taking the supremum over $0 \leq t \leq T$ we obtain the result of the Lemma. □

Following (Higham and Mao, 2005) we construct a sequence of $C^2$ smooth functions, $\phi_k(v)$, that approximate the function $|v|$. This approximation is then used to obtain an upper bound on the expectation of the absolute value between the true ($X_T(t)$) and the approximate solutions ($X(t)$), namely $E|X_T(t) - X(t)|$.

Letting $a_0 = 1$ and $a_k = e^{-k(k+1)/2}$, $k \geq 1$, then there exists a continuous function $\psi_k(v)$ with support in $(a_k, a_{k-1})$ such that

$$0 \leq \psi_k(v) \leq \tfrac{2}{kv}, \quad a_k < v < a_{k-1} \text{ and } \int_{a_k}^{a_{k-1}} \psi_k(u)du = 1.$$

We extend the function $\phi_k(v)$ on $(-\infty, \infty)$ symmetrically, so $\phi_k(-v) = \phi_k(|v|)$, as in Higham and Mao (2005). Therefore the function

$$\phi_k(v) = \int_0^{|v|} dx \int_0^x \psi_k(u)du,$$

is twice continuously differentiable with the first two differentials satisfying the properties

$$|\phi_k'(v)| \leq 1, \quad \forall v \in \mathbb{R}, \quad |\phi_k''(v)| \begin{cases} \leq \frac{2}{k|v|} & a_k < |v| < a_{k-1} \\ = 0 & \text{otherwise.} \end{cases} . \tag{5.35}$$

Furthermore, $\phi_k$ satisfies the inequality

$$|v| - a_{k-1} \leq \phi_k(v) \leq |v|, \quad \forall v \in \mathbb{R}. \tag{5.36}$$

**Lemma 5.4.4.** *Let $X_T(t)$ denote the true solution of* (5.3)*, then for all $\Delta_t$ sufficiently small and for $k = 1, 2, \ldots$,*

$$\begin{aligned} sup_{0\leq t\leq T} E|X_T(t) - X(t)| \leq e^{\lambda T} \left[ a_{k-1} + \frac{C^2 T}{k} \right] + \\ e^{\lambda T} C^2 T \Delta_t^{1/2} \left[ \sqrt{H} \left( \frac{1}{k a_k} + \frac{\lambda}{C^2} \right) + \frac{2L\Delta_t^{1/2}}{k a_k} \right], \end{aligned} \tag{5.37}$$

*where $\lambda = A + B$ and $L > 0$ is a constant independent of $\Delta_t$.*

*Proof.* Letting $\lambda = A+B$, $\sigma(\overline{X}(r)) = 1-(1-\lambda\Delta_t)/\left(1 + d^1(\overline{X}(r))|\overline{W}(r)|\right)$, and using (5.30) and (5.32) we have that

$$\begin{aligned} X_T(t) - X(t) = -\lambda \int_0^t (X_T(r) - \overline{X}(r))dr + \\ C \int_0^t \left[ g(X_T(r)) - g(\overline{X}(r)) + \sigma(\overline{X}(r))g(\overline{X}(r)) \right] dW(r). \end{aligned}$$

Applying Itô's formula to the function $\phi_k(\cdot)$ and using the boundedness property of this function given by (5.35) we get

$$\begin{aligned} E\left(\phi_k(X_T(t) - X(t))\right) &= -\lambda E\left( \int_0^t \phi_k'(X_T(r) - X(r))(X_T(r) - \overline{X}(r))dr \right) \\ &+ \tfrac{C^2}{2} E\left( \int_0^t \phi_k''(X_T(r) - X(r)) \left[ g(X_T(r)) - g(\overline{X}(r)) + \sigma(\overline{X}(r))g(\overline{X}(r)) \right]^2 dr \right) \\ &\leq \lambda \int_0^t E\left( |X_T(r) - \overline{X}(r)| \right) dr + \tfrac{C^2}{2} \mathrm{I}(t), \end{aligned}$$

where,

$$\begin{aligned} \mathrm{I}(t) :&= E\left( \int_0^t \phi_k''(X_T(r) - X(r)) \left( g(X_T(r)) - g(\overline{X}(r)) + \sigma(\overline{X}(r))g(\overline{X}(r)) \right)^2 dr \right) \\ &\leq 2E\left( \int_0^t \phi_k''(X_T(r) - X(r)) \left( [g(X_T(r)) - g(\overline{X}(r))]^2 + [\sigma(\overline{X}(r))g(\overline{X}(r))]^2 \right) dr \right). \end{aligned}$$

Let us first consider the last term in the inequality above. Recalling $g(X) = \sqrt{X(1-X)}$ and $\sigma(\overline{X}(r)) = 1 - (1-\lambda\Delta_t)/\left(1 + d^1(\overline{X}(r))|\overline{W}(r)|\right)$ it follows that

$$\begin{aligned}
&[\sigma(\overline{X}(r))g(\overline{X}(r))]^2 = \frac{\overline{X}(r)(1-\overline{X}(r))}{\left(1 + d^1(\overline{X}(r))|\overline{W}(r)|\right)^2}\times \\
&\left((1 + d^1(\overline{X}(r))|\overline{W}(r)|)^2 - 2(1 + d^1(\overline{X}(r))|\overline{W}(r)|)(1-\lambda\Delta_t) + (1-\lambda\Delta_t)^2\right) \\
&= \frac{\overline{X}(1-\overline{X})}{\left(1 + d^1(\overline{X}(r))|\overline{W}(r)|\right)^2}\left(d^1(\overline{X}(r))^2|\overline{W}(r)|^2 + 2\lambda d^1(\overline{X}(r))|\overline{W}(r)|\Delta_t + \lambda^2\Delta_t^2\right).
\end{aligned}$$

Using Lemma 5.4.1 and the fact that

$$max(g(\overline{X})) = 1/2,$$

since $\overline{X} \in [0,1]$ and

$$1/\left(1 + d^1(\overline{X}(r))|\overline{W}(r)|\right) \leq 1,$$

we have

$$\left(\sigma(\overline{X}(r))g(\overline{X}(r))\right)^2 \leq C^2|\overline{W}(r)|^2 + C\lambda\Delta_t|\overline{W}(r)| + \frac{\lambda^2\Delta_t^2}{4}.$$

Therefore using the boundedness of $\phi_k(\cdot)$ given by (5.35)

$$\begin{aligned}
&E\left(\int_0^t \phi_k''(X_T(r) - X(r))\left(\sigma(\overline{X}(r))g(\overline{X}(r))\right)^2 dr\right) \\
&\leq \int_0^t \frac{2}{ka_k}E\left(C^2|\overline{W}(r)|^2 + C\lambda\Delta_t|\overline{W}(r)| + \frac{\lambda^2\Delta_t^2}{4}\right)dr \\
&\leq \left(C^2 + C\lambda\Delta_t^{1/2} + \frac{\lambda^2\Delta_t}{4}\right)\frac{2t\Delta_t}{ka_k} \\
&\leq p(\Delta_t^{1/2})\frac{2t\Delta_t}{ka_k},
\end{aligned}$$

where $p(\Delta_t^{1/2})$ is a polynomial in $\Delta_t^{1/2}$ with positive coefficients and the above inequality is true for all $k \geq 1$. In the penultimate inequality above we use the fact that $E\left(|\Delta\bar{W}(r)|\right) = E\left(|W(t_{k+1}) - W(t_k)|\right) = \Delta_t^{1/2}$ for $r \in [t_k, t_{k+1})$ for some $k$. Therefore for all $\Delta_t$ small enough,

$$p(\Delta_t^{1/2}) < L,$$

for some constant $L > 0$ independent of $\Delta_t$. If follows that

$$E\int_0^t \phi_k''(X_T(r) - X(r))\left(\sigma(\overline{X}(r))g(\overline{X}(r))\right)^2 dr < \frac{2Lt\Delta_t}{ka_k}.$$

The function $g(X) = \sqrt{X(1-X)}$ is Hölder continuous with exponent $1/2$ and Hölder constant, $1/\sqrt{2}$. Using this fact along with (5.35) and Lemma 5.4.3

$$\begin{aligned}
&E\left(\int_0^t \phi_k''(X_T(r) - X(r))\left(g(X_T(r)) - g(\overline{X}(r))\right)^2 dr\right) \\
&\leq \tfrac{1}{2}E\left(\int_0^t \phi_k''(X_T(r) - X(r))|X_T(r) - X(r)|dr\right) \\
&+ \tfrac{1}{2}E\left(\int_0^t \phi_k''(X_T(r) - X(r))|X(r) - \overline{X}(r)|dr\right) \\
&\leq \tfrac{1}{2}E\left(\int_0^t \tfrac{2}{k}\mathbf{1}_{\{a_k < |X_T(r) - X(r)| < a_{k-1}\}}\right) dr + \tfrac{1}{2}E\left(\int_0^t \frac{2}{ka_k}|X(r) - \overline{X}(r)|\right) dr \\
&\leq \frac{t}{k} + \frac{t}{ka_k}H^{1/2}\Delta_t^{1/2}.
\end{aligned}$$

Therefore, for all $\Delta_t$ small enough the integral $\mathrm{I}(t)$ is bounded by,

$$\mathrm{I}(t) \leq 2\left(\frac{t}{k} + \frac{t}{ka_k}H^{1/2}\Delta_t^{1/2} + \frac{2Lt\Delta_t}{ka_k}\right) =: J(t).$$

Again using Lemma 5.4.3 we obtain,

$$\begin{aligned}
E\left(\phi_k(X_T(t) - X(t))\right) &\leq \lambda\int_0^t E\left(|X_T(r) - X(r)|dr\right) + \lambda\int_0^t E\left(|X(r) - \overline{X}(r)|\right) dr + \tfrac{C^2}{2}J(t) \\
&\leq \lambda\int_0^t E\left(|X_T(r) - X(r)|\right) dr + \lambda t H^{1/2}\Delta_t^{1/2} + \tfrac{C^2}{2}J(t).
\end{aligned}$$

From the inequality that the function $\phi(\cdot)$ satisfies, given by (5.36), it follows that

$$E\left(\phi_k\left(X_T(t) - X(t)\right)\right) \geq E\left(|X_T(t) - X(t)|\right) - a_{k-1}.$$

Therefore,

$$\begin{aligned}
E|X_T(t) - X(t)| \leq a_{k-1} + \frac{C^2t}{k} + H^{1/2}\Delta_t^{1/2}\left(\frac{C^2t}{ka_k} + \lambda t\right) + \\
\frac{2C^2Lt\Delta_t}{ka_k} + \lambda\int_0^t E|X_T(r) - X(r)|dr.
\end{aligned}$$

Applying the Grönwall inequality (see for example Mao (2011)),

$$\begin{aligned}
E\left(|X_T(t) - X(t)|\right) \leq e^{\lambda t}\left[a_{k-1} + \frac{C^2t}{k}\right] + \\
e^{\lambda t}C^2t\Delta_t^{1/2}\left[H^{1/2}\left(\frac{1}{ka_k} + \frac{\lambda}{C^2}\right) + \frac{2L\Delta_t^{1/2}}{ka_k}\right].
\end{aligned} \tag{5.38}$$

Finally, taking the supremum over $0 \leq t \leq T$ gives (5.37). □

**Theorem 5.4.2.**

$$lim_{\Delta_t \to 0} sup_{0 \leq t \leq T} E|X_T(t) - X(t)| = 0.$$

*Proof.* For any $\delta > 0$, there exists a $K \geq 1$ such that for all $k > K$,

$$e^{\lambda T}\left[a_{k-1} + \frac{C^2 T}{k}\right] < \tfrac{1}{2}\delta. \tag{5.39}$$

Then we may take $\Delta_t > 0$ small enough so that

$$e^{\lambda T} C^2 \Delta_t^{1/2} T\left[H^{1/2}\left(\frac{1}{ka_k} + \frac{\lambda}{C^2}\right) + \frac{2L\Delta_t^{1/2}}{ka_k}\right] < \tfrac{1}{2}\delta.$$

Therefore $sup_{0 \leq t \leq T} E|X_T(t) - X(t)| < \delta$ and so $lim_{\Delta_t \to 0} sup_{0 \leq t \leq T} E|X_T(t) - X(t)| = 0$ as required.

□

In Section 5.7 we provide empirical results that suggest the BISS method converges with strong order $1/2$. We note that the final theorem of this section only proves strong convergence, and no rate of convergence was obtained. This was due to the techniques employed in this proof to deal with the fact that the diffusion coefficient does not satisfy the Lipschitz condition, and so standard results do not apply.

## 5.5 The Multidimensional Wright-Fisher Model

So far we have only considered approximation of the simple model by the one-dimensional Wright-Fisher model, and a numerical scheme to solve the resulting SDE that preserves the boundaries of solutions to this system. However, as mentioned in Chapter 3, ion channel dynamics are much more complex than this simple two-state model. In this section we therefore consider the extension of the Wright-Fisher model to higher dimensions. We also discuss how this model can be used to approximate the SDE model that describes the dynamics of a collection of $N$ ion channels, each of which can reside in one of $m$ different states and undergo $k$

different reversible transitions, given by the following,

$$d\boldsymbol{Y} = H\boldsymbol{Y}dt + \tfrac{1}{\sqrt{N}}EF(\boldsymbol{Y})d\boldsymbol{W}, \tag{5.40}$$

see Chapter 4, Section 4.1.2 for the form of the matrices $H$, $E$ and $F(\boldsymbol{Y})$.

The multidimensional Wright-Fisher model considers the dynamics of $m$ different gene or allele types in a fixed population of size $N$ that can undergo $k$ reversible mutations and is described by the following system of $m$ SDEs,

$$d\boldsymbol{X} = A\boldsymbol{X}dt + Ediag\left(c_1\sqrt{f_1(\boldsymbol{X})}dW_1, c_2\sqrt{f_2(\boldsymbol{X})}dW_2, \ldots, c_k\sqrt{f_k(\boldsymbol{X})}dW_k\right), \tag{5.41}$$

where $f_i(\boldsymbol{X})$ are of the form $X_lX_j$ for some $l$, $j$, $A$ is a matrix of constants, $E$ is a matrix with entries $1$, $-1$ and $0$ and $c_1 \ldots c_k$ are some constants, (Griffiths, 1979, 1980). For the Wright-Fisher model that approximates the general SDE model of ion channel dynamics, given by (5.40), the matrix $E$ is the same as in equation (5.40) and the indices of the vector $\boldsymbol{X}$ in the function $f_i(\boldsymbol{X})$ are the same as those of the vector $\boldsymbol{Y}$ in the entry $F_{i,i}(\boldsymbol{Y})$ of the matrix $F$.

This system can be reduced to $m-1$ SDEs, as for (5.40) discussed in Chapter 4 Section 4.1.2,

$$d\boldsymbol{X} = (\tilde{A}\boldsymbol{X}+\beta)dt+\tilde{E}diag\left(c_1\sqrt{f_1(\boldsymbol{X})}dW_1, c_2\sqrt{f_2(\boldsymbol{X})}dW_2, \ldots, c_k\sqrt{f_k(\boldsymbol{X})}dW_k\right), \tag{5.42}$$

where $\tilde{E}$ is equal to the matrix $E$ with the last row removed, $\tilde{A}$ is a $(m-1)\times(m-1)$ matrix with entries $\tilde{A}_{i,j} = A_{i,j} - A_{i,m}$ for $i, j = 1, \cdots, m-1$, and $\beta$ is a vector of length $m-1$ which is equal to the first $m-1$ rows of the last column of $A$. Unlike for the scalar model, we do not provide an explicit Theorem and proof for the choice of constants made that ensure the first two moments of the (5.40) and (5.41), are close. Instead we provide an Ansatz on a choice that ensures the mean of (5.40) and (5.41) are identical and the difference in the second moments is on the order of $1/N$. We note that this choice is not unique and other choices may provide a better approximation to the second moments of (5.40), but this could be at the expense of the estimate of the mean.

As before, we use Itô's Lemma to obtain the means and second moments of each component in (5.40) and (5.41) as described in Chapter 3 Section 3.3.2. Let $E(\boldsymbol{Y})$ and $E(\boldsymbol{X})$ denote the vector of means for (5.40) and (5.41) respectively. Due to the linearity of (5.40) and (5.41), the ODEs that describe the mean are simply,

$$\frac{dE(\boldsymbol{Y})}{dt} = HE(\boldsymbol{Y}), \tag{5.43}$$

$$\frac{dE(\boldsymbol{X})}{dt} = AE(\boldsymbol{X}). \tag{5.44}$$

As for the simple model it is clear that by choosing $A$ such that $A_{ij} = H_{ij}$ for $i, j = 1, \ldots, m$ ensures that the means of these two equations are identical.

The second moment of the $i$ component of (5.40) is given by the following equation

$$\frac{dE(Y_i^2)}{dt} = 2H_{ii}E(Y_i^2) + \sum_{j\neq i, j=1}^{m} 2H_{ij}E(Y_iY_j) + \tfrac{1}{N}\left(\sum_{j\neq i, j=1}^{m} 2H_{ij}E(Y_j) - H_{ii}E(Y_i)\right), \tag{5.45}$$

where $E(Y_iY_j)$ denotes the second moment between the $i$ and $j$ components. Due to the symmetry of the system, we have that $E(Y_iY_j) = E(Y_jY_i)$ and by application of Itô's Lemma to the function $f(\boldsymbol{Y}) = Y_iY_j$ the equation for the second moment between the $i$ and $j$ components of (5.40) is,

$$\begin{aligned}\frac{dE(Y_iY_j)}{dt} &= H_{ji}E(Y_i^2) + H_{ij}E(Y_j^2) + (H_{ii} + H_{jj})\,E(Y_iY_j) \\ &\quad + \sum_{l\neq i,\, j,\, l=1}^{m} (H_{il}E(Y_iY_l) + H_{jl}E(Y_jY_l)) - \tfrac{1}{N}\left(H_{ij}E(Y_i) + H_{ji}E(Y_j)\right).\end{aligned} \tag{5.46}$$

Let $D$ be an $m \times m$ constant matrix. If gene of type $i$ can mutate to gene of type $j$ via mutation $l$, for some $l = 1, \ldots, k$ then the $(i, j)$th entry of $D$ will be $D_{ij} = c_l$. Otherwise if gene $i$ cannot mutate into gene $j$ then $D_{ij} = 0$. The second moment of the $i$ component and the second moment between the $i$ and $j$ components of the multidimensional Wright-Fisher model, (5.41), are then given by the following equations, respectively,

$$\frac{dE(X_i^2)}{dt} = 2A_{ii}E(X_i^2) + \sum_{j=1, j\neq i}^{m} 2A_{ij}E(X_iX_j) + \sum_{j=1, j\neq i}^{m} D_{ij}^2E(X_iX_j), \tag{5.47}$$

$$\frac{dE(X_iX_j)}{dt} = A_{ji}E(X_i^2) + A_{ij}E(X_j^2) + (A_{ii} + A_{jj})\,E(X_iX_j) + \sum_{l=1,l\neq i,\,j}^{m} (A_{il}E(X_iX_l) + A_{jl}E(X_jX_l)) - D_{ij}^2E(X_iX_j). \tag{5.48}$$

Assuming the initial conditions for the two systems are the same, then by the choice of the matrix $A$, the only difference between (5.45) and (5.47), and between (5.46) and (5.48), is the last term. Since we want the choice of constants in the multidimensional system to be equivalent to that in the simple system then for $D_{ij} \neq 0$ we take

$$D_{ij} = \sqrt{\frac{2(H_{ij} + H_{ji})}{N-1}}. \tag{5.49}$$

Therefore, since $D_{ij} = c_l$ where $l$ is the mutation by which $i$ mutates into $j$, we can write the constants $c_l$ in (5.41) in terms of the transition rate constants of (5.40),

$$c_l = \sqrt{\frac{2(r_{ij} + r_{ji})}{N-1}}, \tag{5.50}$$

where $r_{ij}$ and $r_{ji}$ are equal to the rate constants from $F_{l,l}(\boldsymbol{Y})$ in (5.40). This choice ensures that the last two terms in the second moment equations for each component are close.

As an example we consider the Wright-Fisher model that approximates the three state ion channel model given in Chapter 3 Section 3.4.2. Letting $X_1$ denote the proportion of channels in state $O$ and $X_2$ the proportion in state $C$, the three state ion channel model can be approximated by the following reduced form of the Wright-Fisher type model,

$$d\boldsymbol{X} = \left( \begin{pmatrix} -(r_{12}+r_{13}+r_{31}) & r_{21}-r_{31} \\ r_{12}-r_{32} & -(r_{21}+r_{23}-r_{32}) \end{pmatrix} \boldsymbol{X} + \begin{pmatrix} r_{31} \\ r_{32} \end{pmatrix} \right) dt + \begin{pmatrix} 1 & 1 & 0 \\ -1 & 0 & 1 \end{pmatrix} \begin{pmatrix} \sqrt{\frac{2(r_{21}+r_{12})}{N-1}}\sqrt{X_2X_1}\,dW_1 \\ \sqrt{\frac{2(r_{31}+r_{13})}{N-1}}\sqrt{X_1(1-X_1-X_2)}\,dW_2 \\ \sqrt{\frac{2(r_{32}+r_{23})}{N-1}}\sqrt{X_2(1-X_1-X_2)}\,dW_3 \end{pmatrix}. \tag{5.51}$$

The difference between the second moments of the original SDE model, given by (3.26) in Chapter 3, and (5.42) are shown in Figure 5.3.

**Figure 5.3** The difference in the second moments of the ion channel SDE, (3.26) and the Wright-Fisher model for a 3 state model, (5.51). The parameter values used for all simulations are $a = [0.001, 2.1, 1.6]$, $b = [2.4, 3, 3.6]$ and the number of channels are $N = 100$ (top left), $N = 1000$ (top right) and $N = 10000$ (bottom). (Legends are the same on each subplot.)

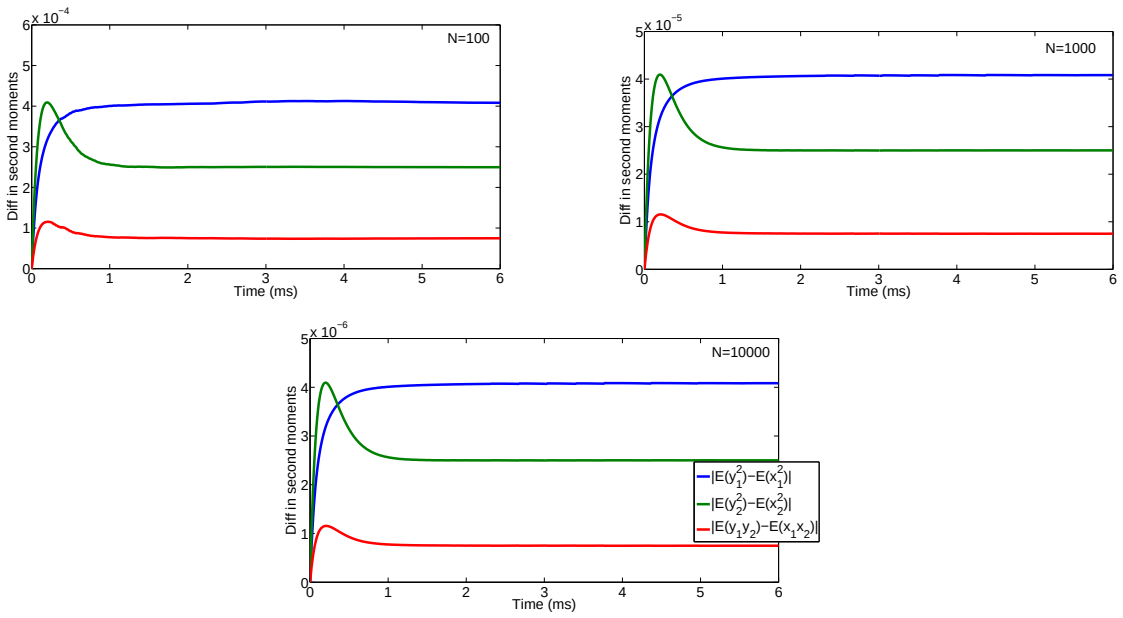


From Figure 5.3 it is clear that the second moments are close and that the differences scale with $1/N$, as for the simple model.

## 5.6 The BISS Method for the Multidimensional Wright-Fisher Model

We consider the application of the BISS method to the reduced form of the general multidimensional Wright-Fisher system, (5.42), given in the previous section, where the tilde is dropped from the matrices $A$ and $E$ in this section for simplicity. Under the BISS scheme, (5.42) is split into the following two equations.

$$d\overline{\boldsymbol{X}} = Ediag\left(c_1\sqrt{f_1(\overline{\boldsymbol{X}})}dW^1, c_2\sqrt{f_2(\overline{\boldsymbol{X}})}dW^2, \cdots, c_k\sqrt{f_k(\overline{\boldsymbol{X}})}dW^k\right), \tag{5.52}$$

$$d\hat{\boldsymbol{X}} = (A\hat{\boldsymbol{X}} + \beta)dt. \tag{5.53}$$

For ease of notation, we drop the bar from the vector $\boldsymbol{X}$ in (5.52). Letting $\boldsymbol{X}^n$ denote the numerical approximation to the first equation, (5.52), at the $n$th time step, the discretisation scheme for the BIM is as follows

$$\begin{aligned}(I + D(\boldsymbol{X}^n))\,\boldsymbol{X}^{n+1} = Ediag\left(c_1\sqrt{f_1(\boldsymbol{X}^n)}\Delta W_n^1, \ldots, c_k\sqrt{f_k(\boldsymbol{X}^n)}\Delta W_n^k\right)\\ + D(\boldsymbol{X}^n)\boldsymbol{X}^n,\end{aligned} \tag{5.54}$$

where $I$ is the $(m-1)\times(m-1)$ identity matrix and $D(\boldsymbol{X}^n)$ is a $(m-1)\times(m-1)$ matrix function. The choice of control function, $D(\boldsymbol{X}^n)$, can be written in terms of scalar functions $d^l(\boldsymbol{X}^n):\mathbb{R}^n\to\mathbb{R}$ as follows,

$$D(\boldsymbol{X}^n) = \sum_{l=1}^{k} d^l(\boldsymbol{X}^n)|\Delta W_n^l| I. \tag{5.55}$$

Providing each component of $\boldsymbol{X}^n$ is a distance $\epsilon$ away from the boundary, we define the scalar functions $d^l(\boldsymbol{X}^n)$ as follows, depending on the form of $f_l(\boldsymbol{X}^n)$. If $f_l(\boldsymbol{X}^n)$ is of the form $f_l(\boldsymbol{X}^n) = X_{i_l}^n X_{j_l}^n$ then for $X_{i_l}^n$, $X_{j_l}^n$ a distance $\epsilon$ or more away from the boundary the function $d^l(\boldsymbol{X}^n)$ takes the following form,

$$d^l(\boldsymbol{X}^n) = \begin{cases} c_l\left[\sqrt{\frac{X_{j_l}^n}{X_{i_l}^n}} + \sqrt{\frac{\epsilon}{X_{i_l}^n X_{j_l}^n}}\right] & if\ X_{i_l}^n < X_{j_l}^n,\\ c_l\left[\sqrt{\frac{X_{i_l}^n}{X_{j_l}^n}} + \sqrt{\frac{\epsilon}{X_{i_l}^n X_{j_l}^n}}\right] & if\ X_{j_l}^n \le X_{i_l}^n. \end{cases} \tag{5.56}$$

Otherwise if $f^l(\boldsymbol{X}^n) = X_{i_l}^n(1-\sum_{p=1}^{m-1} X_p)$, then $d^l(\boldsymbol{X}^n)$ is defined to be

$$d^l(\boldsymbol{X}^n) = \begin{cases} c_l\left[\sqrt{\frac{1-\sum_{p=1}^{m-1} X_p^n}{X_{i_l^n}}} + \sqrt{\frac{\epsilon}{X_{i_l}^n(1-\sum_{l=1}^{m-1} X_p^n)}}\right] & if\ \ \sum_{p=1,p\neq i_l}^{m-1} X_p^n + 2X_{i_l}^n < 1,\\ c_l\left[\sqrt{\frac{X_{i_l}^n}{1-\sum_{p=1}^{m-1} X_p^n}} + \sqrt{\frac{\epsilon}{X_{i_l}^n(1-\sum_{p=1}^{m-1} X_p^n)}}\right] & if\ \ \sum_{p=1,p\neq i_l}^{m-1} X_p^n + 2X_{i_l}^n \ge 1. \end{cases} \tag{5.57}$$

If $X_i^n \le \epsilon$ set $X_i^n$ equal to $\epsilon$ in the formulas above, for each $i$. Similarly if $\sum_{p=1}^{m-1} X_p^n \ge 1-\epsilon$ set this sum equal to $1-\epsilon$ in the formulas above. As for the simple model $c_i > 0$ for $i = 1, \ldots, k$. This choice of control functions ensures that the matrix $(I + D(\boldsymbol{X}^n))$ is always invertible, since this term simplifies to

$$\left(1 + \sum_{l=1}^{k} d^l(\boldsymbol{X}^n)|\Delta W_n^l|\right) I,$$

where $\sum_{l=1}^{k} d^l(\boldsymbol{X}^n) \geq 0$ by the definition of the functions $d^l(\boldsymbol{X}^n)$ for $l = 1, \ldots, k$.

Analogously to the simple model, the ODE part of of the split, (5.53), is approximated using any converging deterministic algorithm of at least order $1$ and the parameter $\epsilon$ is calculated as a function of the time step to ensure that the numerical solution to the ODE always lies a distance $\epsilon$ from the boundary.

As an example of the multidimensional BISS method, we apply it to the three state model of ion channel dynamics (see Chapter 3), that can be approximated by the multidimensional Wright-Fisher model given by (5.51) in the previous section. The one step discretisation scheme for the BIM method used to solve the first equation in the split employed in the BISS method, (5.54) is as follows,

$$X_1^{n+1} = \frac{X_1^n - C_1\sqrt{X_1^n X_2^n}\Delta W_n^1 + C_2\sqrt{(1-X_1^n-X_2^n)X_1^n}\Delta W_n^2 + X_1^n(d_1(\boldsymbol{X}^n)+d_2(\boldsymbol{X}^n)+d_3(\boldsymbol{X}^n))}{1+d_1(\boldsymbol{X}^n)+d_2(\boldsymbol{X}^n)+d_3(\boldsymbol{X}^n)},$$

$$X_2^{n+1} = \frac{X_2^n + C_1\sqrt{X_1^n X_2^n}\Delta W_n^1 - C_3\sqrt{(1-X_1^n-X_2^n)X_2^n}\Delta W_n^3 + X_2^n(d_1(\boldsymbol{X}^n)+d_2(\boldsymbol{X}^n)+d_3(\boldsymbol{X}^n))}{1+d_1(\boldsymbol{X}^n)+d_2(\boldsymbol{X}^n)+d_3(\boldsymbol{X}^n)},$$

where the control functions are

$$d_1(\boldsymbol{X}) = \begin{cases} C_1\left(\sqrt{\frac{X_2}{X_1}} + \sqrt{\frac{\epsilon}{X_1X_2}}\right)|\Delta W_n^1|, & \text{if } \epsilon < X_1 \leq X_2, \\ C_1\left(\sqrt{\frac{X_1}{X_2}} + \sqrt{\frac{\epsilon}{X_1X_2}}\right)|\Delta W_n^1|, & \text{if } \epsilon < X_2 < X_1, \end{cases}$$

$$d_2(\boldsymbol{X}) = \begin{cases} C_2\left(\sqrt{\frac{1-X_1-X_2}{X_1}} + \sqrt{\frac{\epsilon}{X_1(1-X_1-X_2)}}\right)|\Delta W_n^2|, & \text{if } 2X_1+X_2 < 1, \\ C_2\left(\sqrt{\frac{X_1}{1-X_1-X_2}} + \sqrt{\frac{\epsilon}{X_1(1-X_1-X_2)}}\right)|\Delta W_n^2|, & \text{if } 2X_1+X_2 \geq 1, \end{cases}$$

$$d_3(\boldsymbol{X}) = \begin{cases} C_3\left(\sqrt{\frac{1-X_1-X_2}{X_2}} + \sqrt{\frac{\epsilon}{X_2(1-X_1-X_2)}}\right)|\Delta W_n^3|, & \text{if } 2X_2+X_1 < 1, \\ C_3\left(\sqrt{\frac{X_2}{1-X_1-X_2}} + \sqrt{\frac{\epsilon}{X_2(1-X_1-X_2)}}\right)|\Delta W_n^3|, & \text{if } 2X_2+X_1 \geq 1. \end{cases}$$

If $X_1$ or $X_2$ are less than $\epsilon$ then set $X_i = \epsilon$ for $i = 1, 2$ respectively. Also if $X_1 + X_2 \geq 1 - \epsilon$ then set this sum equal to $1 - \epsilon$ in the above formulas. The second equation in the split, (5.53), is then solved using the Euler-Maruyama method.

### 5.6.1 Eternal Lifetime of the Multidimensional BISS Method

For ease of notation, we set the second term in (5.56) and (5.57) to be $\psi_l$ and the two sums $\sum_{p=1}^{m-1} X_p$ and $\sum_{p=1,p\neq i_l}^{m-1} X_p^n$ to be $\mathsf{X}_s^n$ and $\mathsf{X}_{s-i_l}^n$, respectively. We begin by showing that the BIM scheme described by equations (5.54) to (5.57) has $\epsilon$-lifetime. From this, eternal lifetime of the BISS method follows almost immediately.

**Theorem 5.6.1.** *The BIM scheme described by equations* (5.54) *to* (5.57) *possesses $\epsilon$-lifetime when used to obtain the numerical solution to the multidimensional Wright-Fisher model without drift.*

*Proof.* In order for the BIM scheme to possess $\epsilon$-lifetime it must be shown that when the discretisation at the $n$th iteration step, $\boldsymbol{X}^n$, satisfies,

1. $X_i^n \geq \epsilon$ for all $i$,
2. $\sum_{i=1}^{m-1} X_i^n \leq 1-\epsilon$,

so that $\boldsymbol{X}^n$ lies in what shall be called the $\epsilon$ *safe region*, then $\boldsymbol{X}^{n+1}$ must satisfy,

1. $X_i^{n+1} \geq 0$ for all $i$,
2. $\sum_{i=1}^{m-1} X_i^{n+1} \leq 1$.

The left hand side of (5.54) simplifies to

$$\left(1+\sum_{l=1}^{k} d^l(\boldsymbol{X}^n)|\Delta W_n^l|\right)\boldsymbol{X}^{n+1},$$

by the definition of the function $D(\boldsymbol{X}^n)$, where $d^l(\boldsymbol{X}^n)$, $l=1\ldots k$, are scalar functions. By the choice of these scalar functions, given by (5.56) and (5.57) if follows that

$$\left(1+\sum_{l=1}^{k} d^l(\boldsymbol{X}^n)\right) > 0.$$

Therefore to prove the first property above holds, it suffices to show that the righthand side of (5.54) is positive for each $i$, $i=1,\ldots,m-1$. The righthand side of (5.54) can be written

component wise as follows

$$X_i^n + \sum_{l=1}^{k} \left( e_{il} c_l \sqrt{f_l(\boldsymbol{X}^n)} \Delta W_n^l + X_i^n d^l(\boldsymbol{X}^n) |\Delta W_n^l| \right), \tag{5.58}$$

where $e_{il}$ are the entries of the matrix $E$. If $e_{il} = 0$ it is clear that the term within the sum is positive. Otherwise note that $f_l(\boldsymbol{X}^n)$ is either of the form $X_i \mathsf{X}_s$ or $X_i X_p$ for some $p$, and $e_{il}$ is nonzero if and only if $l = i$ or $l = p$. Due to the definition of the functions $d^l(\boldsymbol{X}^n)$ in the $\epsilon$-safe region, it follows that the terms within the sum are positive.

To show the BIM satisfies the second condition given above, it suffices to show that

$$\left( 1 + \sum_{l=1}^{k} d^l(\boldsymbol{X}^n) |\Delta W_n^l| \right)$$

is greater than or equal to the sum of the terms of the vector on the righthand side of (5.54). Put another way, the second condition is satisfied providing the sum of the entries of the vector

$$\left[ 1 + \sum_{l=1}^{k} d^l(\boldsymbol{X}^n) |\Delta W_n^l| \right] \mathbf{1} - \left[ \boldsymbol{X}^n + EM + \boldsymbol{X}^n D(\boldsymbol{X}^n) \right], \tag{5.59}$$

are greater than or equal to $0$, where $\mathbf{1}$ is a vector of ones of length $m - 1$ and $M$ denotes the diagonal matrix in (5.54). The sum over the components of the above vector can be written as follows,

$$1 - \mathsf{X}_s + \sum_{l=1}^{k} \left[ (1 - \mathsf{X}_s) d^l(\boldsymbol{X}) |\Delta W_n^l| - \left( \sum_{q=1}^{n} e_{ql} c_l \sqrt{f_l\left(\boldsymbol{X}^n\right)} \Delta W_n^l \right) \right], \tag{5.60}$$

and so we want to show that the above term is non-negative. Clearly the first term is greater than or equal to $0$ since we are assuming that $X_i$ lie in the $\epsilon$ safe region for all $i$. For $f_l(\boldsymbol{X}^n)$ of the form $X_i^n X_p^n$ for some $p$, $e_{ql}$ will be nonzero for $q = i$ and $q = p$ and the values of these two entries ($e_{il}$, $e_{pl}$) are of opposite signs and therefore will cancel out. Thus the term in the sum simplifies to $(1 - \mathsf{X}_s) d^l(\boldsymbol{X}) \left| \Delta W_n^l \right|$ and so, since $\mathsf{X}_s \leq 1 - \epsilon$, i.e. it lies in the $\epsilon$-safe region, this term is clearly positive. For $f_l(\boldsymbol{X}^n)$ of the form $X_i \mathsf{X}_s$ it is less obvious that the term inside the sum is positive. In this case the $l$th column of the matrix $E$ will have only $1$ nonzero entry when $q = i$, $e_{il} = \pm 1$, and so the term in the sum does not simplify as before. Instead the

positivity of such terms follows from the way in which the functions $d^l(\boldsymbol{X}^n)$ have been defined in the $\epsilon$ safe region. Therefore the second property also holds and so the BIM scheme described by equations (5.54) to (5.57) possess $\epsilon$-lifetime. □

**Theorem 5.6.2.** *The BISS method, given by equations* (5.52) *to* (5.57) *possesses eternal lifetime for the multidimensional Wright-Fisher model,* (5.42)*. That is the BISS method preserves the boundaries of the analytical solution to the multidimensional Wright-Fisher model.*

*Proof.* Using the same inductive argument as in the proof of Theorem 5.3.1, this follows directly from the fact that the BIM possesses $\epsilon$-lifetime, and the choice of $\epsilon$ in terms of the time-step that ensures the solution to the ODE approximation lies in the interval $[\epsilon, 1-\epsilon]$. □

Indeed, the BISS method possesses eternal lifetime for the Wright-Fisher model if equations (5.52) to (5.57) ensure each component of $\boldsymbol{X}^{n+1}$ lies in $[0,\ 1]$ and $\sum_{i=1}^{m-1} X_i^{n+1} \leq 1$ with probability 1, providing at the $n$th iteration each component of $\boldsymbol{X}^n$ is in $[0,\ 1]$ and $\sum_{i=1}^{m-1} X_i^n \leq 1$. The BIM possesses $\epsilon$-lifetime for the first equation, (5.52), of the split in the BISS method. Since the second equation of the split, (5.53) is a deterministic equation, by choosing $\epsilon$ as a function of the discretisation time step $\Delta_t$ we can guarantee that the solution to the deterministic equation will force the solution back into the $\epsilon$ safe region, given that $A_{ij} > 0$ for $i \neq j$, $i, j = 1 \ldots, m-1$, and $\beta_i > 0$ for $i = 1, \ldots, m-1$. Therefore it is clear that the BISS method given by equations (5.52) to (5.57) possesses eternal lifetime for the multidimensional Wright-Fisher model.

## 5.7 Numerical Convergence of the BISS Method

Numerical tests were performed to study the strong convergence of the BISS method for the Wright-Fisher model, (5.3), and the multidimensional form of the Wright-Fisher model involving 3 states, given by (5.51). The error between the true, $X_{true}(t)$ and the approximate solution

**Figure 5.4** Log log plots showing the convergence results for Wright-Fisher models, (5.3) (left) and (5.51) (right). The red dashed line is a reference slope of $1/2$. The parameter values for (5.3) are $A = 1$, $B = 2$ and $C = 0.2462$ and for (5.51) $A_1 = 1$, $A_2 = 2$, $A_3 = 3$, $B_1 = 1.2$, $B_2 = 2.3$, $B_3 = 3.4$, $C_1 = 0.1271$, $C_2 = 0.1798$ and $C_3 = 0.1291$. The initial condition is taken to be the steady state of the deterministic part of (5.3) and (5.51).

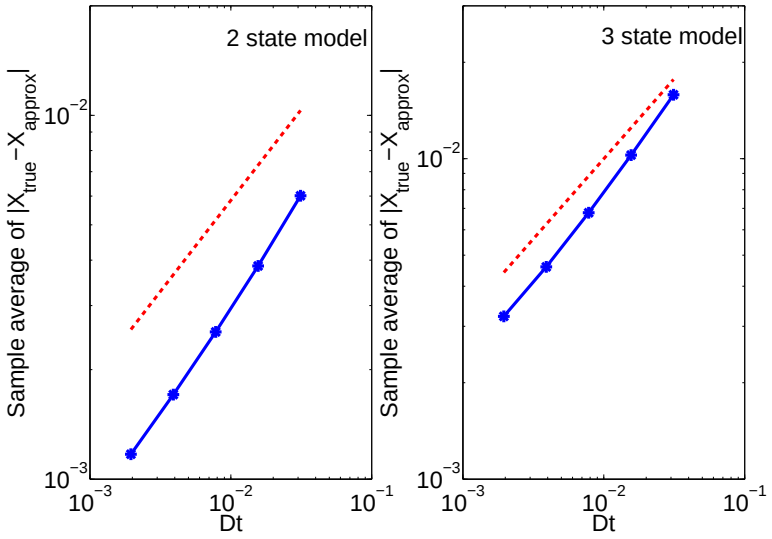


$X_{approx}(t)$ at the final time, $T$, is considered. The "true" solution is calculated using the Euler-Maruyama method over a very fine time discretisation, namely with time step $\Delta_t = 2^{-9}$. We have chosen the parameter regime such that the solution lies far from the boundaries $0$ and $1$ and so the probability of the Euler-Maruyama approximation leaving the desired region is very small. Therefore instead of altering the scheme to ensure solutions remain within $[0, 1]$, paths outside this interval are rejected. Since only a few paths will need to be rejected, for the chosen parameter regime, such an approach is computationally feasible. However, this is not the case for all parameter regimes.

We calculate the error,

$$E|X_{true}(T) - X_{approx}(T)| \tag{5.61}$$

between the "true" solution and a numerical approximation using the following five different time discretisations, $\Delta_t^k = 2^{k-1}$ for $1 \leq k \leq 5$ over a million simulations with final time $T = 1$, (Higham, 2001). Results are given in Figure 5.4.

The slopes of the errors appear to match well with the reference slope of $1/2$, Figure 5.4, suggesting that the BISS method converges with strong order $1/2$ for both the one dimensional and multidimensional Wright-Fisher models, (5.3) and (5.51).

## 5.8 Potential Bias From Altering Existing Numerical Schemes

We consider the solution to the Wright-Fisher model (5.3) for parameter values such that the solution to this equation lies very close to the boundary $1$, and so the chance that the Euler-Maruyama approximation leaves $[0, 1]$ is high. We note that the choice of parameters corresponds to modelling the $m$ gate in the Hodgkin-Huxley model given by equation (A.4) in Appendix A, where the voltage is set to $-30mV$ and so the parameters in the Wright-Fisher model are biologically relevant to approximately modelling ion channel dynamics. In one million simulations, we observed that the Euler-Maruyama path left the desired region in over 700 000 simulations. Therefore if such paths were to be rejected, computing a mean solution using the Euler-Maruyama method over a large number of simulations would not be computationally feasible. Indeed this is not the common method employed in cardiac and neuronal cell stochastic simulation studies. Instead if the solution leaves this region at some time $t$, the Wiener increment is continually resampled until the approximation at that time lies within $[0, 1]$. Thus in practice the Euler-Mauryama scheme is altered to force the path to lie within a biologically realistic region, (Fox, 1997; Pueyo et al., 2011). To the best of our knowledge no convergence has been studied for the Euler-Maruyama method when such an alteration is performed, and it seems plausible that such an adjustment could potentially bias the numerical solution. Since the BISS method ensures solutions remain within $[0, 1]$ without the need for any such alteration, we investigated the potential affect of this modification to the Euler-Maruyama method by comparing numerical solutions to (5.3) obtained using the BISS method with those of the adjusted Euler-Maruyama method. The adjustment employed in the Euler-Maruyama method is to continually resample the Wiener increment to ensure solutions remain in $[0, 1]$, as is the

**Figure 5.5** Left: Mean solution over a million simulations to (5.3) using the Euler-Maruyama method (blue dot dash) and the BISS method (red solid line). Right: Difference between the mean BISS method solution and the mean Euler-Maruyama solution over a million simulations (black solid line) and the mean of the difference between the mean paths (green horizontal dot dash line). The parameter values used for simulation are $a = 7.0064$, $b = 0.0204$, $N = 100$, $\Delta_t = 0.01$ and the initial condition is the steady state of the deterministic system. The maximum standard error for the BISS method is $2.8582 \times 10^{-6}$ and for the Euler-Maruyama method it is $6.9183 \times 10^{-6}$.

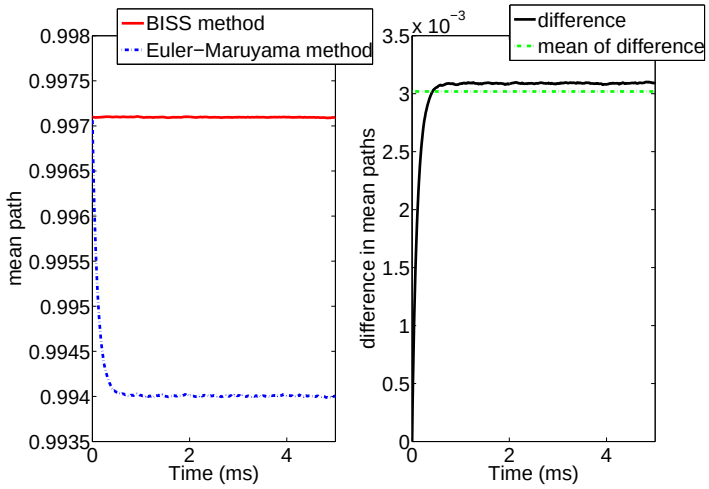


approach taken in (Pueyo et al., 2011).

In any single simulation, out of the one million simulations shown in Figure 5.5, the maximum number of times the modification was utilised in the Euler-Maruyama implementation was $874$. If the resampling of the Wiener increment did not bias the solution obtained using the Euler-Maruyama method then we would expect the difference between the two mean paths to fluctuate about $0$. However, the Euler-Maruyama path is consistently smaller than the path obtained using the BISS method, suggesting the effect of resampling the Wiener increment is to underestimate the solution to (5.3). Such effects are potentially important when the transition rates are no longer constant but are functions of time, as is the case when considering ion channel dynamics within electrophsyiology models.

## 5.9 Chapter Summary

In this chapter we approximated the ion channel SDE model by an SDE which is of the form of the Wright-Fisher model, and showed that this new model closely approximates the first two moments of the discrete-state Markov chain model, whilst ensuring biologically realistic analytic solutions. This was first described for the simple model and then the extension to more complex models of ion channel dynamics was discussed.

Since current numerical techniques are unable to preserve the boundaries inherent in the analytic solution of the Wright-Fisher model, we also proposed a new numerical technique, the BISS method, that preserves the boundaries of solutions to this SDE. The idea is to split the equation into an SDE, consisting only of the diffusion coefficient and an ODE. The SDE is then solved using the BIM where the control functions are chosen so that the approximation remains within $[0, 1]$ providing the solution at the previous time step is a distance $\epsilon$ away from the boundary. This $\epsilon$ is then determined as a function of the discretisation time step so that the approximation to the ODE always lies within the restricted interval $[\epsilon, 1-\epsilon]$. Therefore, the numerical solution remains within $[0, 1]$ with probability $1$ for all time. Strong convergence of this scheme was proved for the simple one-dimensional Wright-Fisher model. Numerical experiments suggest that the order of convergence is $1/2$ for both the one dimensional and multidimensional systems. Finally, we showed that alterations commonly employed in numerical schemes to ensure the numerical approximation satisfies the boundaries inherent in the SDE model can introduce bias into the solution. We have focused on the application of the BISS method to the Wright-Fisher model, however this method could also be applied to other problems in order to preserve the boundaries of solutions to SDEs.

# 6

# Modelling Ion Channel Dynamics through Reflected SDEs

*In the previous chapter we put forward a way to deal with the issue of biologically unrealistic solutions to the SDE model of ion channel behaviour by using the Wright-Fisher model to approximate the dynamics of the system. In this chapter we return to the original derivation of the SDE model, that describes the individual trajectories of the continuous-state stochastic process approximated from the Master equation given in Chapter 3. We firstly examine the controversy that the partial differential equation (PDE) describing the probability distribution of the continuous-state process remains within the correct region, while the corresponding SDE does not. This provides the rationale behind the approach taken in this chapter to ensure that the SDE model of ion channel dynamics is biologically accurate.*

*Instead of altering the SDE model itself, we show how to incorporate boundary conditions into the existing SDE model of ion channel dynamics. The resulting equation is frequently termed a reflected SDE, and we argue that this is the correct equation that describes the individual realisations of the diffusion process obtained from the system size expansion of the discrete-state Markov chain model.*

In Chapter 3 Section 3.4 we obtained the SDE from the Fokker-Planck equation, which we derived directly from the discrete-state Markov model using a system size expansion. For the simple model where the channel is assumed to be either open of closed, the SDE for this system is

$$dY = (a - (a+b)Y)\,dt + \tfrac{1}{\sqrt{N}}\sqrt{a + (a+b)Y}\,dW. \tag{6.1}$$

In (Gillespie, 2000) Gillespie takes a different approach, formulating the SDE directly from the simulation method of the discrete-state model, namely the SSA (see Chapter 3, Section 3.2.3), in the limit as the number of channels becomes large. This approach assumes that the number of channels is large enough so that there exists a time step, over which the transition rate functions are approximately constant, but many transitions occur. The update formula for the number of channels in each state can then be approximated by the one-step discretisation scheme of the Euler-Maryuama method, which converges to (6.1) as the time step becomes infinitesimally small. The approach taken by Gillespie is often seen as the definitive method for obtaining the approximate SDE model within the stochastic biochemical reaction kinetics community.

This derivation of the SDE model has led to some authors arguing that the reason solutions to (6.1) can leave $[0, 1]$ is because near the boundaries of this interval the approximation made by Gillespie in (Gillespie, 2000) is no longer valid, (Gillespie, 2002; Higham, 2011). However, according to the derivation given in Chapter 3 Section 3.4, the SDE describes the individual trajectories of a diffusion process whose probability distribution is described by a PDE, the Fokker-Planck equation. We can impose boundary conditions onto the Fokker-Planck equation to ensure the probability of solutions lying outside $[0, 1]$ is $0$. Thus we can ensure the continuous-state model remains within the desired region, even if the number of channels becomes small. We note that in such situations, the Fokker-Planck equation may no longer provide a good approximation to the stochastic behaviour of the discrete-state Markov chain model, but we emphasise that this diffusion process will still lie within $[0, 1]$ with probability $1$. This suggests that solutions to the SDE lie outside $[0, 1]$ not because the diffusion approximation

breaks down, but rather the SDE has not been formulated in the correct way to account for the boundary conditions imposed on the Fokker-Planck equation. That is, in switching from the Fokker-Planck equation to the SDE, the boundary conditions have in some sense become 'lost'. We show how these boundary conditions can be incorporated into the SDE, thus providing a formulation for the sample paths of the diffusion process that is consistent with the dynamics of the Fokker-Planck equation.

## 6.1 Reflected Stochastic Differential Equations

We begin with the SDE for the simple two state ion channel model and then discuss the generalisation to the SDE for more complex ion channel models.

### 6.1.1 Simple Model

The SDE for the simple two state model, (6.1), gives the individual realisations of the diffusion process $Y(t)$ whose probability distribution is governed by the Fokker-Planck equation

$$\frac{\partial P(y,t)}{\partial t} = -\frac{\partial}{\partial y}\left[(a-(a+b)y)\,P(y,t)\right] + \frac{1}{2N}\frac{\partial^2}{\partial y^2}\left[(a+(b-a)y)\,P(y,t)\right]. \qquad (6.2)$$

Since the total number of channels is assumed to remain constant and $y$ denotes the *proportion* of open channels it follows that

$$\int_0^1 P(y,t)dy = 1,$$

and so

$$\frac{\partial}{\partial t}\int_0^1 P(y,t)dy = 0.$$

Interchanging the integral and the derivative with respect to $t$ in the above formula and using the relation (6.2) we can apply integration by parts to obtain the equation,

$$(a-(a+b)y)\,P(y,t) - \frac{1}{2N}\frac{\partial}{\partial y}\left[(a+(b-a)y)\,P(y,t)\right] = 0, \qquad (6.3)$$

at the boundaries $y = 0$ and $y = 1$, (Van Kampen, 2007). Since condition (6.3) reflects the solution back into the interval $[0, 1]$ at the boundaries, the process $Y(t)$ is often referred to as a reflected diffusion.

In order to impose the boundary condition (6.3) on the dynamics of the SDE (6.1), consider decomposing the diffusion process $Y(t)$ into the sum of two stochastic processes, $Y(t) = X(t) + K(t)$. The dynamics of the first process, $X(t)$, is governed by (6.1), and so determines the behaviour of $Y(t)$ on the interior of the interval $(0, 1)$. Thus we must have that $Y(0) = X(0)$ and in particular it follows that $Y(t) = X(t)$ on $(0, 1)$.

The process $K(t)$ determines the behaviour at the boundary and we set it to have initial value $K(0) = 0$. In some sense $K(t)$ can be thought of as the minimal process which forces $Y(t)$ to remain in the interval $[0, 1]$. The measure induced by this process must thus be concentrated at the times $t_e$ where $Y(t_e) = 1$ or $Y(t_e) = 0$. We can formalise this by requiring $K(t)$ to satisfy the following property,

$$|K|(t) = \int_0^t \mathbf{1}_{\{Y(s)=0, Y(s)=1\}} d|K|(s), \tag{6.4}$$

where $\mathbf{1}_Z$, is the indicator function on the set $Z$, so $\mathbf{1}_Z(x) = 1$ if $x \in Z$ and zero otherwise and $|K|(t)$ is the total variation of $K(t)$ on $[0, t]$. In fact, in (Bayer et al., 2010) the authors informally refer to the process $K(t)$ as a *local time*. In stochastic analysis the *local time* is a process that characterises the amount of time a stochastic process spends at a particular point. So by using this term, the authors in (Bayer et al., 2010) are emphasising that the measure of $K(t)$ is closely linked to the amount of time $Y(t)$ spends at the boundary.

The property above only ensures that $K(t)$ changes at the times when $Y(t)$ is at the boundary, but the way in which $K(t)$ will reflect the process $Y(t)$ back into $(0, 1)$ at the endpoints of this interval must still be specified. We assume that the process $K(t)$ will reflect $Y(t)$ into the interior of the interval in the direction of the inward pointing unit normal. That is, when $Y(t) = 0$, $K(t)$ will push the process in the positive direction, while at $Y(t) = 1$, $K(t)$ will force the process in the opposite direction. To characterise the behaviour of $Y(t)$ at the boundary

in this way we impose the following condition on $K(t)$

$$K(t) = \int_0^t \gamma(Y(s))d|K|(s), \tag{6.5}$$

where $\gamma(Y(s))$ is a unit inward normal to the endpoints of the interval $[0, 1]$ and $|K|(t)$ denotes the total variation of $K(t)$ on $[0, t]$. Other authors also deal with oblique reflection at the boundary (Bossy et al., 2004), however for our problem we focus only on normal reflection at the boundary.

Taking the stochastic differential it follows that $Y(t)$ satisfies the SDE

$$dY = (a - (a + b)Y)dt + \tfrac{1}{\sqrt{N}}\sqrt{a + (b - a)Y}dW + dK, \tag{6.6}$$

with initial condition $Y(0) = y_0 \in [0, 1]$. Such an equation is termed a reflected SDE, since the process $Y(t)$ is instantaneously reflected back into $[0, 1]$ when it reaches the endpoints. We shall refer to the domain into which the reflected SDE forces the solution as the reflecting domain. This equation is also sometimes known as the Skorokhod equation, since Skorokhod first proved the existence and uniqueness of solutions to SDEs of this type (Skorokhod, 1961, 1962).

**Figure 6.1** A frequency plot of the reflected SDE for the simple two state model calculated over $100,000$ simulations with parameter values $N = 500$, $a = 0.004$, $b = 3$ and the initial proportion of open channels set to $0.1$. Solution of the Fokker-Planck equation for the same parameter values (red line with star markers). Both distributions are calculated after $4ms$ of simulation.

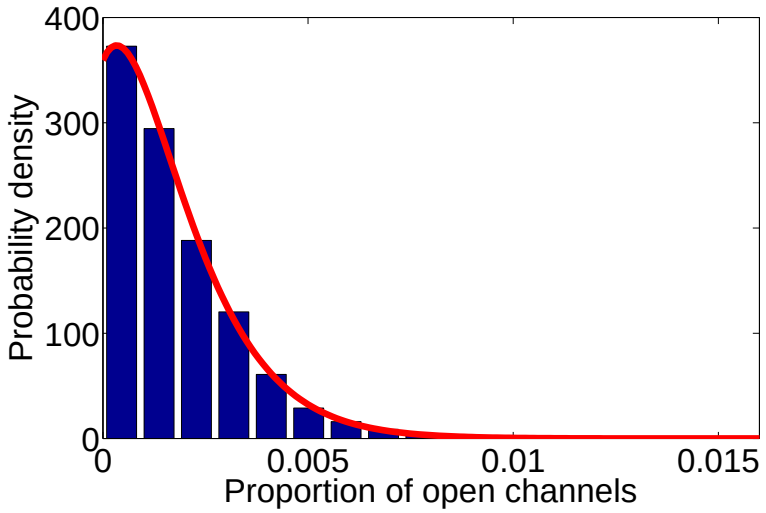

To better understand this reflecting process $K(t)$, we shall for a moment digress from our current domain of reflection, and consider the simplest situation where the process $Y(t)$ is reflected at $0$ (i.e. the domain of reflection is $[0, \infty)$). The smallest value that would have to be added to the process to ensure that it remains in $[0, \infty)$ over the time interval $[0, t]$, will be the maximum amount by which the unreflected process overshoots the zero boundary (i.e. the largest negative value of the unreflected process) up until time $t$. That is, the exact form of the reflecting process in this simple case will be

$$K(t) = sup_{0 \leq s \leq t}(Y(s))^{-},$$

where $a^{-} = max(0, -a)$. In our case there is also reflection at the boundary $y = 1$ and so $K(t)$ will no longer take the form given above. In general it is difficult to characterise the reflecting process $K(t)$ for an arbitrary reflecting domain and so it must be approximated numerically. In Section 6.2 we shall discuss numerical methods to approximate solutions to reflected SDEs.

In Figure 6.1 we compare the probability distribution obtained from solving (6.2) with boundary conditions (6.3), with the distribution obtained from multiple simulations of the reflected SDE (6.6). The two distributions are very similar, supporting the conclusion that the reflected SDE is the correct formulation of the sample paths for the process described by (6.2) and (6.3).

### 6.1.2 Generalisation to Complex Model

We now consider the generalisation of the reflected SDE to more complex models of ion channel dynamics, where each channel can reside in one of $m$ different states and can undergo $k$ reversible reactions. The dynamics of this system can be described by the following SDE

$$d\boldsymbol{Y} = H\boldsymbol{Y}dt + \tfrac{1}{\sqrt{N}}EF(\boldsymbol{Y})d\boldsymbol{W}, \tag{6.7}$$

see Chapter 3 Section 3.4.2 for the form of $H$ and Chapter 4 Section 4.1.2 for the form of the matrices $E$ and $F(\boldsymbol{Y})$.

For $\boldsymbol{Y}(t)$ to have biological meaning, each element, $Y_i(t)$ for $i = 1, \ldots, m$, of the vector must lie within the interval $[0, 1]$ since it represents the proportion of channels in state $i$ at time $t$. Therefore it follows that the individual trajectories of this process, given by (6.7), must remain within a $m$-dimensional hypercube bounded by the intervals $[0, 1]$. Furthermore, by conservation of the number of channels we have that $\sum_{i=1}^{m} Y_i(t) = 1$, and so $\boldsymbol{Y}(t)$ is restricted to the hyperplane given by $\sum_{i=1}^{m} Y_i = 1$ which lies inside this hypercube. We denote the reflected domain of the process $\boldsymbol{Y}(t)$ by $D$. For a channel that can reside in three different states, for example, $D$ will take the form of a plane embedded within a cube, see Figure 6.2.

**Figure 6.2** Left: Example of the reflecting domain, $D$, (shaded region) for an ion channel model that can reside in three different states. Right: Diagramatical representation of the projection scheme for an ion channel that can reside in three different states.

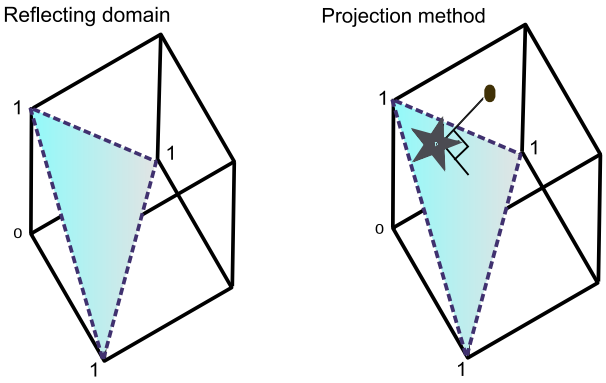


To ensure solutions to (6.7) remain within $D$, as in the previous section we decompose the process $\boldsymbol{Y}(t)$ into the sum of two processes $\boldsymbol{Y}(t) = \boldsymbol{X}(t) + \boldsymbol{K}(t)$. The first, $\boldsymbol{X}(t)$, satisfies (6.7) and describes the behaviour of $\boldsymbol{Y}(t)$ on the interior of the domain $D$ ($int(D)$), i.e. $\boldsymbol{Y}(t) = \boldsymbol{X}(t)$ for $\boldsymbol{X}(t) \in int(D)$. The second, $\boldsymbol{K}(t)$, we again define to be the process that reflects $\boldsymbol{Y}(t)$ into $D$. As before we can describe the individual realisations of the process by a reflected SDE

$$d\boldsymbol{Y} = H\boldsymbol{Y}dt + \tfrac{1}{\sqrt{N}}EF(\boldsymbol{Y})d\boldsymbol{W} + d\boldsymbol{K}. \tag{6.8}$$

Analogously to the simple two state model, we can think of the reflecting process $\boldsymbol{K}(t)$, now vector-valued, as the minimal amount that we need to add to the unreflected process to ensure that $\boldsymbol{Y}(t)$ remains within the domain $D$. The definition of the conditions imposed on the reflect-

ing process in the two state model, (6.4) and (6.5), naturally generalise to the multidimensional setting,

$$|\boldsymbol{K}|(t) = \int_0^t \mathbf{1}_{\{\boldsymbol{Y}(s)\in\partial D\}} d|\boldsymbol{K}|(s),$$
$$\boldsymbol{K}(t) = \int_0^t \gamma(s) d|\boldsymbol{K}|(s), \tag{6.9}$$

where $\gamma(s) \in N(\boldsymbol{Y}(s))$ if $\boldsymbol{Y}(s) \in \partial D$ and $N(\boldsymbol{x})$ is the set of inward pointing unit vectors to the point $\boldsymbol{x}$ which lies on the boundary of $D$ ($\partial D$). The solution to the reflected SDE, (6.8) will be a pair $(\boldsymbol{Y}(t), \boldsymbol{K}(t))$ that satisfy these properties. For a more rigorous definition of the solution to the reflected SDE (6.8), see for example (Pettersson, 1995).

The existence and uniqueness of such a pair was extended to domains in $\mathbb{R}^n$ by (Wantanebe, 1971), providing $D$ is convex (Tanaka, 1979) or satisfies certain regularity conditions (Lions and Sznitman, 1984). Since our domain $D$ is convex, the solution to the reflected SDE that describes the behaviour of a general ion channel model, (6.8), exists and is unique. As for the simple model, the last two conditions in the above definition ensure that the reflecting process only increases on the boundary of $D$, $\partial D$, and that it reflects $\boldsymbol{Y}(t)$ back into the interior of $D$ in the normal direction to the boundary.

## 6.2 Numerical Methods for Reflected SDEs

Although the field of numerical methods for reflected SDEs is far less studied than standard stochastic numerical analysis, a number of techniques have been developed in recent years, and in this section we provide a brief review of these methods. The algorithms typically employed to approximate solutions to reflected SDEs such as (6.8) can broadly be split into two types: projection schemes and penalization methods. Since both types of methods involve the use of the orthogonal projection map, throughout this section we define $\Pi_D(\boldsymbol{z})$ to be the orthogonal projection of the vector $\boldsymbol{z}$ onto the domain $D$.

In the penalization method, the reflecting process is replaced by a diffusion type term that

vanishes inside the domain $D$ and grows rapidly outside $D$ with respect to distance to the boundary, $\partial D$. This diffusion type term is often referred to as the penalization function and is defined to be $\beta_\lambda(y) = (y - \Pi_D(y))/\lambda$ for some $\lambda > 0$. The resulting SDE is referred to as the penalization equation and for the general ion channel model it takes the following form,

$$d\boldsymbol{Y}_\lambda(t) = (H\boldsymbol{Y}_\lambda(t) - \beta_\lambda(\boldsymbol{Y}_\lambda(t)))\,dt + \frac{1}{\sqrt{N}}EF(\boldsymbol{Y}_\lambda(t))dW(t). \tag{6.10}$$

Menaldi (Menaldi, 1983) showed that as $\lambda \to 0$ the solution to (6.10) converges to that of the reflected SDE. The general idea of the penalization method is to solve the penalization equation, for some fixed $\lambda$, using standard SDE numerical methods, in order to obtain an approximation for the associated reflected SDE. Liu (Liu, 1995) showed that using the Euler-Maruyama method to solve (6.10) with $\lambda = \sqrt{\Delta_t}$, the numerical approximation converges to the solution of the reflected SDE in the strong sense with order $\Delta_t^{1/2-\epsilon}$ for all $\epsilon > 0$, where $\Delta_t$ is the time step. In Pettersson (1997), Petterson shows a refined and more general result on the error bounds providing $D$ is open and convex, the drift and diffusion coefficients are Lipschitz and the diffusion coefficient is also bounded. Namely the penalisation scheme introduced in Liu (1995) is shown to converge with order $(\Delta_t log(\Delta_t))^{1/2}$ for all $\Delta_t \leq \lambda$. Pettersson also discusses the optimal choice for $\lambda$, showing that if $\lambda$ is too small then the penalization term in the discretisation scheme may push the solution too far into $D$. Thus Petterson concludes that taking $\lambda = \Delta_t$ in simulations is optimal.

For the one-dimensional reflected SDE with reflection at $0$, Ding (2008) showed that it is possible to improve the convergence and stability of this method by using a split step scheme to approximate the solution to the penalization equation (6.10). The equation is split into an SDE, and an ODE which contains the penalisation term (the authors call this a penalisation ODE). The SDE is solved at each time step using the Euler-Maruyama method and this provides the initial condition for the ODE. The ODE is then approximated using the standard Euler method, and this provides the approximation for the reflected SDE at the next time step. The issue with such methods is that, depending on the choice of $\lambda$, they can result in numerical approximations

that lie outside the domain $D$, even though analytic solutions to (6.8) must lie within $D$. This is because in the discretisation schemes, the penalisation term is calculated in terms of the numerical approximation at the previous time step. Therefore we do not use a penalization method to simulate the reflected SDE for ion channel dynamics.

The projection method can be thought of as a simple extension of the Euler-Maruyama method to the reflected SDE case. At time $t$ the non-reflected process is evaluated at the next time step $t + \Delta_t$ using the Euler-Maruyama algorithm. If this value lies within the closure of $D$, $\overline{D}$, then the reflected process at the next time step is set equal to this value. Otherwise the value of the reflected process at the next time step is set to be the orthogonal projection of this point onto the reflecting domain $D$. For fixed time step $\Delta_t$ the projection method algorithm applied to the reflected SDE for the general ion channel model (6.8) is as follows:

1. Set $t = 0$ and $\boldsymbol{Y}(0) = \boldsymbol{y}_0$.
2. Generate a vector of Wiener increments, $\Delta \boldsymbol{W}_t = (\Delta W_1, \ldots, \Delta W_k)^T$, where $\Delta W_p$ $p = 1, \cdots, k$ are independent normal random variables mean $0$ and variance $\Delta_t$ and set
$$\boldsymbol{Y}_G(t + \Delta_t) = H\boldsymbol{Y}(t)\Delta_t + \tfrac{1}{\sqrt{N}} EF(\boldsymbol{Y}(t))\Delta \boldsymbol{W}_t.$$
3. If $\boldsymbol{Y}_G(t + \Delta_t) \in \overline{D}$ then set $\boldsymbol{Y}(t + \Delta_t) = \boldsymbol{Y}_G(t + \Delta_t)$. Otherwise set $\boldsymbol{Y}(t + \Delta_t) = \Pi\left(\boldsymbol{Y}_G(t + \Delta_t)\right)$.
4. Set $t = t + \Delta_t$ and return to step two.

Figure 6.2 diagrammatically shows how the projection method works at a certain time step for a three state model. The shaded area is the domain of reflection, the round point is the value at some time step of the unreflected process and the star point is the projection of this point onto $D$, i.e. the value taken at the next time step for the projection method.

Note that under this scheme we do not explicitly calculate the reflecting process $\boldsymbol{K}(t)$ at each time step since we are only interested in the solution to the reflected SDE, $\boldsymbol{Y}(t)$. However, it is

straightforward to define $\boldsymbol{K}(t)$ for the projection method numerical algorithm given earlier in this section,

$$\boldsymbol{K}(0) = 0,$$

$$\boldsymbol{K}(t+\Delta_t) = \begin{cases} \boldsymbol{K}(t) + \Pi(\boldsymbol{Y}_G) & \text{if} \quad \boldsymbol{Y}_G \notin \bar{D} \\ \boldsymbol{K}(t) & \text{otherwise.} \end{cases}$$

This scheme has been shown to converge in the mean square sense with order $O(\Delta_t^{1/2-\epsilon})$, for any $\epsilon > 0$, uniformly on compact sets, (Slominski, 1994). In (Pettersson, 1995) a slightly faster rate of $O((\Delta_t log \Delta_t)^{1/2})$ was obtained but this was only for pointwise convergence. Furthermore if $D$ takes the form of a product space as follows $D = \mathbb{R}^p \times D'$ for $1 < p < d$ and $D'$ a closed convex set in $\mathbb{R}^{d-p}$, then the projection method converges with a stronger rate, namely $O(\Delta_t^{1/2})$ and so has the same rate of convergence as the standard Euler-Maruyama method (Pettersson, 1995; Liu, 1995).

For reflected Brownian motion, that is when the drift and diffusion coefficients are constant and the domain of reflection is the non-negative half plane, the projection method converges with strong and weak order $1/2$ and so the weak order of convergence is lower than for the Euler-Maruyama method applied to standard Brownian motion (i.e. Brownian motion without reflection). The lower convergence is due to the fact that between times $t$ and $t+\Delta_t$ the process may leave $\overline{D}$ and lie in $\overline{D}$ at time $t+\Delta_t$ without any effect on the value of the numerical approximation at $t+\Delta_t$. This 'overshoot' of the approximation means that the projected method does not agree with the exact solution at the discrete time points, while the Euler-Maruyama method applied to standard Brownian motion does. Therefore, to improve the order of convergence, this issue with the overshoot must be dealt with. For the simple case of reflected Brownian motion in one dimension, the exact solution of the reflecting process is known, as discussed in the previous section. Furthermore, samples from the distribution of this reflecting process can be obtained as a function of a Wiener increment and a uniform random variable (Seshadri, 1988).

Therefore, in (Asmussen et al., 1995; Asmussen and Glynn, 2010), the authors shows that by sampling from the exact distribution of the reflecting process at each time step, the weak error can be improved from $1/2$ to $1$ and so matches that of the standard Euler-Maruyama method. The improvement in the weak order is achieved since sampling from the exact distribution of the reflecting process means the numerical approximation agrees with the exact solution at discrete time points.

In (Lépingle, 1995), Lépingle extends these ideas to the general reflected diffusion case in one-dimension where the domain of reflection is the non-negative half plane. Lépingle also shows how the scheme can be extended further, to deal with the case when the reflecting domain is an interval in $\mathbb{R}$, so that there are two barriers. The idea is to assume that the scheme can only be close to one or other barrier at a certain time step, and so is only in danger of crossing one of the barriers, rather than both. Therefore the problem effectively reduces to dealing with only one barrier at a certain time step, which can be done in a similar way as in the case of the non-negative half plane. This scheme was shown to converge with weak order $1$. The issue with these extensions of the projection method is that they do not generalise in a straightforward way to more complex domains of reflection in $\mathbb{R}^d$. This is because the higher orders of convergence are obtained using the exact form of the reflecting process, and for more complex domains the exact form of this process is rarely known. In (Gobet, 2001), Gobet tries to extend the ideas of the Lepingle method to reflected diffusions in $\mathbb{R}^d$ . This method uses the fact that the diffusion can be simulated exactly in the half-plane, however only an improved order of weak convergence is obtained for certain types of reflection.

We are interested in the way the stochastic ion channel dynamics affect the membrane potential and so it is the individual stochastic trajectories of the ion channel dynamics that are important, rather than distributional properties. Therefore, we are most concerned with the strong convergence of the numerical method used to simulate the stochastic ion channel dynamics (see Chapter 3 Section 3.3.3 for the definition of strong convergence). In addition the method em-

ployed to approximate solutions to the ion channel reflected SDE must be applicable to both the simple two state model and more complex model of ion channel dynamics. Therefore, in this thesis we use the standard projection method, given by the algorithm stated earlier in this section, to simulate the behaviour of (6.6) and (6.8).

**Figure 6.3** Convergence results for projection method applied to the reflected SDE for the potassium channel in the Hodgkin-Huxley model ((7.3) in Chapter 7). The red dashed line is a reference slope of $1/2$. The number of channels is set to $500$, the parameter values are calculated in terms of the functions for the original Hodgkin-Huxley model given in Appendix A for $V = 10mV$ and the initial condition is taken to be the steady state of the deterministic model.

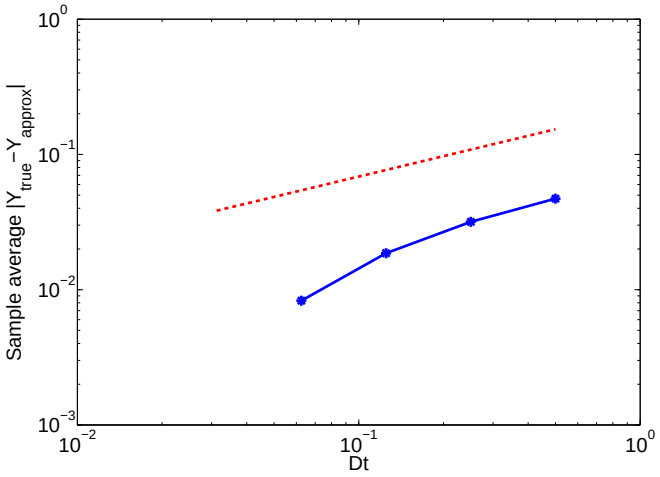


To check the projection scheme converges in the strong sense we numerically investigated the strong convergence of this method when applied to the reflected SDE for the potassium channel in the Hodgkin-Huxley model ((7.3) in Chapter 7). We calculate the error between the "true" solution, $y_{true}(t)$, and the approximate solution, $y_{approx}(t)$, at the final time, $T$, as follows,

$$E|y_{true}(T) - y_{approx}(T)|. \tag{6.11}$$

The "true" solution is taken to be the numerical approximation obtained using the projection method, calculated over a very fine time discretisation, namely with time step $\delta_t = 2^{-9}$. The following five different time discretisations, $\Delta_t = 2^{k-1}\delta_t$ for $1 \leq k \leq 5$ were used over a million simulations with final time $T = 1$, (Higham, 2001). Results are given in Figure 6.3

where it can be seen that the scheme does indeed converge in the strong sense with order very close to $1/2$.

Since the projection method involves calculating the orthogonal projection of a vector onto $D$, we briefly outline the way in which this is implemented in the simulations.

### 6.2.1 The Orthogonal projection method

We briefly describe the orthogonal projection method that is used to numerically approximate solutions to (6.8), for more details see (Chen and Ye, 2011).

For any point $z \in \mathbb{R}^m$, the projection of $z$ onto the closure of the domain $D$, $\bar{D}$, is the solution to the minimisation problem

$$u = arg\ min_{u \in \bar{D}} ||u - z||, \tag{6.12}$$

and since $D$ is closed and convex this set contains a unique point. Chen and Ye, (Chen and Ye, 2011), show that using Moreau's identity, (Combettes and Wajs, 2005), the solution to (6.12) can be simplified to a univariate minimisation problem. Furthermore they show that there are $m$ possible choices for the solution to this problem that can be computed explicitly, and $u$ is the only one of these that falls within the correct interval. Below is an outline of the algorithm used for the orthogonal projection of a point $\boldsymbol{y} = (y_1, \ldots, y_m)^T \in \mathbb{R}^m$ onto the domain $D = \{\boldsymbol{x} \in \mathbb{R}^m : 0 \leq x_i \leq 1, i = 1, \ldots, m \text{ and } \sum_{i=1}^m x_i = 1\}$. For more details see (Chen and Ye, 2011),

1. Sort $\boldsymbol{y}$ into ascending order and set $i = m - 1$.
2. Compute $t_i = \frac{\sum_{j=i+1}^m y_j - 1}{m-i}$. If $t_i \geq y_i$, set $\hat{t} = t_i$ and go to Step 4. Otherwise reduce $i$ by 1 and redo Step 2 if $i \geq 1$ or go to Step 3 if $i = 1$.
3. Set $\hat{t} = \frac{\sum_{j=1}^m y_j - 1}{m}$.
4. Set the projection of $\boldsymbol{y}$ onto $D$ to be $\boldsymbol{x} = max((\boldsymbol{y} - \hat{t}), 0)$.

The MATLAB code for this method is freely available from the authors website [1], and this was implemented in our simulations.

## 6.3 Reflected SDE Simulations for the Simple Ion Model

To ensure that the reflected SDE method does indeed capture the stochastic behaviour of the discrete-state Markov chain model, we compared the mean and variance in the proportion of open channels between the two methods for the simple two state ion channel model. The mean and variance were calculated over $10,000$ simulations using three different sets of parameter regimes and three different numbers of channels. The reflected SDE, (6.6), was solved using the projection method described in the previous section, using a time step of $0.01ms$ over a time span of $100ms$. The dynamics of the discrete-state Markov chain model were simulated using the SSA. For each method the mean and variance in the proportion of open channels are calculated at the final time in the simulations. Results are shown in Figures 6.4 to 6.6.

[1] http://ufdc.ufl.edu/IR00000353/

**Figure 6.4** Mean in the proportion of open channels, plotted as a function of the total number of channels, calculated using the reflected SDE (red line and dots) and SSA (blue solid line) simulation methods. The mean was calculated for the last time point, over $10,000$ simulations, where each simulation was run for $10ms$ using a time step of $\Delta_t = 0.01$. The three different parameter regimes used in simulation were $a = 0.004$, $b = 3$ (top), $a = 2$, $b = 1$ (middle) and $a = 4$, $b = 0.006$ (bottom).

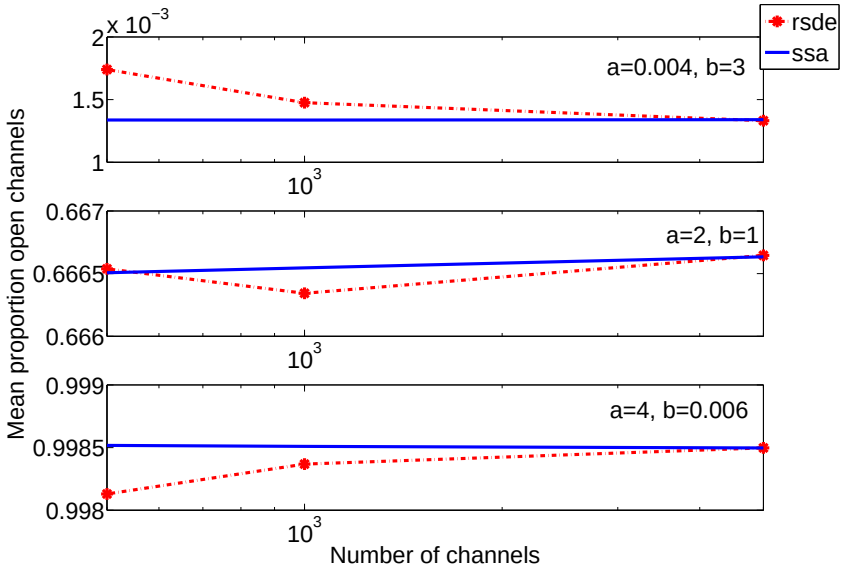

**Figure 6.5** Variance in the proportion of open channels, plotted as a function of the total number of channels, calculated using the reflected SDE (red line and dots) and SSA (blue solid line) simulation methods. The variance was calculated for the last time point, over $10,000$ simulations, where each simulation was run for $10ms$ using a time step of $\Delta_t = 0.01$. The three different parameter regimes used in simulation were $a = 0.004$, $b = 3$ (top), $a = 2$, $b = 1$ (middle) and $a = 4$, $b = 0.006$ (bottom).

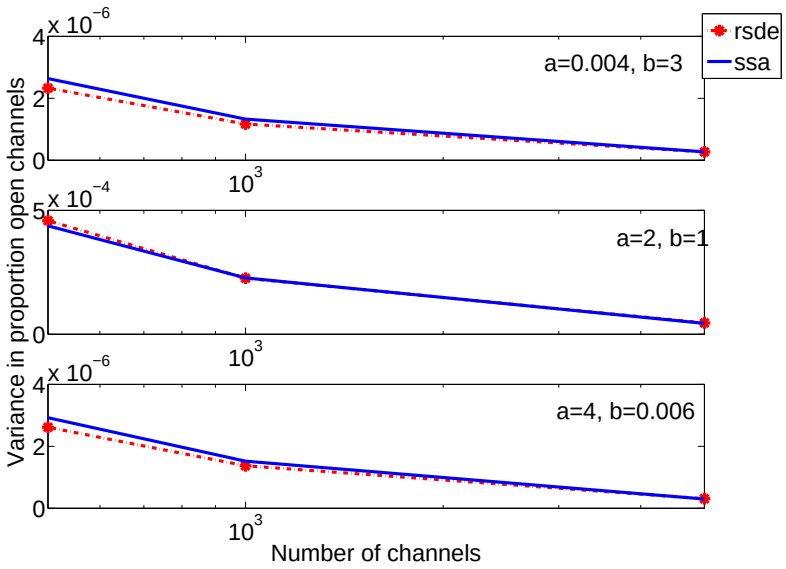


**Figure 6.6** Difference between the means calculated using the reflected SDE and SSA methods (top) and the difference in the variances between these two methods (bottom). Differences plotted as a function of the number of channels, for the three different parameter regimes shown in the legend. Simulation protocol as for the previous Figure.

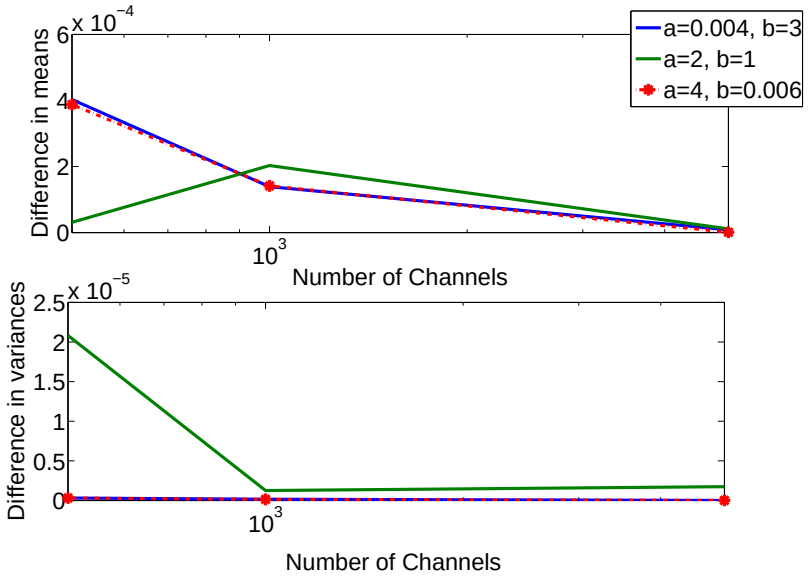

It is clear that the reflected SDE closely approximates the mean and the variance in the proportion of open channels, Figures 6.4, 6.5, for all the different parameter regimes. Furthermore, the difference between the two methods becomes smaller as the number of channels increases, Figure 6.6. This is to be expected since the accuracy of the diffusion approximation improves as the number of channels increases. We note that the reflected SDE method would probably provide better agreement with the SSA method if a numerical method with higher order convergence had been used to approximate solutions to the reflected SDE.

The model used here to show the agreement between the reflected SDE and the discrete-state Markov chain model is very simple and the parameter values used in the simulations have no direct relation to electrophysiology models. In the next chapter we therefore provide a more thorough comparison between the two methods using the Hodgkin-Huxley model and a variant of the Hodgkin-Huxley model, both given in Appendix A. Furthermore we compare not just the open channel statistics but also consider statistics related to the action potential (AP).

## 6.4 Chapter Summary

We demonstrated that by including a reflected term into the SDE that describes ion channel behaviour, solutions are guaranteed to remain within a biologically realistic domain, whilst without this term they are not. We argued that this novel formulation is the correct equation that describes the individual realisations of the diffusion process, whose probability distribution is described by a Fokker-Planck equation obtained in the limit of large $N$ from the Master equation that determines the discrete-state Markov chain model. Thus we conclude that the reflected SDE provides a model of ion channel dynamics that is biologically realistic and mathematically consistent with the approximation from the discrete-state Markov chain to the continuous-state diffusion model.

In Section 6.2 we reviewed current numerical methods to approximate solutions to reflected

SDEs. In particular we described the numerical algorithm employed in this thesis, called the projection method, to simulate the reflected SDE that describes ion channel dynamics. Finally, in Section 6.3 we showed that the first two moments in the proportion of open channels for the reflected SDE is close to that of the discrete-state Markov chain model, in the case of the simple two state model of ion channel dynamics.

In this chapter we have focused on stochastic models of ion channel dynamics. However, the issue of physically unrealistic solutions to the SDE model used to approximate discrete physical systems is present in a number of other fields, such as biochemical reaction kinetics (Higham, 2011). The ideas presented in this chapter could easily be extended to model such systems and so the method described here provides a general framework for modelling stochastic dynamics of physical systems by approximate continuous-state stochastic methods in an accurate and efficient way.

# 7

# Comparison of Different Stochastic Models of Ion Channel Dynamics

*In this chapter we compare how well the reflected SDE and Wright-Fisher approximation capture the stochastic dynamics of the discrete-state Markov chain model. Initially we use these three approaches to describe the ion channel dynamics in the Hodgkin-Huxley model. We use this model as the test case since it is one of the simplest electrophysiology models and it also provides the basis for more complex models of cellular electrical dynamics. We consider the mean and standard deviation in the proportion of open channels both when the voltage is kept fixed and also when the voltage varies through time. We also compare the computational efficiency of the three different stochastic simulation methods. Finally we consider certain properties of the action potential (AP) for a variant of the Hodgkin-Huxley model. In the comparison of the properties of the AP, we also compare the results to those obtained using the steady state SDE method from (Goldwyn et al., 2011), where the authors replace the state variable in the diffusion term by the steady state value to ensure solutions remain real. We only provide a further comparison with this method for the action potential (AP) properties and not for the open channel statistics simulations, since in (Goldwyn et al., 2011) and (Goldwyn and Shea-Brown, 2011) it was shown that this approach preserves the first two moments*

*of the discrete-state Markov chain model.*

## 7.1 Conductance Model with Bounded Stochastic Ion Channel Dynamics

As described in Appendix A, the voltage dynamics in the Hodgkin-Huxley model (Hodgkin and Huxley, 1952) can be described by the following ODE,

$$\begin{aligned} C\frac{dV}{dt} = &- G_{Na}p_O^{Na}(V - E_{Na}) - G_K p_O^K(V - E_K) \\ &- G_L(V - E_L) + I, \end{aligned} \tag{7.1}$$

where $C$ is the membrane capacitance, $I$ is the stimulus current, $E_i$ is the reversal potential for the current of type $i$ and $G_L$ is the conductance of the leakage current. The conductance through the sodium ($Na$) and potassium ($K$) channels is given by the product $G_i p_O^i$, where $G_i$ is the maximal conductance per ion channel of type $i$ and $p_O^i$ is the proportion of open channels of type $i$.

As previously described, the Hodgkin-Huxley model assumes that each sodium channel consists of three identical activation gates, $m$, and one inactivation gate, $h$, while the potassium channel has four identical gates, $n$. As discussed in Chapter 4 Section 4.1 constructing the stochastic model in terms of the individual gating variables leads to inaccuracies in the open channel statistics. Therefore the dynamics of the channel as a whole must be considered.

Letting each possible configuration of open and closed gates represent a different state of the channel, the dynamics of the sodium and potassium channels are given by the following state diagrams respectively:

$$\begin{array}{ccccccc} m_0h_0 & \underset{b_m}{\overset{3a_m}{\rightleftarrows}} & m_1h_0 & \underset{2b_m}{\overset{2a_m}{\rightleftarrows}} & m_2h_0 & \underset{3b_m}{\overset{a_m}{\rightleftarrows}} & m_3h_0 \\ b_h\uparrow\downarrow a_h & & b_h\uparrow\downarrow a_h & & b_h\uparrow\downarrow a_h & & b_h\uparrow\downarrow a_h \\ m_0h_1 & \underset{b_m}{\overset{3a_m}{\rightleftarrows}} & m_1h_1 & \underset{2b_m}{\overset{2a_m}{\rightleftarrows}} & m_2h_1 & \underset{3b_m}{\overset{a_m}{\rightleftarrows}} & m_3h_1 \end{array},$$

$$n_0 \underset{b_n}{\overset{4a_n}{\rightleftarrows}} n_1 \underset{2b_n}{\overset{3a_n}{\rightleftarrows}} n_2 \underset{3b_n}{\overset{2a_n}{\rightleftarrows}} n_3 \underset{4b_n}{\overset{a_n}{\rightleftarrows}} n_4\,,$$

where $a_i$ and $b_i$ are the closed to open and open to closed transition rates of gate of type $i$. The dynamics of the sodium and potassium channels can be described by the SDEs (4.5) and (4.6), respectively, from Chapter 4. We formulate the dynamics of the sodium and potassium channels in the Hodgkin-Huxley model using the two different SDE models described in the previous two chapters, the Wright-Fisher approximation and the reflected SDE. The MATLAB code used to simulate these models is freely available online in the ModelDB repository (http://senselab.med.yale.edu/modeldb/ListByModelName).

### 7.1.1 Reflected Stochastic Differential Equation

As in Chapter 4, let $y_{ij}(t)$ denote the proportion of sodium channels with $i$ open $m$ gates and $j$ open $h$ gates at time $t$. Similarly let $x_i(t)$ denote the proportion of open potassium channels with $i$ open $n$ gates at time $t$. The channel is assumed to be in the open state only when all gating variables are open and so $p_O^{Na} = y_{31}(t)$ and $p_O^K = x_4(t)$, respectively. The state of the potassium channel at time $t$ is given by the vector $\boldsymbol{x}(t) = (x_4, x_3, x_2, x_1, x_0)^T$ and the state of the sodium channel is denoted by $\boldsymbol{y}(t) = (y_{31}, y_{21}, y_{11}, y_{01}, y_{30}, y_{20}, y_{10}, y_{00})^T$. To ensure the stochastic dynamics of the sodium and potassium channels remain within a biologically realistic region, we incorporate the reflecting processes $\boldsymbol{K}_{Na}$ and $\boldsymbol{K}_K$ into (4.5) and (4.6), respectively, in the manner described in Chapter 6 Section 6.1.2 and so the dynamics of the sodium and potassium channels are given by the following reflected SDEs

$$d\boldsymbol{y} = H_{Na}\boldsymbol{y}dt + \tfrac{1}{\sqrt{N_{Na}}}E_{Na}F_{Na}(\boldsymbol{y})d\boldsymbol{W}_{Na} + d\boldsymbol{K}_{Na}, \tag{7.2}$$

$$d\boldsymbol{x} = H_K\boldsymbol{x}dt + \tfrac{1}{\sqrt{N_K}}E_KF_K(\boldsymbol{x})d\boldsymbol{W}_K + d\boldsymbol{K}_K. \tag{7.3}$$

The matrices $H_{Na}$, $E_{Na}$, $F_{Na}(\boldsymbol{y})$, $H_K$, $E_K$ and $F_K(\boldsymbol{x})$ are given in Section 4.1.2 of Chapter 4. In this chapter, the reflected SDEs above are solved numerically using the projection method

described in Chapter 6 Section 6.2 to obtain individual trajectories to (7.2) and (7.3).

### 7.1.2 Wright-Fisher Approximation

Let the vectors $\boldsymbol{y}(t)$ and $\boldsymbol{x}(t)$ be as in the previous section. Then the sodium and potassium channels in the Hodgkin-Huxley model can be approximated by the following Wright-Fisher type SDEs, respectively, using the method discussed in Chapter 5 Section 5.5.

$$d\boldsymbol{y} = H_{Na}\boldsymbol{y}dt + \sqrt{\tfrac{2}{N_{Na}-1}}E_{Na}G_{Na}(\boldsymbol{y})d\boldsymbol{W}_{Na}, \tag{7.4}$$

$$G_{Na}(\boldsymbol{y}) = diag\begin{pmatrix} \sqrt{(a_m+3b_m)y_{21}y_{31}} \\ \sqrt{2(a_m+b_m)y_{11}y_{22}} \\ \sqrt{(3a_m+b_m)y_{01}y_{11}} \\ \sqrt{(a_m+3b_m)y_{20}y_{30}} \\ \sqrt{2(a_m+b_m)y_{10}y_{20}} \\ \sqrt{(3a_m+b_m)y_{00}y_{10}} \\ \sqrt{(a_h+b_h)y_{00}y_{01}} \\ \sqrt{(a_h+b_h)y_{10}y_{11}} \\ \sqrt{(a_h+b_h)y_{20}y_{21}} \\ \sqrt{(a_h+b_h)y_{30}y_{31}} \end{pmatrix}$$

$$d\boldsymbol{x} = H_K\boldsymbol{x}dt + \sqrt{\tfrac{2}{N_K-1}}E_KG_K(\boldsymbol{x})d\boldsymbol{W}_K, \tag{7.5}$$

$$G_K(\boldsymbol{x}) = diag\begin{pmatrix} \sqrt{(a_n+4b_n)x_3x_4} \\ \sqrt{(2a_n+3b_n)x_2x_3} \\ \sqrt{(3a_n+2b_n)x_1x_2} \\ \sqrt{(4a_n+b_n)x_0x_1} \end{pmatrix},$$

where $E_{Na}$, $E_K$, $H_K$ and $H_{Na}$ are the same as in (7.2) and (7.3).

In this chapter (7.4) and (7.5) are solved numerically using the BISS method described in Chapter 5 Section 5.6 in order to obtain individual realisations of the stochastic ion channel dynamics in the Hodgkin-Huxley model. We note that the deterministic equation in the BISS method split is solved using the backward Euler method, rather than the forward Euler method. This should not affect the convergence of the scheme, since the backward Euler method still converges

with strong order 1, which is the only requirement on the deterministic solver in the split-step scheme.

The reason the backward Euler method is employed is so that we can obtain an $\epsilon$ such that even if the solution was to lie on the boundary of the domain at some point in time, the deterministic approximation would ensure the solution was pushed a distance $\epsilon$ away from this boundary. Unlike the systems used as examples in Chapter 5, if the channel is in a certain state it cannot transition to all other states in the system. This is the case for both the sodium and potassium channel in the Hodgkin-Huxley model. Therefore, in the forward Euler approximation, if the solution was to lie at one of the extreme boundaries, for example if $\boldsymbol{x} = [0, 0, 0, 0, 1]^T$ for the potassium channel, then no matter what $\epsilon$ is chosen, the forward Euler approximation will not be able to push $x_1$, $x_2$ and $x_3$ a distance of $\epsilon$ away from the boundary. However, using the backward Euler approximation, then such an $\epsilon$ can be found.

### 7.1.3 Steady-State Stochastic Differential Equation Model

In the simulations of the action potential (AP) we also compare the SDE method given in (Goldwyn et al., 2011), to the reflected SDE and Wright-Fisher approximation. These simulations are performed using a variant of the Hodgkin-Huxley model that includes a sodium current but no potassium current (see Appendix A Section A.2). The authors in (Goldwyn et al., 2011), use the SDE without reflection, where the noise term in the SDE is formulated as in the original derivation by Fox and Lu (1994), and so involves the square root of a matrix. That is, the dynamics of the sodium channel in (Goldwyn et al., 2011) is described by the following SDE

$$d\boldsymbol{y} = H_{Na}\boldsymbol{y}dt + \tfrac{1}{\sqrt{N_{Na}}}\sqrt{B(\boldsymbol{y})}dW_{Na}, \tag{7.6}$$

where $H_{Na}$ is the same as in (7.2).

To ensure numerical solutions to (7.6) remain real, the values $y_{ij}$ in the matrix $B(\boldsymbol{y})$ are replaced by their equilibrium values, and so this term is independent of the state of the system. The matrix

$B$ therefore takes the following form,

$$B = \begin{pmatrix} f_1+f_{10} & -f_1 & 0 & 0 & -f_{10} & 0 & 0 & 0 \\ -f_1 & f_1+f_2+f_9 & -f_2 & 0 & 0 & -f_9 & 0 & 0 \\ 0 & -f_2 & f_2+f_3+f_8 & -f_3 & 0 & 0 & -f_8 & 0 \\ 0 & 0 & -f_3 & f_3+f_7 & 0 & 0 & 0 & -f_7 \\ -f_{10} & 0 & 0 & 0 & f_4+f_{10} & -f_4 & 0 & 0 \\ 0 & -f_9 & 0 & 0 & -f_4 & f_4+f_5+f_9 & -f_5 & 0 \\ 0 & 0 & -f_8 & 0 & 0 & -f_5 & f_5+f_6+f_8 & -f_6 \\ 0 & 0 & 0 & -f_7 & 0 & 0 & -f_6 & f_6+f_7 \end{pmatrix},$$

where

$$f_1 = a_m\bar{y}_{21} + 3b_m\bar{y}_{31}, \quad f_2 = 2a_m\bar{y}_{11} + 2b_m\bar{y}_{22},$$

$$f_3 = 3a_m\bar{y}_{01} + b_m\bar{y}_{11}, \quad f_4 = a_m\bar{y}_{20} + 3b_m\bar{y}_{30},$$

$$f_5 = 2a_m\bar{y}_{10} + 2b_m\bar{y}_{20}, \quad f_6 = 3a_m\bar{y}_{00} + b_m\bar{y}_{10},$$

$$f_7 = a_h\bar{y}_{00} + b_h\bar{y}_{01}, \quad f_8 = a_h\bar{y}_{10} + b_h\bar{y}_{11},$$

$$f_9 = a_h\bar{y}_{20} + b_h\bar{y}_{21}, \quad f_{10} = a_h\bar{y}_{30} + b_h\bar{y}_{31},$$

and

$$\bar{y}_{ij} = \binom{3}{i} \frac{a_m^i b_m^{3-i} a_h^j b_h^{1-j}}{(a_m+b_m)^3(a_h+b_h)}. \tag{7.7}$$

When discussing the results we shall refer to this approach as the steady-state SDE method for simplicity.

### 7.1.4 Discrete-State Markov Chain Model Simulations

Individual trajectories of the discrete-state stochastic model are simulated using the stochastic simulation algorithm (SSA), (Gillespie, 1977), (see Chapter 3 Section 3.2.3). The results of these simulations provide the bench mark for comparison to the reflected SDE, approximate Wright-Fisher model and steady-state SDE method. The SSA method is typically taken to be the 'gold-standard' stochastic simulation approach in the literature and so we use this method in comparisons to remain consistent with the previous literature in this field.

## 7.2 Open Channel Statistics

### 7.2.1 Fixed Voltage

We calculated the mean and standard deviation in the proportion of open sodium and potassium channels in the original Hodgkin-Huxley model, as given by (A.1) in Appendix A. For these simulations, the transition rates are taken to be the functions of the membrane potential, $V$, given by equations (A.4) to (A.6) in Appendix A.

The mean and standard deviation were calculated over $100,000$ simulations and initially the voltage was kept constant throughout the simulation. Each simulation was run for a total of $100ms$, with the mean and standard deviation calculated at the final time point. The open channel statistics were calculated in this way for a range of different voltage values. Figure 7.1 shows the distribution in the number of open sodium and potassium channels at the final simulation time point, where the voltage is set to $28mV$ (this value has been chosen arbitrarily). In Figure 7.2 the mean and standard deviation in the proportion of open channels is plotted as a function of voltage, for the SSA, reflected SDE and approximate Wright-Fisher model. For these simulations the number of channels is set to $1000$. The difference between the mean and standard deviation calculated using the SSA and reflected SDE and also between the SSA and Wright-Fisher approximation, as a function of voltage are shown in Figure 7.3. Finally, we also considered the mean time, calculated over $100,000$ simulations, to simulate the sodium and potassium channel dynamics for a range of fixed voltage values and channel numbers, using the three different simulation methods, Figures 7.4 and 7.5.

**Figure 7.1** Distribution in the number of open sodium (top) and potassium (bottom) channels calculated using the reflected SDE (red line with closed circle markers), the SSA (blue bars) and the Wright-Fisher model (dotted green line with open circle markers) where the number of sodium channels is set to $1000$, the number of potassium channels is $333$ and the voltage is set to $28mV$.

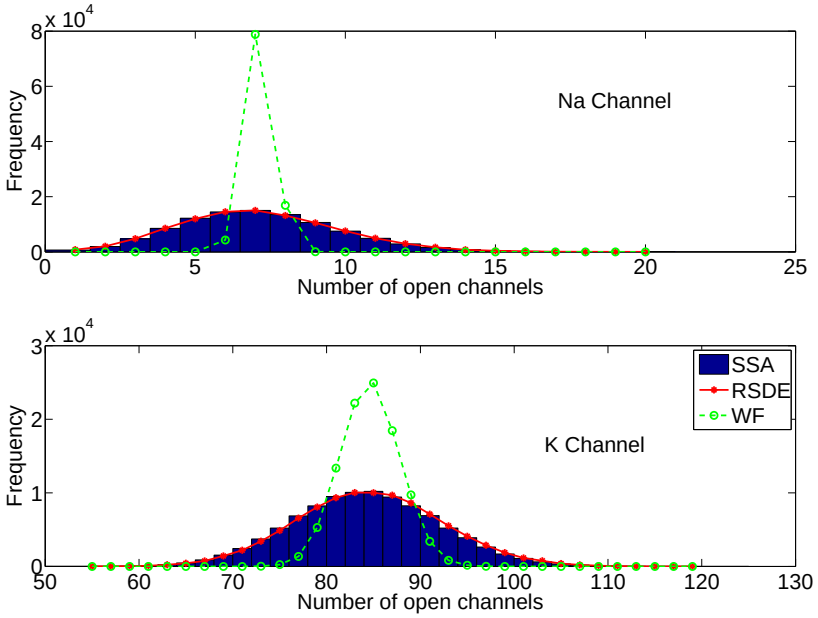

**Figure 7.2** Mean (left) and standard deviation (right) in the proportion of open sodium (top) and potassium (bottom) channels calculated using the reflected SDE (red line), the SSA (blue dotted line with stars) and the Wright-Fisher model (black dotted line with crosses). Statistics calculated over $100,000$ simulations at the final point for a fixed voltage value. In the reflected SDE simulations the initial condition for the sodium channel is taken to be $Y_0 = 1/8e^T$ and for the potassium channel it is $X_0 = 1/5e^T$, where $e$ is the unit vector. For the discrete-state Markov model the initial condition is calculated by multiplying $Y_0$ and $X_0$ by the number of sodium or potassium channels respectively, and rounding to the nearest whole number. The total number of sodium and potassium channels is set to $1000$ and the time step to $\Delta_t = 0.01ms$.

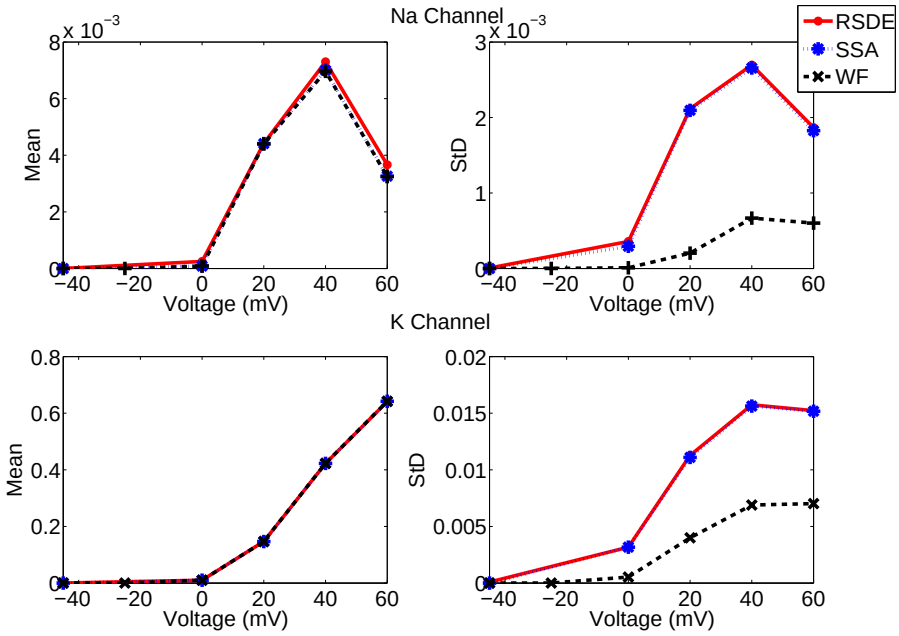

**Figure 7.3** Absolute difference in the mean (left) and standard deviation (right) in the proportion of open sodium (top) and potassium (bottom) channels between the reflected SDE and the SSA (red solid line) and between the SSA and Wright-Fisher approximation (black dot line with crosses) where the total number of sodium and potassium channels is set to $1000$.

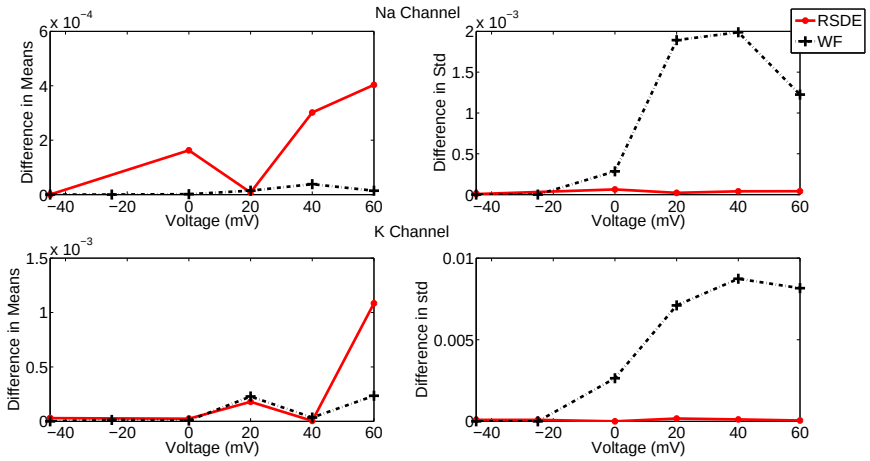


**Figure 7.4** Mean computational time (in seconds) calculated over $100,000$ simulations for the sodium channel in the Hodgkin-Huxley model where the voltage is kept fixed throughout simulation. Results are plotted as a function of number of channels. The voltage values used for each set of simulations are as follows, top left: $V = -45mV$, top right: $V = -25mV$, bottom left: $V = 0mV$, bottom right: $V = 20mV$. Each simulation is run for $10ms$, with time step $\Delta_t = 0.01ms$ and the initial condition is the same as in Figure 7.2.

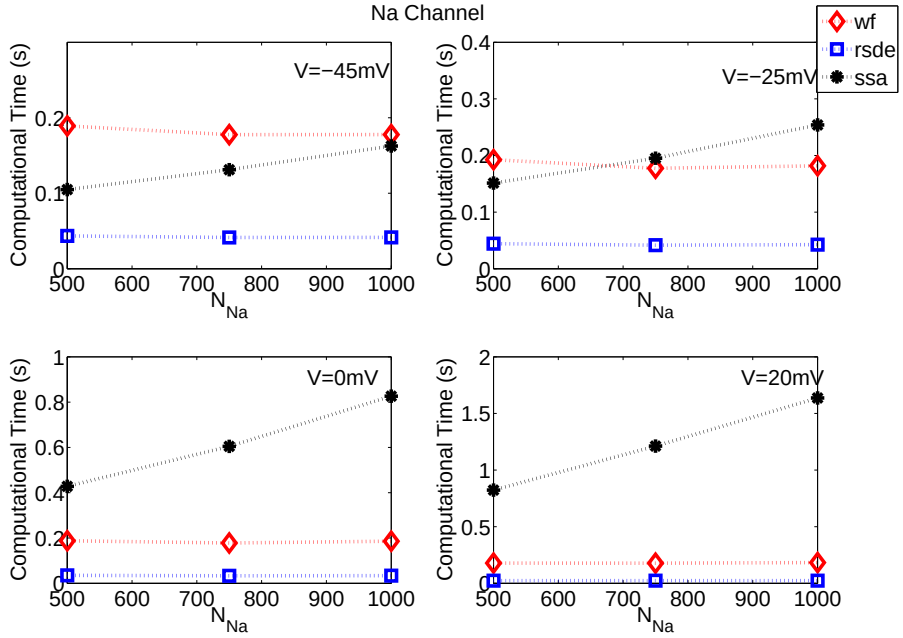

**Figure 7.5** Mean computational time (in seconds) calculated over $100,000$ simulations for the potassium channel in the Hodgkin-Huxley model where the voltage is kept fixed throughout simulation. Results are plotted as a function of number of channels. The voltage values used for each set of simulations are as follows, top left: $V = -45mV$, top right: $V = -25mV$, bottom left: $V = 0mV$, bottom right: $V = 20mV$. Each simulation is run for $10ms$, with time step $\Delta_t = 0.01ms$ and the initial condition is the same as in Figure 7.2.

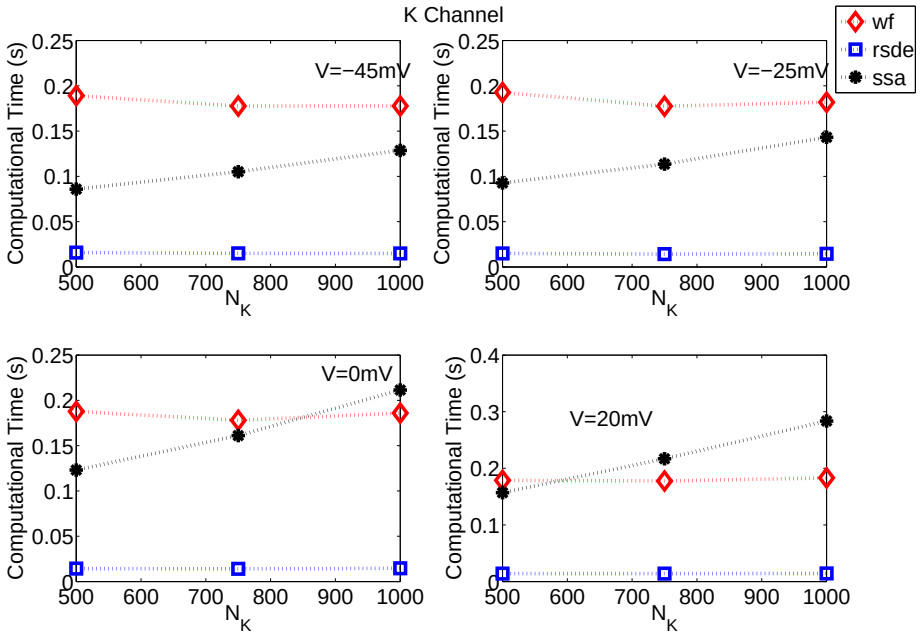


## 7.2.2 Varying Voltage

Next the open channel statistics were calculated for a fixed time course of the transmembrane potential i.e. the voltage. Initially the deterministic Hodgkin-Huxley model was solved over $10ms$ with stimulus current $I = 10pA$ to obtain a path for the voltage that varies through time, shown in Figure 7.6. This path was then used to simulate the dynamics of the sodium and potassium channels over $10ms$ and the open channel statistics were calculated over $100,000$ simulations. Figure 7.7 shows the mean and standard deviation in the number of open channels, as a function of time, where the number of channels is set to $1000$, for the SSA, reflected SDE and approximate Wright-Fisher model. The differences in the means and standard deviations between the SSA and reflected SDE and between the reflected SDE and the approximation

Wright-Fisher model, are plotted as a function of time in Figure 7.8, where the total number of channels is again set to $1000$.

**Figure 7.6** Time course of the transmembrane potential used to calculate the open channel statistics for the sodium and potassium channels, for varying voltage simulations.

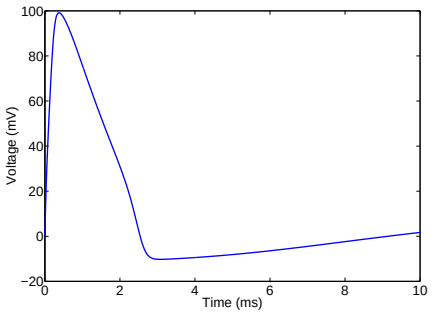


**Figure 7.7** Mean (left) and standard deviation (right) in the proportion of open sodium (top) and potassium (bottom) channels calculated using the reflected SDE (blue dots), the SSA (red line) and Wright-Fisher approximation (black dots) for a set time course of the transmembrane potential. The initial condition is the steady state for $V = 0$ of the deterministic system and the number of channels is set to be $1000$.

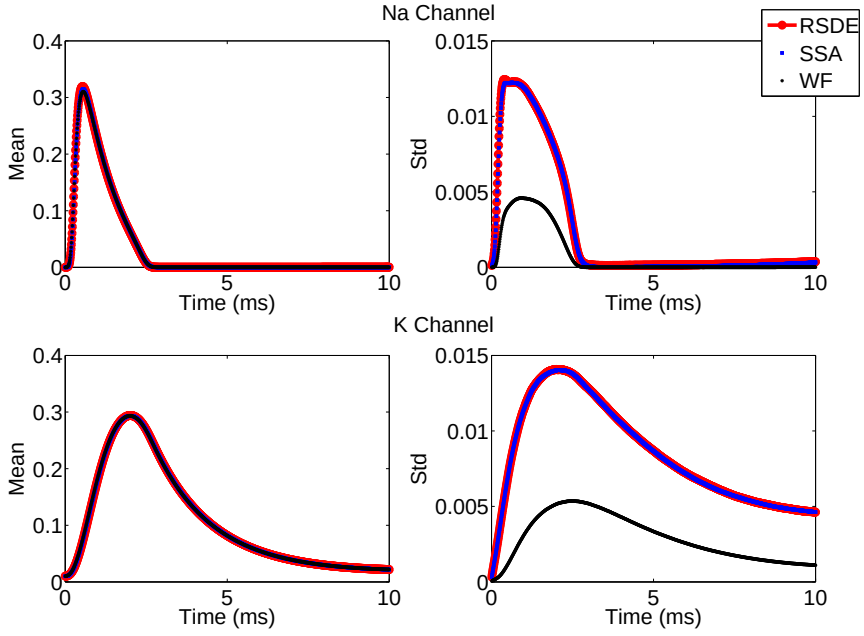

**Figure 7.8** Absolute difference in the mean (left) and standard deviation (right) in the proportion of open sodium (top) and potassium (bottom) channels between the reflected SDE and the SSA (red line with open circles) and between the SSA and Wright-Fisher approximation (black dots) for a fixed time course of the transmembrane potential. The number of channels is set to be 1000.

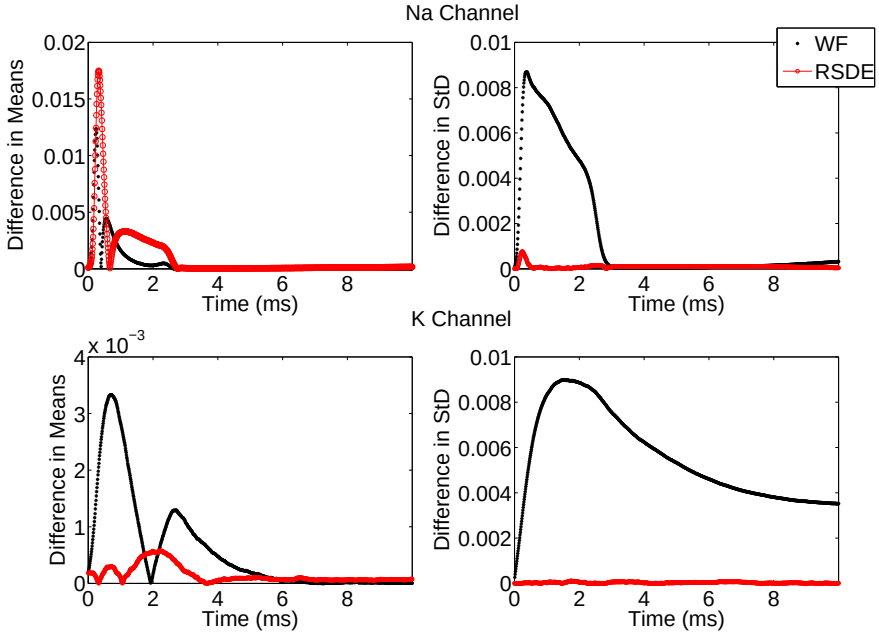

## 7.3 Computational Efficiency

For the original Hodgkin-Huxley model, given by equation (A.1) to (A.6) in Appendix A, we incorporated stochasticity into the sodium channel using only the reflected SDE and discrete-state Markov chain approach, which was again simulated using the SSA. The dynamics of the potassium channel are described using the deterministic ODE given by equation (A.3) in Appendix A. We simulated the full Hodgkin-Huxley model over $10ms$ with a time step of $0.01ms$ and took the mean computational time over $10,000$ simulations. Simulations were performed in MATLAB on a 2.5GHz core Intel Core 2 processor. We did not include the Wright-Fisher method in these simulations since, as shall be discussed in Section 7.5, the results presented thus far suggest that in the simplest case, where the voltage remains fixed, the reflected SDE method greatly outperforms the Wright-Fisher approach in terms of computational speed, Figures 7.4 and 7.5. Indeed the Wright-Fisher model is more computationally costly than the SSA under certain conditions. Therefore, for this more computationally complex simulation protocol we did not think the Wright-Fisher approximation would outperform the reflected SDE method, based on the preliminary results for fixed voltages.

**Figure 7.9** Mean computational time in seconds over $10,000$ simulations of the stochastic Hodgkin-Huxley model, (A.1), over $10ms$ for the reflected SDE approach (red dots) and the SSA approach (blue stars) plotted as a function of the number of channels. The time step in the reflected SDE simulations is taken to be $0.01ms$. The number of sodium channels was set to $1000$. Simulations were performed in MATLAB on a 2.5GHz core Intel Core 2 processor.

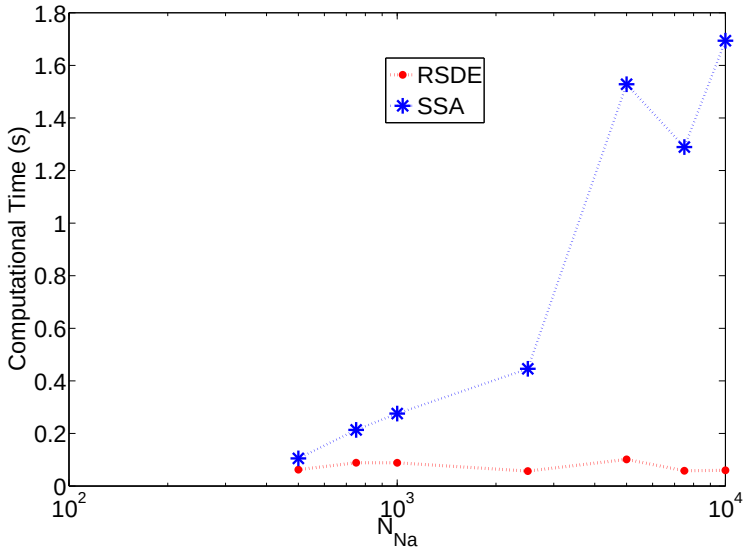


## 7.4 Action Potential Statistics in the Hodgkin-Huxley Model

The effect of incorporating the stochastic behaviour of ion channel dynamics into the Hodgkin-Huxley model on the membrane potential is to cause it to fire multiple times. This effect is quantified in the neuroscience community using a number of different measures which are collectively termed action potential (AP) statistics. We now define the AP statistics used for comparisons in this chapter, along with the simulation protocol employed to calculate these statistics.

### 7.4.1 Simulation Protocol

The comparison between the AP statistics calculated using the different continuous-state models and the discrete-state Markov chain approach is an extension of the simulations in (Bruce, 2009). In this study by Bruce, the effect of stochastic ion channel behaviour on the auditory

fibre, AP statistics were investigated as a function of the number of sodium channels ($N_{Na}$) using the metrics of the mean threshold current ($I_{th}$) and the relative spread (RS). The mean threshold current is the input current that corresponds to a firing efficiency (FE) of $50\%$, where FE is defined to be the fraction of trials in which the stimulus current results in the generation of an AP. It is calculated by fitting the FE versus input current curves using an integrated Gaussian function, as in (Verveen and Derksen, 1968). The relative spread (RS) is a measure of the relative noise level and is calculated as,

$$RS = \frac{\sigma}{I_{th}}, \tag{7.8}$$

where $\sigma$ is the standard deviation in threshold fluctuations and $I_{th}$ is the threshold current. Since the examination of the AP statistics is based on the work of Bruce (2009), we use the same equations as in this study in order to conduct these simulations, rather than using the classical Hodgkin-Huxley model that was used to calculate the open channel statistics. The membrane potential, $V$, for this model is described by the ODE (A.10) in Appendix A, which is variant of the original Hodgkin-Huxley model. For the reflected SDE, the Wright-Fisher approximation and the steady-state SDE, the value for $N_{Na}^{O}$ in (A.10) is obtained by multiplying the proportion of open channels (from the SDE solution) by the total number of channels and rounding to the nearest integer. We employ this method of rounding since the work of Bruce (2007) suggested that this is more accurate than either rounding up or down.

The AP statistics were calculated over $1000$ repetitions of a single $100\mu s$ monophasic depolarising current pulse. That is, for the first $0.1s$ of simulation, a stimulus current was applied (i.e. the term $I$ is (A.10) is non zero) and for the remainder of the simulation the stimulus current is set to $0$. Each repetition was simulated for a total of $2s$. The stimulus current amplitude ranged from $16pA$ to $26pA$, and was kept fixed for each set of $1000$ repetitions. The equation for the membrane potential, (A.10), was solved using the Euler method with a time step $\Delta_t = 0.001s$. The stochastic dynamics of the sodium channel were simulated using the SSA, reflected SDE method and Wright-Fisher approximation, as in the previous section, and also using the steady-

state SDE method described in Section 7.1.3. The transition rates for the sodium channel are calculated according to the functions of $V$ given by (A.7) and (A.8) in Appendix A.

The threshold current $I_{th}$ and the relative spread $RS$ were calculated for sodium channel numbers ranging from $100$ to $10,000$. The effect of varying the total number of channels was considered for two different cases: constant channel density and constant membrane area. As described in (Rubinstein, 1995), the membrane area is scaled proportionally to the number of channels in the case of constant channel density. Assuming the model's capacitance and resistance are based on 1000 sodium channels, as in (Bruce, 2009), in the constant channel density simulations these values will be scaled by the total number of sodium channels $N_{Na}$ (ranging from $100$ to $10,000$) as follows

$$C_m = 0.0714 \times \frac{N_{Na}}{1000} pF, \;\; R_m = 1953.49 \times \frac{1000}{N_{Na}} M\Omega.$$

For constant membrane area the capacitance and resistance are independent of $N_{Na}$ and so are taken to be $C_m = 0.0714pF$ and $R_m = 1953.49M\Omega$ for all values of $N_{Na}$, as in (Bruce, 2009). These parameter values have been chosen to ensure consistency with the simulations in the study by Bruce (Bruce, 2009). We remark that there is natural variability in parameter values between cells, but we do not consider the effects of extrinsic noise here and results are based solely on the values given here. For more details of the simulation protocol used to calculate the AP statistics see (Bruce, 2009) and the MATLAB code [1] therein. In Figure 7.10 the RS and threshold current, calculated using the four different methods, are plotted as a function of the number of channels for the constant area and constant density scaling protocols. Figure 7.11 shows the difference in the RS between the SSA and reflected SDE, the SSA and steady-state SDE method and between the SSA and Wright-Fisher approximation as a function of the number of channels, for constant density and constant area.

[1] http://www.ece.mcmaster.ca/ibruce/bruceevalFox/bruceevalFox.htm

**Figure 7.10** Threshold current (Ith) (top) and relative spread (RS) (bottom) as a function of the total number of sodium channels for constant channel density simulations (left) and constant membrane area simulations (right) calculated using the four different methods, SSA (green line with diamonds), reflected SDE method (red solid line), the steady-state SDE method from (Goldwyn et al., 2011) (blue dotted line with circles) and the Wright-Fisher approximation (black dotted line with crosses).

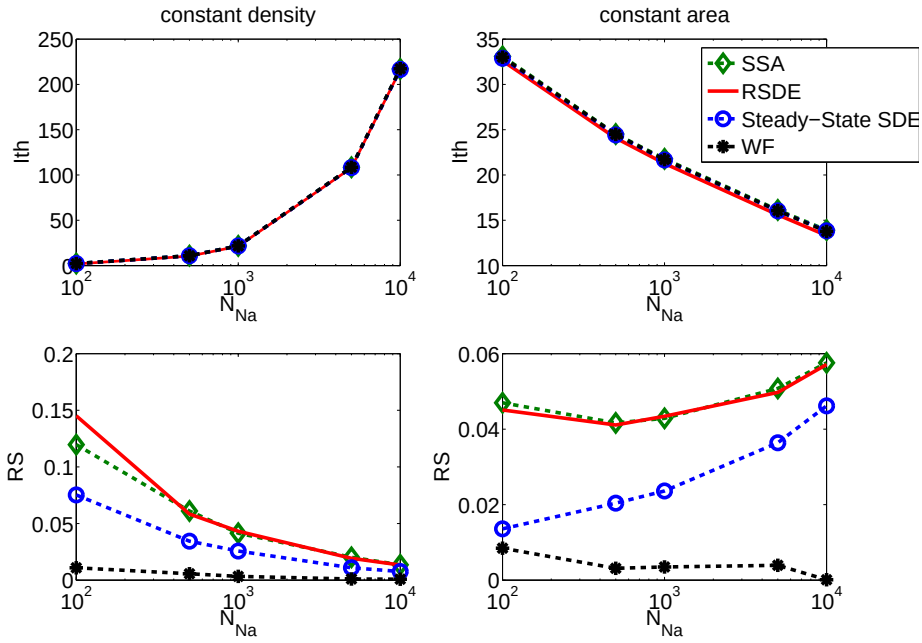

**Figure 7.11** Absolute differences in the relative spread (RS) between the SSA and reflected SDE methods (red line), between the SSA and Wright-Fisher approximation and between the SSA (black dashed line with circles) and steady-state SDE methods (blue dashed line with circle). Results shown as a function of number of channels for constant channel density simulations (left) and constant membrane area simulations (right).

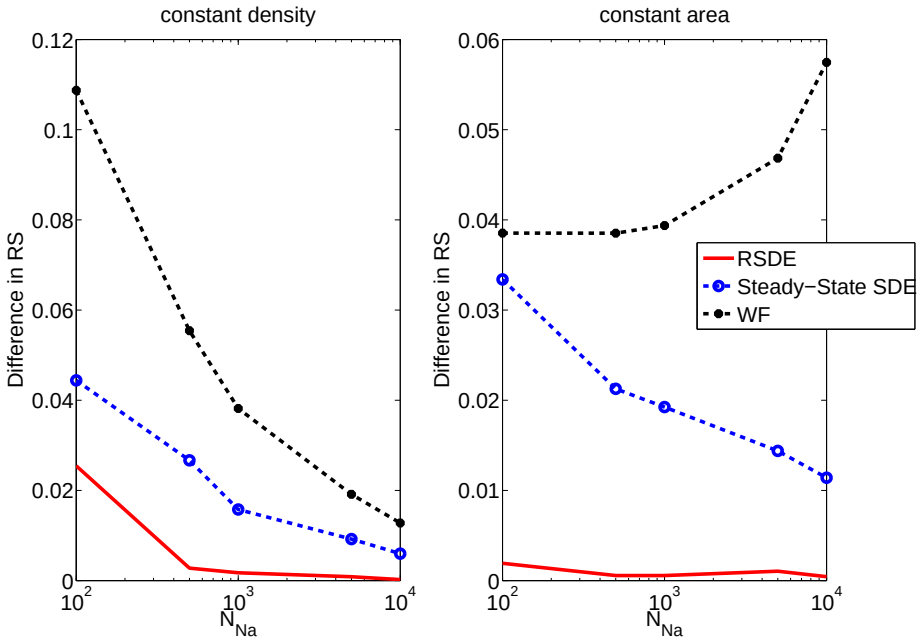

## 7.5 Results

### 7.5.1 Open channel statistics

#### Fixed Voltage

When the voltage is kept fixed, the mean and standard deviation obtained using the reflected SDE is very close to that of the SSA for both the sodium and potassium channels, Figure 7.2. In particular, the difference between the two means is on the order of $10^{-3}$, Figure 7.3. These quantitative results suggest that the reflected SDE accurately captures the distributional properties of the discrete-state Markov chain model. Furthermore, Figure 7.1 qualitatively shows that the distribution in the number of open sodium and potassium channels for the reflected SDE is very similar to that of the discrete-state Markov chain.

On the other hand, while the Wright-Fisher model accurately captures the mean of the discrete-state Markov chain model, it underestimates the standard deviation, Figure 7.2. In particular, the difference between the standard deviation approximated using the Wright-Fisher model and that calculated from the SSA is greater than the difference between the reflected SDE and the SSA, Figure 7.3. This difference is particularly noticeable for larger values of the voltage and for $V = 60mV$ the difference between the Wright-Fisher model and SSA is nearly an order of magnitude larger than the difference between the reflected SDE and SSA.

The computational efficiency of the reflected SDE is much greater than the Wright-Fisher approach, for all voltage values simulated and for both the sodium and potassium channel, Figures 7.4 and 7.5. In fact, for $V = -45mV$ the SSA is actually faster than the Wright-Fisher approach in simulating the stochastic dynamics of the sodium channel, and similarly for the potassium channel when $V = -45mV$, $V = -25mV$ and $V = 0mV$ the Wright-Fisher model is the slowest out of the three methods.

**Varying Voltage**

For a set time course of the transmembrane potential, the reflected SDE still closely matches the mean and standard deviation of the SSA simulations, Figure 7.7. In particular, the difference in the means between the reflected SDE and SSA methods is on the order of $10^{-2}$ for the sodium channel and $10^{-3}$ for the potassium channel. We note that for the comparison of the means in Figure 7.7 it is difficult to distinguish between the three different methods.

As was the case for the fixed voltage simulations, the Wright-Fisher model accurately captures the mean of the SSA simulations, but underestimates the standard deviation in the proportion of open sodium and potassium channels, Figure 7.7. The difference between the standard deviation calculated using the Wright-Fisher model and the SSA is again much greater than the difference between the SSA and the reflected SDE, Figure 7.8.

### 7.5.2 Computational Efficiency

Figure 7.9 shows that the simulation time for the reflected SDE is substantially faster than the SSA, particularly for large numbers of channels. In particular, the speed of the Markov chain model increases with increasing numbers of channels, while the reflected SDE method remains more or less constant.

### 7.5.3 Action Potential Statistics

From Figure 7.10 it can be seen that the relative spread (RS) calculated from the reflected SDE simulations is very close to that of the SSA simulations and the two values quickly converge as the number of channels increases. This is the case for both the constant channel density and constant membrane area simulations. On the other hand, the difference between the RS for the steady-state SDE and the SSA simulations is noticeable, even for large channel numbers, Figure 7.11. The RS calculated using the Wright-Fisher approximation is also markedly different to

that calculated from the SSA simulations, Figure 7.10. Furthermore this difference does not decrease with increasing numbers of channels, Figure 7.11. Indeed the difference between the Wright-Fisher model and the SSA is much greater than that between the reflected SDE and SSA, Figure 7.11.

## 7.6 Discussion

### 7.6.1 Open channel statistics

#### Fixed Voltage

Figures 7.1, 7.2 and 7.3 show that the reflected SDE accurately captures the stochastic dynamics of the discrete-state Markov chain model when the voltage is kept constant. On the other hand the Wright-Fisher model does not seem to preserve the statistical properties of the discrete-state Markov chain model. This is because the Wright-Fisher model underestimates the standard deviation of the discrete-state Markov chain model, Figures 7.2, and the distribution in the number of open channels is qualitatively different from the discrete-state Markov chain model, Figure 7.1.

The effect on the probability distribution of approximating the dynamics by the Wright-Fisher model is to concentrate more of the probability mass towards the mean, thus reducing the standard deviation compared with the discrete-state Markov chain model, Figure 7.1. Thus, qualitatively the probability distribution for the Wright-Fisher model is noticeably different to that of the discrete-state approach, unlike the reflected SDE method, as can be seen in Figure 7.1. When the voltage is lower, the mean of the distribution lies close to the boundary. Therefore, in such situations the distribution will have only one tail, and so the reduction of probability mass in the tails, which occurs for the Wright-Fisher simulations, will be less noticeable. This could provide a possible explanation as to why the difference in the standard deviation between the Wright-Fisher model and SSA simulations is smaller when the voltage is small, Figure 7.2.

We note that in the left hand plots of Figure 7.3, the difference in the means between the reflected SDE and the SSA is greater than the difference between the Wright-Fisher model and the SSA. There are two possible reasons why this might be the case. Firstly, the SDE model without reflection exactly captures the mean of the distribution of the discrete-state Markov chain model, due to the linearity of the transition rate functions. The manner by which the constants are chosen in the Wright-Fisher model ensures the mean agrees exactly with the SDE model without reflection. So it follows that the approximate Wright-Fisher model also precisely captures the mean of the discrete-state Markov chain. On the other hand, the reflecting process, $K(t)$, in the reflected SDE, is itself a stochastic process and so we would expect this process to have a non-zero mean. Since the solution to the reflected SDE is the solution to the SDE plus the reflecting process it is possible that the addition of this reflecting process may slightly alter the mean of the discrete-state Markov chain model. However, the simulations suggest that, if this is the case, the effect of the reflecting process is so small, since the differences in the means are on the order of $10^{-4}$ and $10^{-3}$, that the reflected SDE can still be considered to closely capture the stochastic behaviour of the discrete-state Markov chain model.

Since the differences between the reflected SDE and SSA methods are so very small, another possible explanation could lie with the numerical methods employed to simulate the reflected SDE and Wright-Fisher models. In Chapter 5 we provided numerical results suggesting the BISS method, used to approximate solutions to the Wright-Fisher model, converges with strong order $1/2$. On the other hand the projection method, used to numerically solve the reflected SDE, converges with slightly lower strong order, namely $1/2 - \epsilon$ for $\epsilon > 0$ (Chapter 6 Section 6.2). Therefore, if a higher strong order method had been used to numerically approximate solutions to the reflected SDE then the difference in the means between the reflected SDE and the SSA would probably be closer to the difference between the Wright-Fisher model and the SSA.

However, since the difference between the SSA and reflected SDE is so small and also the

reflected SDE is close to the standard deviation and open channel distribution obtained using the SSA, the reflected SDE captures the stochastic behaviour of the discrete-state Markov chain model more accurately than the Wright-Fisher approach when the voltage is kept constant.

The reflected SDE is clearly the most computationally efficient out of the three stochastic simulation methods, Figure 7.4. Indeed when $V = -45mV$ for the sodium channel and $V = -45mV, -25mV, 0mV$ for the potassium channel, the Wright-Fisher model is actually the most computationally costly simulation method. At each time step the control functions in the Wright-Fisher model need to be defined and this depends on how close to the domain boundaries the current state of the system lies. That is, we need to determine which region of the domain the solution at the previous time step lies, which for larger ion channel models can become quite computationally intensive. On the other hand, the reflected SDE method just employs the Euler-Maruyama method and the only further calculation is to check whether the point lies within the domain and if not perform an orthogonal projection, which involves minimal computational cost. Therefore, for this simple case where the voltage is kept fixed, the reflected SDE method is both more accurate and more computationally efficient than the Wright-Fisher approach.

**Varying Voltage**

Allowing the voltage to vary in simulations adds a further complication since the transition rates of the ion channel dynamics vary at each time step. Figures 7.7 and 7.8 show that even with this added complication, the reflected SDE still captures the stochastic dynamics of the discrete-state Markov chain more accurately than the Wright-Fisher model.

We note that the greatest difference between the standard deviation from the reflected SDE and the SSA occurs at the height of the AP, Figure 7.8, and is likely to happen here since this is where the greatest voltage change (and so the greatest change in channel transition rates) between consecutive time steps takes place. In additional simulations (not shown), where the

step-size was reduced, the greatest difference between the two statistics still occurred at the height of the AP, indicating that this effect is not a function of the time step.

### 7.6.2 Computational Efficiency

The reflected SDE method is more computationally efficient than the SSA at describing the stochastic behaviour of ion channels within an electrophysiology model, Figure 7.9. Furthermore the computational time for the reflected SDE does not grow with increasing channel number, as it does for the SSA method. This is because the computational cost of the reflected SDE is dependent on the step-size used in simulation, while the Markov chain model is restricted by the average time until the next reaction, which can become very small for large channel numbers.

We note that another advantage of the reflected SDE method is that simulations remain within a biologically realistic domain with probability $1$, by definition. On the other hand, in simulations of the original Hodgkin-Huxley model, using the same protocol as for the computational speed simulations, the steady-state SDE method from (Goldwyn et al., 2011) described in Section 7.1.3 resulted in negative solutions to the ion channel model a mean number of $352$ times. Therefore the reflected SDE method is computationally efficient, whilst ensuring solutions to the model are biologically realistic.

### 7.6.3 Action potential statistics

From Figure 7.10, it is clear that for the variant of Hodgkin-Huxley model used here to calculate the AP statistics, (A.10), the steady-state SDE model does not accurately capture the stochastic behaviour of the discrete-state Markov chain model. A possible explanation for this could be because the approximation made in the diffusion term, replacing the variables by their equilibrium value, may not be valid for the variant of the Hodgkin-Huxley model given by (A.10). The authors state in (Goldwyn et al., 2011) that this approximation is accurate if “the relaxation

of $V$ to its equilibrium value occurred on a much slower time scale than the relaxation of the gating variables" and furthermore they note that "this separation of time scales does not appear to be a generic feature of Hodgkin-Huxley models". Therefore for this particular model, the approximation made in the diffusion term of the SDE may not be accurate enough to calculate the AP statistics studied here.

However, in (Goldwyn et al., 2011) the authors show that this approximation accurately captures the mean open channel statistics as well as the mean and coefficient of variation of the interspike intervals in the classical Hodgkin-Huxley model. Therefore it seems that for certain models, the results from the steady-state SDE method in (Goldwyn et al., 2011) are comparable to the discrete-state Markov chain model, while for other models this method is less accurate than the reflected SDE. Thus, these results show that the reflected SDE model faithfully captures the stochastic dynamics of the discrete-state model for a wider class of models than the steady-state SDE method described in (Goldwyn et al., 2011).

Out of the three approximate stochastic simulation methods, namely the reflected SDE, the Wright-Fisher model and the steady-state SDE, the reflected SDE most closely captures the AP statistics for the discrete-state Markov chain model, Figures 7.10 and 7.11. Therefore, the reflected SDE most accurately captures the variability in the membrane potential within an electrophysiology model that arise due to the stochastic behaviour of the ion channels.

## 7.7 Chapter Summary

In this chapter we undertook a thorough comparison between the two continuous-state stochastic methods of ion channel dynamics developed in Chapter's 5 and 6, namely the reflected SDE and the approximate Wright-Fisher model, with the discrete-state Markov model of ion channel dynamics which is seen as the 'gold standard' method within the literature. We compared open channel statistics for the original Hodgkin-Huxley model as well as AP statistics for a variant

of this model. Furthermore, we showed that the reflected SDE model captures the discrete-state Markov model more accurately than an SDE method previously reported in the literature, which we call the steady-state SDE model.

Incorporating stochastic ion channel dynamics into existing electrophysiology models only introduces fluctuations into the ionic current, which arise due to the stochastic dynamics in the proportion of open channels. This in turn causes fluctuations in the AP dynamics. Since the reflected SDE and discrete-state Markov chain model agree in terms of open channel statistics, we would therefore expect this to follow through into agreement in the AP statistics. This was indeed the case with the AP statistics considered for a variant of the Hodgkin-Huxley model in Section 7.4. Therefore, the results presented in this chapter clearly show that the reflected SDE model accurately captures the stochastic dynamics of the discrete-state Markov model, whilst providing significant improvement in computationally efficiency. This method is employed in the next chapter to investigate the effects of stochastic ion channel behaviour in the Decker model of a canine ventricular myocyte (Decker et al., 2009).

# 8

# Role of Stochastic Ion Channel Dynamics in Beat-to-Beat Variability

*The previous four chapters have been devoted to the techniques needed to efficiently and accurately simulate the intrinsic stochastic behaviour of ion channel dynamics within electrophysiology cell models. In this chapter we implement these techniques to investigate the electrophysiological consequences of fluctuations in the repolarisation currents of canine ventricular myocytes using a combined experimental and computational approach. In order to account for extrinsic noise we first construct a population of deterministic models, where the behaviour of each model in the population lies within experimental range. For each model in the population we estimate the number of channels for the following currents: the rapid delayed rectifier potassium ($K^+$) current $I_{Kr}$, the slow delayed rectifier $K^+$ current, $I_{Ks}$, the transient outward $K^+$ current $I_{To1}$ and the L-type calcium ($Ca^{2+}$) current, $I_{CaL}$, using voltage-clamp experimental data and previously reported results from the literature. The intrinsic variability of these four repolarisation currents is modelled using the reflected SDE method described in Chapter 6 and employed in Chapter 7. Finally, we use the resulting population of stochastic models to investigate the effects of the intrinsic stochastic behaviour of $I_{Kr}$, $I_{Ks}$, $I_{To1}$ and $I_{CaL}$ channels on the beat-to-beat variability in the action potential duration (APD) of single cells. In*

*particular, we investigate the effect of this intrinsic stochasticity on the short term variability measure (STV), discussed in Chapter 2. To the best of our knowledge, no computational study has directly studied the effects of stochasticity on this particular measure. We do so here since, as previously discussed, it takes into account the consecutiveness of beats and is a potential predictor of proarrhythmic risk.*

## 8.1 Introduction

As discussed in Chapter 2, there is great variability both within and between individuals in the electrical dynamics of the heart. Variability between individuals means that different patients may react differently to drugs, or pathological conditions such as ischemia. Also, different cells of the same heart may respond differently to a given stimulus. Furthermore, the intrinsic stochastic nature of the processes involved in the generation of an action potential (AP) means that the same cell may exhibit different behaviour at different times, resulting in temporal beat-to-beat variability in repolarisation duration (BVR).

Experimental and clinical studies have suggested that such variability could provide insight into effectively identifying individuals with increased arrhythmic risk (Thomsen et al., 2006; Hinterseer et al., 2008, 2009, 2010). In recent years only a few computational studies have begun to investigate the effects of intrinsic noise on the AP (Pueyo et al., 2011; Lemay et al., 2011). In Pueyo et al. (2011) they found the stochastic behaviour of the slow delayed rectifier potassium current, $I_{Ks}$, caused significant BVR in guinea-pig and human ventricular myocytes using a combined computational and experimental approach. The authors also showed that smaller numbers of $I_{Ks}$ channels resulted in greater beat-to-beat variability in the AP. The AP is controlled by the dynamic interplay between a number of different ionic currents, and so it is likely that the stochastic behaviour of other ionic currents also contribute to BVR. Therefore a major limitation of the study by Pueyo et al. (2011) is that it does not allow for investigation into the contributions of different ionic currents to BVR, as well as the combined effect of the stochastic

behaviour of different ionic currents on BVR. On the other hand the stochastic behaviour of five ionic currents, namely the sodium current, $I_{Na}$, the slow and fast delayed rectifier potassium currents, $I_{Kr}$ and $I_{Ks}$, the inward rectifier potassium current, $I_{K1}$, and the L-type calcium current $I_{CaL}$ are considered in Lemay et al. (2011). They investigated the effects on BVR of the stochastic behaviour of each current individually as well as combined, and their results showed that beat-to-beat variability in the AP is primarily caused by $I_{Ks}$ and $I_{CaL}$ in single cells. However, a limitation of this study is that a purely computational approach is taken. Furthermore, for both studies they use a fixed parameter set and only vary the number of channels in each simulation. This means the conductance of each channel only varies with channel number, but the maximum conductance is determined by the model. Therefore, a limitation of both studies, (Pueyo et al., 2011; Lemay et al., 2011), is that they do not allow for investigation into how the effects of stochastic ion channel behaviour on BVR may be different in cells with different combinations of maximal conductances of the repolarisation currents. In this study we build on these previous works, considering the effects of intrinsic noise in multiple currents and use a combined computational and experimental approach to investigate the ramifications of such stochastic behaviour on the AP. Furthermore, we take into account cell-to-cell differences in ionic conductances by considering a population of models, each with a different set of conductance values, rather than a single model as in previous studies.

Based on previous experimental studies (Zaniboni et al., 2000), (Krogh-Madsen, 2004) we hypothesise that fluctuations in the four key repolarisation currents: the rapid delayed rectifier potassium ($K^+$) current ,$I_{Kr}$, the slow delayed rectifier $K^+$ current, $I_{Ks}$, the transient outward $K^+$ current, $I_{To1}$, and the L-type calcium ($Ca^{2+}$) current, $I_{CaL}$, caused by the stochastic dynamics of the ionic channels, contribute to the beat-to-beat variability in repolarisation duration (BVR) measured experimentally in canine ventricular myocytes under control conditions. Furthermore, we postulate that the stochastic behaviour of these currents also contribute to the change in BVR, caused by complete pharmacological block of $I_{Kr}$ or $I_{Ks}$. We speculate that

the stochastic behaviour of these four currents is important in BVR since these are the main ionic currents that drive and control this phase of the AP. Furthermore, we expect ionic currents with smaller channel numbers to contribute more to repolarisation variability than those with greater channel numbers. This is because smaller channel numbers lead to greater fluctuations in the ionic current, which we anticipate will manifest as greater variability in the AP duration (APD), as was found to be the case in (Pueyo et al., 2011).

The variability in repolarisation duration can be quantified in different ways, as discussed in Chapter 2 Section 2.3. Previous computational studies (Pueyo et al., 2011; Lemay et al., 2011) have focused on the variance in the APD to quantify BVR. The maximum and minimum, Pueyo et al. (2011), in the APD has also been used to evaluate repolarisation variability. In this study, we also employ the short-term-variability (STV) in APD measure, described in Chapter 2 Section sec:STV. While this measure is frequently used in experimental and clinical studies, to the best of our knowledge no computational study has directly linked the intrinsic stochastic behaviour of ion channel dynamics with this quantification of beat-to-beat variability. We use it in this study for two main reasons. Firstly it quantifies the variations between consecutive beats, which some have hypothesised to be an important factor in predicting arrhythmic risk (Hinterseer et al., 2008). Secondly this measure has been shown to be a potential biomarker for assessing an individual's vulnerability to arrhythmic events and the proarrhythmic potential of drugs (Thomsen et al., 2006; Hinterseer et al., 2010).

In previous studies, cell-to-cell variability (extrinsic noise) has been implemented by randomly generating the number of channels to be used in a particular simulation from a given distribution. In (Pueyo et al., 2011), the number of channels is assumed to follow a truncated Gaussian distribution, where the mean number of channels is estimated from experimental data. Whereas Lemay et al. (2011) assume a Poisson distribution with mean channel numbers estimated from the literature. This approach uses a fixed value for the maximum conductance of the channel, and so the magnitude of the current between simulations only varies with respect to the num-

ber of channels. However, as well as variations in the number of channels between different cells, there is also variability in the maximum conductance of the ionic channels, as a result of extrinsic noise. Since intrinsic and extrinsic noise are related, it is difficult to separate these two different effects within the experimental data. Therefore we consider the effects of both intrinsic and extrinsic noise in this study by constructing a population of deterministic models to capture cell-to-cell differences, and then incorporating the intrinsic stochastic behaviour of ion channels into each model.

Initially we construct a population of deterministic models where each model has the same structure for the equations but a unique set of conductance values for $I_{Kr}$, $I_{Ks}$, $I_{To1}$, $I_{CaL}$ and $I_{K1}$ (the time-independent potassium current). Furthermore, we ensure the APD values of all models in the population lie within experimental range both under control conditions and pharmacological block. From the conductance level in each model we then estimate the number of channels used in the stochastic simulations. Finally the stochastic behaviour of ion channels is incorporated into each model using the mathematical techniques developed in this thesis. Therefore we arrive at a population of stochastic models, each with a unique set of ionic conductance values and channel numbers, and where each model captures stochastic ion channel dynamics. The population of stochastic models approach is therefore advantageous since it allows us to investigate the effects of both extrinsic and intrinsic noise, both of which arise in the experimental data, on beat-to-beat variability in repolarisation and directly compare with experimental observations. To the best of our knowledge this is the first population of stochastic models to be constructed in this way.

## 8.2 Methods

We begin by constructing a population of **deterministic** models. Each model has the same structure, based on an existing cardiac model, but the conductance of the repolarisation currents are unique to each model in the population. The model structure is then altered in order to

describe the stochastic ion channel dynamics of $I_{Kr}$, $I_{Ks}$, $I_{To1}$ and $I_{CaL}$, and so we arrive at a population of **stochastic** models. In Figure 8.1 we describe in a flow diagram the main steps in the construction of the population of stochastic models, along with the experimental data used at each step.

The canine epicardial model by Decker et al. (Decker et al., 2009), provided the basic model structure for the population of models, since it is the most up-to-date electrophysiological model of the AP in a canine myocyte. This model is an extension of the earlier Hund-Rudy model (Hund and Rudy, 2004) and incorporates updated versions of the transient outward current ($I_{To1}$), the slow component of the delayed rectifier potassium current ($I_{Ks}$), the L-type calcium current ($I_{CaL}$) and the sodium potassium pump. Due to the complexity of the Decker model we do not give further details here. For a full description of the model the reader is referred to the original papers (Decker et al., 2009), (Hund and Rudy, 2004) as well as the authors website [1], where full MATLAB and C code is freely available.

We implement a refinement to the dynamics of $I_{CaL}$, as in (Pueyo et al., 2010) in the Decker model. Namely the steady state activation parameter for $I_{CaL}$ ($ACT_\infty$) is calculated as follows,

$$ACT_\infty = \frac{1}{(1+exp(-(V-15.3356)/10.7558))\,((1+exp(-(V+12.8824)/2.1957)))}. \tag{8.1}$$

This change has been made to ensure agreement in the morphology of the AP between simulation and experiments when $I_{CaL}$ undergoes complete pharmacological block.

[1] www.rudylab.wustl.edu/research/cell/code/AllCodes

**Figure 8.1** Diagram of the steps involved in the construction of the population of stochastic models.

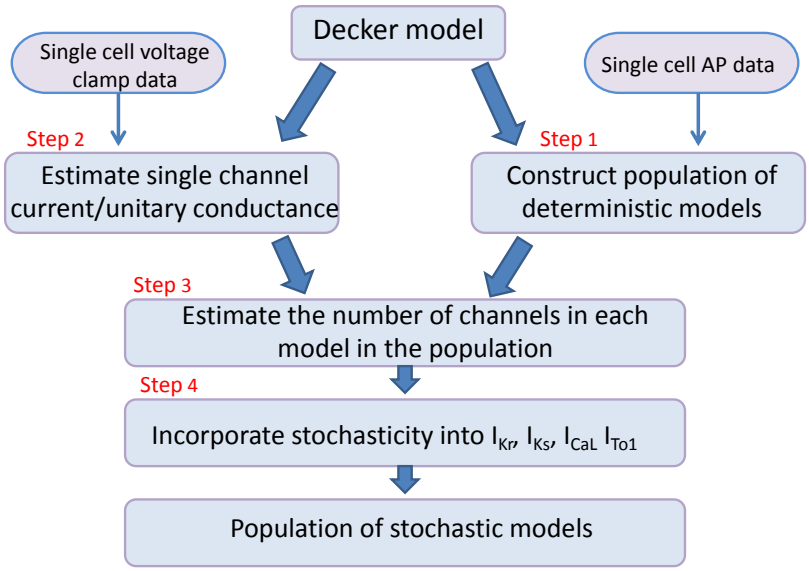


We describe in greater detail each of the main stages in the construction of the population of stochastic models, as well as the experimental methods and simulation protocols used in this study.

### 8.2.1 Construction of the Population of Deterministic Models

Experimental observations are affected by both intrinsic and extrinsic noise, and so it is difficult to separate the variability due to the intrinsic stochastic behaviour of ion channel dynamics from the variations caused by cell-to-cell differences in conductance levels within the experimental results. Our aim is to compare the results from the stochastic model with those obtained experimentally and so the effects of cell-to-cell differences must be represented within the model as well as the intrinsic stochastic behaviour of ion channels. Therefore, instead of using one model that is tied to a single parameter set we construct a population of models, each with a unique set of ionic conductances. This population therefore takes into account the effects of extrinsic and intrinsic noise, both of which contribute to the beat-to-beat variability observed in individual

experimental traces as well as differences between traces.

To construct the deterministic population of models (step $1$ in the flow chart in Figure 8.1), the current equations for $I_{Kr}$, $I_{Ks}$, $I_{To1}$ and $I_{CaL}$ in the Decker model were multiplied by a scaling factor $\rho$. Out of all possible combinations of different scaling factors, which we refer to as the scaling space, a sample from this space was obtained using a grid based sampling method. In this way we obtain an initial population of 'potential' deterministic models.

In brief, the grid based sampling approach taken is as follows. The scaling factor of each current was varied simultaneously over a given range for each current. For $I_{Ks}$, $I_{CaL}$ and $I_{To1}$ this range was $[0.5, 1.5]$ and was chosen in order to allow for both a $50\%$ decrease and increase in maximal conductance of these currents. For $I_{Kr}$ the range was set to be $[0.2, 1]$, since upon block of the $I_{Kr}$ current, the original Decker model produced an increase in the APD that was greater than the maximum increase in APD from experiments, suggesting the conductance of $I_{Kr}$ is much greater than that observed in experiments. Therefore we did not increase the conductance of this current and furthermore reduced $I_{Kr}$ more than the other three currents. We also found that block of $I_{K1}$ in the Decker model produced a smaller increase in APD than the minimum increase observed experimentally, suggesting that $I_{K1}$ conductance is lower in the Decker model than in the experimental results. Therefore, we found that $I_{K1}$ also needed to be rescaled in order to ensure that there was overlap between the APD of the population of 'potential' models and the experimental data. For this current we only increased the conductance of this current by up to $80\%$, and so the scaling range was $[1, 1.8]$.

Therefore we obtain a five-dimensional hypercube which represents the space of different scaling factors over which we want to sample. Each scaling interval is then further divided into five equally spaced subintervals, that is the five-dimensional hypercube is subdivided into five smaller five-dimensional hypercubes of equal size. Within each one of these smaller hypercubes a point is picked at random to provide a scaling factor for each current. More precisely, within a given hypercube this point is obtained by first generating five uniformly distributed random

numbers. Each of these is assigned to one of the edges of the hypercube, which represent one of the five scaling factors. For a given interval (edge of the hypercube), the random number is multiplied by the length of the interval and the minimum of the interval is added to obtain a value for that scaling factor. This is done independently for each of the five scaling factors. In this way we obtain a discrete set of scaling values that is representative of the space of possible scaling factors.

Note that since we only consider scaling five currents, we are able to use this simple method to obtain a representative sample, without the problem becoming computational infeasible. However, if more currents or parameters within the model were allowed to vary, then more sophisticated sampling methods, such as the Latin Hypercube method (McKay et al., 1979), would need to be employed to obtain a representative sample of the scaling space (Britton et al., 2012). We do not provide further detail of such methods here, since this thesis is primarily concerned with modelling intrinsic variability and we refer the interested reader to (Gy, 1992).

Throughout this study we use the APD at $90$% repolarisation, $APD_{90}$, to compare between experimental and simulated results because it is the main biomarker for repolarisation. For each model the $APD_{90}$ is calculated under control conditions and pharmacological block, and the change in $APD_{90}$ due to block of the currents is also calculated. If all these $APD_{90}$ values do not lie within experimental range then the model rejected from the population. Therefore, the $APD_{90}$ and change in $APD_{90}$ as a result of current block in each of the models within the final population lie within experimental range. The experimental range was taken to be the maximum and minimum reported $APD_{90}$ values from experiments under each set of conditions.

### 8.2.2 Simulation Protocol for the Population of Deterministic Models

Each model in the potential population was simulated for $50$ beats at a basic cycle length of $1000$ ms under the following conditions: control conditions (no currents blocked), complete $I_{Kr}$ block, complete $I_{Ks}$ block, $95$% block of $I_{CaL}$ and complete block of $I_{Ks}$ combined with $90$%

block of $I_{To1}$. $X\%$ block of a current was simulated by multiplying that current by $1 - X/100$. The deterministic simulations and the grid based sampling was carried out by a PhD student, Oliver Britton from the Department of Computer Science, University of Oxford.

For each scaling set (i.e. each model in the population) the following were calculated from the simulations: $APD_{90}$ under control conditions, $APD_{90}$ after drug block, absolute change in $APD_{90}$ as a result of drug block. Due to the variability in the $APD_{90}$ between successive beats in the experimental recordings, the mean $APD_{90}$ over the last five beats was taken in order to construct the population of deterministic models. Therefore, in the deterministic simulations the mean in the $APD_{90}$ over the last five beats was calculated to ensure conformity in comparisons with experimental results.

### 8.2.3 Noise Analysis

We estimate single channel current values for $I_{Ks}$ and $I_{CaL}$ from experimental macroscopic current traces obtained from voltage clamp experiments using the whole cell configuration of the patch clamp technique (step $2$ in the flow chart in Figure 8.1). To obtain such estimates the open channel probability was first approximated for each current using nonstationary noise analysis. While nonstationary noise analysis also provides estimates for the number of channels and the single channel current, some studies suggest that such estimates are not reliable without imposing constraints on the estimated variables (Lingle, 2006). Therefore stationary analysis is then applied to obtain an estimate for single channel current. This approach of using a combination of non-stationary and stationary fluctuation analysis is described in (Pueyo et al., 2011), and this part of the work was carried out in collaboration with Dr Esther Pueyo from the Universidad de Zaragoza.

Experimental $I_{Ks}$ traces were measured in canine ventricular myocytes after applying $500ms$ long depolarizing voltage pulses from $-40mV$ to test potentials ranging from $-20mV$ to $50mV$, where the change in voltage over this range was $10mV$ (Szabó et al., 2007; Szen-

tandrássy et al., 2011). Similarly $I_{CaL}$ traces were measured after applying a $400ms$ long pulse from $-40mV$ to test potentials ranging from $-15mV$ to $0mV$, where the change in voltage over this range was $5mV$. For each test potential, seven experimental traces were used to perform the fluctuation analysis. The ensemble mean and variance of each set of current traces was calculated once the current had reached steady-state. Using nonstationary analysis (as described in Chapter 2 Section 2.6) the mean and variance corresponding to the different test potentials for $I_{Ks}$ and $I_{CaL}$ were fit to the following equation

$$\sigma_x^2 = m_x i_x - m_x^2/N_x, \tag{8.2}$$

where $i_x$ is the single channel current, $N_x$ is the number of channels and $m_x$ and $\sigma_x^2$ are the mean and variance in the macroscopic current for $x = Ks,\ CaL$. This fitting was done using the inbuilt *fmincon* function in MATLAB. The resulting function is plotted in Appendix B along with the mean and variance for the experimental current traces at different test potentials. The estimates obtained for $N_{Ks}$, $N_{CaL}$, $i_{Ks}$ and $i_{CaL}$ were then used to calculate the open probability for each test potential, $p_{Ks}^V$, $p_{CaL}^V$, using the following formula

$$p_x^V = m_x^V/(i_x N_x), \tag{8.3}$$

for $x = Ks,\ CaL$, where $m_x^V$ is the mean macroscopic current for test potential $V$.

The current traces for the test potential at which the estimated open probability was maximal were used for stationary analysis. For $I_{Ks}$ this was $50mV$ and for $I_{CaL}$ it was $-10mV$. For this specific voltage, the estimates for the mean open probability for each channel, $p_{Ks}$, $p_{CaL}$, were used. The power spectral densities (PSDs) of the mean-subtracted current traces for $I_{Ks}$ and $I_{CaL}$, respectively were calculated once steady-state had been reached. The single channel current for $I_{Ks}$, $i_{Ks}$, was evaluated as the integral over the averaged PSD divided by the product of the time-averaged mean current and $1 - p_{Ks}^{50}$, (Pueyo et al., 2011). The single channel current for $I_{CaL}$, $i_{CaL}$, was calculated analogously. The mean open probabilities used to estimate the single channel current, $p_{Ks}^{50}$ and $p_{CaL}^{-10}$, are the estimated values obtained from the non-stationary

fluctuation analysis. The spectrum plot showing the results of the stationary analysis is given in Appendix B.

### 8.2.4 Estimating the Number of Channels

The number of $I_{Ks}$ and $I_{CaL}$ channels in each model was estimated as follows (step $3$ in the flow chart in Figure 8.1). For each model in the population of deterministic models, $I_{Ks}$ and $I_{CaL}$ traces were simulated using the same voltage clamp protocol as in experiments. $I_{Ks}$ was calculated for a voltage step of $50$ mV, while for $I_{CaL}$ the voltage step was $-10$mV, which correspond to the voltage values when the estimated open probability of each channel type was maximal. The macroscopic current, $I_{Ks}$ and $I_{CaL}$, and channel open probability, $p_{Ks}$, $p_{CaL}$, was calculated at the end of the simulated time interval. The number of channels was then calculated using the following relation

$$N_x = I_x/(i_x p_x),$$

for $x = Ks,\ CaL$ where $i_x$ is the single channel current estimate from the fluctuation analysis and $I_x$ and $p_x$ are respectively the total ionic current and the proportion of channels in the open state from the final time point in the simulation of the deterministic model.

The number of $I_{To1}$ and $I_{Kr}$ channels are estimated using unitary conductance values from the literature. No such values for either current could be obtained for dog from the literature. Therefore for $I_{Kr}$ we used the unitary conductance value of $2.5335\,pS$ for human ventricular myocytes given in (Veldkamp et al., 1995), which is similar to values reported in other species; $2.2768\,pS$ in mouse ventricular myocytes (Xin et al., 2004), $2.4856\,pS$ in rabbit ventricular myocytes (Veldkamp et al., 1993) and $1.8974\,pS$ for guinea pig atrial myocytes (Shibasaki, 1987) (all values given for an extracellular potassium concentration of $5.4\,mM$). For $I_{To}$ the unitary conductance value of $5.0912\,pS$ for rabbit ventricular myocytes reported in (Fedida and Giles, 1991) (value given for an extracellular potassium concentration of $5.4mM$) was used. The maximal conductance value for each model in the population was divided by the unitary

conductance from the literature to obtain an estimate for the number of $I_{To1}$ and $I_{Kr}$ channels in each model.

### 8.2.5 Population of Stochastic Models

We modified the equations in the Decker model that describe the dynamics of the following repolarisation currents $I_{Ks}$, $I_{CaL}$, $I_{Kr}$ and $I_{To1}$ to include the intrinsic stochastic behaviour of these channels (step $4$ in the flow chart in Figure 8.1). This same modification was made to each of the models within the population of deterministic models. The Decker model describes the kinetics of $I_{Ks}$ and $I_{CaL}$ using a Markov formulation according to the state diagrams given in Figures 8.2 and 8.3, respectively. $I_{Ks}$ is assumed to possess two distinct open states ($O_1$ and $O_2$), as is $I_{CaL}$ ($O$ and $O^{\star}$). The kinetics of the remaining time dependent ionic currents are described using the classical Hodgkin-Huxley formulation.

Since $I_{Ks}$ and $I_{CaL}$ are described using a Markov formulation in the Decker model, we construct the stochastic model for these channels based on their respective kinetic diagrams, given in Figures 8.2 and 8.3, in terms of a reflected SDE, as described in Chapter 6.

**Figure 8.2** State diagram of the $I_{Ks}$ dynamics in the Decker model.

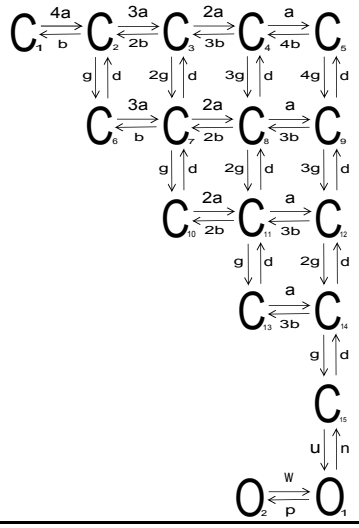

**Figure 8.3** State diagram of the $I_{CaL}$ dynamics in the Decker model.

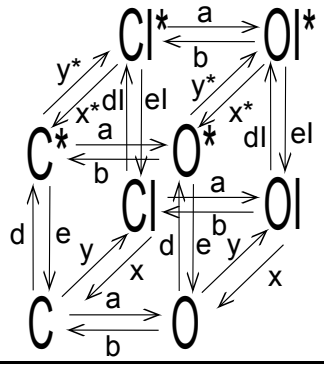


The reflected SDEs describing the stochastic dynamics of $I_{CaL}$ and $I_{Ks}$ therefore take the following form,

$$d\boldsymbol{y}_{CaL} = H_{CaL}\boldsymbol{y}_{CaL}dt + \tfrac{1}{\sqrt{N_{CaL}}}E_{CaL}F_{CaL}(\boldsymbol{y}_{CaL})d\boldsymbol{W}_{CaL} + d\boldsymbol{K}_{CaL}, \tag{8.4}$$

$$d\boldsymbol{y}_{Ks} = H_{Ks}\boldsymbol{y}_{Ks}dt + \tfrac{1}{\sqrt{N_{Ks}}}E_{Ks}F_{Ks}(\boldsymbol{y}_{Ks})d\boldsymbol{W}_{Ks} + d\boldsymbol{K}_{Ks}, \tag{8.5}$$

where $N_x$ is the number of channels of ion type $x$, $x = CaL,\ Ks$, and the matrices $H_x$, $F_x$, $E_x$, $x = CaL,\ Ks$, are given in Appendix C. On the other hand, $I_{Kr}$ and $I_{To1}$ are modelled using the Hodgkin-Huxley formulation, where $I_{Kr}$ is assumed to posses a single activation gate $X_r$ and $I_{To1}$ is described by three identical activation gates ($a$), a fast inactivation gate ($i_f$) and a slow inactivation gate ($i_s$). As discussed in Chapter 4 Section 4.1, incorporating stochasticity directly into the Hodgkin-Huxley formulation of ion channel dynamics can lead to inaccuracies in the stochastic dynamics. Therefore $I_{Kr}$ and $I_{To1}$ kinetics were reformulated in terms of the equivalent Markov formulations by assuming that each combination of gating positions is a distinct channel state, and so the dynamics of $I_{Kr}$ and $I_{To1}$ can be described by the following kinetic diagrams respectively:

$$X_{r,0} \underset{\beta_{X_r}}{\overset{\alpha_{X_r}}{\rightleftarrows}} X_{r,1}$$

$$
\begin{array}{ccccccc}
a_0 i_{f,0} i_{s,1} & & a_1 i_{f,0} i_{s,1} & & a_2 i_{f,0} i_{s,1} & & a_3 i_{f,0} i_{s,1} \\
\alpha_s \uparrow\downarrow \beta_s & & \alpha_s \uparrow\downarrow \beta_s & & \alpha_s \uparrow\downarrow \beta_s & & \alpha_s \uparrow\downarrow \beta_s \\
a_0 i_{f,0} i_{s,0} & \underset{\beta_a}{\overset{3\alpha_a}{\rightleftarrows}} & a_1 i_{f,0} i_{s,0} & \underset{2\beta_a}{\overset{2\alpha_a}{\rightleftarrows}} & a_2 i_{f,0} i_{s,0} & \underset{3\beta_a}{\overset{\alpha_a}{\rightleftarrows}} & a_3 i_{f,0} i_{s,0} \\
\beta_f \uparrow\downarrow \alpha_f & & \beta_f \uparrow\downarrow \alpha_f & & \beta_f \uparrow\downarrow \alpha_f & & \beta_f \uparrow\downarrow \alpha_f \\
a_0 i_{f,1} i_{s,0} & \underset{\beta_a}{\overset{3\alpha_a}{\rightleftarrows}} & a_1 i_{f,1} i_{s,0} & \underset{2\beta_a}{\overset{2\alpha_a}{\rightleftarrows}} & a_2 i_{f,1} i_{s,0} & \underset{3\beta_a}{\overset{\alpha_a}{\rightleftarrows}} & a_3 i_{f,1} i_{s,0} \\
\beta_s \uparrow\downarrow \alpha_s & & \beta_s \uparrow\downarrow \alpha_s & & \beta_s \uparrow\downarrow \alpha_s & & \beta_s \uparrow\downarrow \alpha_s \\
a_0 i_{f,1} i_{s,1} & \underset{\beta_m}{\overset{3\alpha_m}{\rightleftarrows}} & a_1 i_{f,1} i_{s,1} & \underset{2\beta_m}{\overset{2\alpha_m}{\rightleftarrows}} & a_2 i_{f,1} i_{s,1} & \underset{3\beta_m}{\overset{\alpha_m}{\rightleftarrows}} & a_3 i_{f,1} i_{s,1} \\
\alpha_f \uparrow\downarrow \beta_f & & \alpha_f \uparrow\downarrow \beta_f & & \alpha_f \uparrow\downarrow \beta_f & & \alpha_f \uparrow\downarrow \beta_f \\
a_0 i_{f,0} i_{s,1} & \underset{\beta_m}{\overset{3\alpha_m}{\rightleftarrows}} & a_1 i_{f,0} i_{s,1} & \underset{2\beta_m}{\overset{2\alpha_m}{\rightleftarrows}} & a_2 i_{f,0} i_{s,1} & \underset{3\beta_m}{\overset{\alpha_m}{\rightleftarrows}} & a_3 i_{f,0} i_{s,1}
\end{array}.
$$

where $\alpha_y$ and $\beta_y$ are the closed to open and open to closed transition rates, respectively, for gate of type $y$ and $y_i$ denotes the state where $i$ gates of type $y$ are open.

The stochastic dynamics of the ion channels for $I_{Kr}$ and $I_{To1}$ are again described using the reflected SDE formulation, based on the kinetic diagrams given above. The reflected SDEs for $I_{Kr}$, and $I_{To1}$ are, respectively

$$dy_{Kr} = (\alpha_{X_r} - (\beta_{X_r} + \alpha_{X_r})y_{Kr})dt + \frac{1}{\sqrt{N_{Kr}}}\sqrt{\alpha_{X_r} + (\beta_{X_r} - \alpha_{X_r})y_{Kr}}dW_{Kr} + dK_{Kr}, \quad (8.6)$$

$$d\boldsymbol{y}_{To1} = H_{To1}\boldsymbol{y}_{To1}dt + \tfrac{1}{\sqrt{N_{To1}}}E_{To1}F_{To1}(\boldsymbol{y}_{To1})d\boldsymbol{W}_{To1} + d\boldsymbol{K}_{To1}, \quad (8.7)$$

where $N_x$ is the number of channels of ion type $x$, $x = To1,\ Kr$, and the matrices $H_{To1}$, $F_{To1}$, $E_{To1}$, are given in Appendix C. In (8.6), $y_{Kr}$ is simply the proportion of channels in the open state, and due to the conservation in channel numbers, the proportion of channels in the closed state is simply $1 - y_{Kr}$. The entries of the vectors $\boldsymbol{y}_{CaL}$, $\boldsymbol{y}_{Ks}$, and $\boldsymbol{y}_{To1}$ give the proportion of $CaL$, $Ks$ and $To1$ channels, respectively, in each state, and the ordering of these vectors are defined in Appendix C. The most important state, in terms of the dynamics of the membrane potential, is the proportion of channels in the open state for each of these channels, which are as follows,

$$CaL^{open} = y_{CaL}(2) + y_{CaL}(4), \quad Ks^{open} = y_{Ks}(1) + y_{Ks}(2), \quad To1^{open} = y_{To1}(1). \quad (8.8)$$

At each time step the voltage and ionic concentrations are assumed to remain constant and the reflected SDEs are solved using the projection method given in Chapter 6 Section 6.2 and described in (Dangerfield et al., 2012). The voltage and all other variables in the original Decker model are then updated using the Euler method. Due to the stiffness of this system, the time step must be taken to be $< 0.009ms$ in order to resolve the upstroke of the AP.

### 8.2.6 Population of Stochastic Models Simulation Protocol

For each model in the population of stochastic models, a train of 30 beats was simulated at a basic cycle length of $1000$ ms, as in experiments, and this was repeated $50$ times. The $APD_{90}$ was calculated for each beat in each of the simulations. $50$ repetitions were used since using twice as many simulations altered the $STV_{APD90}$ by less than $10\%$ and the mean and variance in $APD_{90}$ by less than $5\%$. Therefore, due to the computational intensiveness of each set of simulations, we concluded $50$ simulations would provide sufficiently accurate estimates for the measures of $APD_{90}$ variability considered here. $30$ beats were used to calculate beat-to-beat variability in $APD_{90}$ since this is the number of beats used in previous studies to calculate $STV$, (Thomsen et al., 2004, 2005, 2006).

The variability in $APD_{90}$ was quantified using the following three measures: short term variability in $APD_{90}$ ($STV_{APD90}$), the range in $APD_{90}$ and the variance in $APD_{90}$. These measures were calculated for each simulation over $30$ beats and the mean and standard deviation over the $50$ simulations was taken for each measure. The $STV_{APD90}$ was calculated using the following formula,

$$STV = \sum_{n=2}^{30} |APD_{90}^{n} - APD_{90}^{n-1}|/(\sqrt{2} \times 29), \tag{8.9}$$

where $APD_{90}^{n}$ is the $APD_{90}$ calculated at beat $n$. The range in $APD_{90}$ was defined to be the difference between the maximum and minimum $APD_{90}$ and the variance was calculated in the standard way. We also computed the mean $APD_{90}$ for each model of the stochastic population. Simulations of the population of stochastic models were performed using the resources of the

Oxford Supercomputing Centre (OSC).

### 8.2.7 Experimental Methods

Single cell experimental data is used both to construct the population of deterministic models and also to obtain estimates for single channel current of the four repolarisation currents, which is subsequently used to estimate the number of channels. The $APD_{90}$ recorded from single cell experiments under control conditions and as a result of drug block are used to determine bounds within which the behaviour of the population of deterministic models lies. This is to ensure that the population of models lies within experimentally observed behaviour. Furthermore, measures of short-term variability in $APD_{90}$, $STV_{APD90}$, from these same experiments are compared with simulation results from the population of stochastic models.

All experimental data obtained is from single canine ventricular cells. Experiments were done by Dr. Norbert Szentandrássy and Dr. László Virág from the University of Szeged, Hungary. Experimental conditions are described in (Szabó et al., 2007) and (Szentandrássy et al., 2011). Here we provide a summary.

#### Cell Isolation

Single canine ventricular cells were acquired from adult beagle dog hearts by enzymatic dispersion using the segment perfusion technique as previously described in (Szabó et al., 2007; Szentandrássy et al., 2011). Animals were anesthetized with 10mg/kg ketamine hydrochloride (Calypsolvet) plus 1mg/kg xylazine hydrochloride (Rometar) using intravenous injection. The heart was quickly removed after opening up the chest and mounted on Landendorff perfusion apparatus. Here the heart was perfused through the left anterior descending coronary artery for the first five minutes using the following solution, Ca2+-free JMM solution (Minimum Essential Medium Eagle, Joklik modification; Sigma Chemicals, product no. 0518, St Louis, MO, USA), supplemented with taurine (2.5 g/l), pyruvic acid (175 mg/l), ribose (750 mg/l), allopuri-

nol (13.5 mg/l) and NaH2PO4 (200 mg/l), to remove Ca2+ and blood from the tissue. NaHCO3 (1.3 g/l) was then added to the solution and the pH of this perfusate was 7.0 when gassed with carbogen (95% O2 + 5% CO2). Cell dispersion was then performed for $30$ min in this solution with the addition of collagenase (660 mg/l, Worthington Cls-1), bovine albumin (2 g/l) and CaCl2 (50 M). The solutions were gassed with carbogen and the temperature was maintained at $37°$C during the isolation procedure. Cells were stored at $14°$C in modified JMM solution (pH 7.4) until use. Experimental protocol conformed with the principles outlined in the Declaration of Helsinki and was approved by the local ethical committee.

**Action Potential Recordings**

Only rod-shaped viable cells showing clear striations were used and all electrophysiology measurements were performed at $37°C$. These were sedimented in a plexiglass chamber and continuously superfused with oxygenated Tyrode solution. Transmembrane potentials were recorded using $3$ M KCl filled sharp glass microelectrodes with tip resistance between $20$ and $40$ M$\Omega$ and these electrodes were connected to the input of an Axoclamp-2B amplifier (Axon Instruments Inc., Foster City, CA, USA). Cells were paced through the recording electrode at a steady cycle length of $1$ s using $1$ ms wide rectangular current pulses with 120% threshold amplitude. Time-dependent changes in the APD were negligible for at least 60 min under these experimental conditions since the cytosol was not dialysed (Szabó et al., 2007).

Before drug application, APs were recorded for $5$ minutes to allow the cells to reach equilibrium. Providing AP parameters remained stable during this period the experiment was continued, otherwise it was aborted. After this initial period $50$ consecutive APs were recorded with a basic cycle length of $1000$ ms, which were used for APD variability measurements under control conditions. To test the effect of drug, the drug was applied after the control measurements were recorded and an incubation period of $5 - 6$ minutes was applied, which was adequate to obtain the steady state drug effect. Once again $50$ consecutive APs were then recorded

with a BCL of $1000$ ms for APD variability measurements due to the effects of drug. The following drug concentrations were used, along with the estimated channel block: $0.1\mu M$ of dofetilide which completely blocked $I_{Kr}$ (5 data sets), $0.5\mu M$ HMR-1556 which completely blocked $I_{Ks}$ (9 data sets) and $1\mu M$ nisoldipine which gives $95$% block of $I_{CaL}$ channel (3 data sets). The effects of double channel block were also investigated using $0.5\mu M$ HMR-1556 plus additional $100\mu M$ Chromanol $293$B which gives complete $I_{Ks}$ block and 90% $I_{To1}$ block ($7$ data sets). After measurements were taken for the initial application of HMR-1556, Chromanol $293$B was applied and again allowed to obtain the steady state drug effect before 50 consecutive AP measurements were taken.

### Voltage Clamp Recordings

For voltage clamp recordings, cells were superfused with oxygenated Tyrode solution and experiments were carried out at $37°C$. Suction pipettes were fabricated from borosilicate glass and had a tip resistance of $2$ M$\Omega$ after filling with pipette solution containing (all in mM), K-aspartate 100, KCl 45, K-ATP 5, MgCl2 1, EGTA 10, and HEPES 5 (pH 7.2) for measuring potassium currents or alternatively KCl 110, KOH 40, EGTA 10, HEPES 10, TEACl 20, MgATP 5, GTP 0.25 (pH was adjusted to 7.2 with KOH) for measuring calcium currents. To measure the potassium currents, $1$ $\mu$M nisoldipine was added to the oxygenated Tyrode solution in order to completely block the inward calcium current ($I_{CaL}$). For measurements of $I_{CaL}$, $3$ mM $4$-aminopyridine was added to the oxygenated Tyrode solution to eliminate the transient potassium outward current. Membrane currents ($I_{Kr}$, $I_{Ks}$, $I_{CaL}$ and $I_{To}$) were recorded with the Axopatch-2B amplifier using the whole cell configuration of the patch clamp technique (Hamill et al., 1981). After establishing a high (110 GW) resistance seal by gentle suction, the cell membrane beneath the tip of the electrode was disrupted by further suction or by applying $1.5$ V electrical pulses for 1 ms. The series resistance was typically $48$ M$\Omega$ before compensation (usually 50-80%) and experiments were discarded when the series resistance was high or sub-

stantially increasing during the measurement. A $1000$ Hz low pass filtering (Bessel filter, 80 dB/decade) was applied to the analogue current signals before the outputs from the amplifier were digitized at 100 kHz under software control (pClamp 6.0, Axon Instruments Inc.). The results were analysed using software programs purchased from Axon (pClamp 6.0 and 7.0, Axon Instruments, Foster City CA, USA).

## 8.3 Results

We begin by showing results that confirm each model in the population does indeed lie within experimental range, and we also compare the estimated number of channels for each ionic current with those previously reported in the literature. Results are then presented from simulations of the population of stochastic models.

### 8.3.1 Population of Deterministic Models

Out of an initial potential $3125$ deterministic models, only $23$ models remained within the population after comparison with experimental data. For each model in the population, the final AP trace, simulated according to the protocol given in Section 8.2.2, is plotted using different colours, with the red vertical lines indicating the maximum and minimum experimentally observed $APD_{90}$ values. The blue star trace is the AP for the original Decker model. The five different conditions used to calibrate the population are shown, namely: control conditions (top), complete $I_{Kr}$ block (middle left), complete $I_{Ks}$ block (middle right), complete $I_{Ks}$ block and 90% $I_{To1}$ block (bottom left) and finally 95% $I_{CaL}$ block (bottom right).

**Figure 8.4** Single AP traces obtained using the population of deterministic models, plotted on top of one another, simulated under the following different conditions: control conditions (top), complete $I_{Kr}$ block (middle left), complete $I_{Ks}$ block (middle right), complete $I_{Ks}$ and $90\%$ $I_{To}$ block (bottom left), $95\%$ $I_{CaL}$ block (bottom right). Red vertical lines are the maximum and minimum $APD_{90}$ values from experimental data for the same protocol as in the simulations and the blue AP is for the Decker model without any rescaling of the ionic currents. In simulations the pacing rate, i.e. the basic cycle length, is $1000$ ms.

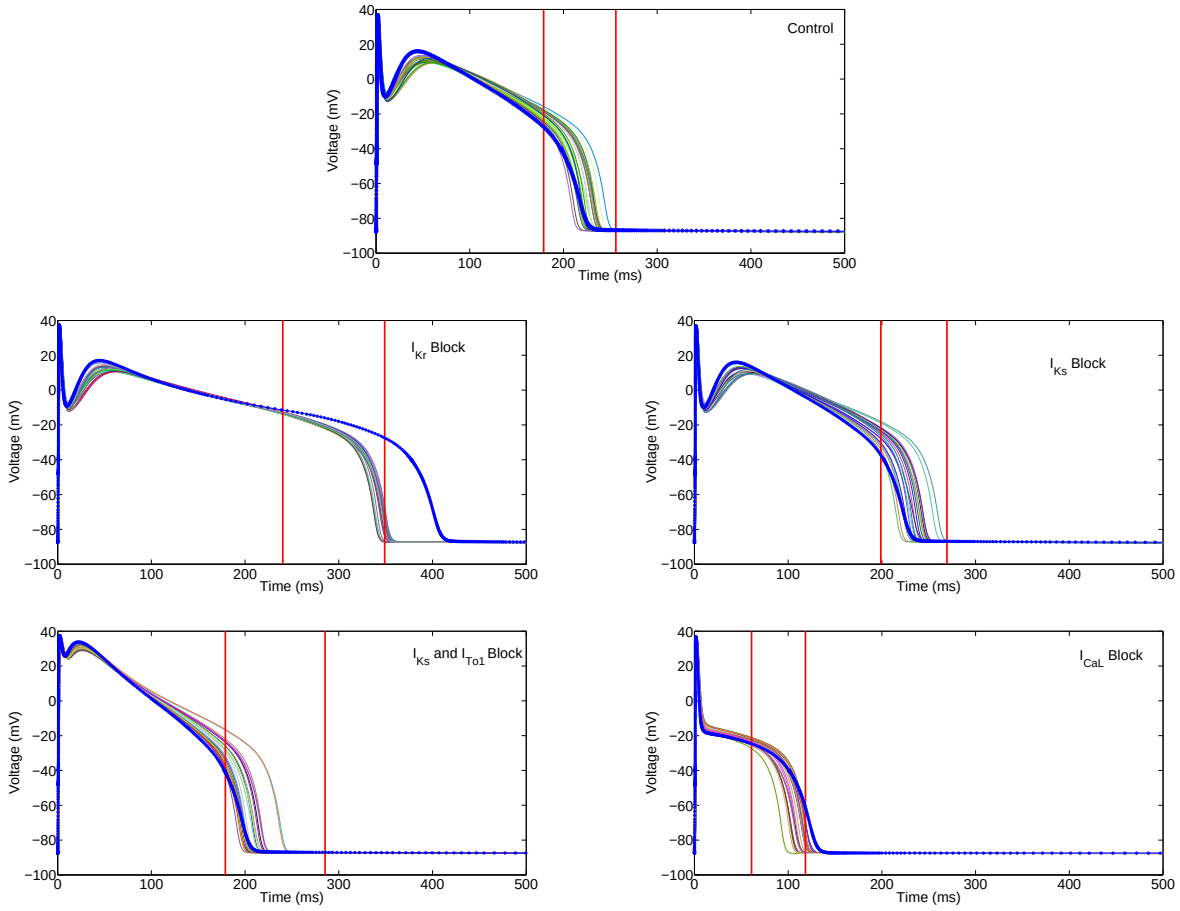


Figure 8.4 shows that for each of the $23$ models in the population, the $APD_{90}$ lies within experimental range both under control and drug block conditions. Indeed, this is not the case for the original Decker model, which results in too long an AP in the presence of complete $I_{Kr}$ block in comparison with the experimental data used in this study, Figure 8.4. Therefore, from Figure 8.4 we conclude that the population of deterministic models constructed here provides a group of models, each with a unique set of conductances and channel numbers, that results in

experimentally observed behaviour.

### Number of Channel Estimates for Each Model

As described in Section 8.2.1, for each model in the population $I_{Kr}$, $I_{Ks}$, $I_{CaL}$, $I_{To1}$ and $I_{K1}$ are individually multiplied by a unique scaling factor. This equates to increasing or decreasing the conductance of these currents by some percentage. We found that in all the models the conductance of $I_{CaL}$, $I_{Kr}$ and $I_{To1}$ was decreased with respect to the original Decker model values. The maximum and minimum percentage decreases across the population for each current are shown by the red dots in Figure 8.5 (left). On the other hand, $I_{K1}$ and $I_{Ks}$ conductance was increased with respect to the original Decker model values, and again the maximum and minimum percentage increases are shown by the blue dots in Figure 8.5 (left). (See Appendix D for the scaling factors for each model individually).

**Figure 8.5** Left: Maximum and minimum percentage change in the population of models with respect to the original Decker model for each current. Percentage decrease is shown by the red dots and percentage increase by the blue dots. Right: Maximum and minimum number of channels in the population of models for each current.

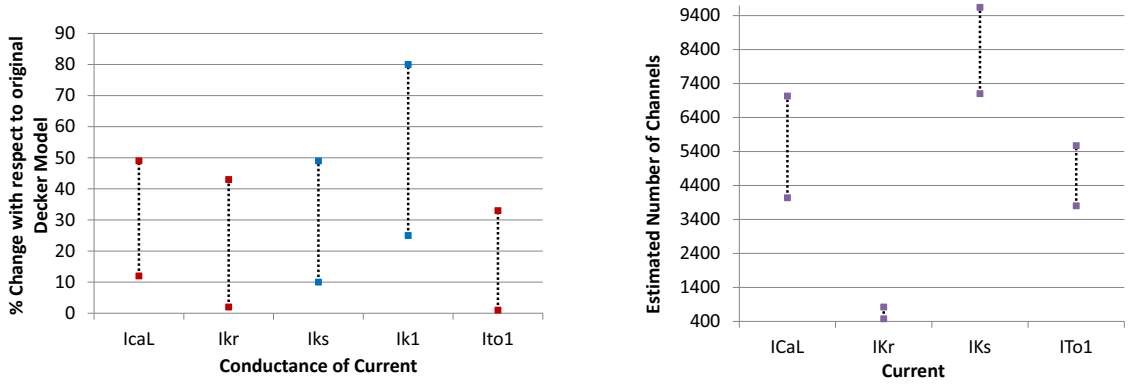


The maximum and minimum in the estimated number of channels for each ionic current is shown on the right hand side of Figure 8.5 (see Appendix D for the estimated number of channels for each model individually). Since each model in the population has a unique number of

channels for each current, it is difficult to directly compare the number of channels estimated here with those reported in previous studies. Therefore, we compare the mean number of channels for each current, where the mean is taken over the $23$ models in the population and from our results we estimate these to be $I_{CaL} = 5148$, $I_{Kr} = 685$, $I_{Ks} = 8874$, $I_{To1} = 4730$.

The number of $I_{Ks}$, $I_{CaL}$ and $I_{Kr}$ channels have previously been reported in Lemay et al. (2011), although these estimates were based on the Faber-Rudy model, (Faber et al., 2007), which described the AP in a guinea-pig ventricular myocyte, rather than a canine cell. Therefore it is unsurprising that number of $I_{Ks}$, $I_{Kr}$ and $I_{CaL}$ channels estimated here varies from those reported in (Lemay et al., 2011). In particular, the number of $I_{CaL}$ channels is around twenty times smaller than in (Lemay et al., 2011), where it was estimated to be $107,726$, the number of $I_{Ks}$ channels estimated here is about half that estimated in (Lemay et al., 2011), where they report it to be $14,962$ and the number of $I_{Kr}$ channels is about two and a half times smaller than that reported in (Lemay et al., 2011) ($2175$). These differences in channel number are most likely due to the differences between the two models used to estimate them, which in turn could be due to variations between species.

In Pueyo et al. (2011) the number of $I_{Ks}$ channels in endocardial, epicardial and midmyocardial cells in both human and guinea-pig myocytes are estimated using the Faber-Rudy model for the guinea-pig cells, (Faber et al., 2007), and the Ten Tusscher model for the human cells, (Tusscher and Panfilov, 2006b). Interestingly the number of $I_{Ks}$ channels we report is similar to the estimated number for guinea-pig endocardial cells in (Pueyo et al., 2011) where the number of channels is estimated to be $6286$. However, our estimate is two to three times larger than reported values for human midmyocardial cells ($3000$) and guinea-pig midmyocardial cells ($2286$), a third smaller than values reported for human epicardial and endocardial cells ($12000$) and half the value for guinea-pig endocardial cell ($20000$), all values as reported in (Pueyo et al., 2011). Again these differences are most likely due to differences in the models used to estimate the number of channels, which could be due to species variation.

The number of ionic channels is important in the population of stochastic models, since in the stochastic model of ion channel dynamics the noise term scales with $1/\sqrt{N}$, where $N$ is the number of channels. Therefore, the smaller the number of channels the larger the fluctuations in the stochastic simulations of the ion channel dynamics and so the number of channels determines the amount of variability that arises in the model due to the stochastic ion channel behaviour. We now discuss the results from the simulations of the population of stochastic models.

### 8.3.2 Population of Stochastic Models Simulations

**The Population of Stochastic Models Reproduces Experimental Variability in $APD_{90}$**

We first investigated the effects of incorporating the stochastic behaviour of all four of the repolarisation currents $I_{CaL}$, $I_{Kr}$, $I_{Ks}$ and $I_{To1}$ on the three measures of $APD_{90}$ variability under control conditions. Results of the mean, and the mean $\pm$ standard deviation (shown as error bars) for each model are shown in Figure 8.6 along with the maximum and minimum experimental values.

**Figure 8.6** Error bars showing the mean (blue dots) and the mean $\pm$ the standard deviation (blue error bars) for each measure of $APD$ variability, calculated over $50$ simulations, plotted for each model in the population of stochastic models where $I_{CaL}$, $I_{Kr}$, $I_{Ks}$ and $I_{To1}$ are all stochastic. The $APD$ variability measures are as follows: $STV_{APD_{90}}$ (top), range in $APD_{90}$ (middle) and variance in $APD_{90}$ (bottom).The maximum and minimum experimentally recorded values (solid horizontal red line) are also shown.

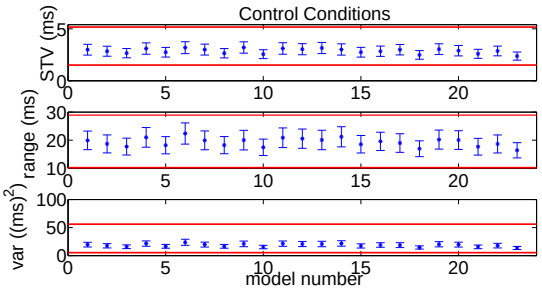


For each model in the population, all three measures of variability lie within experimental range

under control conditions, Figure 8.6, and the change in $APD_{90}$ variability as a result of complete $I_{Kr}$ block or complete $I_{Ks}$ block also lies within experimental range, Figure 8.7. Therefore Figures 8.6 and 8.7 confirm that the stochastic population of models reproduces experimentally observed levels of beat-to-beat variability in $APD_{90}$ under both control and drug block conditions.

**Figure 8.7** Error bars showing the change in the mean (blue dots) and the change in the mean $\pm$ the standard deviation (blue error bars) for each measure of variance as a result of complete $I_{Kr}$ block (left) or $I_{Ks}$ block (right), calculated over $50$ simulations, plotted for each model in the population of stochastic models where $I_{CaL}$, $I_{Kr}$, $I_{Ks}$ and $I_{To1}$ are all stochastic. The variance measures are as follows: $STV_{APD_{90}}$ (top), range in $APD_{90}$ (middle) and variance in $APD_{90}$ (bottom).The maximum and minimum experimentally recorded values (solid horizontal red line) are also shown.

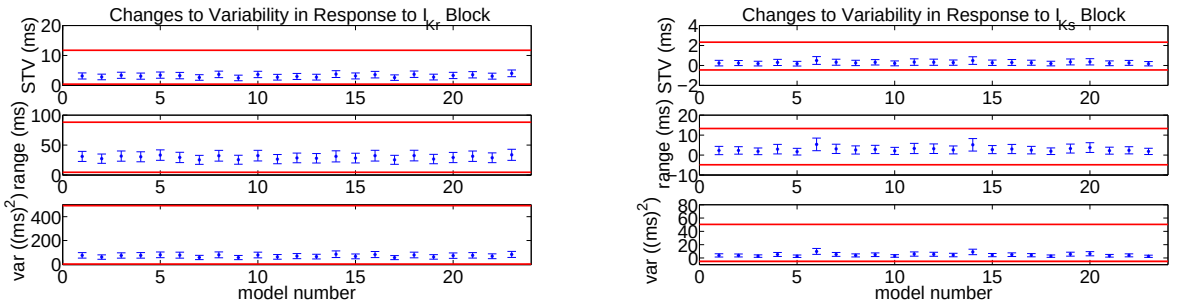


### Contribution of Each Ionic Current to Variability

Next we investigated the effects of each ionic current individually on the variability in $APD_{90}$ by incorporating the stochastic behaviour of only one ionic current at a time into the model. We take the mean over the entire population for each measure of variability, so as to try to separate the effects of the intrinsic stochastic behaviour of ion channel dynamics, from the effects of cell-to-cell differences within the population. Results are shown in Figure 8.8.

**Figure 8.8** Histogram showing the mean variability in $APD_{90}$ across the population from simulations where all currents are stochastic, and also when stochasticity is incorporated into each current individually. The measures of variability are $STV_{APD90}$ (top left), range in $APD_{90}$ (top right) and the variance in $APD_{90}$ (bottom). The error bars in each plot illustrate the standard deviation across the population.

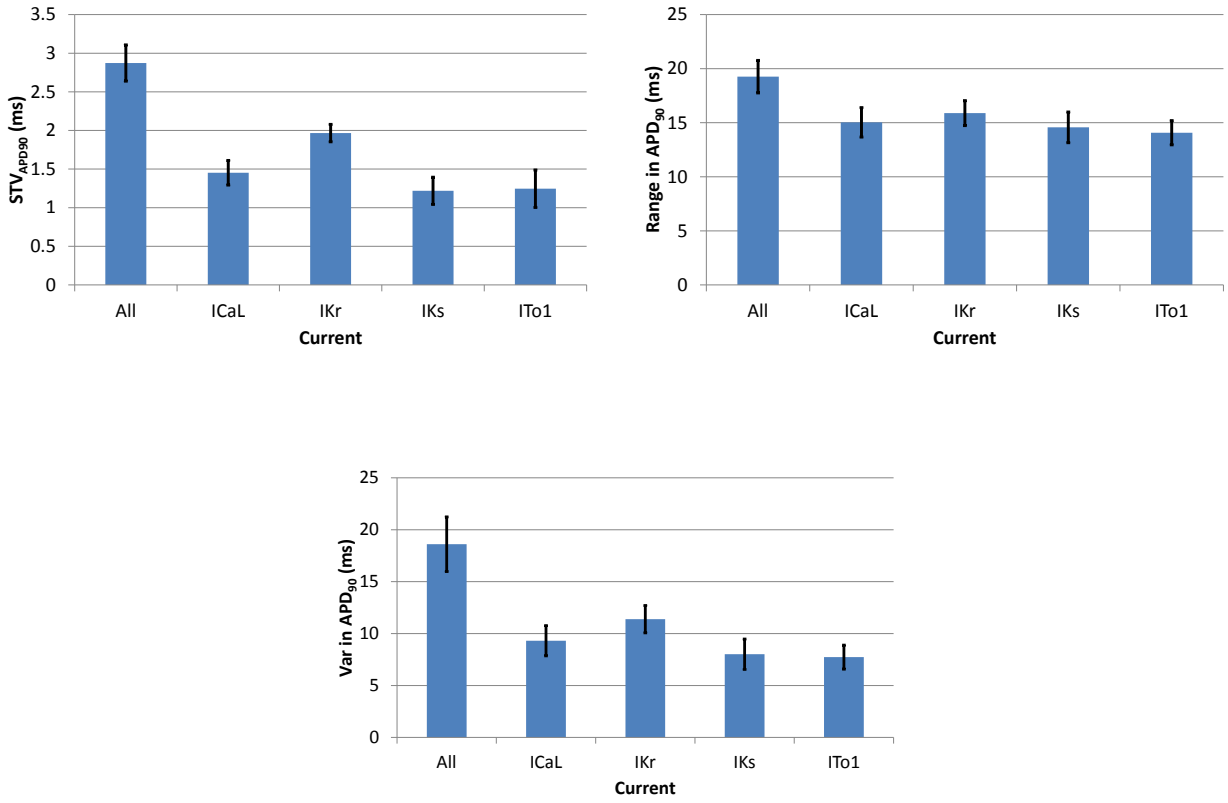


The stochastic behaviour of $I_{Kr}$ contributes the most to all measures of $APD_{90}$ variability, Figure 8.8, with the stochastic behaviour of $I_{Kr}$ alone able to reproduce $68\%$ of the $STV_{APD90}$, $82\%$ of the range in $APD_{90}$ and $61\%$ of the variance in $APD_{90}$. $I_{CaL}$ is the next largest contributor to all measures of $APD_{90}$ variability. Finally $I_{Kr}$ and $I_{To1}$ both contribute the least to all measures of $APD_{90}$ variability. Also, from Figure 8.8 it is clear that each current alone can reproduce more that $1/4$ of the variability observed when all currents are stochastic, and so the contribution of the four different currents does not appear to combine in a simple linear manner.

### Relationships Between Variables

We explore possible relationships between the measures of $APD_{90}$ variability and the channel numbers, to provide insight into the possible mechanisms underlying beat-to-beat variability in repolarisation. All the results presented in this section are from simulations of the population of stochastic models where stochasticity is incorporated into the four repolarisation currents $I_{CaL}$, $I_{Kr}$, $I_{Ks}$ and $I_{To1}$ simultaneously. We perform linear regression, firstly on combinations of two variables, and then on multiple variables, to try to uncover potential correlations. This is done using the inbuilt MATLAB functions *polyfit*, in the simple two variable case, and *regress* in the multiple variable case, both of which use a least squares method to estimate the coefficients in the linear model. To assess how well the linear model obtained from the regression analysis represents the data we calculate the coefficient of determination, more commonly referred to as the $R^2$ statistic. In the case of the two variable linear regression, $R^2$ is simply the square of the correlation coefficient, which indicates the strength of linear dependence between two variables. Therefore, the $R^2$ statistic gives some idea of the goodness of fit, with a value of $1$ indicating that the model perfectly fits the data and a value of $0$ indicating no linear relationship between the variables. Therefore this statistic can be used to infer potential linear relationships between variables and the strength of these correlations. For a more detailed discussion see for example (Draper and Smith, 1998).

**Figure 8.9** Left: Relationship between the $STV_{APD90}$ (top), range (middle) and variance (bottom) in $APD_{90}$ and the mean $APD_{90}$, (blue stars). Right: Relationship between the $STV_{APD90}$ and the range in $APD_{90}$ (top) and also between $STV_{APD90}$ and the variance in $APD_{90}$ (bottom). The fitted linear model is the red solid line in each plot and the $R^2$ value from the linear regression in each case is given. All values are calculated from simulations where stochasticity is incorporated into all ionic currents.

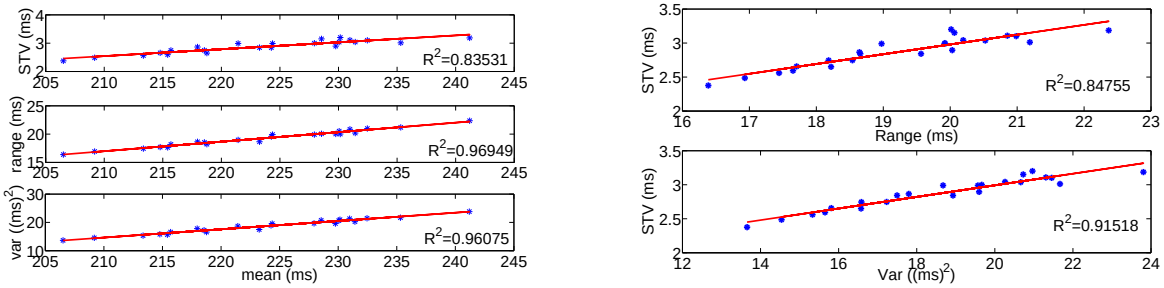


We first investigated the relationship between mean $APD_{90}$ and the three measures of $APD_{90}$ variability. The correlation between $STV_{APD90}$ with the range and variance in $APD_{90}$ was also considered. Results are shown in Figure 8.9 along with the $R^2$ statistic for each linear regression. The $R^2$ value is greater than $0.86$ and so is close to $1$ for the linear regression of all three measures of variability in $APD_{90}$ and mean $APD_{90}$, left hand side of Figure 8.9. In particular, the $R^2$ value is greatest for the linear regression of the variability in $APD_{90}$ and mean $APD_{90}$, and is smallest for the $STV_{APD90}$ and mean $APD_{90}$. These $R^2$ values suggest that there is a strong linear correlation between the mean $APD_{90}$ and beat-to-beat variability in $APD_{90}$. Furthermore, the fitted linear model suggests that this is a positive correlation, with greater variability when the mean $APD_{90}$ is large, left hand side Figure 8.9. The right hand side of Figure 8.9 suggests that there is a positive correlation between the $STV_{APD90}$ and the range and variance in $APD_{90}$. However, the $R^2$ value is much lower than in the case of the linear regression with the mean $APD_{90}$, suggesting that the linear correlation between the $STV_{APD90}$ and the range and variance in $APD_{90}$ is much weaker than the correlation between $STV_{APD90}$ and mean $APD_{90}$.

We explored the potential linear relationships between the number of ion channels of each type

with the three measures of variability and the mean. The only clear relationship we found between the measures of $APD_{90}$ and the number of channels was for $I_{Kr}$, and so only these results are plotted in Figure 8.10.

**Figure 8.10** Relationship between the measures of $APD_{90}$ variability, the mean $APD_{90}$ and the number of $I_{Kr}$ channels in each model. The measures of $APD_{90}$ considered are: $STV_{APD90}$ (top left), variance in $APD_{90}$ (top right), range in $APD_{90}$ (bottom left) and mean in $APD_{90}$ (bottom right). The fitted linear model is the red solid line in each plot. All values are calculated from simulations where stochasticity is incorporated into all ionic currents. The $R^2$ values are given in Figure 8.11

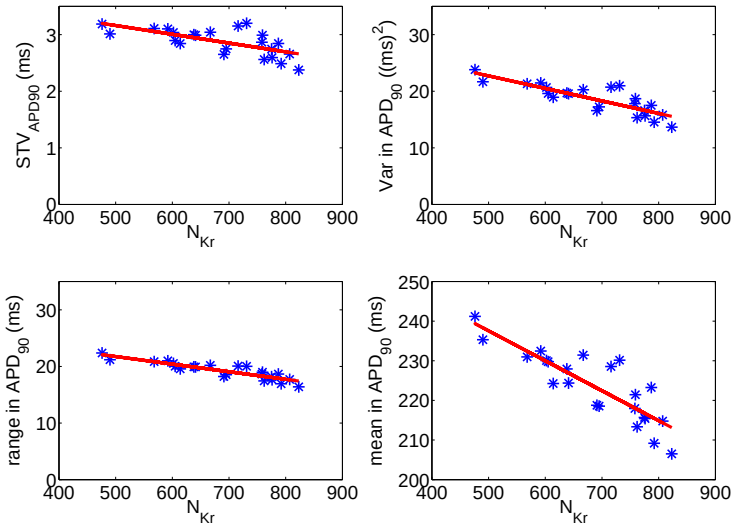


The fitted linear models (red solid lines) in each of the plots in Figure 8.10 suggests that the number of $I_{Kr}$ channels is negatively correlated with all the measures of variability as well as the mean $APD_{90}$. Thus there is greater variation and mean $APD_{90}$ when the number of $I_{Kr}$ channels is small. These correlations do not appear to be as strong as the relationship between the measures of variability and the mean $APD_{90}$ since the $R^2$ values are lower.

To try to investigate the effects of all channel numbers on the measures of $APD_{90}$ variability and the mean $APD_{90}$, we performed multiple linear regression analysis. The $R^2$ statistic for each measure of $APD_{90}$ is shown in Figure 8.11 along with the $R^2$ statistic from the two variable linear regression for each of the currents individually.

**Figure 8.11** Histogram of the $R^2$ values obtained from the two variable linear regression analysis and the multiple linear regression analysis for the number of channels (both individually and combined) and the following measures of $APD_{90}$: $STV_{APD90}$ (top left), variance in $APD_{90}$ (top right), range in $APD_{90}$ (bottom left) and mean in $APD_{90}$ (bottom right).

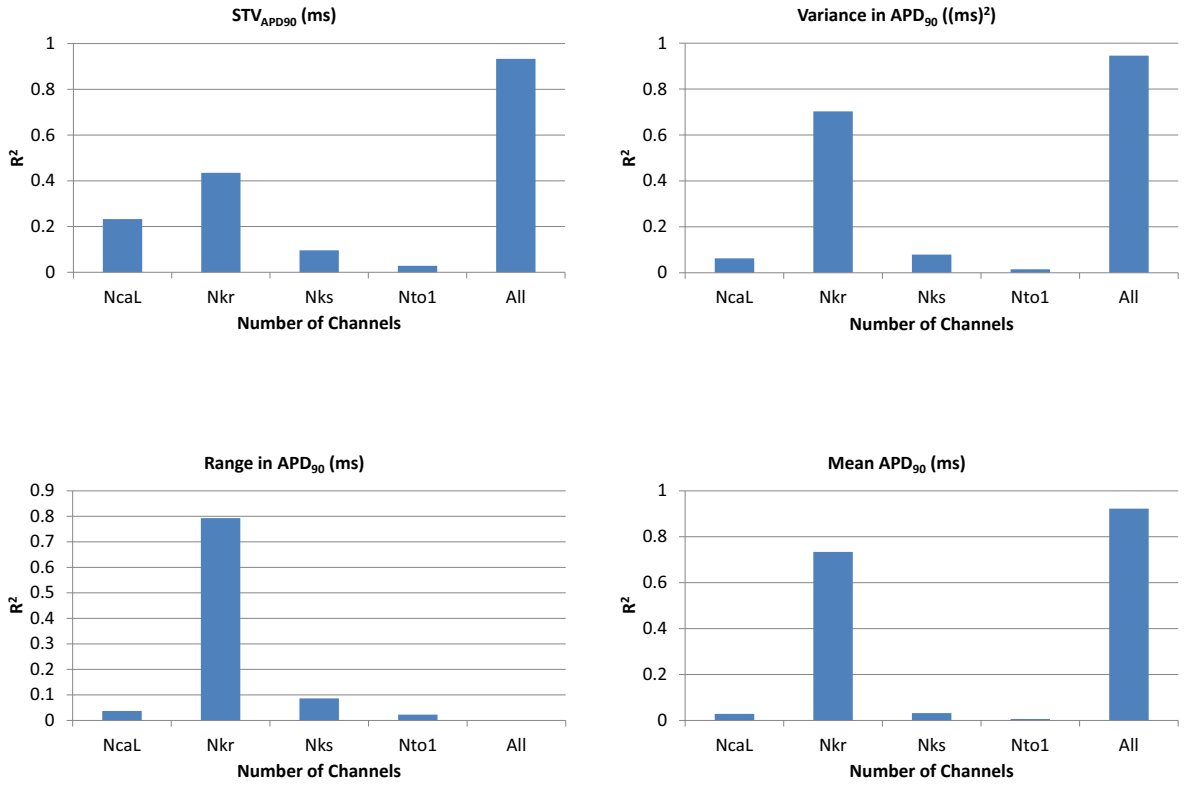


For all measures of $APD_{90}$ $R^2$ is very close to 1 when the number of channels for all currents is considered. Indeed including all currents seems to strengthen the relationship between the number of $I_{Kr}$ channels and the measures of $APD_{90}$ shown in Figure 8.11.

## 8.4 Discussion

### Summary of Main Findings

We have shown that the stochastic behaviour of the four repolarisation currents $I_{Kr}$, $I_{Ks}$, $I_{To1}$ and $I_{CaL}$ contribute to beat-to-beat variability in $APD_{90}$ under control conditions as well as the

increase in beat-to-beat variability in response to complete block of either $I_{Kr}$ or $I_{Ks}$ currents observed in experiments. We found that the $I_{Kr}$ current contributes the most to beat-to-beat variability in $APD_{90}$, with the $I_{CaL}$ current being the second largest contributor. Furthermore, the stochastic behaviour of each current individually is able to reproduce more than $1/4$ of the beat-to-beat variability in $APD_{90}$ when all currents are stochastic, and so the contribution of the stochastic behaviour of each current to beat-to-beat variability in $APD_{90}$ do not combine in a linear way. Finally we found there was a strong positive correlation between the mean $APD_{90}$ and beat-to-beat variability in $APD_{90}$ and that the mean $APD_{90}$ in turn was negatively correlated with the number of $I_{Kr}$ channels. Furthermore, the relationship between the number of channels and beat-to-beat variability in $APD_{90}$ is strongest when the number of all ionic currents is considered.

**Current Fluctuations Due to the Stochastic Behaviour of Ion Channels Contributes to BVR**

Since the variability of all models in the stochastic model population lie within experimental range for both control and drug block conditions (Figures 8.6 and 8.7) this confirms that the population of stochastic models successfully captures the BVR in canine single cell experiments. Furthermore, the stochastic behaviour of the four key repolarisation currents, $I_{Kr}$, $I_{CaL}$, $I_{To1}$ and $I_{Ks}$, only was represented in each of the models. Therefore, these results provide evidence to support our initial hypothesis that the stochastic behaviour of these four currents are an important contributor to variability in $APD_{90}$ in single cell experiments.

However, throughout the population the $APD_{90}$ variability for all three measures seems to be consistently towards the lower end of the experimental range, and this is particularly noticeable under complete block of $I_{Kr}$ and $I_{Ks}$. This suggests an additional possible mechanism is involved in beat-to-beat variability in $APD_{90}$. For example, the stochastic behaviour of the fast sodium current, $I_{Na}$, may also play a role in beat-to-beat variability in $APD_{90}$. We did not include the stochastic behaviour of this current since the variability occurs in the repolarisation

phase of the $AP$ and $I_{Na}$ is mainly involved in the depolarisation phase. Furthermore, the study by Lemay et al. (2011) found that $I_{Na}$ contributed little to beat-to-beat variability in $APD_{90}$ under control conditions. However, $I_{Na}$ is thought to play a role in repolarisation reserve, (Varró and Baczkó, 2011), and so the stochastic behaviour of this current may play a role in beat-to-beat variability in $APD_{90}$, particularly under conditions of reduced repolarisation reserve such as drug block. Indeed this could explain why the $APD_{90}$ variability is most noticeably towards the lower end of the experimental range when there is reduced repolarisation reserve as a result of $I_{Ks}$ or $I_{Kr}$ block. Therefore, while the population of stochastic models lies within experimental range, since they all lie towards the minimum experimentally observed value, this suggests that other mechanisms are involved in beat-to-beat variability in $APD_{90}$, such as the stochastic behaviour of $I_{Na}$. In particular, these additional mechanisms seem to play a greater role when there is reduced repolarisation reserve, since the variability in $APD_{90}$ as a result of $I_{Kr}$ or $I_{Ks}$ block lie much closer to the minimum values from experiments than under control conditions.

#### Stochastic Behaviour of $I_{Kr}$ Contributes the Most to BVR

The stochastic behaviour of $I_{Kr}$ contributes the most to all three measures of $APD_{90}$ variability, Figure 8.8. The mean number of $I_{Kr}$ channels across the population is $685$ which is $6$ times smaller than the mean number of $I_{To1}$ channels ($4730$), $7$ times smaller than the mean number of $I_{CaL}$ channels ($5148$) and $13$ times smaller than the mean number of $I_{Ks}$ channels ($8874$). Therefore, our results support out initial hypothesis that the stochastic behaviour of the ionic current with the smallest number of channels plays the greatest role in beat-to-beat variability. $I_{Kr}$ is a very important current in repolarisation and so it is likely that the prominent role of $I_{Kr}$ fluctuations in BVR is the combined effect of larger current fluctuations due to smaller channel numbers and the significance of $I_{Kr}$ during repolarisation.

Interestingly, our results suggest that individual current fluctuations do not combine in a lin-

ear manner, in terms of the total variation in $APD_{90}$, when the fluctuations of all currents are considered, as can been seen in Figure 8.8. Therefore, it seems as though the fluctuations of individual ionic currents may become dampened by the stochastic behaviour of other currents, which is not surprising due to the complex nonlinear relationship between the ion channel dynamics and the membrane potential. We note that this result differs with the findings in (Lemay et al., 2011), where they find the total variation is the sum of the individual ionic contributions. In (Lemay et al., 2011) the stochastic model depends on a specific conductance value for each current, and the only variability that arises is as a result of the stochastic behaviour of the ion channels. However, we use a population of models to account for the cell-to-cell differences in maximal conductance of each ionic current. In the population of stochastic models used in this study there is variability due to both the intrinsic stochastic behaviour of ion channel dynamics and the different sets of conductance values used in each model. Therefore, our results show that when the effects of extrinsic noise are considered in combination with the effects of intrinsic noise due to stochastic ion channel behaviour, the combined contribution of the fluctuations of individual ionic currents on beat-to-beat variability in $APD_{90}$ does not follow a simple linear relationship.

### $STV_{APD90}$ is Weakly Correlated with the Range and Variance in $APD_{90}$

$STV_{APD90}$ is positively correlated with the range and variance in $APD_{90}$, which is unsurprising since all are different measures of beat-to-beat variability in $APD_{90}$ (right hand side of Figure 8.9). However, the $R^2$ value, which indicates the strength of the relationship, is only $0.62$ for the $STV_{APD90}$ and the range in $APD_{90}$ and $0.67$ for the $STV_{APD90}$ and the variance in $APD_{90}$. Since both these values do not lie close to $1$, which indicates a perfect correlation, this indicates that the relationship between $STV_{APD90}$ and the range and variance in $APD_{90}$ is not strong. Therefore, the $R^2$ values shown in Figure 8.9 suggest that there are differences in the information captured by the $STV$ measure and the range and variance in $APD_{90}$.

**Mean $APD_{90}$ and Number of $I_{Kr}$ Channels are Closely Related to BVR**

Our results show that there is a strong positive correlation between the all three measures of beat-to-beat variability in $APD_{90}$, and the mean $APD_{90}$. We note that this does not necessarily imply that larger mean $APD_{90}$ causes increased $APD_{90}$ variability, since the mean $APD_{90}$ itself is dependent on a number of factors, such as the conductance of ionic currents as well as the structure of the model itself. However, this result provides evidence that larger mean $APD_{90}$ could be an indication of reduced repolarisation reserve, which in turn results in greater variability in repolarisation.

The negative correlation in the number of $I_{Kr}$ channels with the three different measures of $APD_{90}$ variability suggests the number of $I_{Kr}$ channels is related to the beat-to-beat variability in $APD_{90}$ (Figures 8.10 and 8.11). Furthermore since the $R^2$ values between the number of $I_{CaL}$, $I_{Ks}$ and $I_{To1}$ and the measures of $APD_{90}$ variability are all close to $0$ (Figure 8.11), this implies the number of each of these channels individually are not associated to beat-to-beat variability in $APD_{90}$. Thus, taken together this suggests that it is only the number of $I_{Kr}$ channels that affects beat-to-beat variability in $APD_{90}$, Figure 8.11.

However, there is also a strong negative correlation between the number of $I_{Kr}$ channels and the mean $APD_{90}$, which in turn is strongly correlated with the three measures of $APD_{90}$ variability, Figure 8.9. The $R^2$ value for the relationship between $STV_{APD90}$ and mean $APD_{90}$ is greater than for $STV_{APD90}$ and the number of $I_{Kr}$ channels. This suggests that the mean $APD_{90}$ is more important in determining the magnitude of $STV_{APD90}$. The relationship between the number of $I_{Kr}$ channels and mean $APD_{90}$ further implies that smaller numbers of channels lead to greater mean $APD_{90}$ which in turn results in larger $STV_{APD90}$.

While individually the number of $I_{CaL}$, $I_{Kr}$, and $I_{To1}$ channels were not found to be related to the measures of $APD_{90}$ variability and mean $APD_{90}$, the linear combination in the number of $I_{CaL}$, $I_{Kr}$, $I_{Ks}$ and $I_{To1}$ channels was strongly associated with the measures of $APD_{90}$

variability and mean $APD_{90}$. This suggests that the level of variability is not dependent on the number of channels of an individual current, but it is the combination of the number of all the repolarisation currents that has the greatest effect on the magnitude of $APD_{90}$ variability as well as mean $APD_{90}$.

### Implications of the Findings

Beat-to-beat variability in $APD_{90}$ and in particular $STV_{APD90}$ have been shown to be a biomarker of arrhythmic risk in single cell experiments, (Abi-Gerges et al., 2010). Therefore it is important to understand the mechanisms underlying BVR within individual cells. The work of this study provides evidence supporting the hypothesis that BVR is the manifestation of the stochastic behaviour of individual ionic channels. In particular, the mean $APD_{90}$ and the number of $I_{Kr}$ channels were found to be closely related to the magnitude of beat-to-beat variability in $APD_{90}$. These results build on the previous findings of Pueyo et al. (2011) and Lemay et al. (2011), providing a greater understanding of the link between BVR and repolarisation reserve within cells. This is particularly applicable to the development of new drug compounds where $STV_{APD90}$ is used to measure repolarisation reserve in single cell experiments, (Abi-Gerges et al., 2010).

## 8.5 Chapter Summary

In this chapter we applied the reflected SDE method developed in this thesis to describe the stochastic behaviour of the four key repolarisation currents, $I_{CaL}$, $I_{Kr}$, $I_{Ks}$ and $I_{To1}$, in a canine ventricular cell model, so as to investigate the effects of fluctuations in these currents on the variability of the $APD_{90}$. To account for differences in the number of ion channels between cells we first constructed a population of stochastic models, each of which had a unique number of channels as well as a unique conductance for the corresponding current. Furthermore, the population of models was constructed in such a way so as to agree with experimental data un-

der control and drug block conditions in deterministic simulations. The population of stochastic models was then used to simulate the temporal variability in the $APD_{90}$ and the following measures were used to quantify this variability: $STV_{APD90}$, the range in $APD_{90}$ and the variance in $APD_{90}$. The results presented demonstrate that the intrinsic stochastic fluctuations in the repolarisation currents contribute to beat-to-beat variability in $APD_{90}$. Furthermore, the current with the smallest number of channels, namely $I_{Kr}$, contributes the most to beat-to-beat variability in $APD_{90}$. We presented evidence showing there is a stronger relationship between mean $APD_{90}$ and $STV_{APD90}$ than between the number of $I_{Kr}$ channels and $STV_{APD90}$ suggesting that mean $APD_{90}$ is more important in determining the magnitude of $STV_{APD90}$. However, our we also found a strong relationship between mean $APD_{90}$ and the number of $I_{Kr}$ channels. Therefore our results suggest that the number of $I_{Kr}$ channels is important in determining the magnitude of the mean $APD_{90}$ and this in turn affects the magnitude of the $STV_{APD90}$.

# 9

# Conclusions and Future Work

*We conclude this thesis by reviewing the accomplishments discussed in the previous chapters. We begin by recapping the initial motivation for this thesis and briefly summarise the work undertaken to achieve these goals. In Section 9.2 we describe the key contributions of this work. Possible improvements to the models and numerical techniques, as well as extensions to the simulation study, are discussed in Section 9.3. We end with some concluding remarks.*

## 9.1 Summary

Sudden cardiac death as a result of the development of cardiac arrhythmias is one of the main causes of death world-wide. Many of the mechanisms underlying the development of such arrhythmias remain incompletely understood and so biomarkers that successfully predict the onset of such a condition have become an important tool in reducing the incidence of life-threatening arrhythmias. In recent years, multiscale biophysically detailed computational models developed in conjunction with experiments, have played a pivotal role in advancing our knowledge into why, when and how arrhythmias can develop, as well as identifying biomarkers that predict arrhythmic risk. However, such models ignore the variability both intrinsic and extrinsic to cardiac dynamics.

In particular, the magnitude in the beat-to-beat variations in the electrical dynamics of the heart, observed in clinical and experimental recordings, have been shown to correlate well with the incidence of arrhythmia and so this is a potentially powerful new biomarker of arrhythmic risk. This beat-to-beat variability is thought to be caused by the stochastic dynamics of ion channels that lie in the membrane of cardiac cells and play an important role in cardiac electrophsyiology. However, most computational cardiac cell models are deterministic and so are unable to simulate such variability. Furthermore, studies that have tried to incorporate stochastic ion channel dynamics into computational cell models are either computationally intensive, limiting their applicability to simpler cell models, or are not guaranteed to give biologically realistic simulations. The goal of this thesis is therefore to address these issues in a mathematically rigorous manner by developing computationally efficient and biologically accurate models of the stochastic behaviour of ion channel dynamics within cardiac cell models. Such tools open up the possibility for future in-depth investigations into beat-to-beat variability in complex cardiac cell models, an area previously restricted by the limitations of the stochastic description of ion channel dynamics. Indeed, in the final part of this thesis we show the potential value of the mathematical models developed here in uncovering the role of stochastic ion channel dynamics in beat-to-beat variability.

We began in Chapter 2 by describing the structure and function of the heart. Particular attention was given to the electrophysiology of single cardiac cells and the role of ion channels in the generation of an action potential (AP). We described recent work that suggests beat-to-beat variability in the duration of the AP could be an indicator of an individuals arrhythmic potential. This provides the motivation for why we want to incorporate stochasticity into existing cardiac cell models. In the second part of this chapter we turned our attention to computational modelling of cardiac cell electrophysiology, providing the background on the current state of the field. We began with a thorough review of cardiac cell electrophysiology models that have been developed over the past 60 years, beginning with the ground breaking work of Hodgkin

and Huxley, and Noble, right up to the most recent biophysically detailed models of human cardiac cells. Finally we discussed the few studies that have investigated the causes of beat-to-beat variability and the limitations of these works.

In Chapter 3 we introduced the mathematical theory that underlies the models and simulation techniques developed in this thesis. In particular we described the different regimes for modelling and simulating stochastic behaviour of ion channel dynamics, and the way in which these approaches are related. Particular attention was paid to stochastic differential equations, SDEs, and we discussed numerical methods that can be used to approximate solutions to such equations. The SDE model of ion channel dynamics provided the starting point for our investigation into a stochastic model of ion channel dynamics since it is the most computationally efficient stochastic method, and so allows for incorporation into complex cardiac cell models in a computationally tractable way.

In Chapter 4 we discussed the two main challenges posed by simulating stochastic ion channel dynamics within existing cardiac electrophysiology cell models that have arisen within the literature in recent years. Namely, that the SDE model of ion channel dynamics frequently employed in the literature does not preserve the statistical properties of the discrete-state Markov chain model, and secondly, that the solutions to the SDE model can become negative, which is biologically unrealistic. We showed that the first issue is simply dealt with by formulating the SDE in terms of the whole channel dynamics rather than in terms of the collective behaviour of hypothetical gating variables, as was the approach previously employed in this field. The second issue is not so easily solved and the remainder of this chapter was devoted to analysing the simplest SDE model of ion channel dynamics, where the channel is assumed to be either open or closed, to shed light on the causes of this issue. We showed that the root of the issue lies with the form of the SDE model itself, rather than the numerical method used to simulate the dynamics, as is the common assumption within the literature. This finding provided the rationale behind the two biologically accurate methods developed in this thesis. That is, we

focus on ensuring the SDE model of ion channel dynamics itself provides biologically realistic solutions.

In Chapter 5 we described a possible approach to overcome the issue of negative solutions discussed at the end of Chapter 4. We approximated the ion channel SDE model by the Wright-Fisher model, a system of SDEs whose analytic solutions remain within a biologically realistic region. Current numerical methods are unable to preserve the boundaries inherent in the Wright-Fisher model. In the literature, the common approach to deal with this issue is to make alterations in the numerical scheme, to force the numerical approximation to remain in the desired region. However, to the best of our knowledge, such alterations have never been shown to converge to the solution of the SDE model. Therefore, we took a more rigorous approach and developed a new numerical scheme called the BISS method, which we proved preserves the boundaries inherent in the Wright-Fisher model. Strong convergence of this numerical scheme was proved in the simple one-dimensional case (where the channel can be either open or closed), and shown numerically for a multidimensional model. Finally, in this chapter we demonstrated that alterations commonly employed in the literature to force the numerical solution to remain in the correct region, can bias the mean of the Wright-Fisher model. Therefore the BISS method developed in this chapter provides an improvement to the numerical schemes previously employed to numerically approximate solutions to the Wright-Fisher model.

Since the issue with biologically unrealistic solutions to the SDE model was shown to be a result of the form of the model itself, at the beginning of Chapter 6 we reviewed the derivation of the SDE model from the discrete-state Markov chain model. This analysis suggested that solutions to the SDE model can go negative because the boundary conditions imposed on the continuous-state stochastic process, whose trajectories are described by the SDE, have, in some sense, become ‘lost’ in formulating the SDE. We therefore discussed how to incorporate boundaries into the ion channel SDE model to ensure analytic solutions remain in a biologically realistic region, and the resulting system is known in the literature as a reflected SDE. Further-

more, we argued that the reflected SDE model of ion channel dynamics is consistent with the approximation of the discrete-state Markov chain by a continuous-state stochastic process. To the best of our knowledge the reflected SDE model has not previously been used to model ion channel dynamics and is a novel approach to dealing with the issue of biologically unrealistic solutions to the SDE model. Finally, in this chapter we reviewed numerical techniques from the literature that have been developed to solve such systems of equations and in particular, detail the method employed in this thesis. The reflected SDE method therefore is an alternative SDE model of ion channel dynamics to that given in Chapter 5 that ensures biologically realistic solutions.

The two SDE models developed in Chapters 5 and 6 are both potential SDE models of ion channel dynamics that ensure biologically realistic solutions. Since the main goal of this thesis is to develop a stochastic model of ion channel dynamics that is both computationally efficient and accurate, in Chapter 7 we compared these two methods against the discrete-state Markov chain model which is taken as the 'gold-standard' within the literature. The original Hodgkin-Huxley model, as well as a variant of this model, were used for the comparison since the Hodgkin-Huxley model provides the basis for most cardiac cell electrophysiology models. The first two moments in the number of open channels calculated using the two SDE models were compared with the discrete-state Markov model to determine the accuracy of the two SDE models in preserving the statistical properties of the 'gold-standard' approach. We also considered the action potential statistics of the two SDE models developed in this thesis, along with an alternative SDE model recently employed in the literature, to ensure the SDE models accurately capture the variability in the action potential that arises due to the stochastic behaviour of the ion channel dynamics. From these comparisons it was clear that the reflected SDE captured the dynamics of the 'gold standard' stochastic simulation method more accurately than the Wright-Fisher model and the SDE model from the literature. Finally, we also compared the average simulation time for the two SDE models developed in this thesis and the discrete-state Markov

chain model. It was clear that the reflected SDE was the fastest method, particularly for large channel numbers. The analysis of this chapter showed that the reflected SDE method developed in this thesis not only ensures biologically realistic solutions, but is also computationally efficient and accurately captures the stochastic dynamics of the 'gold-standard' approach, therefore successfully achieving the main goal of this thesis.

The reflected SDE model of ion channel dynamics is applied in Chapter 8 to investigate the role of stochastic ion channel dynamics in the beat-to-beat variability in the action potential duration (APD) in a canine cardiac cell model, using a combined simulation and experimental approach. First a population of models, each based on the same model framework but with different parameter values, is constructed to account for the variability between different individuals within the population. Next the stochastic behaviour of the four key repolarisation currents is incorporated into each model using the reflected SDE method developed in this thesis. This population of stochastic models is used to show that the beat-to-beat variability caused by these four repolarisation currents lies within experimental range under both control and drug block conditions. Furthermore, our results showed that the stochastic behaviour of the rapid delayed rectifyer potassium current ($I_{Kr}$) channels contributes the most to beat-to-beat variability. Finally, our results suggest that the mean APD is important in determining the magnitude of variability, with larger mean APD leading to greater variability, but that mean APD is in turn related to the number of $I_{Kr}$ channels. The simulation study undertaken in this chapter demonstrates the potential power of the reflected SDE method in elucidating the potential causes of beat-to-beat variability.

## 9.2 Key Contributions and Main Findings

In addressing the first main goal of this thesis we have developed modelling and simulation techniques of ion channel dynamics in a mathematically rigorous manner, that had not hitherto been done, and so is a key contribution to the area of stochastic modelling and simulation of

ion channel dynamics. Through the analysis in the second part of Chapter 4 we showed that the issue of biologically unrealistic solutions to the SDE model lies with the form of the SDE model itself. This marks a major shift in the current thinking within the stochastic modelling community as to the cause of biologically unrealistic solutions to the SDE model and therefore is an important contribution to this area. Furthermore, this analysis provides a new rationale in dealing with this issue in a mathematically rigorous way and is the approach adopted throughout the thesis. This approach is an improvement over previous attempts to deal with this issue with the SDE model where alterations in the numerical scheme are employed that can lead to erroneous understanding of the system and introduce bias into the results.

The first key contribution of this thesis, presented in Chapter 4, was to show that by formulating the SDE model in terms of the whole channel dynamics, rather than the behaviour of hypothetical gating variables, the SDE model preserves the statistical properties of the discrete-state Markov chain model. Therefore, the contribution of this work has been to dispel the implication within this research community that the SDE model of ion channel dynamics does not preserve the statistical properties of the discrete-state Markov chain model.

The next contribution, presented in Chapter 5, was to show that stochastic ion channel behaviour can be approximately modelled by a system of SDEs, commonly referred to as the Wright-Fisher model, whose analytic solutions remain within a biologically realistic region. We also developed a numerical method, the BISS method, to ensure numerical approximations preserve the boundaries inherent in this system of equations, as current numerical techniques are unable to do so. The work from this chapter therefore allows for the simulation of ion channel dynamics using an SDE model that ensures simulations remain in a biologically realistic region. Furthermore, the Wright-Fisher model is frequently employed in the field of population dynamics and so the BISS method provides a contribution to this area, since it preserves the boundaries of this model in the numerical approximation without the need for any alteration to the numerical scheme. This represents an improvement on previous approaches within this field

to numerically solve the Wright-Fisher model. Indeed the issue that current numerical methods are unable to preserve the boundaries inherent in SDE models is a common challenge in many areas of stochastic modelling, such as in financial modelling. As such the BISS method is potentially applicable to a wider set of bounded SDE models, such as the Cox Ingersoll and Ross (CIR) model of short term interest rates used in financial modelling. During the construction of this method we developed insight into the convergence analysis of SDEs whose coefficients do not possess the Lipschitz condition, which we expect to be applicable in the numerical analysis research community to a wider set of problems.

The reflected SDE model presented in Chapter 6 provides a very important contribution of the first part of this thesis. It provides a computationally efficient method for simulating stochastic ion channel dynamics that preserves the stochastic behaviour of the discrete-state Markov model, as well as guaranteeing analytic and numerical realisations remain within a biologically realistic region, as illustrated in Chapter 7. This modelling and simulation method allows for stochastic ion channel behaviour to be incorporated into complex cardiac cell electrophysiology models, as well as potentially into tissue level models, in a computationally tractable way, but not at the cost of biologically accuracy. Balancing computational efficiency with accuracy in modelling the intrinsic stochastic behaviour of a system is a challenge in modelling many physical systems. Indeed, the reflected SDE method described here provides a general framework for modelling stochastic dynamics of physical systems by approximate methods in an accurate and efficient way and is applicable to a wide class of problems. This work therefore opens up the potential to accurately investigate the effects of stochastic ion channel behaviour in complex multiscale models, an area previously restricted by the inaccuracies of the SDE modelling approach.

The final key contribution of this thesis were the conclusions from the combined simulation and experimental study into the effects of stochastic ion channel behaviour on the variability in the action potential (AP) of a canine ventricular myocyte, presented in Chapter 8. Due to the

complexity of the most up to date canine cardiac cell model (namely the Decker model), without the novel stochastic modelling and simulation techniques developed in this thesis such an investigation would not have been possible as the problem would have become computationally intractable and also inaccurate. That is why previous studies have employed simpler cardiac cell models, such as the Faber-Rudy guinea pig model, (Lemay et al., 2011; Pueyo et al., 2011), in order to investigate the effects of stochastic ion channel dynamics on AP variability. We showed that the beat-to-beat variability in AP duration caused by the stochastic ion channel behaviour of the four key repolarisation currents, $I_{Kr}$, $I_{Ks}$, $I_{To1}$ and $I_{CaL}$, lies within experimental range and that $I_{Kr}$ is the largest contributor to beat-to-beat variability. Our results also suggested that the mean AP duration was significant in determining the magnitude of the variability. Beat-to-beat variability in AP duration is thought to be a measure of repolarisation reserve and so is a potential biomarker for prediction of arrhythmic risk. Therefore the findings of the simulation study undertaken in this thesis are important since they shed light on the role stochastic ion channel dynamics play in beat-to-beat AP variability. Furthermore, this study shows that the stochastic model of ion channel dynamics developed in this thesis can be successfully employed to capture stochastic ion channel behaviour within cardiac cell electrophysiology models in a computationally efficient and accurate manner. We expect this to be applicable to the construction of in-silico methods for testing new drug compounds, since the stochastic ion channel model allows for simulation of beat-to-beat variability which is a new biomarker of arrhythmic risk. We also anticipate these methods to aid in future studies into the underlying mechanisms of beat-to-beat variability in repolarisation.

## 9.3 Future Work

We now suggest a number areas of potential future research. We begin by considering the modelling and numerical aspects that could be improved or developed. We then discuss the way in which the simulation study presented in Chapter 8 could be extended to improve our understand-

ing of the role of stochastic ion channel dynamics in beat-to-beat variability in repolarisation and the implications for arrhythmia development.

### 9.3.1 Improvements to Modelling and Simulation Methods

The BISS method for the multidimensional Wright-Fisher model was only shown to converge numerically in the strong sense in Chapter 5. Therefore an obvious extension would be to analytically prove this convergence. The difficulty, as with the simple one-dimensional (two state model) case, is that the diffusion coefficient does not satisfy the Lipschitz condition, and so many standard results from stochastic analysis can not be applied. However, since the diffusion coefficient satisfies the weaker Hölder condition, the techniques used in the one-dimensional case to obtain convergence could be extended to the multidimensional case. Future investigations could also consider improving the strong convergence of the BISS method to higher orders. For example, instead of using the balanced implicit method to solve the SDE, the balanced Milstein method (BMM) could be used instead. Since this method has a higher strong order it is thought that this would improve the order of convergence of the BISS method.

Through the use of reflected SDEs to model ion channel dynamics, and the presentation of the rational behind such a modelling approach, we have provided a novel technique to capture the intrinsic stochastic dynamics of physical systems that preserves the boundaries inherent in the system. There are therefore many ways in which this work could be extended.

The first obvious avenue of future research would be to employ these methods to study more complex biochemical reaction networks and to see how this method compares to the discrete-state Markov model for these more involved systems. Another area of possible future research would be to perform a more thorough analytical analysis on the reflected SDE model. It is likely that the addition of the reflecting process will have some effect on the mean and variance of the original SDE model. This potential alteration could be analytically quantified, so as to gain a better understanding of the way the continuous-state stochastic process behaves near the

boundaries. Also, in a lecture series by Kurtz (Kurtz, 2007), the author derives a reflected SDE model for a simple single server queuing model directly from the discrete-state Markov chain model. An interesting future avenue of research therefore would be to try to extend these same arguments to a model of ion channel dynamics so as to derive the reflected SDE model directly from the discrete-state Markov chain.

As well as many future areas of possible investigation into the mathematics underlying the reflected SDE model, there is also much that could be done on the development of numerical techniques that better approximate solutions to such systems. There are a limited range of numerical techniques for reflected SDEs and all have relatively low orders of strong convergence. The low convergence is mainly due to the fact that the process can lie in the correct region at two discrete time points, but may have left the boundaries between these time points without any impact on the numerical approximation. This difficulty, that arises in trying to accurately approximate the reflecting process at the time discretisation grid points, has seriously hampered the construction of higher order numerical methods. Therefore, a great challenge for future work is to try to determine a more rigorous manner of capturing the reflecting process so as to improve the accuracy of the numerical approximations to reflected SDEs. Such techniques would be expected to lead to even better agreement in the stochastic dynamics between the reflected SDE and the discrete-state Markov chain model.

### 9.3.2 Investigations into the Effects of Stochastic Ion Channel Behaviour

The population of models, developed to incorporate the effects of extrinsic noise, does not capture the full range of possible experimental behaviour. Therefore an obvious extension to the work presented in Chapter 8 would be to determine a population of models that is more representative of the experimentally observed behaviour. This would allow for a more detailed investigation into the relationship between intrinsic and extrinsic noise. This could be done by varying more parameters within the model, as well as varying the parameters over a greater

range in order to construct the population of models. Also the number of traces for the ionic current block experiments, which were used to construct the population of models, was very small. Therefore, obtaining a larger number of traces would improve the accuracy in the estimation of the experimental range used in constructing the population of models.

The electrical coupling between cells at the tissue level is known to be a modulator of the electrical dynamics seen at the single cell level. Indeed, in both (Pueyo et al., 2011; Lemay et al., 2011), electrotonic interactions between cells are shown to dampen the effects of stochastic ion channel behaviour under normal conditions. However, under conditions of reduced coupling, such as disease, these effects manifest themselves at the tissue level. Therefore a clear avenue of future research would be to incorporate the stochastic single cell model developed here into a tissue level model, so as to compare the effects of stochastic ion channel behaviour at the single cell and tissue level.

Modulation in pacing rate has also been shown to alter the effects of stochastic ion channel behaviour on beat-to-beat AP variability at the single cell level, (Lemay et al., 2011; Pueyo et al., 2011). Therefore, the methods developed here could be used to further investigate how pacing rate is related to changes in the variability of the AP as a result of stochastic ion channel behaviour.

In the simulation study in Chapter 8 we only considered the stochastic behaviour of the four repolarisation currents, and we did not consider the potential effects of the stochastic behaviour of the fast sodium current $I_{Na}$ on beat-to-beat variability in repolarisation. This was because $I_{Na}$ plays a major role in the upstroke of the AP, but is less prominent during the repolarisation phase. However, $I_{Na}$ is thought to play a role in repolarisation reserve, (Varró and Baczkó, 2011), and so may be important in beat-to-beat variability, particularly under pathological conditions such as drug block. Therefore, the reflected SDE model of ion channel dynamics developed in this thesis could be used to model the stochastic behaviour of the sodium current in the Decker model. Such a study could provide further insight into the mechanisms underlying

beat-to-beat variability under control and pathological conditions.

## 9.4 Concluding Remarks

Computational modelling and simulation have played an ever more important and prominent role in cardiovascular research in recent years. The development of mathematical descriptions of the heart in combination with experiments has led to greater insight into the sub-cellular, cellular and tissue level mechanisms of this complex and profoundly multiscale biological organ and what can happen when such mechanisms fail. However, few computational models take into account the heterogeneities and intrinsic stochastic behaviour of the processes involved in this system. In particular, models that have attempted to account for the intrinsic stochastic dynamics within cardiac cells are either computationally intensive or inaccurate.

In this thesis we have developed mathematical modelling and simulation methods that allow for computationally efficient and accurate simulation of stochastic ion channel dynamics within cardiac cell electrophysiology models, whilst ensuring solutions to the model itself as well as simulations remain in a biologically realistic region, without the need for alternations to the numerical scheme. The major contribution has been the proposal to describe the continuous-state stochastic model of ion channel dynamics using a reflected SDE. This represents a significant advancement over previous SDE descriptions of the continuous-state stochastic model, since this method incorporates the boundary constraints of this biological problem into the model formulation directly. This is much more satisfying than altering the numerical method, which can potentially bias the solution, as has been the approach previously employed in the literature. Results indicate that the reflected SDE model accurately captures the stochastic behaviour of the discrete-state Markov chain, whilst achieving a considerable speed up in simulation time.

The results presented show that the reflected SDE model can be used to efficiently simulate the stochastic behaviour of ion channel dynamics whilst ensuring statistical and biological accu-

racy. Furthermore, we implemented this method into a canine cardiac cell electrophysiology model, in order to undertake a preliminary investigation into the role of stochastic ion channel behaviour in beat-to-beat variability in repolarisation of cell electrical dynamics. This study not only showed the potential power of the reflected SDE model in simulating stochastic ion channel behaviour within complex electrophsyiology models but also illustrated the role of the stochastic dynamics of the repolarisation currents in beat-to-beat variability.

Unlike in previous studies, in this thesis we take a mathematically rigorous approach to the modelling and simulation of ion channel dynamics to allow for investigation into fundamental questions surrounding beat-to-beat variability that were previously restricted by the limitations of the stochastic modelling and simulation methods currently employed. The tools developed in this thesis and the preliminary results of the simulation study could be built upon to provide further investigation into the effects of stochastic ion channel dynamics on beat-to-beat variability at the cellular and tissue level, both under normal and pathological conditions. Such studies are vital to improve our understanding into the mechanisms underlying beat-to-beat variability, a potential measure of repolarisation reserve, and in particular to help explain the relationship between beat-to-beat variability and the development of life-threatening arrhythmias. It is therefore hoped that the modelling and simulation techniques along with the simulation study presented in this thesis provide a valuable contribution to the fields of stochastic modelling and simulation, and cardiac electrophysiology.

# A

# Hodgkin-Huxley Equations

## A.1 Original Hodgkin-Huxley Model

The original Hodgkin-Huxley model assumes that the membrane potential is governed by a stimulus current along with three ionic currents: a sodium current ($I_{Na}$), a potassium current ($I_K$) and a leakage current ($I_L$). $I_{Na}$ and $I_K$ are both assumed to depend on the membrane potential and so are time dependent while the leakage current is taken to be constant. The change in transmembrane potential, $V$, is described by the following ordinary differential equation (ODE),

$$\frac{dV}{dt} = -\frac{1}{C}\left(G_{Na}p_O^{Na}(V - E_{Na}) + G_K p_O^K (V - E_K) + G_L(V - E_L) - I\right). \tag{A.1}$$

The constants in the above formula are, $C$, the membrane capacitance, $I$, the stimulus current, $E_i$, the reversal potential for the current of type $i$ and $G_i$, the maximum conductance for current of type $i$. These constants are taken to be the following values,

$$C = 1\,\mu F/cm^2 \quad G_{Na} = 120\,mS/cm^2 \quad G_K = 36\,m\,S/cm^2 \quad G_L = 0.3\,mS/cm^2 \tag{A.2}$$
$$E_{Na} = 115\,mV \quad E_K = -12\,mV \quad E_L = 10.6\,mV,$$

and $I = 0pA$ unless otherwise stated.

In (A.1), $p_O^{Na} = m^3h$, $p_0^K = n^4$, where the gating variables $m$, $h$ and $n$ are each described by the following ODE,

$$\frac{di}{dt} = a_i - (a_i + b_i)i, \tag{A.3}$$

for $i = m, h,$ or $n$. The transition rates $a_i$, $b_i$ for $i = m,\ h,\ n$ are taken to be the following functions of the membrane potential $V$,

$$a_m(V) = 0.1\frac{25 - V}{e^{((25-V)/10)} - 1},\ \ b_m(V) = 4e^{\left(-\frac{V}{18}\right)}, \tag{A.4}$$

$$a_h(V) = 0.07e^{\left(-\frac{V}{20}\right)},\ \ b_h(V) = \frac{1}{e^{((30-V)/10)} + 1}, \tag{A.5}$$

$$a_n(V) = \frac{0.01\,(10 - V)}{e^{((10-V)/10)} - 1},\ \ b_n(V) = 0.125e^{\left(\frac{-V}{80}\right)}. \tag{A.6}$$

## A.2 Variant of The Hodgkin-Huxley Model

In Chapter 4, a variant of the sodium and potassium channel dynamics in the original Hodgkin-Huxley model are used in simulations. The sodium and potassium channels are still assumed to consist of the same gating variables as in the original Hodgkin-Huxley model, however the open to closed and closed to open transition rates, $a_i$ and $b_i$ respectively, are taken to be the following functions of the membrane potential, $V$,

$$a_m(V) = \frac{1.872(V - 25.41)}{1 - e^{(25.41-V)/6.06}},\ \ b_m = \frac{3.973(21.001 - V)}{1 - e^{(V+27.74)/9.41}}, \tag{A.7}$$

$$a_h(V) = \frac{-0.549(27.74 + V)}{1 - e^{(V+27.74)/9.06}},\ \ b_h = \frac{22.57}{1 - e^{(56-V)/12.5}}, \tag{A.8}$$

$$a_n(V) = \frac{0.129(V - 35)}{1 - e^{(35-V)/10}},\ \ b_n = \frac{0.3236(35 - V)}{1 - e^{(V-35)/10}}. \tag{A.9}$$

The above formula describe the channel gating dynamics for an auditory nerve fibre, and are taken from Bruce (2009).

The variant of the Hodgkin-Huxley model, employed in the simulations in Chapter 7 is again taken from (Bruce, 2009). This model describes the generation of an action potential along

an auditory nerve fibre. Unlike the original Hodgkin-Huxley model, the voltage is assumed to be governed only by a single ionic current, the potassium current, $I_{Na}$. Furthermore, instead of determining the conductance of this channel as the product of the maximum conductance and the proportion of open channels, it is equivalently described by the individual current and the *number* of open channels. Therefore, the transmembrane potential, $V$, is described by the following ODE,

$$\frac{dV}{dt} = \frac{1}{C}\left(-\gamma_{Na} N_{Na}^{O}\,(V - E_{Na}) - \frac{V}{R} + I\right). \tag{A.10}$$

The constants in the above equation are, $C$, the membrane capacitance, $R$, the membrane resistance, $\gamma_{Na}$ the single-channel sodium conductance and $I$ the stimulus current. In simulations $C$ and $R$ are scaled with the number of channels assuming either constant channel density or constant membrane area, as described in Chapter 7. The values of the stimulus current used in simulations are also given in Chapter 7. The remaining constants are taken to be the following values,

$$\gamma_{Na} = 25.69 pS/\text{channel}, \quad E_{Na} = 144\,mV, \tag{A.11}$$

where $N_{Na}^{O}$ is the number of open sodium channels. The transition rates for the $m$ and $h$ gates are taken to be the same functions of the voltage as given by (A.7) and (A.8).

# B

# Noise Analysis Figures

**Figure B.1** Left: Mean and variance plots for $I_{Ks}$ (top) and $I_{CaL}$ (bottom). Right: Power spectral densities for $I_{Ks}$ (top) and $I_{CaL}$ (bottom).

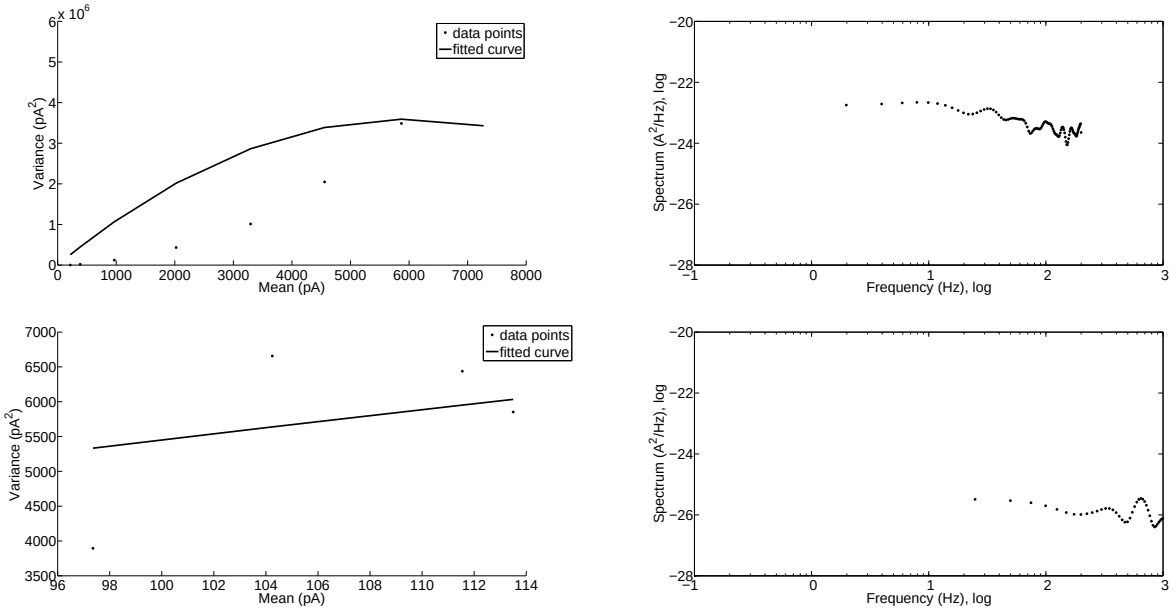


In the left hand plots in Figure B.1, the following contraints were placed on the coefficients estimated using the *fmincon* function in MATLAB: $a_0$ was set to be $0$, $a_1$ was restricted to the interval $[0.1, \infty)$ and $a_2$ was restricted to the interval $(-\infty, -0.1]$. For $I_{Ks}$ the estimated single channel current is $0.39123\ pA$ for membrane potential equal to $50mV$. For $I_{CaL}$ the estimated single channel current is $0.50263\ pA$ for membrane potential equal to $-10mV$.

# C

# Reflected SDEs for Decker model

## C.1 Matrices for $I_{CaL}$ RSDE

$$\boldsymbol{y}_{CaL} = (C, O, C^\star, O^\star, CI, OI, CI^\star, OT^\star)^T .$$

$$E_{CaL} = \begin{pmatrix} -1 & 0 & 0 & 0 & -1 & 0 & 0 & 0 & -1 & 0 & 0 & 0 \\ 1 & 0 & 0 & 0 & 0 & -1 & 0 & 0 & 0 & -1 & 0 & 0 \\ 0 & -1 & 0 & 0 & 1 & 0 & 0 & 0 & 0 & 0 & 1 & 0 \\ 0 & 1 & 0 & 0 & 0 & 1 & 0 & 0 & 0 & 0 & 0 & 1 \\ 0 & 0 & -1 & 0 & 0 & 0 & -1 & 0 & 1 & 0 & 0 & 0 \\ 0 & 0 & 1 & 0 & 0 & 0 & 0 & -1 & 0 & 1 & 0 & 0 \\ 0 & 0 & 0 & -1 & 0 & 0 & 1 & 0 & 0 & 0 & -1 & 0 \\ 0 & 0 & 0 & 1 & 0 & 0 & 0 & 1 & 0 & 0 & 0 & -1 \end{pmatrix} .$$

$$M_{CaL} = \begin{pmatrix} -(a+d+y) & b & e & 0 & x & 0 & 0 & 0 \\ a & -(b+d+y) & 0 & e & 0 & x & 0 & 0 \\ d & 0 & -(a+e+y^\star) & b & 0 & 0 & x^\star & 0 \\ 0 & d & a & -(b+e+y^\star) & 0 & 0 & 0 & x^\star \\ y & 0 & 0 & 0 & -(a+dI+x) & b & eI & 0 \\ 0 & y & 0 & 0 & a & -(b+x+dI) & 0 & eI \\ 0 & 0 & y^\star & 0 & dI & 0 & -(a+eI+x^\star) & b \\ 0 & 0 & 0 & y^\star & 0 & dI & a & -(b+eI+x^\star); \end{pmatrix} .$$

$$F_{CaL} = diag \begin{pmatrix} \sqrt{ay_{CaL,1}+by_{CaL,2}} \\ \sqrt{ay_{CaL,3}+by_{CaL,4}} \\ \sqrt{ay_{CaL,5}+by_{CaL,6}} \\ \sqrt{ay_{CaL,7}+by_{CaL,8}} \\ \sqrt{dy_{CaL,1}+ey_{CaL,3}} \\ \sqrt{dy_{CaL,2}+ey_{CaL,4}} \\ \sqrt{dIy_{CaL,5}+eIy_{CaL,7}} \\ \sqrt{dIy_{CaL,6}+eIy_{CaL,8}} \\ \sqrt{yy_{CaL,1}+xy_{CaL,5}} \\ \sqrt{yy_{CaL,2}+xy_{CaL,6}} \\ \sqrt{y^\star y_{CaL,3}+x^\star y_{CaL,7}} \\ \sqrt{y^\star y_{CaL,4}+x^\star y_{CaL,8}}; \end{pmatrix} .$$

## C.2 Matrices for $I_{Ks}$ RSDE

$$\boldsymbol{y}_{Ks} = (O_2, O_1, C_{15}, C_{14}, C_{13}, C_{12}, C_{11}, C_{10}, C_9, C_8, C_7, C_6, C_5, C_4, C_3, C_2, C_1)^T .$$

$$E_{Ks} = \begin{pmatrix}
1 & 0 & 0 & 0 & 0 & 0 & 0 & 0 & 0 & 0 & 0 & 0 & 0 & 0 & 0 & 0 & 0 & 0 & 0 & 0 & 0 & 0 \\
-1 & 1 & 0 & 0 & 0 & 0 & 0 & 0 & 0 & 0 & 0 & 0 & 0 & 0 & 0 & 0 & 0 & 0 & 0 & 0 & 0 & 0 \\
0 & -1 & 1 & 0 & 0 & 0 & 0 & 0 & 0 & 0 & 0 & 0 & 0 & 0 & 0 & 0 & 0 & 0 & 0 & 0 & 0 & 0 \\
0 & 0 & -1 & 1 & 0 & 1 & 0 & 0 & 0 & 0 & 0 & 0 & 0 & 0 & 0 & 0 & 0 & 0 & 0 & 0 & 0 & 0 \\
0 & 0 & 0 & -1 & 1 & 0 & 0 & 0 & 0 & 0 & 0 & 0 & 0 & 0 & 0 & 0 & 0 & 0 & 0 & 0 & 0 & 0 \\
0 & 0 & 0 & 0 & 0 & -1 & 1 & 0 & 0 & 0 & -1 & 0 & 0 & 0 & 0 & 0 & 0 & 0 & 0 & 0 & 0 & 0 \\
0 & 0 & 0 & 0 & -1 & 0 & 1 & -1 & 0 & -1 & 0 & 0 & 0 & 0 & 0 & 0 & 0 & 0 & 0 & 0 & 0 & 0 \\
0 & 0 & 0 & 0 & 0 & 0 & 0 & 1 & -1 & 0 & 0 & 0 & 0 & 0 & 0 & 0 & 0 & 0 & 0 & 0 & 0 & 0 \\
0 & 0 & 0 & 0 & 0 & 0 & 0 & 0 & 0 & 0 & 1 & -1 & 0 & 0 & 0 & 0 & 0 & -1 & 0 & 0 & 0 & 0 \\
0 & 0 & 0 & 0 & 0 & 0 & 0 & 0 & 0 & 1 & 0 & 1 & -1 & 0 & 0 & 0 & -1 & 0 & 0 & 0 & 0 & 0 \\
0 & 0 & 0 & 0 & 0 & 0 & 0 & 0 & 1 & 0 & 0 & 0 & 1 & -1 & 0 & -1 & 0 & 0 & 0 & 0 & 0 & 0 \\
0 & 0 & 0 & 0 & 0 & 0 & 0 & 0 & 0 & 0 & 0 & 0 & 0 & 1 & -1 & 0 & 0 & 0 & 0 & 0 & 0 & 0 \\
0 & 0 & 0 & 0 & 0 & 0 & 0 & 0 & 0 & 0 & 0 & 0 & 0 & 0 & 0 & 0 & 0 & 1 & -1 & 0 & 0 & 0 \\
0 & 0 & 0 & 0 & 0 & 0 & 0 & 0 & 0 & 0 & 0 & 0 & 0 & 0 & 0 & 0 & 0 & 1 & 0 & 1 & -1 & 0 & 0 \\
0 & 0 & 0 & 0 & 0 & 0 & 0 & 0 & 0 & 0 & 0 & 0 & 0 & 0 & 0 & 1 & 0 & 0 & 0 & 1 & -1 & 0 \\
0 & 0 & 0 & 0 & 0 & 0 & 0 & 0 & 0 & 0 & 0 & 0 & 0 & 0 & 1 & 0 & 0 & 0 & 0 & 0 & 1 & -1 \\
0 & 0 & 0 & 0 & 0 & 0 & 0 & 0 & 0 & 0 & 0 & 0 & 0 & 0 & 0 & 0 & 0 & 0 & 0 & 0 & 0 & 1
\end{pmatrix} .$$

$$M_{Ks} = \begin{pmatrix}
-\delta_1 & p & 0 & 0 & 0 & 0 & 0 & 0 & 0 & 0 & 0 & 0 & 0 & 0 & 0 & 0 & 0 & 0 \\
w & -\delta_2 & u & 0 & 0 & 0 & 0 & 0 & 0 & 0 & 0 & 0 & 0 & 0 & 0 & 0 & 0 & 0 \\
0 & n & -\delta_3 & g & 0 & 0 & 0 & 0 & 0 & 0 & 0 & 0 & 0 & 0 & 0 & 0 & 0 & 0 \\
0 & 0 & 4d & -\delta_4 & a & 2g & 0 & 0 & 0 & 0 & 0 & 0 & 0 & 0 & 0 & 0 & 0 & 0 \\
0 & 0 & 0 & b & -\delta_5 & 0 & g & 0 & 0 & 0 & 0 & 0 & 0 & 0 & 0 & 0 & 0 & 0 \\
0 & 0 & 0 & 3d & 0 & -\delta_6 & a & 0 & 3g & 0 & 0 & 0 & 0 & 0 & 0 & 0 & 0 & 0 \\
0 & 0 & 0 & 0 & 3d & 2b & -\delta_7 & 2a & 0 & 2g & 0 & 0 & 0 & 0 & 0 & 0 & 0 & 0 \\
0 & 0 & 0 & 0 & 0 & 0 & b & -\delta_8 & 0 & 0 & g & 0 & 0 & 0 & 0 & 0 & 0 & 0 \\
0 & 0 & 0 & 0 & 0 & 2d & 0 & 0 & -\delta_9 & a & 0 & 0 & 4g & 0 & 0 & 0 & 0 & 0 \\
0 & 0 & 0 & 0 & 0 & 0 & 2d & 0 & 3b & -\delta_{10} & 2a & 0 & 0 & 3g & 0 & 0 & 0 & 0 \\
0 & 0 & 0 & 0 & 0 & 0 & 0 & 2d & 0 & 2b & -\delta_{11} & 3a & 0 & 0 & 2g & 0 & 0 & 0 \\
0 & 0 & 0 & 0 & 0 & 0 & 0 & 0 & 0 & 0 & b & -\delta_{12} & 0 & 0 & 0 & g & 0 & 0 \\
0 & 0 & 0 & 0 & 0 & 0 & 0 & 0 & d & 0 & 0 & 0 & -\delta_{13} & a & 0 & 0 & 0 & 0 \\
0 & 0 & 0 & 0 & 0 & 0 & 0 & 0 & 0 & d & 0 & 0 & 4b & -\delta_{14} & 2a & 0 & 0 & 0 \\
0 & 0 & 0 & 0 & 0 & 0 & 0 & 0 & 0 & 0 & d & 0 & 0 & 3b & -\delta_{15} & 3a & 0 & 0 \\
0 & 0 & 0 & 0 & 0 & 0 & 0 & 0 & 0 & 0 & 0 & d & 0 & 0 & 2b & -\delta_{16} & 4a & 0 \\
0 & 0 & 0 & 0 & 0 & 0 & 0 & 0 & 0 & 0 & 0 & 0 & 0 & 0 & 0 & b & -\delta_{17} & 0
\end{pmatrix} ,$$

where the diagonal entries in the above matrix are given by,

$$(\delta_1, \ldots, \delta_4) = (w, (p+n), (u+4d), (g+3d+b)) ,$$

$$(\delta_5, \ldots, \delta_8) = ((a+3d), 2(g+d+b), (g+a+2d+b), 2(a+d)) ,$$

$$(\delta_9,\ldots,\delta_{12}) = ((3g+d+3b),(a+2g+d+2b),(2a+b+g+d),(3a+d))\,,$$

$$(\delta_{13},\ldots,\delta_{17}) = (4(g+b),(a+3g+3b),2(a+b+g),(b+3a+g),4a)\,.$$

$$F_{Ks} = diag\begin{pmatrix} \sqrt{wy_{Ks,1}+py_{Ks,2}} \\ \sqrt{uy_{Ks,3}+ny_{Ks,2}} \\ \sqrt{4dy_{Ks,3}+gy_{Ks,4}} \\ \sqrt{ay_{Ks,5}+by_{Ks,4}} \\ \sqrt{3dy_{Ks,5}+gy_{Ks,7}} \\ \sqrt{3dy_{Ks,4}+2gy_{Ks,6}} \\ \sqrt{ay_{Ks,7}+2by_{Ks,6}} \\ \sqrt{2ay_{Ks,8}+by_{Ks,7}} \\ \sqrt{2dy_{Ks,8}+gy_{Ks,11}} \\ \sqrt{2gy_{Ks,10}+2dy_{Ks,7}} \\ \sqrt{3gy_{Ks,9}+2dy_{Ks,6}} \\ \sqrt{ay_{Ks,10}+3by_{Ks,9}} \\ \sqrt{2ay_{Ks,11}+2by_{Ks,10}} \\ \sqrt{3ay_{Ks,12}+by_{Ks,11}} \\ \sqrt{dy_{Ks,12}+gy_{Ks,16}} \\ \sqrt{dy_{Ks,11}+2gy_{Ks,15}} \\ \sqrt{dy_{Ks,10}+3gy_{Ks,14}} \\ \sqrt{dy_{Ks,9}+4gy_{Ks,13}} \\ \sqrt{ay_{Ks,14}+4by_{Ks,13}} \\ \sqrt{2ay_{Ks,15}+3by_{Ks,14}} \\ \sqrt{3ay_{Ks,16}+2by_{Ks,15}} \\ \sqrt{4ay_{Ks,17}+by_{Ks,16}} \end{pmatrix}.$$

## C.3 Matrices for $I_{To1}$ RSDE

$$\boldsymbol{y}_{To1} = \left(y_{To1,1}, \ldots, y_{To1,16}\right)^T, \tag{C.1}$$

where

$$\left(y_{To1,1}, \ldots, y_{To1,3}\right) = \left(\alpha_3 i_{f,1} i_{s,1}, \alpha_2 i_{f,1} i_{s,1}, \alpha_1 i_{f,1} i_{s,1}\right),$$

$$\left(y_{To1,4}, \ldots, y_{To1,6}\right) = \left(\alpha_0 i_{f,1}, i_{s,1}, \alpha_3 i_{f,0} i_{s,1}, \alpha_2 i_{f,0} i_{s,1}\right),$$

$$\left(y_{To1,7}, \ldots, y_{To1,9}\right) = \left(\alpha_1 i_{f,0} i_{s,1}, \alpha_0 i_{f,0} i_{s,1}, \alpha_3 i_{f,1} i_{s,0}\right),$$

$$\left(y_{To1,10}, \ldots, y_{To1,12}\right) = \left(\alpha_2 i_{f,1} i_{s,0}, \alpha_1 i_{f,1} i_{s,0}, \alpha_0 i_{f,1} i_{s,0}\right),$$

$$\left(y_{To1,13}, \ldots, y_{To1,16}\right) = \left(\alpha_3 i_{f,0} i_{s,0}, \alpha_2 i_{f,0} i_{s,0}, \alpha_1 i_{f,0} i_{s,0}, \alpha_0 i_{f,0} i_{s,0}\right).$$

$$E_{To1} = \begin{pmatrix}
1 & 0 & 0 & 0 & 0 & 0 & 0 & 0 & 0 & 0 & 0 & 0 & -1 & 0 & 0 & 0 & 0 & 0 & 0 & 0 & -1 & 0 & 0 & 0 & 0 & 0 & 0 & 0 \\
-1 & 1 & 0 & 0 & 0 & 0 & 0 & 0 & 0 & 0 & 0 & 0 & 0 & -1 & 0 & 0 & 0 & 0 & 0 & 0 & 0 & -1 & 0 & 0 & 0 & 0 & 0 & 0 \\
0 & -1 & 1 & 0 & 0 & 0 & 0 & 0 & 0 & 0 & 0 & 0 & 0 & 0 & -1 & 0 & 0 & 0 & 0 & 0 & 0 & 0 & -1 & 0 & 0 & 0 & 0 & 0 \\
0 & 0 & -1 & 0 & 0 & 0 & 0 & 0 & 0 & 0 & 0 & 0 & 0 & 0 & 0 & -1 & 0 & 0 & 0 & 0 & 0 & 0 & 0 & -1 & 0 & 0 & 0 & 0 \\
0 & 0 & 0 & 1 & 0 & 0 & 0 & 0 & 0 & 0 & 0 & 0 & 1 & 0 & 0 & 0 & 0 & 0 & 0 & 0 & 0 & 0 & 0 & 0 & -1 & 0 & 0 & 0 \\
0 & 0 & 0 & -1 & 1 & 0 & 0 & 0 & 0 & 0 & 0 & 0 & 0 & 1 & 0 & 0 & 0 & 0 & 0 & 0 & 0 & 0 & 0 & 0 & 0 & -1 & 0 & 0 \\
0 & 0 & 0 & 0 & -1 & 1 & 0 & 0 & 0 & 0 & 0 & 0 & 0 & 0 & 1 & 0 & 0 & 0 & 0 & 0 & 0 & 0 & 0 & 0 & 0 & 0 & -1 & 0 \\
0 & 0 & 0 & 0 & 0 & -1 & 0 & 0 & 0 & 0 & 0 & 0 & 0 & 0 & 0 & 1 & 0 & 0 & 0 & 0 & 0 & 0 & 0 & 0 & 0 & 0 & 0 & -1 \\
0 & 0 & 0 & 0 & 0 & 0 & 1 & 0 & 0 & 0 & 0 & 0 & 0 & 0 & 0 & -1 & 0 & 0 & 0 & 1 & 0 & 0 & 0 & 0 & 0 & 0 & 0 & 0 \\
0 & 0 & 0 & 0 & 0 & 0 & -1 & 1 & 0 & 0 & 0 & 0 & 0 & 0 & 0 & 0 & 0 & -1 & 0 & 0 & 0 & 1 & 0 & 0 & 0 & 0 & 0 & 0 \\
0 & 0 & 0 & 0 & 0 & 0 & 0 & -1 & 1 & 0 & 0 & 0 & 0 & 0 & 0 & 0 & 0 & -1 & 0 & 0 & 0 & 1 & 0 & 0 & 0 & 0 & 0 & 0 \\
0 & 0 & 0 & 0 & 0 & 0 & 0 & 0 & -1 & 0 & 0 & 0 & 0 & 0 & 0 & 0 & 0 & 0 & 0 & -1 & 0 & 0 & 0 & 1 & 0 & 0 & 0 & 0 \\
0 & 0 & 0 & 0 & 0 & 0 & 0 & 0 & 0 & 1 & 0 & 0 & 0 & 0 & 0 & 1 & 0 & 0 & 0 & 0 & 0 & 0 & 0 & 0 & 1 & 0 & 0 & 0 \\
0 & 0 & 0 & 0 & 0 & 0 & 0 & 0 & 0 & -1 & 1 & 0 & 0 & 0 & 0 & 0 & 0 & 0 & 1 & 0 & 0 & 0 & 0 & 0 & 0 & 1 & 0 & 0 \\
0 & 0 & 0 & 0 & 0 & 0 & 0 & 0 & 0 & 0 & -1 & 1 & 0 & 0 & 0 & 0 & 0 & 0 & 0 & 1 & 0 & 0 & 0 & 0 & 0 & 0 & 1 & 0 \\
0 & 0 & 0 & 0 & 0 & 0 & 0 & 0 & 0 & 0 & 0 & -1 & 0 & 0 & 0 & 0 & 0 & 0 & 0 & 0 & 1 & 0 & 0 & 0 & 0 & 0 & 0 & 1
\end{pmatrix}.$$

$$M_{To1} = \begin{pmatrix}
-d_1 & \alpha_a & 0 & 0 & \alpha_f & 0 & 0 & 0 & \alpha_s & 0 & 0 & 0 & 0 & 0 & 0 & 0 \\
3\beta_a & -d_2 & 2\alpha_a & 0 & 0 & \alpha_f & 0 & 0 & 0 & \alpha_s & 0 & 0 & 0 & 0 & 0 & 0 \\
0 & 2\beta_a & -d_3 & 3\alpha_a & 0 & 0 & \alpha_f & 0 & 0 & 0 & \alpha_s & 0 & 0 & 0 & 0 & 0 \\
0 & 0 & \beta_a & -d_4 & 0 & 0 & 0 & \alpha_f & 0 & 0 & 0 & \alpha_s & 0 & 0 & 0 & 0 \\
\beta_f & 0 & 0 & 0 & -d_5 & \alpha_a & 0 & 0 & 0 & 0 & 0 & 0 & \alpha_s & 0 & 0 & 0 \\
0 & \beta_f & 0 & 0 & 3\beta_a & -d_6 & 2\alpha_a & 0 & 0 & 0 & 0 & 0 & 0 & \alpha_s & 0 & 0 \\
0 & 0 & \beta_f & 0 & 0 & 2\beta_a & -d_7 & 0 & 0 & 0 & 0 & 0 & 0 & \alpha_s & 0 & 0 \\
0 & 0 & 0 & \beta_f & 0 & 0 & \beta_a & -d_8 & 0 & 0 & 0 & 0 & 0 & 0 & 0 & \alpha_s \\
\beta_s & 0 & 0 & 0 & 0 & 0 & 0 & 0 & -d_9 & 0 & 0 & \alpha_f & 0 & 0 & 0 & \\
0 & \beta_s & 0 & 0 & 0 & 0 & 0 & 0 & 3\beta_a & -d_{10} & 2\alpha_a & 0 & 0 & \alpha_f & 0 & 0 \\
0 & 0 & \beta_s & 0 & 0 & 0 & 0 & 0 & 0 & 2\beta_a & -d_{11} & 3\alpha_a & 0 & 0 & \alpha_f & 0 \\
0 & 0 & 0 & \beta_s & 0 & 0 & 0 & 0 & 0 & 0 & \beta_a & -d_{12} & 0 & 0 & 0 & \alpha_f \\
0 & 0 & 0 & 0 & \beta_s & 0 & 0 & 0 & \beta_f & 0 & 0 & 0 & -d_{13} & \alpha_a & 0 & 0 \\
0 & 0 & 0 & 0 & 0 & \beta_s & 0 & 0 & 0 & \beta_f & 0 & 0 & 3\beta_a & -d_{14} & 2\alpha_a & 0 \\
0 & 0 & 0 & 0 & 0 & 0 & \beta_s & 0 & 0 & 0 & \beta_f & 0 & 0 & 2\beta_a & -d_{15} & 3\alpha_a \\
0 & 0 & 0 & 0 & 0 & 0 & 0 & \beta_s & 0 & 0 & 0 & \beta_f & 0 & 0 & \beta_a & -d_{16}
\end{pmatrix},$$

where the diagonal entries in the above matrix are,

$$(d_1, \ldots, d_3) = (3\beta_a + \beta_f + \beta_s, \alpha_a + 2\beta_a + \beta_f + \beta_s, 2\alpha_a + \beta_a + \beta_f + \beta_s)\,,$$

$$(d_4, \ldots, d_6) = (3\alpha_a + \beta_f + \beta_s, \alpha_f + 3\beta_a + \beta_s, \alpha_a + \alpha_f + 2\beta_a + \beta_s)\,,$$

$$(d_7, \ldots, d_9) = (2\alpha_a + \alpha_f + \beta_a + \beta_s, 3\alpha_a + \alpha_f + \beta_s, \alpha_s + 3\beta_a + \beta_f)\,,$$

$$(d_{10}, \ldots, d_{12}) = (\alpha_a + \alpha_s + 2\beta_a + \beta_f, 2\alpha_a + \alpha_s + \beta_a + \beta_f, 3\alpha_a + \alpha_s + \beta_f)\,,$$

$$(d_{13}, \ldots, d_{16}) = (3\alpha_a + \alpha_s + \beta_f, \alpha_f + \alpha_s + 3\beta_a, \alpha_a + \alpha_f + \alpha_s + 2\beta_a, 2\alpha_a + \alpha_f + \alpha_s + \beta_a)\,.$$

$$F_{To1} = diag\begin{pmatrix}
\sqrt{\alpha_a y_{To1,2}+3\beta_a y_{To1,1}} \\
\sqrt{2\alpha_a y_{To1,3}+2\beta_a y_{To1,2}} \\
\sqrt{3\alpha_a y_{To1,4}+\beta_a y_{To1,3}} \\
\sqrt{\alpha_a y_{To1,6}+3\beta_a y_{To1,5}} \\
\sqrt{2\alpha_a y_{To1,7}+2\beta_a y_{To1,6}} \\
\sqrt{3\alpha_a y_{To1,8}+\beta_a y_{To1,7}} \\
\sqrt{\alpha_a y_{To1,10}+3\beta_a y_{To1,9}} \\
\sqrt{2\alpha_a y_{To1,11}+2\beta_a y_{To1,10}} \\
\sqrt{3\alpha_a y_{To1,12}+\beta_a y_{To1,11}} \\
\sqrt{\alpha_a y_{To1,14}+3\beta_a y_{To1,13}} \\
\sqrt{2\alpha_a y_{To1,15}+2\beta_a y_{To1,14}} \\
\sqrt{3\alpha_a y_{To1,16}+\beta_a y_{To1,15}} \\
\sqrt{\beta_f y_{To1,1}+\alpha_f y_{To1,5}} \\
\sqrt{\beta_f y_{To1,2}+\alpha_f y_{To1,6}} \\
\sqrt{\beta_f y_{To1,3}+\alpha_f y_{To1,7}} \\
\sqrt{\beta_f y_{To1,4}+\alpha_f y_{To1,8}} \\
\sqrt{\beta_f y_{To1,9}+\alpha_f y_{To1,13}} \\
\sqrt{\beta_f y_{To1,10}+\alpha_f y_{To1,14}} \\
\sqrt{\beta_f y_{To1,11}+\alpha_f y_{To1,15}} \\
\sqrt{\beta_f y_{To1,12}+\alpha_f y_{To1,16}} \\
\sqrt{\beta_s y_{To1,1}+\alpha_s y_{To1,9}} \\
\sqrt{\beta_s y_{To1,2}+\alpha_s y_{To1,10}} \\
\sqrt{\beta_s y_{To1,3}+\alpha_s y_{To1,11}} \\
\sqrt{\beta_s y_{To1,4}+\alpha_s y_{To1,12}} \\
\sqrt{\beta_s y_{To1,5}+\alpha_s y_{To1,13}} \\
\sqrt{\beta_s y_{To1,6}+\alpha_s y_{To1,14}} \\
\sqrt{\beta_s y_{To1,7}+\alpha_s y_{To1,15}} \\
\sqrt{\beta_s y_{To1,8}+\alpha_s y_{To1,16}}
\end{pmatrix}.$$

# D

# Tables of Results from Population of Models

**Table D.2** Table of the scaling factors for each ionic current, $I_{CaL}$, $I_{Kr}$, $I_{Ks}$ and $I_{K1}$, for each of the models in the population. Note that the numbering of the models is arbitrary.

| Model | Scaling $I_{CaL}$ | Scaling $I_{Kr}$ | Scaling $I_{Ks}$ | Scaling $I_{K1}$ | Scaling $I_{To1}$ |
|---|---|---|---|---|---|
| 1 | 0.5074 | 0.7671 | 1.0995 | 1.7218 | 0.6747 |
| 2 | 0.5358 | 0.9415 | 1.4926 | 1.2454 | 0.7959 |
| 3 | 0.6094 | 0.9656 | 1.3389 | 1.4395 | 0.7951 |
| 4 | 0.5578 | 0.7076 | 1.1647 | 1.6082 | 0.7599 |
| 5 | 0.5375 | 0.9273 | 1.1510 | 1.5289 | 0.7031 |
| 6 | 0.7632 | 0.5698 | 1.3690 | 1.5866 | 0.8722 |
| 7 | 0.5336 | 0.7632 | 1.4255 | 1.5942 | 0.7613 |
| 8 | 0.7527 | 0.8266 | 1.4230 | 1.4949 | 0.8255 |
| 9 | 0.5123 | 0.8742 | 1.4088 | 1.5457 | 0.8802 |
| 10 | 0.7113 | 0.9110 | 1.4076 | 1.5014 | 0.8082 |
| 11 | 0.5212 | 0.6797 | 1.2733 | 1.7384 | 0.7054 |
| 12 | 0.5903 | 0.7200 | 1.2911 | 1.6628 | 0.8025 |
| 13 | 0.5237 | 0.8558 | 1.2781 | 1.6453 | 0.8678 |
| 14 | 0.8838 | 0.5857 | 1.4465 | 1.6642 | 0.8630 |
| 15 | 0.6855 | 0.8311 | 1.4807 | 1.7367 | 0.8852 |
| 16 | 0.7234 | 0.7345 | 1.3073 | 1.7261 | 0.8475 |
| 17 | 0.5275 | 0.9079 | 1.4529 | 1.7239 | 0.8509 |
| 18 | 0.7340 | 0.9476 | 1.4237 | 1.6411 | 0.8480 |
| 19 | 0.6270 | 0.7975 | 1.4775 | 1.4265 | 0.9241 |
| 20 | 0.7882 | 0.7234 | 1.4888 | 1.5627 | 0.9891 |
| 21 | 0.7432 | 0.9283 | 1.4725 | 1.4808 | 0.9250 |
| 22 | 0.6838 | 0.9064 | 1.4423 | 1.7953 | 0.9871 |
| 23 | 0.8271 | 0.9842 | 1.4743 | 1.6628 | 0.9401 |

**Table D.3** Estimated Number of Channels for Each Model

| Model | $N_{CaL}$ | $N_{Kr}$ | $N_{Ks}$ | $N_{To1}$ |
|---|---|---|---|---|
| 1 | 4038 | 641 | 7103 | 3801 |
| 2 | 4264 | 787 | 9643 | 4484 |
| 3 | 4850 | 807 | 8651 | 4479 |
| 4 | 4439 | 592 | 7525 | 4281 |
| 5 | 4277 | 775 | 7436 | 3961 |
| 6 | 6073 | 476 | 8846 | 4914 |
| 7 | 4247 | 638 | 9210 | 4289 |
| 8 | 5990 | 691 | 9195 | 4650 |
| 9 | 4077 | 731 | 9102 | 4959 |
| 10 | 5660 | 762 | 9095 | 4553 |
| 11 | 4148 | 568 | 8226 | 3974 |
| 12 | 4697 | 602 | 8342 | 4521 |
| 13 | 4168 | 716 | 8257 | 4889 |
| 14 | 7033 | 490 | 9348 | 4862 |
| 15 | 5455 | 695 | 9568 | 4987 |
| 16 | 5757 | 614 | 8447 | 4774 |
| 17 | 4198 | 759 | 9387 | 4794 |
| 18 | 5841 | 792 | 9200 | 4777 |
| 19 | 4989 | 667 | 9547 | 5206 |
| 20 | 6272 | 605 | 9621 | 5572 |
| 21 | 5914 | 776 | 9515 | 5211 |
| 22 | 5442 | 758 | 9320 | 5561 |
| 23 | 6581 | 823 | 9527 | 5296 |

# Bibliography


Abi-Gerges, N., Valentin, J.-P. P., and Pollard, C. E. (2010). Dog left ventricular midmyocardial myocytes for assessment of drug-induced delayed repolarization: short-term variability and proarrhythmic potential. *British journal of pharmacology*, 159(1):77–92.

Alcock, J. and Burrage, K. (2006). A note on the Balanced method. *Bit Numerical Mathematics*, 46(4):689–710.

Antzelevitch, C. (2001). The Brugada syndrome: ionic basis and arrhythmia mechanisms. *Journal of cardiovascular electrophysiology*, 12(2):268–272.

Asmussen, S. and Glynn, P. W. (2010). *Stochastic Simulation: Algorithms and Analysis*. Springer.

Asmussen, S., Glynn, P. W., and Pitman, J. (1995). Discretization Error in Simulation of One-dimensional Reflecting Brownian Motion. *The Annals of Applied Probability*, 5(4):875–896.

Atiga, W. L., Calkins, H., Lawrence, J. H., Tomaselli, G. F., Smith, J. M., and Berger, R. D. (1998). Beat-to-beat repolarization lability identifies patients at risk for sudden cardiac death. *Journal of cardiovascular electrophysiology*, 9(9):899–908.

Bayer, C., Szepessy, A., and Tempone, R. (2010). Adaptive weak approximation of reflected and stopped diffusions. *Monte Carlo Methods and Applications*, 16(1):1–67.

Beeler, G. W. and Reuter, H. (1977). Reconstruction of the action potential of ventricular myocardial fibres. *The Journal of physiology*, 268(1):177–210.

Berger, R. D., Kasper, E. K., Baughman, K. L., Marban, E., Calkins, H., and Tomaselli, G. F. (1997). Beat-to-Beat QT Interval Variability. *Circulation*, 96(5):1557–1565.

Berkaoui, A., Bossy, M., and Diop, A. (2008). Euler Scheme for SDEs with Non-Lipschitz Diffusion Coefficient: Strong Convergence. *ESAIM: Probability and Statistics*, 12:1+.

Bezanilla, F. (2000). The voltage sensor in voltage-dependent ion channels. *Physiological reviews*, 80(2):555–592.

Bezanilla, F. (2007). Voltage-Gated Ion Channels. In Greenbaum, E., Aizawa, M., Andersen, O. ., Austin, R. ., Barber, J., Berg, H. ., Bloomfield, V., Callender, R., Chance, B., Chu, S., DeFelice, L. ., Deisenhofer, J., Feher, G., Frauenfelder, H., Giaever, I., Gruner, S. ., Herzfeld, J., Joliot, P., Keszthelyi, L., Knox, R. ., Lewis, A., Lindsay, S. ., Mauzerall, D., Mielczarek, E. ., Niemz, M. ., Parsegian, V. d. r. i. a. n., Powers, L. ., Prohofsky, E. ., Rubin, A., Seibert, M., Thomas, D. ., Williamson, S. ., Chung, S.-H., Andersen, O. ., and Krishnamurthy, V., editors, *Biological Membrane Ion Channels*, Biological and Medical Physics Biomedical Engineering, chapter 3, pages 81–118. Springer New York, New York, NY.

Bhattacharya, R. N. and Waymire, E. C. (2007). *Stochastic Processes with Applications (Graduate Texts in Mathematics)*. Springer, 2nd edition.

Bossy, M., Gobet, E., and Talay, D. (2004). A Symmetrized Euler Scheme for an Efficient Approximation of Reflected Diffusions. *Journal of Applied Probability*, 41(3):877–889.

Britton, O., Bueno-Orovio, A., Van Ammel, K., Lu, H. R., Gallacher, D. J., Towart, R., and Rodriguez, B. (2012). Experimentally-calibrated population of models predicts and explains inter-subject variability in cardiac cellular electrophysiology. *In preparation*.

Bruce, I. C. (2007). Implementation Issues in Approximate Methods for Stochastic Hodgkin-Huxley Models. *Annals of Biomedical Engineering*, 35(2):315–318.

Bruce, I. C. (2009). Evaluation of stochastic differential equation approximation of ion channel gating models. *Annals of biomedical engineering*, 37(4):824–838.

Burrage, K. (1995). *Parallel and Sequential Methods for Ordinary Differential Equations (Numerical Mathematics and Scientific Computation)*. Oxford University Press, USA.

Burrage, K., Burrage, P. M., and Tian, T. (2004). Numerical methods for strong solutions of stochastic differential equations: an overview. *Proceedings of the Royal Society of London. Series A: Mathematical, Physical and Engineering Sciences*, 460(2041):373–402.

Chen, Y. and Ye, X. (2011). Projection Onto A Simplex. *ArXiv e-prints*.

Chow, C. and White, J. (1996). Spontaneous action potentials due to channel fluctuations. *Biophysical Journal*, 71(6):3013–3021.

Clancy, C. E. and Rudy, Y. (1999). Linking a genetic defect to its cellular phenotype in a cardiac arrhythmia. *Nature*, 400(6744):566–569.

Clancy, C. E., Zhu, Z. I., and Rudy, Y. (2007). Pharmacogenetics and anti-arrhythmic drug therapy: a theoretical investigation. *Am J Physiol Heart Circ Physiol*, 292(1):H66–75.

Combettes, P. L. and Wajs, V. R. (2005). Signal recovery by proximal forward-backward splitting. *Multiscale Modeling Simulation*, 4(4):1168–1200.

Corrias, A., Jie, X., Romero, L., Bishop, M. J., Bernabeu, M., Pueyo, E., and Rodriguez, B. (2010). Arrhythmic risk biomarkers for the assessment of drug cardiotoxicity: from experiments to computer simulations. *Philosophical Transactions of the Royal Society A: Mathematical, Physical and Engineering Sciences*, 368(1921):3001–3025.

Cox, J. C., Ingersoll, J. E., and Ross, S. A. (1985). A Theory of the Term Structure of Interest Rates. *Econometrica*, 53(2):385–407.

Dangerfield, C. E., Kay, D., and Burrage, K. (2010). Stochastic models and simulation of ion channel dynamics. *Procedia Computer Science*, 1(1):1581–1590.

Dangerfield, C. E., Kay, D., and Burrage, K. (2012). Modeling ion channel dynamics through reflected stochastic differential equations. *Physical Review E*, 85:051907+.

De Vries, G. and Sherman, A. (2000). Channel Sharing in Pancreatic Beta Cells Revisited:Enhancement of Emergent Bursting by Noise. *Journal of Theoretical Biology*, 207:513–530.

Decker, K. F., Heijman, J., Silva, J. R., Hund, T. J., and Rudy, Y. (2009). Properties and ionic mechanisms of action potential adaptation, restitution, and accommodation in canine epicardium. *American journal of physiology. Heart and circulatory physiology*, 296(4).

DeFelice, L. J. and Isaac, A. (1993). Chaotic states in a random world: Relationship between the nonlinear differential equations of excitability and the stochastic properties of ion channels. *Journal of Statistical Physics*, 70(1):339–354–354.

Detre, E., Thomsen, M. B., Beekman, J. D., Petersen, K.-U. U., and Vos, M. A. (2005). Decreasing the infusion rate reduces the proarrhythmic risk of NS-7: confirming the relevance of short-term variability of repolarisation in predicting drug-induced torsades de pointes. *British journal of pharmacology*, 145(3):397–404.

DiFrancesco, D. and Noble, D. (1985). A model of cardiac electrical activity incorporating ionic pumps and concentration changes. *Philosophical transactions of the Royal Society of London. Series B, Biological sciences*, 307(1133):353–398.

Ding, D. (2008). A splitting-step algorithm for reflected stochastic differential equations in R+1. *Computers & Mathematics with Applications*, 55(11):2413–2425.

Draper, N. R. and Smith, H. (1998). *Applied Regression Analysis (Wiley Series in Probability and Statistics)*. Wiley-Interscience, third edition.

Ellen, C., Kay, D., and Burrage, K. (2011). Comparison of continuous and discrete stochastic ion channel models. *Conference proceedings : ... Annual International Conference of the IEEE Engineering in Medicine and Biology Society. IEEE Engineering in Medicine and Biology Society. Conference*, 2011:704–707.

Elowitz, M. B., Levine, A. J., Siggia, E. D., and Swain, P. S. (2002). Stochastic Gene Expression in a Single Cell. *Science*, 297(5584):1183–1186.

Faber, G. and Rudy, Y. (2000). Action Potential and Contractility Changes in [Na+]i Overloaded Cardiac Myocytes: A Simulation Study. *Biophysical Journal*, 78(5):2392–2404.

Faber, G. M., Silva, J., Livshitz, L., and Rudy, Y. (2007). Kinetic properties of the cardiac L-type Ca2+ channel and its role in myocyte electrophysiology: a theoretical investigation. *Biophysical journal*, 92(5):1522–1543.

Fedida, D. and Giles, W. R. (1991). Regional variations in action potentials and transient outward current in myocytes isolated from rabbit left ventricle. *The Journal of physiology*, 442:191–209.

Feller, W. (1951). Two Singular Diffusion Problems. *The Annals of Mathematics*, 54(1):173–182.

Fink, M., Giles, W. R., and Noble, D. (2006). Contributions of inwardly rectifying K+ currents to repolarization assessed using mathematical models of human ventricular myocytes. *Philosophical transactions. Series A, Mathematical, physical, and engineering sciences*, 364(1842):1207–1222.

Fisher, R. A. (1930). *The Genetical Theory of Natural Selection*. Clarendon Press, Oxford.

Fox, R. (1997). Stochastic versions of the Hodgkin-Huxley equations. *Biophysical Journal*, 72(5):2068–2074.

Fox, R. F. and Lu, Y. N. (1994). Emergent collective behavior in large numbers of globally coupled independently stochastic ion channels. *Physical Review E*, 49(4):3421–3431.

Gard, T. C. (1987). *Introduction to Stochastic Differential Equations (Pure and Applied Mathematics)*. Marcel Dekker Inc.

Garny, A., Noble, D., Hunter, P. J., and Kohl, P. (2009). CELLULAR OPEN RESOURCE (COR): current status and future directions. *Philosophical Transactions of the Royal Society A: Mathematical, Physical and Engineering Sciences*, 367(1895):1885–1905.

Gihman, I. I. and Skorokhod, A. V. (1972). *Stochastic differential equations*. Berlin : Springer-Verlag.

Gillespie, D. (1976). A general method for numerically simulating the stochastic time evolution of coupled chemical reactions. *Journal of Computational Physics*, 22(4):403–434.

Gillespie, D. T. (1977). Exact stochastic simulation of coupled chemical reactions. *Journal of Physical Chemisty*, 81(25):2340–2361.

Gillespie, D. T. (1992). A rigorous derivation of the chemical master equation. *Physica A Statistical Mechanics and its Applications*, 188(1-3):404–425.

Gillespie, D. T. (2000). The chemical Langevin equation. *The Journal of Chemical Physics*, 113(1):297–306.

Gillespie, D. T. (2002). The Chemical Langevin and FokkerPlanck Equations for the Reversible Isomerization Reaction. *The Journal of Physical Chemistry A*, 106(20):5063–5071.

Gillespie, D. T. (2007). Stochastic Simulation of Chemical Kinetics. *Annuls Review Physics Chemical*, 58:35–55.

Gobet, E. (2001). Euler schemes and half-space approximation for the simulation of diffusion in a domain. *ESAIM: Probability and Statistics*, 5:261–297.

Goldwyn, J. H., Imennov, N. S., Famulare, M., and Shea-Brown, E. (2011). Stochastic differential equation models for ion channel noise in Hodgkin-Huxley neurons. *Physical Review E*, 83(4):041908+.

Goldwyn, J. H. and Shea-Brown, E. (2011). The What and Where of Adding Channel Noise to the Hodgkin-Huxley Equations. *PLoS Computational Biology*, 7(11):e1002247+.

Grandi, E., Pasqualini, F. S., and Bers, D. M. (2010). A novel computational model of the human ventricular action potential and Ca transient. *Journal of Molecular and Cellular Cardiology*, 48(1):112–121.

Griffiths, R. (1979). On the distribution of allele frequencies in a diffusion model. *Theoretical Population Biology*, 15(1):140–158.

Griffiths, R. (1980). Allele frequencies in multidimensional Wright-Fisher models with a general symmetric mutation structure. *Theoretical Population Biology*, 17(1):51–70.

Groff, J. R., DeRemigio, H., and Smith, G. D. (2010). Markov chain models of ion channels and the collective gating of Ca2 + release sites. In Laing, C. and Gabriel, L., editors, *Stochastic Methods in Neuroscience*, pages 29–64. Oxford: Oxford University Press.

Gy (1992). *Sampling of Heterogeneous and Dynamic Material Systems*. Elsevier Science Ltd.

Hall, B. C. (2003). *Lie Groups, Lie Algebras, and Representations: An Elementary Introduction*. Springer, second printing edition.

Halley, W., Malham, S. J. A., and Wiese, A. (2008). Positive stochastic volatility simulation. *ArXiv e-prints*.

Halley, W., Malham, S. J. A., and Wiese, A. (2009). Positive and implicit stochastic volatility simulation. *ArXiv e-prints*.

Hamill, O. P., Marty, A., Neher, E., Sakmann, B., and Sigworth, F. J. (1981). Improved patch-clamp techniques for high-resolution current recording from cells and cell-free membrane patches. *Pflügers Archiv : European journal of physiology*, 391(2):85–100.

Higham, D. and Mao, X. (2005). Convergence of Monte Carlo Simulations Involving the Mean-Reverting Square Root Process. *Journal of Computational Finance*, 8(3):35–61.

Higham, D. J. (2001). An Algorithmic Introduction to Numerical Simulation of Stochastic Differential Equations. *SIAM Review*, 43(3).

Higham, D. J. (2011). Stochastic ordinary differential equations in applied and computational mathematics. *IMA Journal of Applied Mathematics*, 76(3):449–474.

Higham, D. J., Mao, X., and Stuart, A. M. (2003). Strong Convergence of Euler-Type Methods for Nonlinear Stochastic Differential Equations. *SIAM Journal on Numerical Analysis*, 40(3):1041–1063.

Hille, B. (1991). *Ionic Channels of Excitable Membranes*. Sinauer Associates, third edition.

Hinterseer, M., Beckmann, B.-M. M., Thomsen, M. B., Pfeufer, A., Dalla Pozza, R., Loeff, M., Netz, H., Steinbeck, G., Vos, M. A., and Kääb, S. (2009). Relation of increased short-term variability of QT interval to congenital long-QT syndrome. *The American journal of cardiology*, 103(9):1244–1248.

Hinterseer, M., Beckmann, B.-M. M., Thomsen, M. B., Pfeufer, A., Ulbrich, M., Sinner, M. F., Perz, S., Wichmann, H.-E. E., Lengyel, C., Schimpf, R., Maier, S. K., Varró, A., Vos, M. A., Steinbeck, G., and Kääb, S. (2010). Usefulness of short-term variability of QT intervals as a predictor for electrical remodeling and proarrhythmia in patients with nonischemic heart failure. *The American journal of cardiology*, 106(2):216–220.

Hinterseer, M., Thomsen, M. B., Beckmann, B.-M. M., Pfeufer, A., Schimpf, R., Wichmann, H.-E. E., Steinbeck, G., Vos, M. A., and Kaab, S. (2008). Beat-to-beat variability of QT intervals is increased in patients with drug-induced long-QT syndrome: a case control pilot study. *European heart journal*, 29(2):185–190.

Hodgkin, A. L. and Huxley, A. F. (1952). A quantitative description of membrane current and its application to conduction and excitation in nerve. *Journal of Physiology*, 117(1):500–544.

Hondeghem, L. M. (2006). Thorough QT/QTc not so thorough: removes torsadogenic predictors from the T-wave, incriminates safe drugs, and misses profibrillatory drugs. *Journal of cardiovascular electrophysiology*, 17(3):337–340.

Hondeghem, L. M. (2008). QT and TdP. QT: an unreliable predictor of proarrhythmia. *Acta cardiologica*, 63(1):1–7.

Hund, T. J. and Rudy, Y. (2004). Rate dependence and regulation of action potential and calcium transient in a canine cardiac ventricular cell model. *Circulation*, 110(20):3168–3174.

Jahnke, T. and Huisinga, W. (2007). Solving the chemical master equation for monomolecular reaction systems analytically. *Journal of Mathematical Biology*, 54(1):1–26.

Johnson, D. M., Heijman, J., Pollard, C. E., Valentin, J.-P. P., Crijns, H. J., Abi-Gerges, N., and Volders, P. G. (2010). I(Ks) restricts excessive beat-to-beat variability of repolarization during beta-adrenergic receptor stimulation. *Journal of molecular and cellular cardiology*, 48(1):122–130.

Jost, N., Virág, L., Bitay, M., Takács, J., Lengyel, C., Biliczki, P., Nagy, Z., Bogáts, G., Lathrop, D. A., Papp, J. G., and Varró, A. (2005). Restricting excessive cardiac action potential and QT prolongation: a vital role for IKs in human ventricular muscle. *Circulation*, 112(10):1392–1399.

Kaern, M., Elston, T. C., Blake, W. J., and Collins, J. J. (2005). Stochasticity in gene expression: from theories to phenotypes. *Nature reviews. Genetics*, 6(6):451–464.

Kahl, C. and Jäckel, P. (2006). Fast strong approximation Monte Carlo schemes for stochastic volatility models. *Quantitative Finance*, 6(6):513–536.

Kahl, C. and Schurz, H. (2005). Balanced Milstein Methods for Ordinary SDEs. *Technical report, Department of Mathematics, Southern Illinois University*.

Karatzas, I. and Shreve, S. E. (1991). *Brownian Motion and Stochastic Calculus (Graduate Texts in Mathematics)*. Springer, 2nd edition.

Karlin, S. and Taylor, H. M. (1981). *A Second Course in Stochastic Processes*. Academic Press.

Katz, A. M. (2005). *Physiology of the Heart*. Lippincott Williams & Wilkins, fourth edition.

Khanin, R. and Higham, D. J. (2008). Chemical Master Equation and Langevin regimes for a gene transcription model. *Theoretical Computer Science*, 408(1):31–40.

Klebaner, F. C. (2012). *Introduction to Stochastic Calculus With Applications*. Imperial College Press, 3 edition.

Kloeden, P. E. and Platen, E. (2011). *Numerical Solution of Stochastic Differential Equations (Stochastic Modelling and Applied Probability)*. Springer, corrected edition.

Krogh-Madsen, T. (2004). Effects of single-channel noise on spontaneous beating and the phase-resetting response of cardiac oscillators. *DPhil Thesis, Department of Physiology McGill University, Montreal*.

Kurtz, T. G. (2007). Lectures on Stochastic Analysis. *Departments of Mathematics and Statistics University of Wisconsin*.

Lemay, M., de Lange, E., and Kucera, J. P. (2011). Effects of stochastic channel gating and distribution on the cardiac action potential. *Journal of theoretical biology*, 281(1):84–96.

Lengyel, C., Iost, N., Virág, L., Varró, A., Lathrop, D. A., and Papp, J. G. (2001). Pharmacological block of the slow component of the outward delayed rectifier current (I(Ks)) fails to lengthen rabbit ventricular muscle QT(c) and action potential duration. *British journal of pharmacology*, 132(1):101–110.

Lengyel, C., Varró, A., Tábori, K., Papp, J. G., and Baczkó, I. (2007). Combined pharmacological block of I(Kr) and I(Ks) increases short-term QT interval variability and provokes torsades de pointes. *British journal of pharmacology*, 151(7):941–951.

Lépingle, D. (1995). Euler scheme for reflected stochastic differential equations. *Mathematics and Computers in Simulation*, 38(1):119–126.

Lingle, C. J. (2006). Empirical considerations regarding the use of ensemble-variance analysis of macroscopic currents. *Journal of neuroscience methods*, 158(1):121–132.

Lions, P. L. and Sznitman, A. S. (1984). Stochastic Boundary Equations with Reflecting Boundary Conditions. *Communications on Pure and Applied Mathematics*, 37:511–537.

Liu, Y. (1995). Discretization of a class of reflected diffusion processes. *Mathematics and Computers in Simulation*, 38(1-3):103–108.

Lloyd, C. M., Halstead, M. D., and Nielsen, P. F. (2004). CellML: its future, present and past. *Progress in biophysics and molecular biology*, 85(2-3):433–450.

Lord, R., Koekkoek, R., and Dijk, D. V. (2010). A comparison of biased simulation schemes for stochastic volatility models. *Quantitative Finance*, 10(2):177–194.

Luo, C. H. and Rudy, Y. (1991). A model of the ventricular cardiac action potential. Depolarization, repolarization, and their interaction. *Circulation Research*, 68(6):1501–1526.

Luo, C. H. and Rudy, Y. (1994a). A dynamic model of the cardiac ventricular action potential. I. Simulations of ionic currents and concentration changes. *Circulation Research*, 74(6):1071–1096.

Luo, C. H. and Rudy, Y. (1994b). A dynamic model of the cardiac ventricular action potential. II. Afterdepolarizations, triggered activity, and potentiation. *Circulation Research*, 74(6):1097–1113.

MacNamara, S. and Burrage, K. (2009). Krylov and steady-state techniques for the solution of the chemical master equation for the mitogen-activated protein kinase cascade. *Numerical Algorithms*, 51(3):281–307.

Mao, X. (2011). *Stochastic Differential Equations and Applications*. Woodhead Publishing, second edition edition.

Marder, E. (2011). Variability, compensation, and modulation in neurons and circuits. *Proceedings of the National Academy of Sciences*, 108(Supplement 3):15542–15548.

Marder, E. and Taylor, A. L. (2011). Multiple models to capture the variability in biological neurons and networks. *Nature neuroscience*, 14(2):133–138.

Maruyama, G. (1955). Continuous Markov processes and stochastic equations. *Rendiconti del Circolo Matematico di Palermo*, 4(1):48–90.

McAllister, R. E., Noble, D., and Tsien, R. W. (1975). Reconstruction of the electrical activity of cardiac Purkinje fibres. *The Journal of physiology*, 251(1):1–59.

McKay, M. D., Beckman, R. J., and Conover, W. J. (1979). A Comparison of Three Methods for Selecting Values of Input Variables in the Analysis of Output from a Computer Code. *Technometrics*, 42(1):55–61.

Melykuti, B., Burrage, K., and Zygalakis, K. C. (2010). Fast stochastic simulation of biochemical reaction systems by alternative formulations of the chemical Langevin equation. *The Journal of Chemical Physics*, 132(16).

Menaldi, J. (1983). Stochastic Variational Inequality for Reflected Diffusion. *Indiana University Mathematics Journal*, 32(5):733–744.

Milstein, G. N. (1979). A Method of Second-Order Accuracy Integration of Stochastic Differential Equations. *Theory of Probability and its Applications*, 23(2):396–401.

Milstein, G. N., Platen, E., and Schurz, H. (1998). Balanced Implicit Methods for Stiff Stochastic Systems. *SIAM Journal of Numerical Anaysis*, 35(3):1010–1019.

Mino, H., Rubinstein, J. T., and White, J. A. (2002). Comparison of Algorithms for the Simulation of Action Potentials with Stochastic Sodium Channels. *Annals of Biomedical Engineering*, 30(4):578–587–587.

Mitra, R. and Morad, M. (1985). A uniform enzymatic method for dissociation of myocytes from hearts and stomachs of vertebrates. *The American journal of physiology*, 249(5):H1056–1060.

Moro, E. and Schurz, H. (2007). Boundary Preserving Semianalytic Numerical Algorithms for Stochastic Differential Equations. *SIAM Journal on Scientific Computing*, 29(4):1525–1549.

Neher, E. and Sakmann, B. (1976). Single-channel currents recorded from membrane of denervated frog muscle fibres. *Nature*, 260(5554):799–802.

Ninomiya, S. and Victoir, N. (2008). Weak approximation of stochastic differential equations and application to derivative pricing. *Applied Mathematical Finance*, 15(2):107–121.

Noble, D. (1962). A modification of the hodgkin-huxley equations applicable to purkinje fibre action and pace-maker potentials. *Journal of Physiology*, 160:317–352.

Noble, D., Garny, A., and Noble, P. J. (2012). How the HodgkinHuxley equations inspired the Cardiac Physiome Project. *The Journal of Physiology*, 590(11):2613–2628.

O'Hara, T., Virág, L., Varró, A., and Rudy, Y. (2011). Simulation of the Undiseased Human Cardiac Ventricular Action Potential: Model Formulation and Experimental Validation. *PLoS Computational Biology*, 7(5):e1002061+.

Øksendal, B. (2010). *Stochastic Differential Equations: An Introduction with Applications (Universitext)*. Springer, 6th edition.

Oosterhoff, P., Oros, A., and Vos, M. A. (2007). Beat-to-beat variability of repolarization: a new parameter to determine arrhythmic risk of an individual or identify proarrhythmic drugs. *The Anatolian Journal of Cardiology*, 7 Suppl 1:73–78.

Oosterhoff, P., Tereshchenko, L. G., van der Heyden, M. A., Ghanem, R. N., Fetics, B. J., Berger, R. D., and Vos, M. A. (2011). Short-term variability of repolarization predicts ventricular tachycardia and sudden cardiac death in patients with structural heart disease: a comparison with QT variability index. *Heart rhythm : the official journal of the Heart Rhythm Society*, 8(10):1584–1590.

Orio, P. and Soudry, D. (2012). Simple, Fast and Accurate Implementation of the Diffusion Approximation Algorithm for Stochastic Ion Channels with Multiple States. *PLoS ONE*, 7(5):e36670+.

Pakdaman, K., Thieullen, M., and Wainrib, G. (2010). Fluid limit theorems for stochastic hybrid systems with application to neuron models. *Advancements in Applied Probability*, 42(3):761–794.

Pettersson, R. (1995). Approximations for stochastic differential equations with reflecting convex boundaries. *Stochastic Processes and their Applications*, 59(2):295–308.

Pettersson, R. (1997). Penalization Schemes for Reflecting Stochastic Differential Equations. *Bernoulli*, 3(4):403–414.

Priebe, L. and Beuckelmann, D. J. (1998). Simulation Study of Cellular Electric Properties in Heart Failure. *Circulation Research*, 82(11):1206–1223.

Pueyo, E., Corrias, A., Virág, L., Jost, N., Szél, T., Varró, A., Szentandrássy, N., Nánási, P. P., Burrage, K., and Rodríguez, B. (2011). A multiscale investigation of repolarization variability and its role in cardiac arrhythmogenesis. *Biophysical journal*, 101(12):2892–2902.

Pueyo, E., Husti, Z., Hornyik, T., Baczkó, I., Laguna, P., Varró, A., and Rodríguez, B. (2010). Mechanisms of ventricular rate adaptation as a predictor of arrhythmic risk. *American journal of physiology. Heart and circulatory physiology*, 298(5).

Pullan, A. J., Cheng, L. K., and Buist, M. L. (2005). *Mathematically Modeling the Electrical Activity of the Heart: From Cell to Body Surface and Back*. World Scientific Publishing Company.

Raj, A. and van Oudenaarden, A. (2008). Nature, nurture, or chance: stochastic gene expression and its consequences. *Cell*, 135(2):216–226.

Roden, D. M. (1998). Taking the idio out of idiosyncratic: predicting torsades de pointes. *Pacing and clinical electrophysiology : PACE*, 21(5):1029–1034.

Romero, L., Pueyo, E., Fink, M., and Rodríguez, B. (2009). Impact of ionic current variability on human ventricular cellular electrophysiology. *American journal of physiology. Heart and circulatory physiology*, 297(4):H1436–H1445.

Rubinstein, J. T. (1995). Threshold fluctuations in an N sodium channel model of the node of Ranvier. *Biophysical journal*, 68(3):779–785.

Rudy, Y. and Silva, J. R. (2006). Computational biology in the study of cardiac ion channels and cell electrophysiology. *Quarterly Reviews of Biophysics*, 39(01):57–116.

Sanguinetti, M. C. (2000). Long QT syndrome: ionic basis and arrhythmia mechanism in long QT syndrome type 1. *Journal of cardiovascular electrophysiology*, 11(6):710–712.

Sarkar, A. X., Christini, D. J., and Sobie, E. A. (2012). Exploiting mathematical models to illuminate electrophysiological variability between individuals. *The Journal of Physiology*, 590(11):2555–2567.

Sarkar, A. X. and Sobie, E. A. (2011). Quantification of repolarization reserve to understand interpatient variability in the response to proarrhythmic drugs: a computational analysis. *Heart rhythm : the official journal of the Heart Rhythm Society*, 8(11):1749–1755.

Schmid, G., Goychuk, I., and Hänggi, P. (2004). Effect of channel block on the spiking activity of excitable membranes in a stochastic HodgkinHuxley model. *Physical Biology*, 1(2):61–66.

Schneider, J., Hauser, R., Andreas, J.-O. O., Linz, K., and Jahnel, U. (2005). Differential effects of human ether-a-go-go-related gene (HERG) blocking agents on QT duration variability in conscious dogs. *European journal of pharmacology*, 512(1):53–60.

Schneidman, E., Freedman, B., and Segev, I. (1998). Ion channel stochasticity may be critical in determining the reliability and precision of spike timing. *Neural computation*, 10(7):1679–1703.

Schurz, H. (1996). Numerical regularization for SDE's: Construction of nonnegative solutions. *Dynamical Systems Appllications*, (5):323–352.

Sengupta, B., Laughlin, S. B., and Niven, J. E. (2010). Comparison of Langevin and Markov channel noise models for neuronal signal generation. *Physical review. E*, 81(1):011918+.

Seshadri, V. (1988). Exponential Models, Brownian Motion, and Independence. *The Canadian Journal of Statistics*, 16(3):209–221.

Shah, R. R. and Hondeghem, L. M. (2005). Refining detection of drug-induced proarrhythmia: QT interval and TRIaD. *Heart rhythm : the official journal of the Heart Rhythm Society*, 2(7):758–772.

Shibasaki, T. (1987). Conductance and kinetics of delayed rectifier potassium channels in nodal cells of the rabbit heart. *The Journal of physiology*, 387:227–250.

Skorokhod, A. V. (1961). Stochastic Equations for Diffusion Processes in a Bounded Region. *Theory of Probability and its Applications*, 6(3):264–274.

Skorokhod, A. V. (1962). Stochastic Equations for Diffusion Processes in a Bounded Region. II. *Theory of Probability and its Applications*, 7(1):3–23.

Slominski, L. (1994). On approximation of solutions of multidimensional SDE's with reflecting boundary conditions. *Stochastic Processes and their Applications*, 50(2):197–219.

Smaill, B. H. and Hunter, P. J. (2010). Computer Modeling of Electrical Activation: From Cellular Dynamics to the Whole Heart Cardiac Electrophysiology Methods and Models. In

Sigg, D. C., Iaizzo, P. A., Xiao, Y.-F., and He, B., editors, *Cardiac Electrophysiology Methods and Models*, chapter 8, pages 159–185. Springer US, Boston, MA.

Snyders, D. J. and Chaudhary, A. (1996). High affinity open channel block by dofetilide of HERG expressed in a human cell line. *Molecular Pharmacololgy*, 49(6):949–955.

Stirk, E. R., Lythe, G., van den Berg, H. A., Hurst, G. A. D., and Molina-París, C. (2010). The limiting conditional probability distribution in a stochastic model of T cell repertoire maintenance. *Mathematical Biosciences*, 224(2):74–86.

Strang, G. (1968). On the Construction and Comparison of Difference Schemes. *SIAM Journal on Numerical Analysis*, 5(3):506–517.

Strassberg, A. F. and DeFelice, L. J. (1993). Limitations of the Hodgkin-Huxley Formalism: Effects of Single Channel Kinetics on Transmembrane Voltage Dynamics. *Neural Computation*, 5(6):843–855.

Sun, X. J., Lei, J. Z., Perc, M., Lu, Q. S., and Lv, S. J. (2011). Effects of channel noise on firing coherence of small-world Hodgkin-Huxley neuronal networks. *The European Physical Journal B - Condensed Matter and Complex Systems*, 79(1):61–66.

Swain, P. S., Elowitz, M. B., and Siggia, E. D. (2002). Intrinsic and extrinsic contributions to stochasticity in gene expression. *Proceedings of the National Academy of Sciences of the United States of America*, 99(20):12795–12800.

Szabó, A., Szentandrássy, N., Birinyi, P., Horváth, B., Szabó, G., Bányász, T., Márton, I., Nánási, P. P., and Magyar, J. (2007). Effects of articaine on action potential characteristics and the underlying ion currents in canine ventricular myocytes. *British journal of anaesthesia*, 99(5):726–733.

Szentandrássy, N., Harmati, G., Bárándi, L., Simkó, J., Horváth, B., Magyar, J., Bányász, T., Lorincz, I., Szebeni, A., Kecskeméti, V., and Nánási, P. P. (2011). Effects of rosiglitazone on the configuration of action potentials and ion currents in canine ventricular cells. *British journal of pharmacology*, 163(3):499–509.

Takahara, A., Nakamura, Y., and Sugiyama, A. (2008). Beat-to-beat variability of repolarization differentiates the extent of torsadogenic potential of multi ion channel-blockers bepridil and amiodarone. *European journal of pharmacology*, 596(1-3):127–131.

Tanaka, H. (1979). Stochastic differential equations with reflecting boundary condition in convex regions. *Hiroshima Mathematics Journal*, 9(1):162–177.

Tanskanen, A. J., Greenstein, J. L., O'Rourke, B., and Winslow, R. L. (2005). The role of stochastic and modal gating of cardiac L-type Ca2+ channels on early after-depolarizations. *Biophysical journal*, 88(1):85–95.

Thomsen, M. B., Oros, A., Schoenmakers, M., van Opstal, J. M., Maas, J. N., Beekman, J. D. M., and Vos, M. A. (2007). Proarrhythmic electrical remodelling is associated with increased beat-to-beat variability of repolarisation. *Cardiovascular Research*, 73(3):521–530.

Thomsen, M. B., Truin, M., van Opstal, J. M., Beekman, J. D., Volders, P. G., Stengl, M., and Vos, M. A. (2005). Sudden cardiac death in dogs with remodeled hearts is associated with larger beat-to-beat variability of repolarization. *Basic research in cardiology*, 100(3):279–287.

Thomsen, M. B., Verduyn, S. C., Stengl, M., Beekman, J. D., de Pater, G., van Opstal, J., Volders, P. G., and Vos, M. A. (2004). Increased short-term variability of repolarization predicts d-sotalol-induced torsades de pointes in dogs. *Circulation*, 110(16):2453–2459.

Thomsen, M. B., Volders, P. G., Beekman, J. D., Matz, J., and Vos, M. A. (2006). Beat-to-Beat variability of repolarization determines proarrhythmic outcome in dogs susceptible to drug-induced torsades de pointes. *Journal of the American College of Cardiology*, 48(6):1268–1276.

Tusscher, K. H. W. J. T., Noble, D., Noble, P. J., and Panfilov, A. V. (2004). A model for human ventricular tissue. *American Journal of Physiology - Heart and Circulatory Physiology*, 286(4):H1573–H1589.

Tusscher, K. H. W. J. T. and Panfilov, A. V. (2006a). Alternans and spiral breakup in a human ventricular tissue model. *American Journal of Physiology - Heart and Circulatory Physiology*, 291(3):H1088–H1100.

Tusscher, K. H. W. J. T. and Panfilov, A. V. (2006b). Cell model for efficient simulation of wave propagation in human ventricular tissue under normal and pathological conditions. *Physics in Medicine and Biology*, 51(23):6141–6156.

Tytgat, J. (1994). How to isolate cardiac myocytes. *Cardiovascular Research*, 28(2):280–283.

Van Kampen, N. G. (2007). *Stochastic Processes in Physics and Chemistry, Third Edition (North-Holland Personal Library)*. North Holland, 3 edition.

Vandenberg, J. I., Walker, B. D., and Campbell, T. J. (2001). HERG K+ channels: friend and foe. *Trends in pharmacological sciences*, 22(5):240–246.

Varró, A. and Baczkó, I. (2011). Cardiac ventricular repolarization reserve: a principle for understanding drug-related proarrhythmic risk. *British Journal of Pharmacology*, 164(1):14–36.

Varro, A., Baláti, B., Iost, N., Takács, J., Virág, L., Lathrop, D. A., Csaba, L., Tálosi, L., and Papp, J. G. (2000). The role of the delayed rectifier component IKs in dog ventricular muscle and Purkinje fibre repolarization. *The Journal of Physiology*, 523:67–81.

Veldkamp, M. W., van Ginneken, A. C., and Bouman, L. N. (1993). Single delayed rectifier channels in the membrane of rabbit ventricular myocytes. *Circulation Research*, 72(4):865–878.

Veldkamp, M. W., van Ginneken, A. C., Opthof, T., and Bouman, L. N. (1995). Delayed rectifier channels in human ventricular myocytes. *Circulation*, 92(12):3497–3504.

Verveen, A. A. and Derksen, H. E. (1968). Fluctuation phenomena in nerve membrane. *Proceedings of the IEEE*, 56(6):906–916.

Wantanebe, S. (1971). On stochastic differential equations for multi-dimensional diffusion processes with boundary conditions. *Journal of Mathematics Kyoto University*, 11(1):169–180.

White, J. A., Rubinstein, J. T., and Kay, A. R. (2000). Channel noise in neurons. *Trends in neurosciences*, 23(3):131–137.

Wright, S. (1931). Evolution in Mendelian Populations. *Genetics*, 16(2):97–159.

Xiao, L., Xiao, J., Luo, X., Lin, H., Wang, Z., and Nattel, S. (2008). Feedback remodeling of cardiac potassium current expression: a novel potential mechanism for control of repolarization reserve. *Circulation*, 118(10):983–992.

Xin, G., Zhou, J., Nattel, S., and Koren, G. (2004). Single-channel recordings of a rapid delayed rectifier current in adult mouse ventricular myocytes: basic properties and effects of divalent cations. *The Journal of Physiology*, 556(Pt 2):401–413.

Zaniboni, M., Pollard, A. E., Yang, L., and Spitzer, K. W. (2000). Beat-to-beat repolarization variability in ventricular myocytes and its suppression by electrical coupling. *American Journal of Physiology - Heart and Circulatory Physiology*, 278(3):H677–H687.